Metabolic Networks in Pancreatic Cancer

by

Samuel A. Kerk

A dissertation submitted in partial fulfillment
of the requirements for the degree of
Doctor of Philosophy
(Cancer Biology)
in the University of Michigan
2023

Doctoral Committee:

Professor Carole A. Parent, Chair
Associate Professor Costas A. Lyssiotis
Associate Professor Deepak Nagrath
Professor Yatrik M. Shah
Professor Stephen J. Weiss

Samuel Kerk

skerk@umich.edu

ORCID iD: 0000-0001-9786-2245

Dedication

To my family, friends, and mentors for supporting me tirelessly, encouraging me wholeheartedly, and guiding me faithfully. And, most importantly, to all those afflicted by this terrible disease looking to science for hope.

Acknowledgements

First, Costas and Yatrik, thank you for not only guiding me scientifically, but for being role models both professionally and personally. I will spend the rest of my scientific career striving to emulate your ardor, curiosity, and work ethic. Also, thank you to my former undergraduate mentor, Larry Louters; I never would have been able to achieve any of this without your support.

I would also like to thank the members of the Lyssiotis and Shah labs for the collegial, collaborative, and respectful atmosphere in which I had the privilege to work for nearly six years. Thank you to the investigators, trainees, and staff of the Pancreatic Tumor Eradication Alliance (PanTERA). I believe it is abundantly clear from the long list of authors on my papers just how much help and support I've received from so many sources; I am grateful for and have learned from each and every one of you. And to my committee, I sincerely looked forward to our meetings as I knew I would receive valuable, insightful feedback. Thank you for keeping my dissertation on track and supporting me every step along the way.

To my friends both near and far, this journey was infinitely richer and more worthwhile with you. Matt and Stef, thank you for being the most steadfast friends for so many years (and the best Quarantine Pod). We have already shared so many experiences and I know we will make many more memories in this next chapter. Aric, Ben, Brian, Kevin, Mike – this has been the time of my life and you all have played such

an integral part. Thank you for always being down for a good time and helping me not take myself too seriously.

I am extraordinarily fortunate to have expanded my family during grad school. To my in-laws, Dwayne, Colleen, George, Patrick, and Mel, along with the entire extended family, thank you for truly welcoming me into your clan and making me feel loved and supported from the very beginning. You have shown enduring support and patience with me for which I will always be grateful. Thank you for teaching me new things, bringing me along on adventures, and broadening my life in the best possible ways.

To my mom and dad, Andy and Julie, you are my heroes. You have given me every tool and opportunity to succeed, and my goals have always been to make the most of that and make you proud. You have supported me in every endeavor, through successes and failures. You instilled in me a love of learning and encouraged my curiosity. Whatever drive and work ethic I have, I learned from watching you two in your professions. I love you immensely and will always be grateful I lucked out having you as my parents. Jonah, you have always pushed me to better, even if it was disguised in the most creatively irritating forms of brotherly love. Thank you for simply being my brother.

Finally, and most importantly, to my wife, Claire, thank you for your limitless love, unending patience, and unwavering support throughout grad school. Your creativity, enthusiasm, grace, selflessness, and never-ending drive amaze and inspire me every day. I love you and I know our best years are ahead of us as we embark on this exciting next adventure.

Table of Contents

List of Figures

Abstract

Cancer metabolism involves the mechanisms by which transformed cells utilize nutrients to sustain oncogenic programs. Cell-intrinsic rewiring of metabolism inherent to the tissue of origin is directed by activation of oncogenic drivers and loss of tumor suppressors. Cell-extrinsic metabolic crosstalk is determined by tissue architecture and resident cellular populations as well as nutrient availability. Together, this dysregulated metabolism promotes the overall growth and survival of cancer cells. Furthermore, distinct metabolic requirements of cancer cells present potential therapeutic opportunities.

My thesis work has focused on cancer metabolism in the context of pancreatic cancer, a deadly disease for which effective alternative treatment strategies are desperately needed. As background, Chapter 1 presents a comprehensive and nuanced review on the current knowledge of pancreatic cancer metabolism, compared and contrasted with lung and colon cancer. This introductory chapter covers 1) how activation of oncogenic driver genes and/or loss of tumor-suppressor genes influence metabolic pathways in pancreatic cancer, 2) distinct metabolic programs inherent to the cells/tissue of origin, 3) unique metabolic crosstalk determined by tissue architecture, and 4) potential therapeutic inroads targeting tumor metabolism.

Chapter 2 describes the identification of a novel nutrient scavenging pathway in pancreatic cancer cells. Critical glycosylation products needed for post-translation protein modifications are synthesized de novo using the hexosamine biosynthesis

pathway (HBP). However, pancreatic cancer cells are able to compensate for inhibition of this pathway by scavenging downstream products from the extracellular environment. Dual inhibition of both the HBP and scavenging mechanisms blocked this metabolic rewiring.

The remaining chapters of this dissertation center on mitochondrial glutamate-oxaloacetate transaminase 2 (GOT2), beginning with a review of the current literature related to GOT2 in cancer (Chapter 3). Chapter 4 demonstrates while GOT2 is required for in vitro pancreatic cancer cell proliferation, loss of GOT2 has no effect on the growth of pancreatic tumor growth and progression in vivo. GOT2 loss leads to intracellular reductive stress which can be ameliorated through uptake of environmental pyruvate in tumors. The generation of novel, physiologically relevant genetically engineered mouse models of GOT2 loss in murine pancreatic tumorigenesis and tumor growth is presented in Chapter 5, further supporting the finding that GOT2 is dispensable for in vivo pancreatic tumor growth.

Chapter 6 delves into the metabolic reprogramming of pro-tumorigenic immune cells in the pancreatic tumor microenvironment using genetic models of Got1 or Got2 deletion in myeloid cells. Specifically, tumor-associated macrophages have been implicated in chemoresistance, immunosuppression, and pro-growth signaling in pancreatic cancer. Since Got1/Got2-related metabolism underlies several of these mechanisms, this chapter contains preliminary data using both ex vivo and in vivo models to determine if targeting Got1/Got2 metabolism in myeloid cells is a viable strategy to reprogram macrophages from pro- to anti-tumorigenic states in pancreatic tumors.

The metabolic pathways necessary during development are often inappropriately re-activated in cancer. Therefore, understanding metabolic developmental defects can shed light on cancer metabolism. Indeed, global, constitutive deletion of Got2 is embryonic lethal in mice and inducible deletion in adult mice results in body weight loss and a failure to thrive. Chapter 7 characterizes the phenotypes involving Got2 loss in both embryonic and adult mice and proposes future interventions to resolve this metabolic defect, drawing from knowledge gleaned studying the role of GOT2 in pancreatic cancer. Finally, Chapter 8 concludes this dissertation by discussing future directions and highlighting key concepts in cancer metabolism.

Chapter 1 – Introduction to Pancreatic Cancer Metabolism*

1.1 Overview

Pancreatic ductal adenocarcinoma (PDA), the most common form of pancreatic cancer, is a deadly disease with few effective therapies. Patients typically present with late-stage, inoperable, metastatic disease refractory to radiation, chemotherapy, or immunotherapy. Mutant KRAS (KRAS*) is the oncogenic driver in >95% of PDA and, thus far, has not been successfully targeted in this context. Furthermore, PDA tumors develop a desmoplastic tumor microenvironment (TME) composed of prominent stromal and immune compartments shown to promote treatment resistance and suppress anti-tumor immunity. The dense, inflamed pancreatic TME also collapses and/or prevents vascularization. As such, the various cell types in the tumor experience extreme gradients of oxygen, pH, waste, and nutrients. This forces both malignant and supporting cell types to rely on alternative metabolic pathways to sustain pro-tumorigenic functions. As an alternative approach to targeting PDA, these distinct metabolic networks in PDA present potential therapeutic avenues. In this chapter, I comprehensively review PDA metabolism to provide a framework for the work described in subsequent chapters of this dissertation. For reference, I also compare and contrast PDA with two other KRAS*-driven cancers, non-small cell lung cancer (NSCLC) and

* This chapter consists of a published review article: **Kerk SA**, Papagiannakopoulos T, Shah YM, Lyssiotis CA. Metabolic networks in mutant KRAS-driven tumours: tissue specificities and the microenvironment. ***Nat Rev Cancer***. 2021 Aug;21(8):510-525. doi: 10.1038/s41568-021-00375-9. Epub 2021 Jul 9. PMID: 34244683.

colorectal carcinoma (CRC), to illustrate shared and distinct metabolic features between different malignancies.

1.2 Oncogenic KRAS rewiring of cancer metabolism

The RAS family of proteins is ubiquitously expressed in mammals and consists of *KRAS*, *NRAS*, and *HRAS* isoforms(1). RAS proteins drive signaling through growth and survival pathways, such as the phosphatidylinositol-3-kinase (PI3K) and mitogen activated protein kinase (MAPK) cascades(2). Point mutations in genes encoding RAS proteins are common across numerous cancer types(3, 4). Among these, *KRAS* is most frequently mutated in colorectal carcinoma (CRC, 40%), non-small cell lung cancer (NSCLC, 35%), and pancreatic ductal adenocarcinoma (PDA, >95%)(5), and its associated oncogenic activity is implicated in all the hallmarks of cancer(6, 7). *KRAS* mutations render the protein constitutively active, thereby driving signaling through pro-growth and anti-apoptotic pathways in the absence of stimulation. Thus, in principle, KRAS has considerable potential as an oncology drug target. Indeed, substantial progress has been made in recent years developing potent, $KRAS^{G12C}$ isoform-specific inhibitors(2, 6, 8, 9). Tempering this optimism, a significant percentage of oncogenic mutant KRAS (KRAS*) tumors are not driven by G12C mutations, and the complexity of RAS signaling still presents a significant therapeutic obstacle.

Despite *KRAS* mutations being common among colon, lung, and pancreas tumors, nuanced aspects of KRAS signaling and tissue physiology differentially influence how KRAS* impacts cancer biology. Expression levels of KRAS*, as well as the specific mutations to *KRAS*, influence its activity and also differ between the tissues of origin(10-12). For example, NSCLC more frequently harbors the tobacco smoking-

associated KRAS^{G12C} mutation, while the KRAS^{G12D} mutation is predominant in PDA[5]. In contrast to PDA and NSCLC where KRAS* is the disease initiating event, *KRAS* mutations are secondary hits in CRC progression(13-15). The expression levels and activity of KRAS* can also vary based on mutation type(10).

Adding further complexity, tissue-specific, co-occurring mutations cooperate with KRAS* to dictate downstream effector signaling(16). And, the unique physiological function, architecture, and cellular composition of the tissue of origin impact crosstalk between KRAS*-driven cancer cells and surrounding parenchymal, stromal, and immune cell types(17-19). Thus, despite sharing the expression of KRAS* protein, CRC, NSCLC, and PDA develop distinct phenotypes with unique TMEs that regulate tumor properties and response to therapy.

In the past decade, a wealth of studies has delineated how KRAS* signaling can reprogram cancer cell metabolism to support tumor growth. In addition, tumors arising in different tissues have unique metabolic programs and associated dependencies. Because KRAS* promotes a number of targetable common and/or tissue-specific pathways across cancer types, an alternative approach to directly targeting KRAS* is to block KRAS* metabolic effector pathways (ref(2, 20)). Furthermore, the exposure of tissue-specific supporting cell types to the dysregulated metabolism of KRAS*-driven cancer cells can affect their own metabolism and function. In this chapter, I therefore examine how KRAS* orchestrates the metabolism of CRC, NSCLC, and PDA. I will discuss the intrinsic metabolism of KRAS*-driven cancer cells and metabolic interactions in the broader TME. Finally, I will describe novel metabolic vulnerabilities garnered from these studies and the associated therapeutic inroads.

1.3 Cancer cell-intrinsic metabolism

1.3.1 Common metabolic pathways between cancers

KRAS* drives bioenergetic, biosynthetic, and redox programs, many of which in a manner independent of tumor type(21, 22). These programs build biomass and support an overall energetic state within the cancer cell favorable to deregulated proliferation **(Fig.1-1)**.

Central carbon metabolism

KRAS* signaling confers a competitive advantage to cancer cells through increased glucose uptake and elevated flux through glycolysis, concurrently fueling numerous branching biosynthetic pathways(23-29). Cells harboring KRAS* highly express glucose transporters (GLUTs) leading to efficient glucose uptake **(Fig.1-1)**(30, 31). The flux of glucose through glycolysis is elevated due to KRAS*-regulated expression and/or activity of key glycolytic enzymes(ref(32, 33)). Several glycolytic intermediates are shunted into biosynthetic pathways essential for nucleotide production, amino acid synthesis, or glycosylation reactions(23, 34), the activity of which is coordinated by KRAS* signaling **(Fig.1-1)**(35-38). To prevent an unfavorable cellular oxidative state and glycolytic stalling, KRAS* also promotes the rapid reduction of glycolysis-derived pyruvate to lactate(23, 39, 40) **(Fig.1-1)**. Lactate transporters are expressed in a KRAS*-dependent manner and efficiently export lactate from the cell **(Fig.1-1)**(40-42). As a whole, this glycolytic phenotype driven by KRAS* supports malignant progression and correlates with poorer prognoses in patients with KRAS*-driven cancers(40, 43).

Mitochondria

Mitochondria are hubs for biosynthesis(44-46), regulate signaling and gene expression, and are implicated in tumor initiation and progression(47-49). KRAS* modulates the total mitochondrial content and function through induction of mitophagy, and disrupted mitophagy delays tumor progression(50). Mitochondrial metabolism and flux of electrons through the electron transport chain (ETC) generate reactive oxygen species (ROS)(51). Mitochondrial ROS are required for KRAS*-driven tumor growth in mouse models(52). However, damaged mitochondria are inefficient and aberrant or excessive mitochondrial metabolism can lead to toxic ROS levels. As noted, KRAS* signaling leads to removal of defective mitochondria through mitophagy and prevents excessive ROS(50). Additionally, KRAS* signaling is vital for fine-tuning mitochondrial dynamics, maintaining an optimal balance of mitochondrial fission or mitochondrial fusion (Fig.1)(53-55).

Amino acids and protein synthesis

In addition to their classical role in protein biosynthesis, amino acids can also be a valuable fuel. For example, glutamine is a vital source of carbon and nitrogen for tumors(56). KRAS* also promotes alternative glutamine catabolism, leading to the reduced levels of nicotinamide adenine dinucleotide phosphate (NADPH) **(Fig.1-1)**(26, 57) Cultured colon, lung, and pancreatic cancer cells expressing KRAS* have been shown to be ‘addicted’ to glutaminolysis (57-59) (Fig.1) for growth and survival. While glutamine is the most abundant amino acid in serum(56), in vitro studies are often conducted in media with supraphysiological concentrations of glutamine and lacking stromal or immune compartments. These factors have contributed to an important

debate on the degree of this dependency on glutaminolysis in vivo (which substantially differs from that determined in vitro), as well as its tissue specificity(56, 58, 60, 61). Nevertheless, the expression of mitochondrial glutamate transporters was elevated in KRAS* tumor tissue compared to matched non-transformed tissue, and blockade of mitochondrial glutamate transport in cells with KRAS* decreased the abundances of tricarboxylic acid (TCA) cycle intermediates, disrupted redox homeostasis, and impaired proliferation both in vitro and in tumor xenografts(62).

Glutamine anaplerosis is also important for the production of amino acids like aspartate and asparagine from TCA cycle intermediates, which are critical for nucleotide and protein synthesis (Fig.1)(63-65) (unpublished data in ref[64]). Aside from glutamine catabolism, recent work in cell lines and mouse models demonstrated that glutamine synthesis is crucial to PDA, as glutamine serves as a vital source of nitrogen needed to produce nucleotides and other amino acids(66). Clearly, the role of glutamine metabolism in KRAS* tumors is complex and requires further study.

Nutrient scavenging

Rapid tumor growth and lack of proper vasculature leads to oxygen and nutrient deprivation in tumors. Therefore, cancer cells often rely on scavenging and recycling pathways to fuel biosynthesis and combat cellular stressors(67). RAS pathway activation induces macropinocytosis(68, 69), which provides an array of fuel sources that can be degraded in the lysosome, endowing cancer cells the building blocks to support biomass generation in nutrient-deprived conditions **(Fig.1-1)**(70). Recent studies have illustrated that the regulation of macropinocytosis by KRAS requires a complex interplay with other signaling cascades(67, 70-75).

Autophagy is tightly regulated in cancer cells expressing KRAS* and is a crucial scavenging pathway under acute nutrient deprivation, by which intracellular nutrients can be diverted to meet metabolic demands required for survival **(Fig.1-1)**(76-83). As such, during culture in buffered saline lacking essential nutrients, limited mitochondrial substrate availability can lead to dangerous levels of ROS and depleted nucleotide pools. In this setting, autophagic flux provided KRAS*-driven cancer cells with glutamine and glutamate to fuel the TCA cycle and support nucleotide production(84). Interestingly, blockade of downstream KRAS* signaling through ERK or RAF promoted autophagic activity, suggesting a potential mechanism by which cancer cells might sustain metabolism even when KRAS* signaling is targeted directly(85, 86). In a broader context, autophagy within the host has also been shown to maintain circulating glucose and arginine levels, and ablation of the autophagic machinery systemically led to regression of KRAS* tumors in mice, though tumors with other oncogenic drivers were similarly affected(87, 88).

Lipid metabolism

Proliferating cells require fatty acid synthesis (FAS) to generate lipids for processes like membrane synthesis. Lipids derived from intracellular stores or through extracellular uptake can also be utilized as a fuel source through fatty acid oxidation (FAO) to generate ATP(89). FAS requires reducing potential, while FAO generates reducing potential. Therefore, the redox state of a cancer cell can determine whether FAS or FAO is predominant **(Fig.1-1)**. In studies with human and murine models of NSCLC, tumors showed increased expression of FAS-related enzymes and were sensitive to FAS inhibition compared with either the normal lung or non-KRAS* lung

adenocarcinoma(90-93). Conversely, in another study KRAS* promoted fatty acid uptake and FAO in mouse models of NSCLC, and deletion of a key FAO enzyme impaired tumor growth(94). Additionally, in PDA KRAS* induces scavenging of environmental lipids or utilization of previously stored lipid droplets, both in cell culture and in mouse KRAS*-expressing allografts, under conditions that are unfavorable for FAS such as hypoxia or during invasion(95-97). These findings highlight that lipid metabolism is not regulated by mutant KRAS* alone, but also by other contextual factors, such as the energetic state of the cell, tissue of origin, or experimental model.

1.3.2 Dependence on co-occurring mutations

Co-occurring mutations in oncogenic drivers or tumor suppressors cooperate with KRAS* to shape the phenotype of a cancer cell, and these depend on the tissue of origin **(Fig.1-2)**.

Tissue-specific metabolism: oncogenic KRAS and the cell of origin

The physiological properties and functions of an organ influence tissue metabolism. These include oxygen tension, microbiome presence/composition, vascularity, and immune surveillance. The cell within a tissue that experiences the initial oncogenic hit and drives tumorigenesis is known as the ‘cell-of-origin’(98). The intrinsic metabolic programs in the cell-of-origin, or those available through dedifferentiation events, can be hijacked by oncogenic mutant KRAS (KRAS*) to support transformation. Collectively, the metabolic parameters in the tissues and cell of origin interact with KRAS* to impose distinct features, some of which enact unique metabolic vulnerabilities.

Lgr5+ intestinal stem cells residing in the crypt are a major cell of origin in colon cancer. In these cells, loss of tumor suppressor APC and overactive β-catenin/Wnt pathway activity drive adenoma formation(99). These cells rely on FAO for self-renewal and regeneration, which is similarly utilized by transformed stem cells following loss of APC to enhance tumorigenicity(100, 101). Since KRAS mutations follow loss of APC, an existing question remains as to how KRAS* changes fatty acid metabolism to support the progression of adenomas to carcinomas(14).

Bronchiolar, alveolar type II, and bronchoalveolar stem cells have been postulated as the cell of origin in lung cancer(102-105). Susceptibility to transformation is complex and influenced by cell type, physical location, co-occurring mutations, and immune signaling(106-108). A common requirement for transformation is the ability to adapt to oxidative stress, as KRAS* induces high levels of ROS and the lung is a naturally oxidative environment. Indeed, loss of function mutations to KEAP1 and gain of function NRF2 mutations lead to overactive NRF2 signaling in lung cancer, relative to other tumor types. In the KRAS* lung, these additional mutations confer a survival advantage for transformed cells to buffer ROS due to an oxygenated environment.

In the normal pancreas, acinar cells avidly consume amino acids to synthesize digestive enzymes, whereas ductal cells are primarily responsible for transport of peptides and hormones. Acinar cells in the pancreas transdifferentiate into ductal cells in response to injury or KRAS mutation and are the presumed cell of origin in PDA, though ongoing investigations have also implicated ductal cells(109-113). In the transformed state, KRAS* PDA cells possess metabolic programs inherent to both

acinar and ductal cells. This could explain why acinar-derived tumors demonstrate a ductal-like program of decreased BCAA uptake and metabolism(114).

APC and KRAS in colorectal cancer metabolism*

Loss of function (LOF) mutations in the gene encoding the tumor suppressor adenomatous polyposis coli (*APC*) initially drive tumorigenesis in ~80% of CRC(14). APC is a negative regulator of the transcription factor β-catenin, and APC loss in colon epithelial cells results in the activation and nuclear translocation of the transcription factor β-catenin, which then promotes aberrant WNT signaling and early adenoma formation. Subsequent oncogenic activation of KRAS* occurs in 40% of colon adenomas and enables maximal activation of β-catenin and WNT signaling and progression to carcinoma(115). One metabolic mechanism that supports this finding is KRAS* induced production of succinate from glutamine in colorectal cancer cells in vitro, which in turn inhibits demethylases, resulting in hypermethylation and increased expression of WNT pathway components, along with elevated β-catenin activity **(Fig.1-2A)**(116).

MYC is a target of β-catenin and cooperates with KRAS* during malignant transformation in CRC(117). Indeed, MYC is required for activation of the majority of WNT target genes following loss of APC(118). An in-depth metabolomics analysis of CRC cells demonstrated that MYC mediated metabolic reprogramming in early adenoma formation in tumours from patients(119). Furthermore, APC loss induced the expression of metabolic target genes of MYC(120). These data show that loss of APC requires MYC for induction of oncogenic programs, yet how KRAS* and MYC cooperate in CRC following loss of APC warrants deeper investigation. As an aside, MYC activity

has also been shown to be essential in KRAS*-driven NSCLC and there is considerable overlap in the metabolic programs induced by KRAS* and MYC, emphasizing the complex interplay between these two oncogenic drivers(121, 122).

Fatty acid metabolism in *APC*-null progenitor cells also plays a role in tumorigenesis. A high fat diet (HFD) induces FAO in intestinal stem and progenitor cells in mice, and FAO increases stem cell function and renewal in mice and in ex vivo organoid cultures(101, 123). These more numerous progenitor cells are susceptible to oncogenic transformation and subsequent loss of APC combined with elevated FAO resulted in increased tumor formation and progression(101). However, cooperation between loss of APC and KRAS* in fatty acid metabolism and stem cell fate remains to be elucidated.

Colorectal tumors at the primary site display heterogeneity in *KRAS* status, as not all transformed cells harbor *KRAS* mutations. Therefore, it is reasonable to assume that remarkable metabolic heterogeneity exists within a colorectal tumor. Because KRAS* is sufficient to drive invasive and metastatic disease progression(124), it is tempting to speculate that targeting KRAS*-driven metabolism could preferentially block invasion and regress metastatic tumors. In mouse models, aggressive tumors arise from cells harboring KRAS* and LOF *APC* mutations, compared to cells with single mutations of either gene, suggesting a highly complex genotype-dependent interaction(125-127). An area that has not been well-studied in CRC is cooperative network regulation by LOF *APC* mutations and KRAS* that promote metabolic pathways critical for tumor progression. Additional work into intratumoral metabolic differences

based on the driving oncogenic events could uncover differential dependence on metabolic pathways for primary tumor maintenance or metastasis of CRC.

LKB1 and KEAP1 loss synergize with KRAS in lung tumor metabolism*

Serine/threonine kinase 11 (*STK11*) encodes the tumor suppressor liver kinase B1 (LKB1) and is lost in approximately 20% of NSCLCs(15, 16). LKB1 enacts its tumor suppressive program primarily through phosphorylation and activation of 5' adenosine-monophosphate activated protein kinase (AMPK) and related AMPK family members(128-131). In this manner, the LKB1-AMPK axis senses energetic stress and acts as a metabolic brake under unfavorable nutrient conditions(129, 132, 133). In line with this, loss of LKB1 in human NSCLC cell lines induced an aberrant metabolic program supportive of malignant progression, with increased consumption and metabolism of glucose and glutamine **(Fig.1-2B)**[134]. Dysregulated AMPK activity is also required for tumor growth in vivo as loss of AMPK in a KRAS*, LKB1-deficient autochthonous mouse model of NSCLC reduced tumor burden(135).

During energetic stress, AMPK promotes FAO(128), a pathway also utilized by normal lung epithelial cells during starvation(136). Suggesting a role for AMPK activity, KRAS*, LKB-deficient lung tumors relied on FAO following acute energy crisis caused by deletion of autophagic components, a finding that was not observed in NSCLC with p53 mutations(137). AMPK activity following loss of LKB1 also induces scavenging of nitrogen from urea cycle ammonia for incorporation into pyrimidines and is required for the growth of KRAS*-driven, LKB1-deficient human NSCLC cell lines and xenografts **(Fig.1-2B)**(138). As a side note, some PDA tumors have also been shown to harbor LOF mutations in *STK11*, and pre-clinical studies in mouse models of PDA

demonstrated that LKB1 loss cooperates with KRAS* to drive tumor progression(139-141). Further work remains to determine if the metabolic programs found in KRAS*-driven, LKB1-deficient NSCLC are relevant for PDA.

Approximately 20% of patients with KRAS*-driven NSCLC have tumours that harbor LOF mutations in the gene encoding Kelch-like ECH associated protein 1 (KEAP1), the negative regulator of nuclear factor erythroid 2-related factor 2 (NRF2)(15, 16, 142). KEAP1 loss promotes NSCLC progression(143), and conversely, loss of NRF2 blocks tumor growth in autochthonous mouse models of both NSCLC and PDA(144). It has been shown that NRF2 induces an antioxidant transcriptional program in NSCLC cell lines and in human tumors in part through modulation of activating transcription factor 4 (ATF4)(145). Similarly, KRAS* promotes expression of asparagine synthase (ASNS) and asparagine production through ATF4(65) **(Fig.1-2B)**, demonstrating the cooperation between KRAS* and NRF2 following KEAP1 deletion. In the normal lung, production of NAPDH through the PPP is necessary for protection against free radicals, detoxification reactions, and lipid synthesis(146, 147). NRF2 activity due to loss of KEAP1 also enhances PPP flux and production of NADPH and GSH in human NSCLC cell lines(148) Remarkably, despite the essentiality of the PPP for KRAS*-driven tumors, a recent study demonstrated that loss of a key PPP enzyme did not abrogate growth of CRC or NSCLC tumor models, suggesting KRAS* can adapt to loss of PPP activity via compensatory metabolic pathways (149).

Indeed, KEAP1-mutant cells can utilize glutaminolysis as an alternative to the PPP to produce glutathione and to replenish intracellular glutamate pools(143, 150). In particular, NRF2 can induce transcription of *SLC7A11*, which encodes for xCT, the rate

limiting subunit of the glutamate-cystine exchanger system X_C^-. While this NRF2-driven glutamate-cystine exchange promotes cystine import and GSH production, it also depletes intracellular glutamate which is also needed for the TCA cycle. Therefore, cancer cells with overactive NRF2 rely on glutaminolysis through glutaminase 1 (GLS1) to maintain sufficient glutamate pools to both import cystine and fuel the TCA cycle **(Fig.1-2B)**(151). Conversely, KEAP1-wildtype NSCLC cells were insensitive to GLS1 inhibition *in vivo* due to compensatory incorporation of glucose into the TCA cycle, as opposed to relying on glutamine for anapleurosis(58). Collectively, these data illustrate how co-occurring mutations can drive metabolic heterogeneity in lung tumors and highlight the importance of characterizing metabolic dependencies in genetic subtypes of lung cancer(152).

Loss of TP53, INK4A, or SMAD4 cooperates with KRAS to direct PDA metabolism*

LOF mutations in the gene encoding p53 in the context of KRAS* are observed in about 50% of PDA(153, 154). As mentioned previously, KRAS*-driven cells rely on nutrient scavenging and recycling pathways.(6, 67, 68, 81). Surprisingly, an initial study in KRAS*-driven PDA lacking p53 showed inhibition of autophagy with hydroxychloroquine actually increased tumor growth compared with KRAS*-driven tumors with p53(155). A follow up study using a mouse model of PDA with *Trp53* loss of heterozygosity (LOH), one that more closely resembles the tissue and immune architecture of human disease, showed that autophagy is critical for PDA metabolism independently of p53 status(156). Furthermore, an earlier study established that autophagy is required for oxidative phosphorylation, ROS modulation, and tumor growth

in PDA, regardless of p53 status(157), therefore overall inducing some debate into the role of p53 in the regulation of PDA autophagy.

p53 has also been shown to play a role in the epigenetic regulation of cell state in PDA through modulation of the TCA cycle intermediate α-ketoglutarate (αKG) in orthotopic allografts, autochthonous mouse models, and human PDA. Decreased levels of αKG resulting from loss of p53 impairs the activity of certain chromatin modifying enzymes, ultimately inducing a de-differentiated cell state with enhanced cellular fitness. Conversely, re-expression of wild type p53 leads to elevated levels of αKG and promotes a differentiated, less aggressive state(158). This represents an important mechanism by which p53 suppresses tumor progression in PDA **(Fig.1-2C)**.

The tumor suppressor P16/INK4A is inactivated in >90% of KRAS* PDA(159). Loss of p16 in the context of KRAS* cell lines in vitro resulted in upregulation of levels of NADPH oxidase 4 (NOX4) and increased glycolytic flux compared with cells expressing p16(160). Thus, NOX4 activity, which sustains glycolysis by oxidizing NADPH, and resulting from loss of p16, supports the broader metabolic programs induced by KRAS* **(Fig.1-2C)**.

The genomic locus for the tumor suppressor *SMAD4* is deleted in >50% of KRAS* PDA(159). This non-specific process often results in the concurrent deletion of neighboring chromosomal genes. In the case of *SMAD4*, the gene encoding mitochondrial malic enzyme 2 (ME2) is in close genomic proximity and is co-deleted in ~25% of cases. ME2 converts malate to pyruvate and is required for NADPH production(161). KRAS* PDA cells can compensate for ME2 loss by upregulating ME3 activity, and this genomic context creates a vulnerability for inhibition of ME3 in ME2-

null cells **(Fig.1-2C)**(161). This is an important example in which a co-occurring genetic event indirectly influences KRAS* metabolism and provides a novel therapeutic target. It is important to note that these highlighted co-occurring mutations are not exclusive to the tumor types in which they are discussed here. For instance, *TP53* is also commonly mutated in colon and lung tumors and the metabolic perturbations induced by mutant p53 have been reviewed extensively elsewhere(14, 162, 163). Nor are these the only co-occurring mutations. Each tumor is a complex amalgam of unique and sometimes rare mutations all working in tandem with KRAS* to drive aberrant metabolism. We have aimed to utilize these studies in colon, lung, and pancreas tumors to demonstrate the importance of co-occurring mutations in shaping tumor metabolism. Given the genetic heterogeneity seen in patients, much work remains to both model this heterogeneity and identify metabolic pathways that can be targeted in certain genetic subtypes of these diseases.

1.3.3 Tissue-dependent features

Even though we can rapidly identify the driving mutations in a patient's tumor using advanced genomics and high throughput sequencing, we must also consider the effects of the cell of origin and tissue constraints on the biology of the tumor. While the metabolic features discussed below are not exclusive to the indicated tumor type there are instances in which KRAS* transformed cells co-opt the metabolic machinery in the tissues of origin **(Fig.1-3)**. Here, we discuss how this is influenced by tissue structure and how this impacts nutrient and oxygen access

Hypoxia, inflammation, iron in the colon

The oxygen tension (pO_2) in the colonic lumen can be as much as ten times lower than that in oxygenated blood or tissue (i.e. ~10 mmHg) **(Fig.1-3A)**(164). This hypoxic lumen supports growth of facultative anaerobic microbiota, and consequently symbiotic metabolic interactions with colonocytes(165) which, in certain contexts such as dysbiosis or wound healing can drive inflammatory signaling in the colon(166). Both hypoxia and chronic inflammation can contribute to the development of CRC. Hypoxia-inducible factors (HIFs) modulate the cellular response to low oxygen and serve to integrate oxygen sensing, metabolism, and inflammation(166-169). They are thus essential for proper functioning of cells in the colon(168, 170-172). Some evidence indicates an overlap between KRAS*- and HIF-regulated genes in CRC(173, 174). Hypoxia increases expression of KRAS* in CRC cell lines(175), and KRAS* reciprocally stabilizes HIF1α via several effector pathways, indicating a potential positive feedback loop between HIFs and KRAS* **(Fig.1-3A)**(176-178), thereby promoting CRC cell survival in hypoxia. It also renders CRC cells dependent on HIF activity, since loss of HIF1α or HIF2α in CRC xenografts and autochthonous models has been shown to impair tumor cell proliferation(179).

A crucial function of the colon is to absorb nutrients from the diet. Iron is required for red blood cell development and systemic delivery of oxygen and is a cofactor in numerous metabolic reactions. Iron import is regulated primarily by HIF2α in the colon(180, 181). In CRC, HIF2α-mediated iron import through divalent metal transporter 1 (DMT1) promoted JAK-STAT signaling and tumor growth in vivo **(Fig.1-3A)**(182, 183). Currently the role of KRAS* in iron metabolism is unclear, though heme iron intake is

correlated with an increased risk for colon tumors harboring KRAS*(173, 174). Indeed, TCGA data revealed that in CRC, KRAS* potentiates the expression of iron importers **(Fig.1-3A)**(182). Therefore, KRAS* may initiate a feedforward cycle via regulation of HIF2α to sustain high iron levels for CRC growth. Further work on iron metabolism in CRC is warranted, especially given the recent interest in ferroptosis(184-186) and the discovery that ferroptosis-inducing compounds are selectively lethal in cells engineered to express oncogenic RAS (either RAS^{V12} or $HRAS^{G12V}$)[171].

Oxygen gradients and alternative fuel sources in the lung

The lung is essential for oxygen transfer and transport throughout the body(136, 146, 147). Despite its high oxygen tension and proximity to oxygen-laden blood vessels, oxygen gradients still develop throughout the lungs **(Fig.1-3B)**(164). Interestingly, work with tissue slices and perfused lungs decades ago discovered the normal lung is glucose avid and releases lactate(146, 147). This finding was confirmed recently using isotope tracing and metabolomics analysis(187) in normal lungs of pigs showing that glucose-derived lactate was released in large quantities from the lung. Lactate was a major source of carbon for the TCA cycle within lung cells (in contrast to other organs like the pancreas and colon)(187). It is tempting to speculate that cells further from blood vessels convert glucose to lactate, which can be used by cells closer to oxygenated blood vessels as an alternative fuel source **(Fig.1-3B)**(136). The release of lactate from one cell population and its use as a carbon source in other cells seems to be operating in NSCLC as well. Isotopic tracing experiments with labelled glucose in human patients demonstrated that NSCLC tumors are metabolically heterogeneous in their glucose utilization(152). More perfused areas of the tumors used alternative fuel

sources like lactate, while poorly perfused regions relied on glycolysis and glucose incorporation into TCA cycle **(Fig.1-3B)**(152, 188).

Branched-chain amino acid metabolism in the pancreas

Recent work has shown that PDA can arise from either acinar or ductal cells depending on mutational profiles and stromal cues. This has fueled a critical debate regarding the putative cell of origin in PDA, though a common theory ascribes the origin of PDA to the dedifferentiation program known as acinar-ductal metaplasia (ADM)(112, 113). In normal physiology, acinar cells of the exocrine pancreas produce copious peptides and enzymes to aid digestion, making the pancreas highly amino acid-avid to obtain the building blocks for these zymogens **(Fig.1-3C)**(187, 189). Compared with ductal cells, acinar cells display elevated expression of the mitochondrial branch-chain amino acid transaminase 2 (BCAT2) protein and rapidly incorporate branched-chain amino acids (BCAAs) into protein **(Fig.1-3C)**(189, 190). Despite low levels of BCAT2 protein in normal ductal cells, BCAT2 expression increased as KRAS*-transformed cells progressed from an acinar to a ductal fate(190). Indeed, overexpression of KRAS in normal pancreatic ductal cells stabilized BCAT2 expression, and inhibition of BCAT2 hindered formation of early pancreatic lesions in a genetic mouse model of tumorigenesis driven by $Kras^{G12D}$ (ref(190)). These results suggest a model by which normal acinar cells utilize BCAT2 for incorporation of BCAAs into proteins to carry out their cellular functions, while KRAS*-harboring ductal cells hijack BCAT2 catabolic activity to meet biosynthetic and energetic demands **(Fig.1-3C)**

However, unlike in this model of PDA driven solely by KRAS*, tumors with both KRAS* and loss of p53 displayed low BCAA catabolism and the growth of

subcutaneous allografts in mice was not affected by dual loss of BCAT1 and BCAT2(ref [178]). Furthermore, a recent study found that pancreatic cancer-associated fibroblasts (CAFs) in the tumor stroma synthesized and released BCAAs, and that BCAT activity in human PDA cells was required for the use of BCAAs for oxidation and protein synthesis(191). These seemingly contradictory findings regarding BCAA metabolism showcase the complex interplay between KRAS*, co-occurring mutations, and environmental context.

Comparative studies of metabolic pathways

In some studies, KRAS*-driven metabolic pathways have been directly contrasted between cancer types in different tissues. For instance, while glutamate oxaloacetate transaminase 1 (GOT1) is essential in PDA for protection from ROS, and GOT1 inhibition sensitized PDA cell lines to radiation in vitro and in murine xenografts, CRC cells were not affected by loss of GOT1(192). Interestingly, the aforementioned study demonstrating BCAA metabolism is not an essential pathway in PDA concurrently showed that NSCLC tumors also driven by KRAS* and LOF p53 had elevated flux through the BCATs and relied on BCAAs for tumor growth(114)**,** emphasizing the tissue dependence of the metabolic phenotype in cancer cells driven by the same genotype. Finally, tissue of origin dictates whether a cancer cell depends on the Preiss-Handler (PH) de novo NAD+ synthesis or NAD salvage pathways(193). Tumors arising in the pancreas have greater amplifications in PH enzymes compared to those of the lung or colon, suggesting PDA depends more on NAD synthesis than salvage, compared to NSCLC or CRC(193). These studies collectively demonstrate that contextual cues such

as the TME, cell of origin, and model system must be considered in addition to oncogenic drivers when studying tumor metabolism.

1.4 Metabolism in the tumor microenvironment

KRAS* driven programs in cancer cells can shape the cellular composition and thus the vascularity and architecture of the TME. This, in turn, impacts the availability of nutrients and oxygen while establishing gradients of pH and metabolic byproducts, collectively dictating the metabolic nature of the TME(194). Furthermore, the depletion or accumulation of metabolites, resulting from aberrant cancer metabolism has ramifications for the function of surrounding immune and stromal cells(194-198). To manage the metabolic challenges imposed by the TME, cancer and non-cancer cells participate in cooperative metabolic interactions that support tumor growth, as well as competitive metabolic interactions that promote tumor survival by limiting nutrient availability to, and thus the activity of, the anti-tumor immune system(194, 199, 200) **(Fig.1-4)**.

1.4.1 Hypoxia and inflammation

Solid tumors are marked by a prolonged, dysregulated inflammatory response(201). KRAS* drives inflammatory signaling early in tumor progression and cooperates with exogenous factors such as tobacco or pollutants in the lung, the microbiome in the colon, and secretory enzymes in the pancreas to generate an inflammatory environment that potentiates oncogenic signaling(202-205). Similarly, KRAS* drives aberrant proliferation and signalling which contributes to tumor hypoxia(194).

KRAS* signaling, tumor hypoxia and the activation of HIFs remodel the immune microenvironment in the tumor. For example, hypoxia in a poorly perfused, late-stage KRAS* driven tumor drives expression of HIF1α which led to B cell exclusion from the tumor in a mouse model of PDA(206, 207)**(Fig.1-4A)**. This could be speculated as a mechanism by which KRAS* leads to recruitment of immune cells to support tumor initiation under conditions of sufficient oxygen and low HIF expression, and exclusion of metabolically competitive immune cells via HIF activity late in tumor progression when oxygen and nutrients are scarce.

Pro-inflammatory signaling in the TME enhances dysregulated metabolic programs in PDA. For instance, upon recruitment to the PDA tumor stroma, CD4+ T cells differentiate into the Th2 subtype, which creates an immunosuppressive environment by promoting the anti-inflammatory phenotype of tumor-associated macrophages (TAMs)(208). Of note, Th2 cell -derived IL4 and IL13 signaling supports the metabolism of PDA cells. In a mouse model of PDA, KRAS* upregulated surface expression of IL4Rα(209), rendering cancer cells more sensitive to Th2 cell-derived cytokines. This in turn elevated MYC activity via JAK-STAT signaling and increased glycolytic gene expression and flux in cancer cells, thereby contributing to tumor growth(209)**(Fig.1-4A)**. Future work with KRAS*-driven mouse models of NSCLC and CRC could determine if these phenotypes are unique to PDA, or dependent on KRAS* across tumor types.

1.4.2 Glucose competition

Proliferative cell types in the TME, like effector immune cells, are sensitive to the glucose depleted state common in, but not exclusive to, KRAS*-driven tumors(196, 197,

200). Low glucose levels in the TME resulting from elevated uptake and utilization by cancer cells prevents expansion and cytokine release of T cells **(Fig.1-4B)**. Also, expression of glycolytic enzymes in NSCLC patient samples was inversely correlated with T cell infiltration(210). Mechanistically, interactions between programmed death ligand 1 (PD-L1) on murine CRC cancer cells and PD-1 on T cells can stimulate glycolysis in cancer cells(199)**(Fig.1-4B)**. This suggests that immune checkpoint blockade could dampen glycolysis in cancer cells, increasing glucose availability for effector T cells.

CAFs undergo metabolic reprogramming upon activation, marked by increased glycolysis and dependence on glucose **(Fig.1-4B)**(195). In support of this, CAFs from human CRC tissue had increased expression of glycolytic enzymes and decreased TCA cycle activity compared to normal fibroblasts(211). Co-injection of these CAFs with CRC cell lines in mouse subcutaneous xenografts promoted tumor growth(211). Isotope tracing studies similarly demonstrated that pancreatic CAFs are highly glycolytic9(41)). Thus, while depriving anti-tumor immune cells of glucose clearly conferred a survival advantage to cancer cells as reported in several studies, limiting CAF access to glucose could impair tumor-promoting interactions between cancer cells and CAFs. Therefore, further work remains to determine how CAFs and cancer cells engage in cooperative glucose metabolism in a TME with limited glucose.

1.4.3 Lactate accumulation

Rapid glucose metabolism through glycolysis in KRAS*-driven cancer cells leads to an accumulation of lactate in the TME **(Fig.1-4B)**. Lactate is transported by the family of MCTs(212, 213). Interestingly, in tissue from primary PDA tumors, expression of the

lactate export protein MCT4 correlated with expression of immunosuppressive markers in the TME(214). In support of an immunosuppressive role of extracellular lactate in tumors, a recent study discovered that macrophages exposed to lactate-high media conditioned by KRAS*-driven CRC cells, or supplemented with exogenous lactate, demonstrated increased expression of genes associated with the TAM anti-inflammatory state in contrast with macrophages cultured in normal growth media(215) **(Fig.1-4B)**. Moreover, the accumulation of intracellular lactate in T cells blocked glycolytic flux, rendering T cells unable to carry out cytotoxic functions against cancer cells(216) **(Fig.1-4B)**. Furthermore, lactate in the TME of colon liver metastases induced apoptosis in infiltrating NK cells due to increased intracellular pH and production of mitochondrial ROS(217) **(Fig.1-4B)**. Collectively, these data demonstrate how lactate, a metabolic byproduct of KRAS*-driven metabolism in cancer cells, creates an immunosuppressive TME.

1.4.4 Regulation of amino acid levels

Effector T cells require specific amino acids to mount an anti-tumor response(197). The metabolic pathways in KRAS*-expressing cancer cells lead to depletion of certain amino acids from the TME **(Fig.1-4C)**. Specifically, increased glutamine uptake and metabolism mediated by KRAS* depletes glutamine from the TME **(Fig.1-4C)**(57, 218, 219). This process deprives T cells of a fuel source vital for their activation, because effector T cells also rely on glutamine to proliferate and produce cytokines during an anti-tumor response(219).

Tryptophan is another important amino acid for T cell responses and its depletion limits effector T cell infiltration and expansion(220-224). Though direct links between

KRAS* driving tryptophan depletion remain to be uncovered, tryptophan is depleted from the TME in colon, lung, and pancreas tumors due to the activity of tryptophan-degrading enzymes (TDEs) expressed by cancer cells, CAFs, myeloid-derived suppressor cells (MDSCs), and regulatory T cells (Tregs)(197, 219, 224, 225) **(Fig.1-4C)**.

There is considerable competition for the amino acid arginine in the KRAS*-shaped TME **(Fig.1-4C)**(194). Arginine catabolism or conversion serves as a source of nitrogen through the urea cycle, and generates proline, polyamines, and/or nitric oxide (NO). Arginine thus contributes to the biosynthetic capacity of tumor cells and/or the activity of pro- or anti-inflammatory immune cells(197, 226). Lung and pancreatic cancer cells are unable to synthesize arginine as they do not express argininosuccinate synthetase (ASS) and therefore depend on exogenous arginine(226). Colon cancer cells however express ASS and can generate arginine, providing them with a survival advantage in an arginine-depleted TME(226). In terms of immune cells in the TME, pro-inflammatory M1-like macrophages have been shown to generate NO from arginine via inducible nitric oxide synthase (iNOS) to carry out an anti-tumor cytotoxic response, whereas TAMs express arginase 1 (ARG1) to breakdown arginine into polyamines, which supports the anti-inflammatory response(197). In addition, CAFs, and MDSCs in the TME express ARG1 **(Fig.1-4C)**[195,215]. Since effector T cells require arginine for full activation and cytotoxic responses(219), these processes, combined with increased uptake of arginine by arginine-auxotrophic cancer cells, suppress the inflammatory, anti-tumor immune response(194, 203, 215, 224).

Cooperative interactions between cancer cells and the tumor stroma compensate for limited amino acid availability **(Fig.1-4D)**. As mentioned above, during nutrient deprivation, autophagy can be deployed to recycle critical metabolites. Indeed, CAFs in both NSCLC and PDA displayed elevated autophagy compared with normal fibroblasts(227, 228). This can be to the advantage of cancer cells, because for example, elevated autophagy in pancreatic CAFs increased the availability of alanine to PDA cells, which was released by CAFs and taken up by PDA cells to fuel the TCA cycle(228) **(Fig.1-4D)**. Pancreatic CAFs have also been shown to package numerous metabolites, including amino acids, into exosomes for delivery to cancer cells(229) **(Fig.1-4D)**. Moreover, recent work has demonstrated that pancreatic CAFs display elevated synthesis and release of BCAAs to be taken up and metabolized by PDA cells(191), as highlighted above and in **(Fig.1-4D)**.

Lastly, an emerging area of research concerns the role of the nervous system in regulating tumor metabolism. Pancreatic tumors are highly innervated, and the presence of neurons correlates with more aggressive disease and poorer outcomes[219]. A recent study has revealed that under conditions of serine deprivation in mice with PDA, such as a serine-free diet, neurons were recruited to the tumor and synthesized and released serine for uptake by PDA cells **(Fig.1-4D)**. This allowed translation of proteins in cancer cells to proceed uninterrupted (230). While this study was specific to PDA, future work in this emerging area could reveal if this mechanism is also active in NSCLC or CRC.

1.4.5 Dysregulated lipid metabolism

The composition of lipids in the TME is affected by fatty acid metabolism of KRAS*-driven cancer cells, which access intracellular lipid stores or take up extracellular lipids(91, 97). This leads to the accumulation or depletion of lipid species in the TME, which can affect the metabolism of surrounding cells. For instance, long chain fatty acids (LCFAs) are abundant in the pancreatic TME(231). In a mouse model of PDA, cytotoxic CD8+ T cells infiltrating PDA tumors imported LCFAs. However, these T cells had low expression of the enzyme critical for breakdown of LCFAs and therefore, fatty acids accumulated in T cells, leading to metabolic exhaustion and impaired cytotoxic activity(231). T cells possess remarkable metabolic plasticity and it is possible that signaling induced by KRAS* in cancer cells indirectly prevents utilization of alternative fuel sources in T cells, though this remains to be proven mechanistically(219). New metabolomics technologies for studying lipidomics will enable further characterization of lipid metabolism in other non-cancer cell types in the TME.

1.4.6 Metabolic interactions between oncogenic KRAS and the microbiome

Symbiotic interactions between commensal microbiota and host cells maintain tissue homeostasis. For instance, colonocytes in the normal colon rely on oxidative phosphorylation and deplete the lumen of oxygen, fostering the growth of obligate anaerobes that process dietary fiber into byproducts for epithelial cells(232). Some microbial products, like the short chain fatty acid (SCFA) butyrate, inhibit proliferation and renewal of stem cells located at the base of intestinal crypts, so colonocytes in the upper crypt consume and oxidize SCFA for fuel as well as to protect the intestinal stem cells(233).

Transformation by oncogenic KRAS (KRAS*) disrupts tissue architecture in the colon, lung, and pancreas and rewires metabolism. This induces dysbiosis to promote tumor progression and suppress the innate and adaptive immune system(234-237). Increased KRAS*-driven ERK and PI3K signaling can lead to enriched commensal bacteria in lung tumors(238). In the diseased lung, changes to the metabolome positively correlated with the bacterial load in the lower airways, indicating the microbiome could also shape the metabolic environment encountered by cancer cells(239).

Exposure to the SCFA butyrate produced by obligate anaerobes also caused cell cycle arrest in colon cancer cells in vitro(240). Colon cells transformed by KRAS* upregulate glycolysis and lactate release and decrease oxygen consumption. Elevated lactate in the lumen and increased oxygenation skews the microbiome toward facultative anaerobes that do not produce SCFAs from fiber(232). In this manner, KRAS* signaling might lead to avoidance of the growth inhibitory effects of butyrate. Future work will investigate how KRAS* dysregulated metabolism shapes the tumor microbiome. For example, an understudied area concerns how the microbiome affects the composition of metabolites that regulate immune responses to cancer. Additionally, systemic changes to the broader host microbiome resulting from KRAS*-driven tumors could reciprocally affect the nutrients available to tumors.

1.5 Targeting metabolism in KRAS* tumors

KRAS*-driven tumors have a remarkable ability to develop resistance to inhibition of KRAS* even after ablation of the oncogenic driver(241-244). For instance, PI3K-mediated reactivation of the MAPK pathway, as well as focal adhesion kinase signaling,

have been shown to drive resistance to KRAS* genetic silencing in vitro and in vivo(245, 246) (however, there is evidence suggesting *in vitro* culture conditions underestimate the essentiality of KRAS* for *in vivo* tumor growth(247)). Furthermore, a $KRAS^{G12C}$-specific chemical inhibitor effectively inhibited in vitro and in vivo tumor growth emphasizing caution must be used when drawing inferences from genetic silencing of KRAS* (247). Nevertheless, an important strategy to consider is to target downstream metabolic effector pathways either alone, in combinations with other effectors, or in combination with inhibition of KRAS* to block resistance mechanisms either inherent to cancer cells or driven by the TME.

1.5.1 Drug-induced vulnerabilities

Cancer cells can utilize metabolic mechanisms to compensate for loss of KRAS*. As such, genetic ablation of KRAS* in a mouse model of PDA led to tumor regression, but a subset of cancer cells persisted and reconstituted the tumor. These residual cells relied on oxidative phosphorylation (as opposed to glycolysis), inhibition of which in combination with oncogene ablation prevented tumor recurrence(241).

As mentioned earlier, scavenging mechanisms are upregulated by KRAS* and represent potential targets in combination with KRAS* inhibition. As such, knockdown of KRAS* or ERK inhibition in PDA cells in vitro led to an increase in autophagy, potentially to manage the impact of MAPK pathway inhibition(85, 86, 241).This notion was confirmed by blocking autophagy with chloroquine in combination with ERK inhibitors, which slowed PDA tumor growth in mice and increased apoptosis in PDA cells in vitro(85). Combining autophagy and ERK inhibition in PDA is now being examined in clinical trials (NCT04214418, NCT04386057). Furthermore, targeting the regulatory

machinery or signaling pathways associated with macropinocytosis inhibits tumor progression in NSCLC and PDA tumors(70, 248), suggesting this strategy could undermine the ability of KRAS* cancer cells to survive under metabolic stress.

Like the cell intrinsic pathways, the TME can also support tumor growth after loss of KRAS* signaling. For example, pancreatic TAMs have been shown to release TGFβ, which drove tumour progression via SMAD4 in mice after doxycycline-inducible KRAS* had been extinguished(242). Furthermore, shRNA-mediated knockdown of IL4Rα or JAK chemical inhibition in KRAS* PDA cells abrogated the Th2 cell-derived cytokine cascade discussed above, and reduced tumor progression in mice(209). While these findings were shown in PDA, similar mechanisms might occur in lung and colon tumors, which remains to be determined.

1.5.2 Vulnerabilities from co-occurring mutations

The inhibition of mechanisms induced by co-occurring mutations that cooperate with KRAS* is another avenue to consider when targeting metabolism in KRAS*driven tumours. As such, LKB1-loss mediated activation of AMPK in cell lines and a mouse model of KRAS*-driven NSCLC rendered cells sensitive to phenformin. This ETC-inhibiting drug selectively induced apoptosis and slowed growth in LKB1-deficient cells both in vitro and in vivo compared to NSCLC cells with loss of p53 (ref(249)). Also, inhibiting the pyrimidine synthesis enzyme CPS1 in LKB1-deficient, KRAS*-driven human NSCLC cell lines (as compared to cell lines harboring either single mutation) led to cellular DNA damage, cell cycle stalling, and impaired tumor growth in murine xenografts(138). Inhibition of another pyrimidine synthesis enzyme, deoxythymidylate kinase (DTYMK), was synthetic lethal in human and mouse LKB1-deficient lung cancer

cells in vitro compared to LKB1-wild type NSCLC cell lines(250). Similarly, LKB1-deficient, KRAS*-driven mouse NSCLC cells cultured ex vivo were sensitized to inhibition of the SBP or DNA methylation while cells with either KRAS* alone or co-occurring loss of p53 remained unaffected(141). Additionally, inhibition of the HBP enzyme glutamine-fructose-6-phosphate transaminase [isomerizing] 2 (GFPT2) with azaserine was a unique vulnerability for KRAS/LKB1 co-mutated NSCLC cell lines, xenografts, and genetic tumor models compared to NSCLC with mutant p53(34). Finally, loss of the autophagic gene *Atg7* was synthetic lethal in a KRAS*, LKB1-deficient NSCLC mouse model compared with KRAS*, p53-deficient tumors, suggesting that LKB1-deficient NSCLC tumors may be selectively sensitive to inhibition of autophagy(137).

In NSCLC, KEAP1 mutations rendered mouse NSCLC orthotopic allografts and patient-derived xenografts dependent on glutaminolysis and sensitive to chemical inhibition of GLS1 with CB-839, while tumors with active KEAP1 were unaffected(58, 143).CB-839 is currently being tested in a clinical trial (NCT03872427). In addition, the overactive NRF2 antioxidant program resulting from KEAP1 deficiency depleted intracellular glutamate levels in mouse NSCLC cells. Since glutamate is needed to synthesize non-essential amino acids (NEAAs), including serine and glycine, glutamate depletion rendered these cells reliant on exogenous NEAAs. Thus, using a systemic, dietary intervention to deprive tumors of NEAAs, such as a serine and glycine-free diet, slowed mouse KEAP1-mutant allograft growth yet had no effect on KEAP1-wild type tumors. Furthermore, GLS1 inhibition with CB-839 further reduced intracellular glutamate and synergized with the NEAA-free diet in these models(251). This is one

example of how a specific dietary intervention informed by tumor genotype can improve metabolic therapies downstream of KRAS*.

1.5.3 Cooperative interactions in the stroma

The KRAS*-driven remodeling of the TME observed in PDA dictates much of the biology of these tumors(154). As such, PDA is an optimal model in which to study metabolic interactions with the TME and a wealth of literature exists on reprogramming the pancreatic tumor stroma. The activation and expansion of CAFs from quiescent fibroblasts drives the desmoplastic response in pancreatic tumors(252), and CAFs can contribute to therapy resistance mechanisms in PDA. One of these mechanisms involves expression of the vitamin D receptor (VDR) in CAFs. Treatment of PDA-bearing mice with the VDR agonist calcipotriol reverted CAFs to an inactivated cell state, induced stromal remodeling, and improved delivery of the chemotherapeutic gemcitabine(252). Another mechanism of treatment resistance involves the release of pyruvate by CAFs **(Fig.1-4D)**. CAF-derived pyruvate decreased the efficacy of ETC complex I inhibitors in cancer cells, and blocking pyruvate import increased sensitivity to these therapeutics in vitro (unpublished data in ref(41)). As mentioned previously, interactions with cancer cells induce CAFs in NSCLC and PDA to increase autophagy and supply cancer cells with critical metabolites(227-229). Treatment of mice bearing KRAS*-driven tumors with autophagy inhibitors could block not only cancer cell metabolism but could also limit the availability of nutrients derived from the tumor stroma by reprogramming CAFs to a less activated state(253).

CAFs have also been shown to release deoxycytidine (dC)(254). From a study on TAMs in KRAS*-driven PDA, we know that dC can be released by TAMs and

contribute to gemcitabine resistance(255). Gemcitabine is structurally similar to dC, and TAM-derived dC was shown to compete with gemcitabine for uptake and metabolism by PDA cells, thereby lessening this chemotherapeutic's efficacy. Thus, ablation of TAMs from tumors or targeting dC production in TAMs increased the response of PDA tumors to gemcitabine(255). As dC secretion from CAFs might contribute to chemoresistance, these findings indicate that multiple cell types may cooperate to provide resistance to PDA cells from chemotherapy **(Fig.1-4D)**.

Lastly, as mentioned earlier, neurons recruited to the pancreatic TME release serine to support PDA metabolism. This interaction was impaired by treatment with a neuron-specific Trk inhibitor to block innervation in combination with a serine-free diet impaired tumor growth in PDA mouse models(230).

Myriad cell types exist in KRAS* tumors. We have only recently begun to disentangle cooperative metabolic crosstalk between cancer cells and the TME, and future work has the potential to identify additional opportunities to block these supportive interactions.

1.5.4 Harnessing the immune system

The advent of immunotherapy has improved treatments for some cancers and demonstrated that the immune system can be reprogrammed to recognize and attack cancer cells(256). Yet, colon, lung, and pancreas tumors with KRAS* are among the least responsive cancers to immune checkpoint-based therapy(257, 258). This is in part due to non-metabolic factors such as the type of oncogenic driver, overall tumor mutational burden, or the degree of microsatellite instability (MSI), as for example MSI-high CRC tumors typically respond better to immunotherapy than MSI-low tumors(257). The metabolic changes in the TME induced by KRAS* also suppress the anti-tumor

immune system. Targeting these metabolic networks to reprogram immune cells and/or prevent the depletion of metabolites required for an immune response has considerable potential to improve the efficacy of immunotherapy in these cancers.

The glutamine antagonist 6-diazo-5-oxo-L-norleucine (DON) broadly inhibits glutaminolysis by blocking the activities of glutamine deamidases. Because KRAS* induced dependence on glutamine in colon cancer cells, mice bearing syngeneic transplants of murine colon tumor cells were treated with DON to analyse its effect on tumour growth(259). Surprisingly, DON treatment resulted not only in impaired mouse CRC allograft growth, but also in an increased number of tumor infiltrating T cells compared with untreated tumour-bearing mice(259). While DON impaired glutamine metabolism in both cancer cells and T cells, T cells displayed remarkable metabolic plasticity and compensated for the lack of glutamine-derived carbon in the TCA cycle by incorporating glucose or acetate-derived carbons instead(259-261). This endowed T cells with a robust proliferative and energetic response and conferred a long-lasting memory phenotype(259, 261). Immune checkpoint inhibition with anti-PD-1 synergized with DON treatment to inhibit tumor progression(259). KRAS*-driven NSCLC that harbor co-occurring mutations in KEAP1 and/or LKB1 are often resistant to immune checkpoint-based therapy(262-265). Thus, a pro-drug derivative of DON is now in clinical trials against multiple cancers, and a phase II trial will test its efficacy in KEAP1 and LKB1 mutant NSCLC (NCT04471415).

Similarly, a potential synergy between GLS1 inhibition and immune checkpoint blockade is currently being tested in a phase II clinical trial in KEAP1 mutant tumors (NCT04265534). Future studies will need to determine how LKB1 and KEAP1 mutations

might promote immune evasion in NSCLC and identify novel or existing metabolic therapies that can enhance anti-tumor immune responses in combination with immune checkpoint blockade.

Immunologically “cold” PDA tumors are also resistant to immune checkpoint blockade(266). A recent study demonstrated that activity of autophagy in PDA in vivo leads to the selective lysosomal degradation of major histocompatibility complex class I (MHC-I) in cancer cells(267). MHC-I is required for antigen presentation on cancer cells and recognition by the immune system. Thus, MHC-I downregulation allowed PDA cells to evade the anti-tumor immune system. Additionally, autophagy was implicated in preventing T cell killing through modulation of TNFα signaling(268). Indeed, in mouse models of PDA, autophagy inhibition with chloroquine synergized with both anti-PD-1 and anti-CTLA4 to inhibit tumor progression(267).

In summary, targeting the metabolism of KRAS* tumors can provide nutrients to the immune system to increase the number and heighten the activity of the anti-tumor effector cells, priming tumors for immune checkpoint blockade therapy.

1.6 Conclusion

A better understanding of effector pathways downstream of KRAS*, such as dysregulated metabolism, could lead to enhanced therapeutic interventions in combination with direct inhibition of KRAS*. This will require future work to disentangle metabolic pathways mediated by specific KRAS mutations and synergy with co-occurring mutations, as well contextual cues determined by the tissue of origin.
We are only beginning to appreciate how KRAS* signaling directly and indirectly shapes the broader metabolism of the TME. Continuing to identify metabolic networks that

support KRAS*-driven metabolism, mediate resistance to therapy, and suppress the immune system will identify opportunities to cut off nutrient sources, enhance chemotherapy, and/or promote anti-tumor immune responses. Cutting-edge approaches like in vivo isotope tracing, spatially-resolved mass spectrometry, and advances in single-cell sequencing technologies will be critical in these endeavors. Moving forward, exploiting metabolic networks in CRC, NSCLC, and PDA according to both genetic and environment contexts is a promising therapeutic strategy for improving the treatment of KRAS*-driven tumors.

1.7 References

1. Mo SP, Coulson JM, Prior IA. RAS variant signalling. Biochemical Society Transactions. 2018;46(5):1325-32. doi: 10.1042/BST20180173.

2. Moore AR, Rosenberg SC, McCormick F, Malek S. RAS-targeted therapies: is the undruggable drugged? Nature reviews Drug discovery. 2020;19(8):533-52. Epub 2020/06/13. doi: 10.1038/s41573-020-0068-6. PubMed PMID: 32528145.

3. Prior IA, Lewis PD, Mattos C. A comprehensive survey of Ras mutations in cancer. Cancer research. 2012;72(10):2457-67. Epub 2012/05/17. doi: 10.1158/0008-5472.Can-11-2612. PubMed PMID: 22589270; PMCID: PMC3354961.

4. Sanchez-Vega F, Mina M, Armenia J, Chatila WK, Luna A, La KC, Dimitriadoy S, Liu DL, Kantheti HS, Saghafinia S, Chakravarty D, Daian F, Gao Q, Bailey MH, Liang W-W, Foltz SM, Shmulevich I, Ding L, Heins Z, Ochoa A, Gross B, Gao J, Zhang H, Kundra R, Kandoth C, Bahceci I, Dervishi L, Dogrusoz U, Zhou W, Shen H, Laird PW, Way GP, Greene CS, Liang H, Xiao Y, Wang C, Iavarone A, Berger AH, Bivona TG, Lazar AJ, Hammer GD, Giordano T, Kwong LN, McArthur G, Huang C, Tward AD, Frederick MJ, McCormick F, Meyerson M, Caesar-Johnson SJ, Demchok JA, Felau I, Kasapi M, Ferguson ML, Hutter CM, Sofia HJ, Tarnuzzer R, Wang Z, Yang L, Zenklusen JC, Zhang J, Chudamani S, Liu J, Lolla L, Naresh R, Pihl T, Sun Q, Wan Y, Wu Y, Cho J, DeFreitas T, Frazer S, Gehlenborg N, Getz G, Heiman DI, Kim J, Lawrence MS, Lin P, Meier S, Noble MS, Saksena G, Voet D, Zhang H, Bernard B, Chambwe N, Dhankani V, Knijnenburg T, Kramer R, Leinonen K, Liu Y, Miller M, Reynolds S, Shmulevich I, Thorsson V, Zhang W, Akbani R, Broom BM, Hegde AM, Ju Z, Kanchi RS, Korkut A, Li J, Liang H, Ling S, Liu W, Lu Y, Mills GB, Ng K-S, Rao A, Ryan M, Wang J, Weinstein JN, Zhang J, Abeshouse A, Armenia J, Chakravarty D, Chatila WK, de Bruijn I, Gao J, Gross BE, Heins ZJ, Kundra R, La K, Ladanyi M, Luna A, Nissan MG, Ochoa A, Phillips SM, Reznik E, Sanchez-Vega F, Sander C, Schultz N,

Sheridan R, Sumer SO, Sun Y, Taylor BS, Wang J, Zhang H, Anur P, Peto M, Spellman P, Benz C, Stuart JM, Wong CK, Yau C, Hayes DN, Parker JS, Wilkerson MD, Ally A, Balasundaram M, Bowlby R, Brooks D, Carlsen R, Chuah E, Dhalla N, Holt R, Jones SJM, Kasaian K, Lee D, Ma Y, Marra MA, Mayo M, Moore RA, Mungall AJ, Mungall K, Robertson AG, Sadeghi S, Schein JE, Sipahimalani P, Tam A, Thiessen N, Tse K, Wong T, Berger AC, Beroukhim R, Cherniack AD, Cibulskis C, Gabriel SB, Gao GF, Ha G, Meyerson M, Schumacher SE, Shih J, Kucherlapati MH, Kucherlapati RS, Baylin S, Cope L, Danilova L, Bootwalla MS, Lai PH, Maglinte DT, Van Den Berg DJ, Weisenberger DJ, Auman JT, Balu S, Bodenheimer T, Fan C, Hoadley KA, Hoyle AP, Jefferys SR, Jones CD, Meng S, Mieczkowski PA, Mose LE, Perou AH, Perou CM, Roach J, Shi Y, Simons JV, Skelly T, Soloway MG, Tan D, Veluvolu U, Fan H, Hinoue T, Laird PW, Shen H, Zhou W, Bellair M, Chang K, Covington K, Creighton CJ, Dinh H, Doddapaneni H, Donehower LA, Drummond J, Gibbs RA, Glenn R, Hale W, Han Y, Hu J, Korchina V, Lee S, Lewis L, Li W, Liu X, Morgan M, Morton D, Muzny D, Santibanez J, Sheth M, Shinbrot E, Wang L, Wang M, Wheeler DA, Xi L, Zhao F, Hess J, Appelbaum EL, Bailey M, Cordes MG, Ding L, Fronick CC, Fulton LA, Fulton RS, Kandoth C, Mardis ER, McLellan MD, Miller CA, Schmidt HK, Wilson RK, Crain D, Curley E, Gardner J, Lau K, Mallery D, Morris S, Paulauskis J, Penny R, Shelton C, Shelton T, Sherman M, Thompson E, Yena P, Bowen J, Gastier-Foster JM, Gerken M, Leraas KM, Lichtenberg TM, Ramirez NC, Wise L, Zmuda E, Corcoran N, Costello T, Hovens C, Carvalho AL, de Carvalho AC, Fregnani JH, Longatto-Filho A, Reis RM, Scapulatempo-Neto C, Silveira HCS, Vidal DO, Burnette A, Eschbacher J, Hermes B, Noss A, Singh R, Anderson ML, Castro PD, Ittmann M, Huntsman D, Kohl B, Le X, Thorp R, Andry C, Duffy ER, Lyadov V, Paklina O, Setdikova G, Shabunin A, Tavobilov M, McPherson C, Warnick R, Berkowitz R, Cramer D, Feltmate C, Horowitz N, Kibel A, Muto M, Raut CP, Malykh A, Barnholtz-Sloan JS, Barrett W, Devine K, Fulop J, Ostrom QT, Shimmel K, Wolinsky Y, Sloan AE, De Rose A, Giuliante F, Goodman M, Karlan BY, Hagedorn CH, Eckman J, Harr J, Myers J, Tucker K, Zach LA, Deyarmin B, Hu H, Kvecher L, Larson C, Mural RJ, Somiari S, Vicha A, Zelinka T, Bennett J, Iacocca M, Rabeno B, Swanson P, Latour M, Lacombe L, Têtu B, Bergeron A, McGraw M, Staugaitis SM, Chabot J, Hibshoosh H, Sepulveda A, Su T, Wang T, Potapova O, Voronina O, Desjardins L, Mariani O, Roman-Roman S, Sastre X, Stern M-H, Cheng F, Signoretti S, Berchuck A, Bigner D, Lipp E, Marks J, McCall S, McLendon R, Secord A, Sharp A, Behera M, Brat DJ, Chen A, Delman K, Force S, Khuri F, Magliocca K, Maithel S, Olson JJ, Owonikoko T, Pickens A, Ramalingam S, Shin DM, Sica G, Van Meir EG, Zhang H, Eijckenboom W, Gillis A, Korpershoek E, Looijenga L, Oosterhuis W, Stoop H, van Kessel KE, Zwarthoff EC, Calatozzolo C, Cuppini L, Cuzzubbo S, DiMeco F, Finocchiaro G, Mattei L, Perin A, Pollo B, Chen C, Houck J, Lohavanichbutr P, Hartmann A, Stoehr C, Stoehr R, Taubert H, Wach S, Wullich B, Kycler W, Murawa D, Wiznerowicz M, Chung K, Edenfield WJ, Martin J, Baudin E, Bubley G, Bueno R, De Rienzo A, Richards WG, Kalkanis S, Mikkelsen T, Noushmehr H, Scarpace L, Girard N, Aymerich M, Campo E, Giné E, Guillermo AL, Van Bang N, Hanh PT, Phu BD, Tang Y, Colman H, Evason K, Dottino PR, Martignetti JA, Gabra H, Juhl H, Akeredolu T, Stepa S, Hoon D, Ahn K, Kang KJ, Beuschlein F, Breggia A, Birrer M, Bell D, Borad M, Bryce AH, Castle E, Chandan V, Cheville J, Copland JA, Farnell M, Flotte T, Giama N, Ho T, Kendrick M, Kocher J-P, Kopp K, Moser C, Nagorney D, O'Brien D, O'Neill BP, Patel T,

Petersen G, Que F, Rivera M, Roberts L, Smallridge R, Smyrk T, Stanton M, Thompson RH, Torbenson M, Yang JD, Zhang L, Brimo F, Ajani JA, Gonzalez AMA, Behrens C, Bondaruk J, Broaddus R, Czerniak B, Esmaeli B, Fujimoto J, Gershenwald J, Guo C, Lazar AJ, Logothetis C, Meric-Bernstam F, Moran C, Ramondetta L, Rice D, Sood A, Tamboli P, Thompson T, Troncoso P, Tsao A, Wistuba I, Carter C, Haydu L, Hersey P, Jakrot V, Kakavand H, Kefford R, Lee K, Long G, Mann G, Quinn M, Saw R, Scolyer R, Shannon K, Spillane A, Stretch J, Synott M, Thompson J, Wilmott J, Al-Ahmadie H, Chan TA, Ghossein R, Gopalan A, Levine DA, Reuter V, Singer S, Singh B, Tien NV, Broudy T, Mirsaidi C, Nair P, Drwiega P, Miller J, Smith J, Zaren H, Park J-W, Hung NP, Kebebew E, Linehan WM, Metwalli AR, Pacak K, Pinto PA, Schiffman M, Schmidt LS, Vocke CD, Wentzensen N, Worrell R, Yang H, Moncrieff M, Goparaju C, Melamed J, Pass H, Botnariuc N, Caraman I, Cernat M, Chemencedji I, Clipca A, Doruc S, Gorincioi G, Mura S, Pirtac M, Stancul I, Tcaciuc D, Albert M, Alexopoulou I, Arnaout A, Bartlett J, Engel J, Gilbert S, Parfitt J, Sekhon H, Thomas G, Rassl DM, Rintoul RC, Bifulco C, Tamakawa R, Urba W, Hayward N, Timmers H, Antenucci A, Facciolo F, Grazi G, Marino M, Merola R, de Krijger R, Gimenez-Roqueplo A-P, Piché A, Chevalier S, McKercher G, Birsoy K, Barnett G, Brewer C, Farver C, Naska T, Pennell NA, Raymond D, Schilero C, Smolenski K, Williams F, Morrison C, Borgia JA, Liptay MJ, Pool M, Seder CW, Junker K, Omberg L, Dinkin M, Manikhas G, Alvaro D, Bragazzi MC, Cardinale V, Carpino G, Gaudio E, Chesla D, Cottingham S, Dubina M, Moiseenko F, Dhanasekaran R, Becker K-F, Janssen K-P, Slotta-Huspenina J, Abdel-Rahman MH, Aziz D, Bell S, Cebulla CM, Davis A, Duell R, Elder JB, Hilty J, Kumar B, Lang J, Lehman NL, Mandt R, Nguyen P, Pilarski R, Rai K, Schoenfield L, Senecal K, Wakely P, Hansen P, Lechan R, Powers J, Tischler A, Grizzle WE, Sexton KC, Kastl A, Henderson J, Porten S, Waldmann J, Fassnacht M, Asa SL, Schadendorf D, Couce M, Graefen M, Huland H, Sauter G, Schlomm T, Simon R, Tennstedt P, Olabode O, Nelson M, Bathe O, Carroll PR, Chan JM, Disaia P, Glenn P, Kelley RK, Landen CN, Phillips J, Prados M, Simko J, Smith-McCune K, VandenBerg S, Roggin K, Fehrenbach A, Kendler A, Sifri S, Steele R, Jimeno A, Carey F, Forgie I, Mannelli M, Carney M, Hernandez B, Campos B, Herold-Mende C, Jungk C, Unterberg A, von Deimling A, Bossler A, Galbraith J, Jacobus L, Knudson M, Knutson T, Ma D, Milhem M, Sigmund R, Godwin AK, Madan R, Rosenthal HG, Adebamowo C, Adebamowo SN, Boussioutas A, Beer D, Giordano T, Mes-Masson A-M, Saad F, Bocklage T, Landrum L, Mannel R, Moore K, Moxley K, Postier R, Walker J, Zuna R, Feldman M, Valdivieso F, Dhir R, Luketich J, Pinero EMM, Quintero-Aguilo M, Carlotti CG, Jr., Dos Santos JS, Kemp R, Sankarankuty A, Tirapelli D, Catto J, Agnew K, Swisher E, Creaney J, Robinson B, Shelley CS, Godwin EM, Kendall S, Shipman C, Bradford C, Carey T, Haddad A, Moyer J, Peterson L, Prince M, Rozek L, Wolf G, Bowman R, Fong KM, Yang I, Korst R, Rathmell WK, Fantacone-Campbell JL, Hooke JA, Kovatich AJ, Shriver CD, DiPersio J, Drake B, Govindan R, Heath S, Ley T, Van Tine B, Westervelt P, Rubin MA, Lee JI, Aredes ND, Mariamidze A, Van Allen EM, Cherniack AD, Ciriello G, Sander C, Schultz N. Oncogenic Signaling Pathways in The Cancer Genome Atlas. Cell. 2018;173(2):321-37.e10. doi: 10.1016/j.cell.2018.03.035.

5. Prior IA, Hood FE, Hartley JL. The Frequency of Ras Mutations in Cancer. Cancer research. 2020;80(14):2969-74. Epub 2020/03/27. doi: 10.1158/0008-5472.CAN-19-3682. PubMed PMID: 32209560; PMCID: PMC7367715.

6. Cox AD, Fesik SW, Kimmelman AC, Luo J, Der CJ. Drugging the undruggable RAS: Mission possible? Nature reviews Drug discovery. 2014;13(11):828-51. Epub 2014/10/18. doi: 10.1038/nrd4389. PubMed PMID: 25323927; PMCID: PMC4355017.

7. Hanahan D, Weinberg RA. Hallmarks of cancer: the next generation. Cell. 2011;144(5):646-74. Epub 2011/03/08. doi: 10.1016/j.cell.2011.02.013. PubMed PMID: 21376230.

8. Ledford H. Cancer: The Ras renaissance. Nature. 2015;520(7547):278-80. Epub 2015/04/17. doi: 10.1038/520278a. PubMed PMID: 25877186.

9. Cox AD, Der CJ, Philips MR. Targeting RAS Membrane Association: Back to the Future for Anti-RAS Drug Discovery? Clinical cancer research : an official journal of the American Association for Cancer Research. 2015;21(8):1819-27. Epub 2015/04/17. doi: 10.1158/1078-0432.CCR-14-3214. PubMed PMID: 25878363; PMCID: PMC4400837.

10. Li S, Balmain A, Counter CM. A model for RAS mutation patterns in cancers: finding the sweet spot. Nature reviews Cancer. 2018;18(12):767-77. Epub 2018/11/14. doi: 10.1038/s41568-018-0076-6. PubMed PMID: 30420765.

11. Zafra MP, Parsons MJ, Kim J, Alonso-Curbelo D, Goswami S, Schatoff EM, Han T, Katti A, Fernandez MTC, Wilkinson JE, Piskounova E, Dow LE. An In Vivo Kras Allelic Series Reveals Distinct Phenotypes of Common Oncogenic Variants. Cancer Discov. 2020;10(11):1654-71. Epub 2020/08/15. doi: 10.1158/2159-8290.CD-20-0442. PubMed PMID: 32792368; PMCID: PMC7642097.

12. Serebriiskii IG, Connelly C, Frampton G, Newberg J, Cooke M, Miller V, Ali S, Ross JS, Handorf E, Arora S, Lieu C, Golemis EA, Meyer JE. Comprehensive characterization of RAS mutations in colon and rectal cancers in old and young patients. Nature Communications. 2019;10(1):3722. doi: 10.1038/s41467-019-11530-0.

13. Collins MA, Bednar F, Zhang Y, Brisset JC, Galban S, Galban CJ, Rakshit S, Flannagan KS, Adsay NV, Pasca di Magliano M. Oncogenic Kras is required for both the initiation and maintenance of pancreatic cancer in mice. The Journal of clinical investigation. 2012;122(2):639-53. Epub 2012/01/11. doi: 10.1172/JCI59227. PubMed PMID: 22232209; PMCID: PMC3266788.

14. Fearon ER, Vogelstein B. A genetic model for colorectal tumorigenesis. Cell. 1990;61(5):759-67. Epub 1990/06/01. doi: 10.1016/0092-8674(90)90186-i. PubMed PMID: 2188735.

15. Herbst RS, Morgensztern D, Boshoff C. The biology and management of non-small cell lung cancer. Nature. 2018;553(7689):446-54. Epub 2018/01/25. doi: 10.1038/nature25183. PubMed PMID: 29364287.

16. Skoulidis F, Heymach JV. Co-occurring genomic alterations in non-small-cell lung cancer biology and therapy. Nature reviews Cancer. 2019;19(9):495-509. Epub

2019/08/14. doi: 10.1038/s41568-019-0179-8. PubMed PMID: 31406302; PMCID: PMC7043073.

17. Crawford HC, Pasca di Magliano M, Banerjee S. Signaling Networks That Control Cellular Plasticity in Pancreatic Tumorigenesis, Progression, and Metastasis. Gastroenterology. 2019;156(7):2073-84. Epub 2019/02/05. doi: 10.1053/j.gastro.2018.12.042. PubMed PMID: 30716326; PMCID: PMC6545585.

18. Peddareddigari VG, Wang D, Dubois RN. The tumor microenvironment in colorectal carcinogenesis. Cancer Microenviron. 2010;3(1):149-66. Epub 2011/01/07. doi: 10.1007/s12307-010-0038-3. PubMed PMID: 21209781; PMCID: PMC2990487.

19. Lambrechts D, Wauters E, Boeckx B, Aibar S, Nittner D, Burton O, Bassez A, Decaluwe H, Pircher A, Van den Eynde K, Weynand B, Verbeken E, De Leyn P, Liston A, Vansteenkiste J, Carmeliet P, Aerts S, Thienpont B. Phenotype molding of stromal cells in the lung tumor microenvironment. Nature medicine. 2018;24(8):1277-89. Epub 2018/07/11. doi: 10.1038/s41591-018-0096-5. PubMed PMID: 29988129.

20. Zeitouni D, Pylayeva-Gupta Y, Der CJ, Bryant KL. KRAS Mutant Pancreatic Cancer: No Lone Path to an Effective Treatment. Cancers (Basel). 2016;8(4):45. Epub 2016/04/21. doi: 10.3390/cancers8040045. PubMed PMID: 27096871; PMCID: PMC4846854.

21. Bryant KL, Mancias JD, Kimmelman AC, Der CJ. KRAS: feeding pancreatic cancer proliferation. Trends in biochemical sciences. 2014;39(2):91-100. Epub 2014/01/07. doi: 10.1016/j.tibs.2013.12.004. PubMed PMID: 24388967; PMCID: PMC3955735.

22. Kerr EM, Gaude E, Turrell FK, Frezza C, Martins CP. Mutant Kras copy number defines metabolic reprogramming and therapeutic susceptibilities. Nature. 2016;531(7592):110-3. Epub 2016/02/26. doi: 10.1038/nature16967. PubMed PMID: 26909577; PMCID: PMC4780242.

23. Ying H, Kimmelman AC, Lyssiotis CA, Hua S, Chu GC, Fletcher-Sananikone E, Locasale JW, Son J, Zhang H, Coloff JL, Yan H, Wang W, Chen S, Viale A, Zheng H, Paik JH, Lim C, Guimaraes AR, Martin ES, Chang J, Hezel AF, Perry SR, Hu J, Gan B, Xiao Y, Asara JM, Weissleder R, Wang YA, Chin L, Cantley LC, DePinho RA. Oncogenic Kras maintains pancreatic tumors through regulation of anabolic glucose metabolism. Cell. 2012;149(3):656-70. Epub 2012/05/01. doi: 10.1016/j.cell.2012.01.058. PubMed PMID: 22541435; PMCID: PMC3472002.

24. Yun J, Rago C, Cheong I, Pagliarini R, Angenendt P, Rajagopalan H, Schmidt K, Willson JK, Markowitz S, Zhou S, Diaz LA, Jr., Velculescu VE, Lengauer C, Kinzler KW, Vogelstein B, Papadopoulos N. Glucose deprivation contributes to the development of KRAS pathway mutations in tumor cells. Science (New York, NY). 2009;325(5947):1555-9. Epub 2009/08/08. doi: 10.1126/science.1174229. PubMed PMID: 19661383; PMCID: PMC2820374.

25. Pupo E, Avanzato D, Middonti E, Bussolino F, Lanzetti L. KRAS-Driven Metabolic Rewiring Reveals Novel Actionable Targets in Cancer. Front Oncol. 2019;9:848. Epub 2019/09/24. doi: 10.3389/fonc.2019.00848. PubMed PMID: 31544066; PMCID: PMC6730590.

26. Gaglio D, Metallo CM, Gameiro PA, Hiller K, Danna LS, Balestrieri C, Alberghina L, Stephanopoulos G, Chiaradonna F. Oncogenic K-Ras decouples glucose and glutamine metabolism to support cancer cell growth. Mol Syst Biol. 2011;7:523. Epub 2011/08/19. doi: 10.1038/msb.2011.56. PubMed PMID: 21847114; PMCID: PMC3202795.

27. Kerr EM, Martins CP. Metabolic rewiring in mutant Kras lung cancer. FEBS J. 2018;285(1):28-41. Epub 2017/06/02. doi: 10.1111/febs.14125. PubMed PMID: 28570035; PMCID: PMC6005344.

28. Hutton JE, Wang X, Zimmerman LJ, Slebos RJ, Trenary IA, Young JD, Li M, Liebler DC. Oncogenic KRAS and BRAF Drive Metabolic Reprogramming in Colorectal Cancer. Mol Cell Proteomics. 2016;15(9):2924-38. Epub 2016/06/25. doi: 10.1074/mcp.M116.058925. PubMed PMID: 27340238; PMCID: PMC5013308.

29. Aguilera O, Munoz-Sagastibelza M, Torrejon B, Borrero-Palacios A, Del Puerto-Nevado L, Martinez-Useros J, Rodriguez-Remirez M, Zazo S, Garcia E, Fraga M, Rojo F, Garcia-Foncillas J. Vitamin C uncouples the Warburg metabolic switch in KRAS mutant colon cancer. Oncotarget. 2016;7(30):47954-65. Epub 2016/06/22. doi: 10.18632/oncotarget.10087. PubMed PMID: 27323830; PMCID: PMC5216991.

30. Iwamoto M, Kawada K, Nakamoto Y, Itatani Y, Inamoto S, Toda K, Kimura H, Sasazuki T, Shirasawa S, Okuyama H, Inoue M, Hasegawa S, Togashi K, Sakai Y. Regulation of 18F-FDG accumulation in colorectal cancer cells with mutated KRAS. J Nucl Med. 2014;55(12):2038-44. Epub 2014/12/03. doi: 10.2967/jnumed.114.142927. PubMed PMID: 25453050.

31. Kawada K, Nakamoto Y, Kawada M, Hida K, Matsumoto T, Murakami T, Hasegawa S, Togashi K, Sakai Y. Relationship between ¹⁸F-Fluorodeoxyglucose Accumulation and KRAS/BRAF Mutations in Colorectal Cancer. Clinical Cancer Research. 2012;18(6):1696. doi: 10.1158/1078-0432.CCR-11-1909.

32. Amendola CR, Mahaffey JP, Parker SJ, Ahearn IM, Chen W-C, Zhou M, Court H, Shi J, Mendoza SL, Morten MJ, Rothenberg E, Gottlieb E, Wadghiri YZ, Possemato R, Hubbard SR, Balmain A, Kimmelman AC, Philips MR. KRAS4A directly regulates hexokinase 1. Nature. 2019;576(7787):482-6. doi: 10.1038/s41586-019-1832-9.

33. Wang H, Wang L, Zhang Y, Wang J, Deng Y, Lin D. Inhibition of glycolytic enzyme hexokinase II (HK2) suppresses lung tumor growth. Cancer Cell Int. 2016;16(1):9. Epub 2016/02/18. doi: 10.1186/s12935-016-0280-y. PubMed PMID: 26884725; PMCID: PMC4755025.

34. Kim J, Lee HM, Cai F, Ko B, Yang C, Lieu EL, Muhammad N, Rhyne S, Li K, Haloul M, Gu W, Faubert B, Kaushik AK, Cai L, Kasiri S, Marriam U, Nham K, Girard L, Wang H, Sun X, Kim J, Minna JD, Unsal-Kacmaz K, DeBerardinis RJ. The hexosamine biosynthesis pathway is a targetable liability in KRAS/LKB1 mutant lung cancer. Nature Metabolism. 2020. doi: 10.1038/s42255-020-00316-0.

35. Santana-Codina N, Roeth AA, Zhang Y, Yang A, Mashadova O, Asara JM, Wang X, Bronson RT, Lyssiotis CA, Ying H, Kimmelman AC. Oncogenic KRAS supports pancreatic cancer through regulation of nucleotide synthesis. Nat Commun. 2018;9(1):4945. Epub 2018/11/25. doi: 10.1038/s41467-018-07472-8. PubMed PMID: 30470748; PMCID: PMC6251888.

36. Ali ES, Sahu U, Villa E, O'Hara BP, Gao P, Beaudet C, Wood AW, Asara JM, Ben-Sahra I. ERK2 Phosphorylates PFAS to Mediate Posttranslational Control of De Novo Purine Synthesis. Molecular Cell. 2020;78(6):1178-91.e6. doi: 10.1016/j.molcel.2020.05.001.

37. Mattaini KR, Sullivan MR, Vander Heiden MG. The importance of serine metabolism in cancer. The Journal of cell biology. 2016;214(3):249-57. Epub 2016/07/28. doi: 10.1083/jcb.201604085. PubMed PMID: 27458133; PMCID: PMC4970329.

38. Maddocks ODK, Athineos D, Cheung EC, Lee P, Zhang T, van den Broek NJF, Mackay GM, Labuschagne CF, Gay D, Kruiswijk F, Blagih J, Vincent DF, Campbell KJ, Ceteci F, Sansom OJ, Blyth K, Vousden KH. Modulating the therapeutic response of tumours to dietary serine and glycine starvation. Nature. 2017;544(7650):372-6. Epub 2017/04/21. doi: 10.1038/nature22056. PubMed PMID: 28425994.

39. Xie H, Hanai J, Ren JG, Kats L, Burgess K, Bhargava P, Signoretti S, Billiard J, Duffy KJ, Grant A, Wang X, Lorkiewicz PK, Schatzman S, Bousamra M, 2nd, Lane AN, Higashi RM, Fan TW, Pandolfi PP, Sukhatme VP, Seth P. Targeting lactate dehydrogenase--a inhibits tumorigenesis and tumor progression in mouse models of lung cancer and impacts tumor-initiating cells. Cell metabolism. 2014;19(5):795-809. Epub 2014/04/15. doi: 10.1016/j.cmet.2014.03.003. PubMed PMID: 24726384; PMCID: PMC4096909.

40. McCleland ML, Adler AS, Deming L, Cosino E, Lee L, Blackwood EM, Solon M, Tao J, Li L, Shames D, Jackson E, Forrest WF, Firestein R. Lactate dehydrogenase B is required for the growth of KRAS-dependent lung adenocarcinomas. Clinical cancer research : an official journal of the American Association for Cancer Research. 2013;19(4):773-84. Epub 2012/12/12. doi: 10.1158/1078-0432.CCR-12-2638. PubMed PMID: 23224736.

41. Kerk SA, Lin L, Myers AL, Chen B, Sajjakulnukit P, Robinson A, Thurston G, Nelson BS, Kemp SB, Steele NG, Hoffman MT, Wen H-J, Long D, Ackenhusen SE, Ramos J, Gao X, Zhang L, Andren A, Nwosu ZC, Galbán S, Halbrook CJ, Lombard DB, Ying H, Crawford HC, di Magliano MP, Shah YM, Lyssiotis CA. The Pancreatic Tumor

Microenvironment Buffers Redox Imbalance Imposed by Disrupted Mitochondrial Metabolism. bioRxiv. 2020:2020.08.07.238766. doi: 10.1101/2020.08.07.238766.

42. Baek G, Tse YF, Hu Z, Cox D, Buboltz N, McCue P, Yeo CJ, White MA, DeBerardinis RJ, Knudsen ES, Witkiewicz AK. MCT4 defines a glycolytic subtype of pancreatic cancer with poor prognosis and unique metabolic dependencies. Cell Rep. 2014;9(6):2233-49. Epub 2014/12/17. doi: 10.1016/j.celrep.2014.11.025. PubMed PMID: 25497091.

43. Graziano F, Ruzzo A, Giacomini E, Ricciardi T, Aprile G, Loupakis F, Lorenzini P, Ongaro E, Zoratto F, Catalano V, Sarti D, Rulli E, Cremolini C, De Nictolis M, De Maglio G, Falcone A, Fiorentini G, Magnani M. Glycolysis gene expression analysis and selective metabolic advantage in the clinical progression of colorectal cancer. Pharmacogenomics J. 2017;17(3):258-64. Epub 2016/03/02. doi: 10.1038/tpj.2016.13. PubMed PMID: 26927284.

44. Martinez-Reyes I, Chandel NS. Mitochondrial TCA cycle metabolites control physiology and disease. Nat Commun. 2020;11(1):102. Epub 2020/01/05. doi: 10.1038/s41467-019-13668-3. PubMed PMID: 31900386; PMCID: PMC6941980.

45. Weinberg SE, Chandel NS. Targeting mitochondria metabolism for cancer therapy. Nature chemical biology. 2015;11(1):9-15. Epub 2014/12/18. doi: 10.1038/nchembio.1712. PubMed PMID: 25517383; PMCID: PMC4340667.

46. Schvartzman JM, Thompson CB, Finley LWS. Metabolic regulation of chromatin modifications and gene expression. The Journal of cell biology. 2018;217(7):2247-59. Epub 2018/05/16. doi: 10.1083/jcb.201803061. PubMed PMID: 29760106; PMCID: PMC6028552.

47. Vasan K, Werner M, Chandel NS. Mitochondrial Metabolism as a Target for Cancer Therapy. Cell metabolism. 2020;32(3):341-52. Epub 2020/07/16. doi: 10.1016/j.cmet.2020.06.019. PubMed PMID: 32668195; PMCID: PMC7483781.

48. Kong H, Chandel NS. Regulation of redox balance in cancer and T cells. The Journal of biological chemistry. 2018;293(20):7499-507. Epub 2017/12/29. doi: 10.1074/jbc.TM117.000257. PubMed PMID: 29282291; PMCID: PMC5961053.

49. Chandel NS. Evolution of Mitochondria as Signaling Organelles. Cell metabolism. 2015;22(2):204-6. Epub 2015/06/16. doi: 10.1016/j.cmet.2015.05.013. PubMed PMID: 26073494.

50. Humpton TJ, Alagesan B, DeNicola GM, Lu D, Yordanov GN, Leonhardt CS, Yao MA, Alagesan P, Zaatari MN, Park Y, Skepper JN, Macleod KF, Perez-Mancera PA, Murphy MP, Evan GI, Vousden KH, Tuveson DA. Oncogenic KRAS Induces NIX-Mediated Mitophagy to Promote Pancreatic Cancer. Cancer Discov. 2019;9(9):1268-87. Epub 2019/07/03. doi: 10.1158/2159-8290.CD-18-1409. PubMed PMID: 31263025; PMCID: PMC6726540.

51. Sullivan LB, Chandel NS. Mitochondrial reactive oxygen species and cancer. Cancer Metab. 2014;2(2049-3002 (Print)):17. Epub 2015/02/12. doi: 10.1186/2049-3002-2-17. PubMed PMID: 25671107; PMCID: PMC4323058.

52. Weinberg F, Hamanaka R, Wheaton WW, Weinberg S, Joseph J, Lopez M, Kalyanaraman B, Mutlu GM, Budinger GR, Chandel NS. Mitochondrial metabolism and ROS generation are essential for Kras-mediated tumorigenicity. Proceedings of the National Academy of Sciences of the United States of America. 2010;107(19):8788-93. Epub 2010/04/28. doi: 10.1073/pnas.1003428107. PubMed PMID: 20421486; PMCID: PMC2889315.

53. Chauhan SS, Toth RK, Jensen CC, Casillas AL, Kashatus DF, Warfel NA. PIM kinases alter mitochondrial dynamics and chemosensitivity in lung cancer. Oncogene. 2020;39(12):2597-611. Epub 2020/01/30. doi: 10.1038/s41388-020-1168-9. PubMed PMID: 31992853; PMCID: PMC7545584.

54. Kashatus JA, Nascimento A, Myers LJ, Sher A, Byrne FL, Hoehn KL, Counter CM, Kashatus DF. Erk2 phosphorylation of Drp1 promotes mitochondrial fission and MAPK-driven tumor growth. Mol Cell. 2015;57(3):537-51. Epub 2015/02/07. doi: 10.1016/j.molcel.2015.01.002. PubMed PMID: 25658205; PMCID: PMC4393013.

55. Yu M, Nguyen ND, Huang Y, Lin D, Fujimoto TN, Molkentine JM, Deorukhkar A, Kang Y, San Lucas FA, Fernandes CJ, Koay EJ, Gupta S, Ying H, Koong AC, Herman JM, Fleming JB, Maitra A, Taniguchi CM. Mitochondrial fusion exploits a therapeutic vulnerability of pancreatic cancer. JCI Insight. 2019;5(16). Epub 2019/07/25. doi: 10.1172/jci.insight.126915. PubMed PMID: 31335325; PMCID: PMC6777817.

56. Hensley CT, Wasti AT, DeBerardinis RJ. Glutamine and cancer: cell biology, physiology, and clinical opportunities. The Journal of clinical investigation. 2013;123(9):3678-84. Epub 2013/09/04. doi: 10.1172/JCI69600. PubMed PMID: 23999442; PMCID: PMC3754270.

57. Son J, Lyssiotis CA, Ying H, Wang X, Hua S, Ligorio M, Perera RM, Ferrone CR, Mullarky E, Shyh-Chang N, Kang Y, Fleming JB, Bardeesy N, Asara JM, Haigis MC, DePinho RA, Cantley LC, Kimmelman AC. Glutamine supports pancreatic cancer growth through a KRAS-regulated metabolic pathway. Nature. 2013;496(7443):101-5. Epub 2013/03/29. doi: 10.1038/nature12040. PubMed PMID: 23535601; PMCID: PMC3656466.

58. Davidson SM, Papagiannakopoulos T, Olenchock BA, Heyman JE, Keibler MA, Luengo A, Bauer MR, Jha AK, O'Brien JP, Pierce KA, Gui DY, Sullivan LB, Wasylenko TM, Subbaraj L, Chin CR, Stephanopolous G, Mott BT, Jacks T, Clish CB, Vander Heiden MG. Environment Impacts the Metabolic Dependencies of Ras-Driven Non-Small Cell Lung Cancer. Cell metabolism. 2016;23(3):517-28. Epub 2016/02/09. doi: 10.1016/j.cmet.2016.01.007. PubMed PMID: 26853747; PMCID: PMC4785096.

59. Miyo M, Konno M, Nishida N, Sueda T, Noguchi K, Matsui H, Colvin H, Kawamoto K, Koseki J, Haraguchi N, Nishimura J, Hata T, Gotoh N, Matsuda F, Satoh

T, Mizushima T, Shimizu H, Doki Y, Mori M, Ishii H. Metabolic Adaptation to Nutritional Stress in Human Colorectal Cancer. Scientific Reports. 2016;6(1):38415. doi: 10.1038/srep38415.

60. Yuneva MO, Fan TW, Allen TD, Higashi RM, Ferraris DV, Tsukamoto T, Mates JM, Alonso FJ, Wang C, Seo Y, Chen X, Bishop JM. The metabolic profile of tumors depends on both the responsible genetic lesion and tissue type. Cell metabolism. 2012;15(2):157-70. Epub 2012/02/14. doi: 10.1016/j.cmet.2011.12.015. PubMed PMID: 22326218; PMCID: PMC3282107.

61. Mayers JR, Vander Heiden MG. Famine versus feast: understanding the metabolism of tumors in vivo. Trends in biochemical sciences. 2015;40(3):130-40. Epub 2015/02/03. doi: 10.1016/j.tibs.2015.01.004. PubMed PMID: 25639751; PMCID: PMC4340757.

62. Wong CC, Qian Y, Li X, Xu J, Kang W, Tong JH, To KF, Jin Y, Li W, Chen H, Go MY, Wu JL, Cheng KW, Ng SS, Sung JJ, Cai Z, Yu J. SLC25A22 Promotes Proliferation and Survival of Colorectal Cancer Cells With KRAS Mutations and Xenograft Tumor Progression in Mice via Intracellular Synthesis of Aspartate. Gastroenterology. 2016;151(5):945-60 e6. Epub 2016/07/28. doi: 10.1053/j.gastro.2016.07.011. PubMed PMID: 27451147.

63. Toda K, Kawada K, Iwamoto M, Inamoto S, Sasazuki T, Shirasawa S, Hasegawa S, Sakai Y. Metabolic Alterations Caused by KRAS Mutations in Colorectal Cancer Contribute to Cell Adaptation to Glutamine Depletion by Upregulation of Asparagine Synthetase. Neoplasia. 2016;18(11):654-65. doi: https://doi.org/10.1016/j.neo.2016.09.004.

64. Halbrook CJ, Thurston G, McCarthy A, Nelson BS, Sajjakulnukit P, Krall AS, Mullen PJ, Zhang L, Batra S, Viale A, Stanger BZ, Christofk HR, Zhang J, di Magliano MP, Jorgensen C, Lyssiotis CA. Clonal Heterogeneity Supports Mitochondrial Metabolism in Pancreatic Cancer. bioRxiv. 2020:2020.05.15.098368. doi: 10.1101/2020.05.15.098368.

65. Gwinn DM, Lee AG, Briones-Martin-Del-Campo M, Conn CS, Simpson DR, Scott AI, Le A, Cowan TM, Ruggero D, Sweet-Cordero EA. Oncogenic KRAS Regulates Amino Acid Homeostasis and Asparagine Biosynthesis via ATF4 and Alters Sensitivity to L-Asparaginase. Cancer cell. 2018;33(1):91-107.e6. Epub 2018/01/10. doi: 10.1016/j.ccell.2017.12.003. PubMed PMID: 29316436; PMCID: PMC5761662.

66. Bott AJ, Shen J, Tonelli C, Zhan L, Sivaram N, Jiang Y-P, Yu X, Bhatt V, Chiles E, Zhong H, Maimouni S, Dai W, Velasquez S, Pan J-A, Muthalagu N, Morton J, Anthony TG, Feng H, Lamers WH, Murphy DJ, Guo JY, Jin J, Crawford HC, Zhang L, White E, Lin RZ, Su X, Tuveson DA, Zong W-X. Glutamine Anabolism Plays a Critical Role in Pancreatic Cancer by Coupling Carbon and Nitrogen Metabolism. Cell Reports. 2019;29(5):1287-98.e6. doi: https://doi.org/10.1016/j.celrep.2019.09.056.

67. Kamphorst JJ, Nofal M, Commisso C, Hackett SR, Lu W, Grabocka E, Vander Heiden MG, Miller G, Drebin JA, Bar-Sagi D, Thompson CB, Rabinowitz JD. Human pancreatic cancer tumors are nutrient poor and tumor cells actively scavenge extracellular protein. Cancer research. 2015;75(3):544-53. Epub 2015/02/04. doi: 10.1158/0008-5472.CAN-14-2211. PubMed PMID: 25644265; PMCID: PMC4316379.

68. Commisso C, Davidson SM, Soydaner-Azeloglu RG, Parker SJ, Kamphorst JJ, Hackett S, Grabocka E, Nofal M, Drebin JA, Thompson CB, Rabinowitz JD, Metallo CM, Vander Heiden MG, Bar-Sagi D. Macropinocytosis of protein is an amino acid supply route in Ras-transformed cells. Nature. 2013;497(7451):633-7. Epub 2013/05/15. doi: 10.1038/nature12138. PubMed PMID: 23665962; PMCID: PMC3810415.

69. Ramirez C, Hauser AD, Vucic EA, Bar-Sagi D. Plasma membrane V-ATPase controls oncogenic RAS-induced macropinocytosis. Nature. 2019;576(7787):477-81. Epub 2019/12/13. doi: 10.1038/s41586-019-1831-x. PubMed PMID: 31827278; PMCID: PMC7048194.

70. Hodakoski C, Hopkins BD, Zhang G, Su T, Cheng Z, Morris R, Rhee KY, Goncalves MD, Cantley LC. Rac-Mediated Macropinocytosis of Extracellular Protein Promotes Glucose Independence in Non-Small Cell Lung Cancer. Cancers (Basel). 2019;11(1). Epub 2019/01/06. doi: 10.3390/cancers11010037. PubMed PMID: 30609754; PMCID: PMC6356657.

71. King B, Araki J, Palm W, Thompson CB. Yap/Taz promote the scavenging of extracellular nutrients through macropinocytosis. Genes Dev. 2020;34(19-20):1345-58. Epub 2020/09/12. doi: 10.1101/gad.340661.120. PubMed PMID: 32912902; PMCID: PMC7528706.

72. Palm W, Araki J, King B, DeMatteo RG, Thompson CB. Critical role for PI3-kinase in regulating the use of proteins as an amino acid source. Proceedings of the National Academy of Sciences of the United States of America. 2017;114(41):E8628-E36. Epub 2017/10/05. doi: 10.1073/pnas.1712726114. PubMed PMID: 28973876; PMCID: PMC5642723.

73. Zhang Y, Commisso C. Macropinocytosis in Cancer: A Complex Signaling Network. Trends Cancer. 2019;5(6):332-4. Epub 2019/06/19. doi: 10.1016/j.trecan.2019.04.002. PubMed PMID: 31208695; PMCID: PMC7325493.

74. Lee SW, Zhang Y, Jung M, Cruz N, Alas B, Commisso C. EGFR-Pak Signaling Selectively Regulates Glutamine Deprivation-Induced Macropinocytosis. Dev Cell. 2019;50(3):381-92 e5. Epub 2019/07/02. doi: 10.1016/j.devcel.2019.05.043. PubMed PMID: 31257175; PMCID: PMC6684838.

75. Hobbs GA, Baker NM, Miermont AM, Thurman RD, Pierobon M, Tran TH, Anderson AO, Waters AM, Diehl JN, Papke B, Hodge RG, Klomp JE, Goodwin CM, DeLiberty JM, Wang J, Ng RWS, Gautam P, Bryant KL, Esposito D, Campbell SL, Petricoin EF, 3rd, Simanshu DK, Aguirre AJ, Wolpin BM, Wennerberg K, Rudloff U, Cox AD, Der CJ. Atypical KRAS(G12R) Mutant Is Impaired in PI3K Signaling and

Macropinocytosis in Pancreatic Cancer. Cancer Discov. 2020;10(1):104-23. Epub 2019/10/28. doi: 10.1158/2159-8290.CD-19-1006. PubMed PMID: 31649109; PMCID: PMC6954322.

76. Kimmelman AC, White E. Autophagy and Tumor Metabolism. Cell metabolism. 2017;25(5):1037-43. Epub 2017/05/04. doi: 10.1016/j.cmet.2017.04.004. PubMed PMID: 28467923; PMCID: PMC5604466.

77. Perera RM, Stoykova S, Nicolay BN, Ross KN, Fitamant J, Boukhali M, Lengrand J, Deshpande V, Selig MK, Ferrone CR, Settleman J, Stephanopoulos G, Dyson NJ, Zoncu R, Ramaswamy S, Haas W, Bardeesy N. Transcriptional control of autophagy-lysosome function drives pancreatic cancer metabolism. Nature. 2015;524(7565):361-5. Epub 2015/07/15. doi: 10.1038/nature14587. PubMed PMID: 26168401; PMCID: PMC5086585.

78. Perera RM, Bardeesy N. Pancreatic Cancer Metabolism: Breaking It Down to Build It Back Up. Cancer Discov. 2015;5(12):1247-61. Epub 2015/11/05. doi: 10.1158/2159-8290.CD-15-0671. PubMed PMID: 26534901; PMCID: PMC4687899.

79. Yang A, Herter-Sprie G, Zhang H, Lin EY, Biancur D, Wang X, Deng J, Hai J, Yang S, Wong KK, Kimmelman AC. Autophagy Sustains Pancreatic Cancer Growth through Both Cell-Autonomous and Nonautonomous Mechanisms. Cancer Discov. 2018;8(3):276-87. Epub 2018/01/11. doi: 10.1158/2159-8290.CD-17-0952. PubMed PMID: 29317452; PMCID: PMC5835190.

80. Yang S, Imamura Y, Jenkins RW, Canadas I, Kitajima S, Aref A, Brannon A, Oki E, Castoreno A, Zhu Z, Thai T, Reibel J, Qian Z, Ogino S, Wong KK, Baba H, Kimmelman AC, Pasca Di Magliano M, Barbie DA. Autophagy Inhibition Dysregulates TBK1 Signaling and Promotes Pancreatic Inflammation. Cancer immunology research. 2016;4(6):520-30. Epub 2016/04/14. doi: 10.1158/2326-6066.CIR-15-0235. PubMed PMID: 27068336; PMCID: PMC4891226.

81. Guo JY, Chen HY, Mathew R, Fan J, Strohecker AM, Karsli-Uzunbas G, Kamphorst JJ, Chen G, Lemons JM, Karantza V, Coller HA, Dipaola RS, Gelinas C, Rabinowitz JD, White E. Activated Ras requires autophagy to maintain oxidative metabolism and tumorigenesis. Genes Dev. 2011;25(5):460-70. Epub 2011/02/15. doi: 10.1101/gad.2016311. PubMed PMID: 21317241; PMCID: PMC3049287.

82. Amaravadi RK, Kimmelman AC, Debnath J. Targeting Autophagy in Cancer: Recent Advances and Future Directions. Cancer Discov. 2019;9(9):1167-81. Epub 2019/08/23. doi: 10.1158/2159-8290.CD-19-0292. PubMed PMID: 31434711; PMCID: PMC7306856.

83. White E. Exploiting the bad eating habits of Ras-driven cancers. Genes Dev. 2013;27(19):2065-71. Epub 2013/10/12. doi: 10.1101/gad.228122.113. PubMed PMID: 24115766; PMCID: PMC3850091.

84. Guo JY, Teng X, Laddha SV, Ma S, Van Nostrand SC, Yang Y, Khor S, Chan CS, Rabinowitz JD, White E. Autophagy provides metabolic substrates to maintain energy charge and nucleotide pools in Ras-driven lung cancer cells. Genes Dev. 2016;30(15):1704-17. Epub 2016/08/16. doi: 10.1101/gad.283416.116. PubMed PMID: 27516533; PMCID: PMC5002976.

85. Bryant KL, Stalnecker CA, Zeitouni D, Klomp JE, Peng S, Tikunov AP, Gunda V, Pierobon M, Waters AM, George SD, Tomar G, Papke B, Hobbs GA, Yan L, Hayes TK, Diehl JN, Goode GD, Chaika NV, Wang Y, Zhang GF, Witkiewicz AK, Knudsen ES, Petricoin EF, 3rd, Singh PK, Macdonald JM, Tran NL, Lyssiotis CA, Ying H, Kimmelman AC, Cox AD, Der CJ. Combination of ERK and autophagy inhibition as a treatment approach for pancreatic cancer. Nature medicine. 2019;25(4):628-40. Epub 2019/03/06. doi: 10.1038/s41591-019-0368-8. PubMed PMID: 30833752; PMCID: PMC6484853.

86. White E. Blockade of RAF and autophagy is the one-two punch to take out Ras. Proceedings of the National Academy of Sciences of the United States of America. 2019;116(10):3965-7. Epub 2019/02/21. doi: 10.1073/pnas.1900800116. PubMed PMID: 30782814; PMCID: PMC6410840 LLC and a stockholder in Forma Therapeutics.

87. Poillet-Perez L, Xie X, Zhan L, Yang Y, Sharp DW, Hu ZS, Su X, Maganti A, Jiang C, Lu W, Zheng H, Bosenberg MW, Mehnert JM, Guo JY, Lattime E, Rabinowitz JD, White E. Autophagy maintains tumour growth through circulating arginine. Nature. 2018;563(7732):569-73. Epub 2018/11/16. doi: 10.1038/s41586-018-0697-7. PubMed PMID: 30429607; PMCID: PMC6287937.

88. Karsli-Uzunbas G, Guo JY, Price S, Teng X, Laddha SV, Khor S, Kalaany NY, Jacks T, Chan CS, Rabinowitz JD, White E. Autophagy is required for glucose homeostasis and lung tumor maintenance. Cancer Discov. 2014;4(8):914-27. Epub 2014/05/31. doi: 10.1158/2159-8290.CD-14-0363. PubMed PMID: 24875857; PMCID: PMC4125614.

89. Currie E, Schulze A, Zechner R, Walther Tobias C, Farese Robert V, Jr. Cellular Fatty Acid Metabolism and Cancer. Cell metabolism. 2013;18(2):153-61. doi: 10.1016/j.cmet.2013.05.017.

90. Singh A, Ruiz C, Bhalla K, Haley JA, Li QK, Acquaah-Mensah G, Montal E, Sudini KR, Skoulidis F, Wistuba, II, Papadimitrakopoulou V, Heymach JV, Boros LG, Gabrielson E, Carretero J, Wong KK, Haley JD, Biswal S, Girnun GD. De novo lipogenesis represents a therapeutic target in mutant Kras non-small cell lung cancer. FASEB J. 2018:fj201800204. Epub 2018/06/16. doi: 10.1096/fj.201800204. PubMed PMID: 29906244; PMCID: PMC6219836.

91. Gouw AM, Eberlin LS, Margulis K, Sullivan DK, Toal GG, Tong L, Zare RN, Felsher DW. Oncogene KRAS activates fatty acid synthase, resulting in specific ERK and lipid signatures associated with lung adenocarcinoma. Proceedings of the National Academy of Sciences of the United States of America. 2017;114(17):4300-5. Epub

2017/04/13. doi: 10.1073/pnas.1617709114. PubMed PMID: 28400509; PMCID: PMC5410819.

92. Svensson RU, Parker SJ, Eichner LJ, Kolar MJ, Wallace M, Brun SN, Lombardo PS, Van Nostrand JL, Hutchins A, Vera L, Gerken L, Greenwood J, Bhat S, Harriman G, Westlin WF, Harwood HJ, Jr., Saghatelian A, Kapeller R, Metallo CM, Shaw RJ. Inhibition of acetyl-CoA carboxylase suppresses fatty acid synthesis and tumor growth of non-small-cell lung cancer in preclinical models. Nature medicine. 2016;22(10):1108-19. Epub 2016/09/20. doi: 10.1038/nm.4181. PubMed PMID: 27643638; PMCID: PMC5053891.

93. Zaytseva YY, Harris JW, Mitov MI, Kim JT, Butterfield DA, Lee EY, Weiss HL, Gao T, Evers BM. Increased expression of fatty acid synthase provides a survival advantage to colorectal cancer cells via upregulation of cellular respiration. Oncotarget. 2015;6(22):18891-904. Epub 2015/05/15. doi: 10.18632/oncotarget.3783. PubMed PMID: 25970773; PMCID: PMC4662462.

94. Padanad MS, Konstantinidou G, Venkateswaran N, Melegari M, Rindhe S, Mitsche M, Yang C, Batten K, Huffman KE, Liu J, Tang X, Rodriguez-Canales J, Kalhor N, Shay JW, Minna JD, McDonald J, Wistuba, II, DeBerardinis RJ, Scaglioni PP. Fatty Acid Oxidation Mediated by Acyl-CoA Synthetase Long Chain 3 Is Required for Mutant KRAS Lung Tumorigenesis. Cell Rep. 2016;16(6):1614-28. Epub 2016/08/02. doi: 10.1016/j.celrep.2016.07.009. PubMed PMID: 27477280; PMCID: PMC4981512.

95. Kamphorst JJ, Cross JR, Fan J, de Stanchina E, Mathew R, White EP, Thompson CB, Rabinowitz JD. Hypoxic and Ras-transformed cells support growth by scavenging unsaturated fatty acids from lysophospholipids. Proceedings of the National Academy of Sciences of the United States of America. 2013;110(22):8882-7. Epub 2013/05/15. doi: 10.1073/pnas.1307237110. PubMed PMID: 23671091; PMCID: PMC3670379.

96. Guillaumond F, Bidaut G, Ouaissi M, Servais S, Gouirand V, Olivares O, Lac S, Borge L, Roques J, Gayet O, Pinault M, Guimaraes C, Nigri J, Loncle C, Lavaut MN, Garcia S, Tailleux A, Staels B, Calvo E, Tomasini R, Iovanna JL, Vasseur S. Cholesterol uptake disruption, in association with chemotherapy, is a promising combined metabolic therapy for pancreatic adenocarcinoma. Proceedings of the National Academy of Sciences of the United States of America. 2015;112(8):2473-8. Epub 2015/02/13. doi: 10.1073/pnas.1421601112. PubMed PMID: 25675507; PMCID: PMC4345573.

97. Rozeveld CN, Johnson KM, Zhang L, Razidlo GL. KRAS Controls Pancreatic Cancer Cell Lipid Metabolism and Invasive Potential through the Lipase HSL. Cancer research. 2020;80(22):4932. doi: 10.1158/0008-5472.CAN-20-1255.

98. Visvader JE. Cells of origin in cancer. Nature. 2011;469(7330):314-22. Epub 2011/01/21. doi: 10.1038/nature09781. PubMed PMID: 21248838.

99. Barker N, Ridgway RA, van Es JH, van de Wetering M, Begthel H, van den Born M, Danenberg E, Clarke AR, Sansom OJ, Clevers H. Crypt stem cells as the cells-of-origin of intestinal cancer. Nature. 2009;457(7229):608-11. doi: 10.1038/nature07602.

100. Mihaylova MM, Cheng CW, Cao AQ, Tripathi S, Mana MD, Bauer-Rowe KE, Abu-Remaileh M, Clavain L, Erdemir A, Lewis CA, Freinkman E, Dickey AS, La Spada AR, Huang Y, Bell GW, Deshpande V, Carmeliet P, Katajisto P, Sabatini DM, Yilmaz Ö H. Fasting Activates Fatty Acid Oxidation to Enhance Intestinal Stem Cell Function during Homeostasis and Aging. Cell Stem Cell. 2018;22(5):769-78.e4. Epub 2018/05/05. doi: 10.1016/j.stem.2018.04.001. PubMed PMID: 29727683; PMCID: PMC5940005.

101. Beyaz S, Mana MD, Roper J, Kedrin D, Saadatpour A, Hong S-J, Bauer-Rowe KE, Xifaras ME, Akkad A, Arias E, Pinello L, Katz Y, Shinagare S, Abu-Remaileh M, Mihaylova MM, Lamming DW, Dogum R, Guo G, Bell GW, Selig M, Nielsen GP, Gupta N, Ferrone CR, Deshpande V, Yuan G-C, Orkin SH, Sabatini DM, Yilmaz ÖH. High-fat diet enhances stemness and tumorigenicity of intestinal progenitors. Nature. 2016;531(7592):53-8. doi: 10.1038/nature17173.

102. Kim CF, Jackson EL, Woolfenden AE, Lawrence S, Babar I, Vogel S, Crowley D, Bronson RT, Jacks T. Identification of bronchioalveolar stem cells in normal lung and lung cancer. Cell. 2005;121(6):823-35. Epub 2005/06/18. doi: 10.1016/j.cell.2005.03.032. PubMed PMID: 15960971.

103. Xu X, Rock JR, Lu Y, Futtner C, Schwab B, Guinney J, Hogan BL, Onaitis MW. Evidence for type II cells as cells of origin of K-Ras-induced distal lung adenocarcinoma. Proceedings of the National Academy of Sciences of the United States of America. 2012;109(13):4910-5. Epub 2012/03/14. doi: 10.1073/pnas.1112499109. PubMed PMID: 22411819; PMCID: PMC3323959.

104. Mainardi S, Mijimolle N, Francoz S, Vicente-Dueñas C, Sánchez-García I, Barbacid M. Identification of cancer initiating cells in K-Ras driven lung adenocarcinoma. Proceedings of the National Academy of Sciences of the United States of America. 2014;111(1):255-60. Epub 2013/12/25. doi: 10.1073/pnas.1320383110. PubMed PMID: 24367082; PMCID: PMC3890787.

105. Sutherland KD, Song JY, Kwon MC, Proost N, Zevenhoven J, Berns A. Multiple cells-of-origin of mutant K-Ras-induced mouse lung adenocarcinoma. Proceedings of the National Academy of Sciences of the United States of America. 2014;111(13):4952-7. Epub 2014/03/04. doi: 10.1073/pnas.1319963111. PubMed PMID: 24586047; PMCID: PMC3977239.

106. Guerra C, Mijimolle N, Dhawahir A, Dubus P, Barradas M, Serrano M, Campuzano V, Barbacid M. Tumor induction by an endogenous K-ras oncogene is highly dependent on cellular context. Cancer cell. 2003;4(2):111-20. Epub 2003/09/06. doi: 10.1016/s1535-6108(03)00191-0. PubMed PMID: 12957286.

107. Best SA, De Souza DP, Kersbergen A, Policheni AN, Dayalan S, Tull D, Rathi V, Gray DH, Ritchie ME, McConville MJ, Sutherland KD. Synergy between the KEAP1/NRF2 and PI3K Pathways Drives Non-Small-Cell Lung Cancer with an Altered Immune Microenvironment. Cell metabolism. 2018;27(4):935-43.e4. Epub 2018/03/13. doi: 10.1016/j.cmet.2018.02.006. PubMed PMID: 29526543.

108. Best SA, Ding S, Kersbergen A, Dong X, Song JY, Xie Y, Reljic B, Li K, Vince JE, Rathi V, Wright GM, Ritchie ME, Sutherland KD. Distinct initiating events underpin the immune and metabolic heterogeneity of KRAS-mutant lung adenocarcinoma. Nat Commun. 2019;10(1):4190. Epub 2019/09/15. doi: 10.1038/s41467-019-12164-y. PubMed PMID: 31519898; PMCID: PMC6744438.

109. Gidekel Friedlander SY, Chu GC, Snyder EL, Girnius N, Dibelius G, Crowley D, Vasile E, DePinho RA, Jacks T. Context-dependent transformation of adult pancreatic cells by oncogenic K-Ras. Cancer cell. 2009;16(5):379-89. Epub 2009/11/03. doi: 10.1016/j.ccr.2009.09.027. PubMed PMID: 19878870; PMCID: PMC3048064.

110. De La O J-P, Emerson LL, Goodman JL, Froebe SC, Illum BE, Curtis AB, Murtaugh LC. Notch and Kras reprogram pancreatic acinar cells to ductal intraepithelial neoplasia. Proceedings of the National Academy of Sciences. 2008:pnas.0810111105. doi: 10.1073/pnas.0810111105.

111. Habbe N, Shi G, Meguid RA, Fendrich V, Esni F, Chen H, Feldmann G, Stoffers DA, Konieczny SF, Leach SD, Maitra A. Spontaneous induction of murine pancreatic intraepithelial neoplasia (mPanIN) by acinar cell targeting of oncogenic Kras in adult mice. Proceedings of the National Academy of Sciences. 2008:pnas.0810097105. doi: 10.1073/pnas.0810097105.

112. Bailey JM, Hendley AM, Lafaro KJ, Pruski MA, Jones NC, Alsina J, Younes M, Maitra A, McAllister F, Iacobuzio-Donahue CA, Leach SD. p53 mutations cooperate with oncogenic Kras to promote adenocarcinoma from pancreatic ductal cells. Oncogene. 2016;35(32):4282-8. doi: 10.1038/onc.2015.441.

113. Seino T, Kawasaki S, Shimokawa M, Tamagawa H, Toshimitsu K, Fujii M, Ohta Y, Matano M, Nanki K, Kawasaki K, Takahashi S, Sugimoto S, Iwasaki E, Takagi J, Itoi T, Kitago M, Kitagawa Y, Kanai T, Sato T. Human Pancreatic Tumor Organoids Reveal Loss of Stem Cell Niche Factor Dependence during Disease Progression. Cell Stem Cell. 2018;22(3):454-67.e6. doi: https://doi.org/10.1016/j.stem.2017.12.009.

114. Mayers JR, Torrence ME, Danai LV, Papagiannakopoulos T, Davidson SM, Bauer MR, Lau AN, Ji BW, Dixit PD, Hosios AM, Muir A, Chin CR, Freinkman E, Jacks T, Wolpin BM, Vitkup D, Vander Heiden MG. Tissue of origin dictates branched-chain amino acid metabolism in mutant Kras-driven cancers. Science (New York, NY). 2016;353(6304):1161-5. Epub 2016/09/10. doi: 10.1126/science.aaf5171. PubMed PMID: 27609895; PMCID: PMC5245791.

115. Phelps RA, Chidester S, Dehghanizadeh S, Phelps J, Sandoval IT, Rai K, Broadbent T, Sarkar S, Burt RW, Jones DA. A two-step model for colon adenoma

initiation and progression caused by APC loss. Cell. 2009;137(4):623-34. Epub 2009/05/20. doi: 10.1016/j.cell.2009.02.037. PubMed PMID: 19450512; PMCID: PMC2706149.

116. Wong CC, Xu J, Bian X, Wu JL, Kang W, Qian Y, Li W, Chen H, Gou H, Liu D, Yat Luk ST, Zhou Q, Ji F, Chan LS, Shirasawa S, Sung JJ, Yu J. In Colorectal Cancer Cells With Mutant KRAS, SLC25A22-Mediated Glutaminolysis Reduces DNA Demethylation to Increase WNT Signaling, Stemness, and Drug Resistance. Gastroenterology. 2020. Epub 2020/08/20. doi: 10.1053/j.gastro.2020.08.016. PubMed PMID: 32814111.

117. Stine ZE, Walton ZE, Altman BJ, Hsieh AL, Dang CV. MYC, Metabolism, and Cancer. Cancer Discovery. 2015;5(10):1024. doi: 10.1158/2159-8290.CD-15-0507.

118. Sansom OJ, Meniel VS, Muncan V, Phesse TJ, Wilkins JA, Reed KR, Vass JK, Athineos D, Clevers H, Clarke AR. Myc deletion rescues Apc deficiency in the small intestine. Nature. 2007;446(7136):676-9. Epub 2007/03/23. doi: 10.1038/nature05674. PubMed PMID: 17377531.

119. Satoh K, Yachida S, Sugimoto M, Oshima M, Nakagawa T, Akamoto S, Tabata S, Saitoh K, Kato K, Sato S, Igarashi K, Aizawa Y, Kajino-Sakamoto R, Kojima Y, Fujishita T, Enomoto A, Hirayama A, Ishikawa T, Taketo MM, Kushida Y, Haba R, Okano K, Tomita M, Suzuki Y, Fukuda S, Aoki M, Soga T. Global metabolic reprogramming of colorectal cancer occurs at adenoma stage and is induced by MYC. Proceedings of the National Academy of Sciences of the United States of America. 2017;114(37):E7697-e706. Epub 2017/08/30. doi: 10.1073/pnas.1710366114. PubMed PMID: 28847964; PMCID: PMC5604037.

120. Venkateswaran N, Lafita-Navarro MC, Hao YH, Kilgore JA, Perez-Castro L, Braverman J, Borenstein-Auerbach N, Kim M, Lesner NP, Mishra P, Brabletz T, Shay JW, DeBerardinis RJ, Williams NS, Yilmaz OH, Conacci-Sorrell M. MYC promotes tryptophan uptake and metabolism by the kynurenine pathway in colon cancer. Genes Dev. 2019;33(17-18):1236-51. Epub 2019/08/17. doi: 10.1101/gad.327056.119. PubMed PMID: 31416966; PMCID: PMC6719621.

121. Soucek L, Whitfield JR, Sodir NM, Massó-Vallés D, Serrano E, Karnezis AN, Swigart LB, Evan GI. Inhibition of Myc family proteins eradicates KRas-driven lung cancer in mice. Genes Dev. 2013;27(5):504-13. Epub 2013/03/12. doi: 10.1101/gad.205542.112. PubMed PMID: 23475959; PMCID: PMC3605464.

122. Stine ZE, Walton ZE, Altman BJ, Hsieh AL, Dang CV. MYC, Metabolism, and Cancer. Cancer Discovery. 2015. doi: 10.1158/2159-8290.CD-15-0507.

123. Mihaylova MM, Cheng C-W, Cao AQ, Tripathi S, Mana MD, Bauer-Rowe KE, Abu-Remaileh M, Clavain L, Erdemir A, Lewis CA, Freinkman E, Dickey AS, La Spada AR, Huang Y, Bell GW, Deshpande V, Carmeliet P, Katajisto P, Sabatini DM, Yilmaz ÖH. Fasting Activates Fatty Acid Oxidation to Enhance Intestinal Stem Cell Function

during Homeostasis and Aging. Cell Stem Cell. 2018;22(5):769-78.e4. doi: 10.1016/j.stem.2018.04.001.

124. Boutin AT, Liao WT, Wang M, Hwang SS, Karpinets TV, Cheung H, Chu GC, Jiang S, Hu J, Chang K, Vilar E, Song X, Zhang J, Kopetz S, Futreal A, Wang YA, Kwong LN, DePinho RA. Oncogenic Kras drives invasion and maintains metastases in colorectal cancer. Genes Dev. 2017;31(4):370-82. Epub 2017/03/16. doi: 10.1101/gad.293449.116. PubMed PMID: 28289141; PMCID: PMC5358757.

125. Feng Y, Bommer GT, Zhao J, Green M, Sands E, Zhai Y, Brown K, Burberry A, Cho KR, Fearon ER. Mutant Kras Promotes Hyperplasia and Alters Differentiation in the Colon Epithelium but Does Not Expand the Presumptive Stem Cell Pool. Gastroenterology. 2011;141(3):1003-13.e10. doi: 10.1053/j.gastro.2011.05.007.

126. Hinoi T, Akyol A, Theisen BK, Ferguson DO, Greenson JK, Williams BO, Cho KR, Fearon ER. Mouse Model of Colonic Adenoma-Carcinoma Progression Based on Somatic Apc Inactivation. Cancer research. 2007;67(20):9721. doi: 10.1158/0008-5472.CAN-07-2735.

127. Tang J, Feng Y, Kuick R, Green M, Green M, Sakamoto N, Kurosu Y, Lin J, Cho KR, Fearon ER. Trp53 null and R270H mutant alleles have comparable effects in regulating invasion, metastasis, and gene expression in mouse colon tumorigenesis. Lab Invest. 2019;99(10):1454-69. Epub 2019/06/01. doi: 10.1038/s41374-019-0269-y. PubMed PMID: 31148594; PMCID: PMC6759392.

128. Jeon SM, Chandel NS, Hay N. AMPK regulates NADPH homeostasis to promote tumour cell survival during energy stress. Nature. 2012;485(7400):661-5. Epub 2012/06/05. doi: 10.1038/nature11066. PubMed PMID: 22660331; PMCID: PMC3607316.

129. Shackelford DB, Shaw RJ. The LKB1-AMPK pathway: metabolism and growth control in tumour suppression. Nature reviews Cancer. 2009;9(8):563-75. Epub 2009/07/25. doi: 10.1038/nrc2676. PubMed PMID: 19629071; PMCID: PMC2756045.

130. Murray CW, Brady JJ, Tsai MK, Li C, Winters IP, Tang R, Andrejka L, Ma RK, Kunder CA, Chu P, Winslow MM. An LKB1-SIK Axis Suppresses Lung Tumor Growth and Controls Differentiation. Cancer Discov. 2019;9(11):1590-605. Epub 2019/07/28. doi: 10.1158/2159-8290.Cd-18-1237. PubMed PMID: 31350327; PMCID: PMC6825558.

131. Hollstein PE, Eichner LJ, Brun SN, Kamireddy A, Svensson RU, Vera LI, Ross DS, Rymoff TJ, Hutchins A, Galvez HM, Williams AE, Shokhirev MN, Screaton RA, Berdeaux R, Shaw RJ. The AMPK-Related Kinases SIK1 and SIK3 Mediate Key Tumor-Suppressive Effects of LKB1 in NSCLC. Cancer Discov. 2019;9(11):1606-27. Epub 2019/07/28. doi: 10.1158/2159-8290.Cd-18-1261. PubMed PMID: 31350328; PMCID: PMC6825547.

132. Shaw RJ, Kosmatka M, Bardeesy N, Hurley RL, Witters LA, DePinho RA, Cantley LC. The tumor suppressor LKB1 kinase directly activates AMP-activated kinase

and regulates apoptosis in response to energy stress. Proceedings of the National Academy of Sciences of the United States of America. 2004;101(10):3329-35. Epub 2004/02/27. doi: 10.1073/pnas.0308061100. PubMed PMID: 14985505; PMCID: PMC373461.

133. Shaw RJ, Lamia KA, Vasquez D, Koo SH, Bardeesy N, Depinho RA, Montminy M, Cantley LC. The kinase LKB1 mediates glucose homeostasis in liver and therapeutic effects of metformin. Science (New York, NY). 2005;310(5754):1642-6. Epub 2005/11/26. doi: 10.1126/science.1120781. PubMed PMID: 16308421; PMCID: PMC3074427.

134. Faubert B, Vincent EE, Griss T, Samborska B, Izreig S, Svensson RU, Mamer OA, Avizonis D, Shackelford DB, Shaw RJ, Jones RG. Loss of the tumor suppressor LKB1 promotes metabolic reprogramming of cancer cells via HIF-1alpha. Proceedings of the National Academy of Sciences of the United States of America. 2014;111(7):2554-9. Epub 2014/02/20. doi: 10.1073/pnas.1312570111. PubMed PMID: 24550282; PMCID: PMC3932920.

135. Eichner LJ, Brun SN, Herzig S, Young NP, Curtis SD, Shackelford DB, Shokhirev MN, Leblanc M, Vera LI, Hutchins A, Ross DS, Shaw RJ, Svensson RU. Genetic Analysis Reveals AMPK Is Required to Support Tumor Growth in Murine Kras-Dependent Lung Cancer Models. Cell metabolism. 2019;29(2):285-302 e7. Epub 2018/11/13. doi: 10.1016/j.cmet.2018.10.005. PubMed PMID: 30415923; PMCID: PMC6365213.

136. Liu G, Summer R. Cellular Metabolism in Lung Health and Disease. Annu Rev Physiol. 2019;81:403-28. Epub 2018/11/30. doi: 10.1146/annurev-physiol-020518-114640. PubMed PMID: 30485759; PMCID: PMC6853603.

137. Bhatt V, Khayati K, Hu ZS, Lee A, Kamran W, Su X, Guo JY. Autophagy modulates lipid metabolism to maintain metabolic flexibility for Lkb1-deficient Kras-driven lung tumorigenesis. Genes Dev. 2019;33(3-4):150-65. Epub 2019/01/30. doi: 10.1101/gad.320481.118. PubMed PMID: 30692209; PMCID: PMC6362813.

138. Kim J, Hu Z, Cai L, Li K, Choi E, Faubert B, Bezwada D, Rodriguez-Canales J, Villalobos P, Lin YF, Ni M, Huffman KE, Girard L, Byers LA, Unsal-Kacmaz K, Pena CG, Heymach JV, Wauters E, Vansteenkiste J, Castrillon DH, Chen BPC, Wistuba I, Lambrechts D, Xu J, Minna JD, DeBerardinis RJ. CPS1 maintains pyrimidine pools and DNA synthesis in KRAS/LKB1-mutant lung cancer cells. Nature. 2017;546(7656):168-72. Epub 2017/05/26. doi: 10.1038/nature22359. PubMed PMID: 28538732; PMCID: PMC5472349.

139. Su GH, Hruban RH, Bansal RK, Bova GS, Tang DJ, Shekher MC, Westerman AM, Entius MM, Goggins M, Yeo CJ, Kern SE. Germline and somatic mutations of the STK11/LKB1 Peutz-Jeghers gene in pancreatic and biliary cancers. Am J Pathol. 1999;154(6):1835-40. doi: 10.1016/S0002-9440(10)65440-5. PubMed PMID: 10362809.

140. Morton JP, Jamieson NB, Karim SA, Athineos D, Ridgway RA, Nixon C, McKay CJ, Carter R, Brunton VG, Frame MC, Ashworth A, Oien KA, Evans TRJ, Sansom OJ. LKB1 haploinsufficiency cooperates with Kras to promote pancreatic cancer through suppression of p21-dependent growth arrest. Gastroenterology. 2010;139(2):586-97.e5976. Epub 2010/05/06. doi: 10.1053/j.gastro.2010.04.055. PubMed PMID: 20452353.

141. Kottakis F, Nicolay BN, Roumane A, Karnik R, Gu H, Nagle JM, Boukhali M, Hayward MC, Li YY, Chen T, Liesa M, Hammerman PS, Wong KK, Hayes DN, Shirihai OS, Dyson NJ, Haas W, Meissner A, Bardeesy N. LKB1 loss links serine metabolism to DNA methylation and tumorigenesis. Nature. 2016;539(7629):390-5. Epub 2016/11/04. doi: 10.1038/nature20132. PubMed PMID: 27799657; PMCID: PMC5988435.

142. Campbell JD, Alexandrov A, Kim J, Wala J, Berger AH, Pedamallu CS, Shukla SA, Guo G, Brooks AN, Murray BA, Imielinski M, Hu X, Ling S, Akbani R, Rosenberg M, Cibulskis C, Ramachandran A, Collisson EA, Kwiatkowski DJ, Lawrence MS, Weinstein JN, Verhaak RGW, Wu CJ, Hammerman PS, Cherniack AD, Getz G, Cancer Genome Atlas Research N, Artyomov MN, Schreiber R, Govindan R, Meyerson M. Distinct patterns of somatic genome alterations in lung adenocarcinomas and squamous cell carcinomas. Nature genetics. 2016;48(6):607-16. Epub 2016/05/09. doi: 10.1038/ng.3564. PubMed PMID: 27158780.

143. Romero R, Sayin VI, Davidson SM, Bauer MR, Singh SX, LeBoeuf SE, Karakousi TR, Ellis DC, Bhutkar A, Sanchez-Rivera FJ, Subbaraj L, Martinez B, Bronson RT, Prigge JR, Schmidt EE, Thomas CJ, Goparaju C, Davies A, Dolgalev I, Heguy A, Allaj V, Poirier JT, Moreira AL, Rudin CM, Pass HI, Vander Heiden MG, Jacks T, Papagiannakopoulos T. Keap1 loss promotes Kras-driven lung cancer and results in dependence on glutaminolysis. Nature medicine. 2017;23(11):1362-8. Epub 2017/10/03. doi: 10.1038/nm.4407. PubMed PMID: 28967920; PMCID: PMC5677540.

144. DeNicola GM, Karreth FA, Humpton TJ, Gopinathan A, Wei C, Frese K, Mangal D, Yu KH, Yeo CJ, Calhoun ES, Scrimieri F, Winter JM, Hruban RH, Iacobuzio-Donahue C, Kern SE, Blair IA, Tuveson DA. Oncogene-induced Nrf2 transcription promotes ROS detoxification and tumorigenesis. Nature. 2011;475(7354):106-9. Epub 2011/07/08. doi: 10.1038/nature10189. PubMed PMID: 21734707; PMCID: PMC3404470.

145. DeNicola GM, Chen PH, Mullarky E, Sudderth JA, Hu Z, Wu D, Tang H, Xie Y, Asara JM, Huffman KE, Wistuba, II, Minna JD, DeBerardinis RJ, Cantley LC. NRF2 regulates serine biosynthesis in non-small cell lung cancer. Nat Genet. 2015;47(12):1475-81. Epub 2015/10/21. doi: 10.1038/ng.3421. PubMed PMID: 26482881; PMCID: PMC4721512.

146. Tierney DF. Lung metabolism and biochemistry. Annu Rev Physiol. 1974;36:209-31. Epub 1974/01/01. doi: 10.1146/annurev.ph.36.030174.001233. PubMed PMID: 19400662.

147. Fisher AB. Intermediary metabolism of the lung. Environ Health Perspect. 1984;55:149-58. Epub 1984/04/01. doi: 10.1289/ehp.8455149. PubMed PMID: 6376097; PMCID: PMC1568362.

148. Mitsuishi Y, Taguchi K, Kawatani Y, Shibata T, Nukiwa T, Aburatani H, Yamamoto M, Motohashi H. Nrf2 redirects glucose and glutamine into anabolic pathways in metabolic reprogramming. Cancer cell. 2012;22(1):66-79. Epub 2012/07/14. doi: 10.1016/j.ccr.2012.05.016. PubMed PMID: 22789539.

149. Ghergurovich JM, Esposito M, Chen Z, Wang JZ, Bhatt V, Lan T, White E, Kang Y, Guo JY, Rabinowitz JD. Glucose-6-Phosphate Dehydrogenase Is Not Essential for K-Ras–Driven Tumor Growth or Metastasis. Cancer research. 2020;80(18):3820. doi: 10.1158/0008-5472.CAN-19-2486.

150. Galan-Cobo A, Sitthideatphaiboon P, Qu X, Poteete A, Pisegna MA, Tong P, Chen PH, Boroughs LK, Rodriguez MLM, Zhang W, Parlati F, Wang J, Gandhi V, Skoulidis F, DeBerardinis RJ, Minna JD, Heymach JV. LKB1 and KEAP1/NRF2 Pathways Cooperatively Promote Metabolic Reprogramming with Enhanced Glutamine Dependence in KRAS-Mutant Lung Adenocarcinoma. Cancer research. 2019;79(13):3251-67. Epub 2019/05/02. doi: 10.1158/0008-5472.CAN-18-3527. PubMed PMID: 31040157; PMCID: PMC6606351.

151. Sayin VI, LeBoeuf SE, Singh SX, Davidson SM, Biancur D, Guzelhan BS, Alvarez SW, Wu WL, Karakousi TR, Zavitsanou AM, Ubriaco J, Muir A, Karagiannis D, Morris PJ, Thomas CJ, Possemato R, Vander Heiden MG, Papagiannakopoulos T. Activation of the NRF2 antioxidant program generates an imbalance in central carbon metabolism in cancer. Elife. 2017;6. Epub 2017/10/03. doi: 10.7554/eLife.28083. PubMed PMID: 28967864; PMCID: PMC5624783.

152. Hensley CT, Faubert B, Yuan Q, Lev-Cohain N, Jin E, Kim J, Jiang L, Ko B, Skelton R, Loudat L, Wodzak M, Klimko C, McMillan E, Butt Y, Ni M, Oliver D, Torrealba J, Malloy CR, Kernstine K, Lenkinski RE, DeBerardinis RJ. Metabolic Heterogeneity in Human Lung Tumors. Cell. 2016;164(4):681-94. Epub 2016/02/09. doi: 10.1016/j.cell.2015.12.034. PubMed PMID: 26853473; PMCID: PMC4752889.

153. Bailey P, Chang DK, Nones K, Johns AL, Patch AM, Gingras MC, Miller DK, Christ AN, Bruxner TJ, Quinn MC, Nourse C, Murtaugh LC, Harliwong I, Idrisoglu S, Manning S, Nourbakhsh E, Wani S, Fink L, Holmes O, Chin V, Anderson MJ, Kazakoff S, Leonard C, Newell F, Waddell N, Wood S, Xu Q, Wilson PJ, Cloonan N, Kassahn KS, Taylor D, Quek K, Robertson A, Pantano L, Mincarelli L, Sanchez LN, Evers L, Wu J, Pinese M, Cowley MJ, Jones MD, Colvin EK, Nagrial AM, Humphrey ES, Chantrill LA, Mawson A, Humphris J, Chou A, Pajic M, Scarlett CJ, Pinho AV, Giry-Laterriere M, Rooman I, Samra JS, Kench JG, Lovell JA, Merrett ND, Toon CW, Epari K, Nguyen NQ, Barbour A, Zeps N, Moran-Jones K, Jamieson NB, Graham JS, Duthie F, Oien K, Hair J, Grutzmann R, Maitra A, Iacobuzio-Donahue CA, Wolfgang CL, Morgan RA, Lawlor RT, Corbo V, Bassi C, Rusev B, Capelli P, Salvia R, Tortora G, Mukhopadhyay D, Petersen GM, Australian Pancreatic Cancer Genome I, Munzy DM, Fisher WE, Karim

SA, Eshleman JR, Hruban RH, Pilarsky C, Morton JP, Sansom OJ, Scarpa A, Musgrove EA, Bailey UM, Hofmann O, Sutherland RL, Wheeler DA, Gill AJ, Gibbs RA, Pearson JV, Waddell N, Biankin AV, Grimmond SM. Genomic analyses identify molecular subtypes of pancreatic cancer. Nature. 2016;531(7592):47-52. Epub 2016/02/26. doi: 10.1038/nature16965. PubMed PMID: 26909576.

154. Ryan DP, Hong TS, Bardeesy N. Pancreatic adenocarcinoma. N Engl J Med. 2014;371(11):1039-49. Epub 2014/09/11. doi: 10.1056/NEJMra1404198. PubMed PMID: 25207767.

155. Rosenfeldt MT, O'Prey J, Morton JP, Nixon C, MacKay G, Mrowinska A, Au A, Rai TS, Zheng L, Ridgway R, Adams PD, Anderson KI, Gottlieb E, Sansom OJ, Ryan KM. p53 status determines the role of autophagy in pancreatic tumour development. Nature. 2013;504(7479):296-300. Epub 2013/12/07. doi: 10.1038/nature12865. PubMed PMID: 24305049.

156. Yang A, Rajeshkumar NV, Wang X, Yabuuchi S, Alexander BM, Chu GC, Von Hoff DD, Maitra A, Kimmelman AC. Autophagy is critical for pancreatic tumor growth and progression in tumors with p53 alterations. Cancer Discov. 2014;4(8):905-13. Epub 2014/05/31. doi: 10.1158/2159-8290.CD-14-0362. PubMed PMID: 24875860; PMCID: PMC4125497.

157. Yang S, Wang X, Contino G, Liesa M, Sahin E, Ying H, Bause A, Li Y, Stommel JM, Dell'antonio G, Mautner J, Tonon G, Haigis M, Shirihai OS, Doglioni C, Bardeesy N, Kimmelman AC. Pancreatic cancers require autophagy for tumor growth. Genes Dev. 2011;25(7):717-29. Epub 2011/03/17. doi: 10.1101/gad.2016111. PubMed PMID: 21406549; PMCID: PMC3070934.

158. Morris JPt, Yashinskie JJ, Koche R, Chandwani R, Tian S, Chen CC, Baslan T, Marinkovic ZS, Sanchez-Rivera FJ, Leach SD, Carmona-Fontaine C, Thompson CB, Finley LWS, Lowe SW. alpha-Ketoglutarate links p53 to cell fate during tumour suppression. Nature. 2019;573(7775):595-9. Epub 2019/09/20. doi: 10.1038/s41586-019-1577-5. PubMed PMID: 31534224; PMCID: PMC6830448.

159. Aguirre AJ, Bardeesy N, Sinha M, Lopez L, Tuveson DA, Horner J, Redston MS, DePinho RA. Activated Kras and Ink4a/Arf deficiency cooperate to produce metastatic pancreatic ductal adenocarcinoma. Genes & development. 2003;17(24):3112-26. Epub 2003/12/17. doi: 10.1101/gad.1158703. PubMed PMID: 14681207.

160. Ju HQ, Ying H, Tian T, Ling J, Fu J, Lu Y, Wu M, Yang L, Achreja A, Chen G, Zhuang Z, Wang H, Nagrath D, Yao J, Hung MC, DePinho RA, Huang P, Xu RH, Chiao PJ. Mutant Kras- and p16-regulated NOX4 activation overcomes metabolic checkpoints in development of pancreatic ductal adenocarcinoma. Nat Commun. 2017;8(1):14437. Epub 2017/02/25. doi: 10.1038/ncomms14437. PubMed PMID: 28232723; PMCID: PMC5333128.

161. Dey P, Baddour J, Muller F, Wu CC, Wang H, Liao W-T, Lan Z, Chen A, Gutschner T, Kang Y, Fleming J, Satani N, Zhao D, Achreja A, Yang L, Lee J, Chang E,

Genovese G, Viale A, Ying H, Draetta G, Maitra A, Wang YA, Nagrath D, DePinho RA. Genomic deletion of malic enzyme 2 confers collateral lethality in pancreatic cancer. Nature. 2017;542(7639):119-23. doi: 10.1038/nature21052.

162. Collisson EA, Campbell JD, Brooks AN, Berger AH, Lee W, Chmielecki J, Beer DG, Cope L, Creighton CJ, Danilova L, Ding L, Getz G, Hammerman PS, Neil Hayes D, Hernandez B, Herman JG, Heymach JV, Jurisica I, Kucherlapati R, Kwiatkowski D, Ladanyi M, Robertson G, Schultz N, Shen R, Sinha R, Sougnez C, Tsao M-S, Travis WD, Weinstein JN, Wigle DA, Wilkerson MD, Chu A, Cherniack AD, Hadjipanayis A, Rosenberg M, Weisenberger DJ, Laird PW, Radenbaugh A, Ma S, Stuart JM, Averett Byers L, Baylin SB, Govindan R, Meyerson M, Rosenberg M, Gabriel SB, Cibulskis K, Sougnez C, Kim J, Stewart C, Lichtenstein L, Lander ES, Lawrence MS, Getz G, Kandoth C, Fulton R, Fulton LL, McLellan MD, Wilson RK, Ye K, Fronick CC, Maher CA, Miller CA, Wendl MC, Cabanski C, Ding L, Mardis E, Govindan R, Creighton CJ, Wheeler D, Balasundaram M, Butterfield YSN, Carlsen R, Chu A, Chuah E, Dhalla N, Guin R, Hirst C, Lee D, Li HI, Mayo M, Moore RA, Mungall AJ, Schein JE, Sipahimalani P, Tam A, Varhol R, Gordon Robertson A, Wye N, Thiessen N, Holt RA, Jones SJM, Marra MA, Campbell JD, Brooks AN, Chmielecki J, Imielinski M, Onofrio RC, Hodis E, Zack T, Sougnez C, Helman E, Sekhar Pedamallu C, Mesirov J, Cherniack AD, Saksena G, Schumacher SE, Carter SL, Hernandez B, Garraway L, Beroukhim R, Gabriel SB, Getz G, Meyerson M, Hadjipanayis A, Lee S, Mahadeshwar HS, Pantazi A, Protopopov A, Ren X, Seth S, Song X, Tang J, Yang L, Zhang J, Chen P-C, Parfenov M, Wei Xu A, Santoso N, Chin L, Park PJ, Kucherlapati R, Hoadley KA, Todd Auman J, Meng S, Shi Y, Buda E, Waring S, Veluvolu U, Tan D, Mieczkowski PA, Jones CD, Simons JV, Soloway MG, Bodenheimer T, Jefferys SR, Roach J, Hoyle AP, Wu J, Balu S, Singh D, Prins JF, Marron JS, Parker JS, Neil Hayes D, Perou CM, Liu J, Cope L, Danilova L, Weisenberger DJ, Maglinte DT, Lai PH, Bootwalla MS, Van Den Berg DJ, Triche Jr T, Baylin SB, Laird PW, Rosenberg M, Chin L, Zhang J, Cho J, DiCara D, Heiman D, Lin P, Mallard W, Voet D, Zhang H, Zou L, Noble MS, Lawrence MS, Saksena G, Gehlenborg N, Thorvaldsdottir H, Mesirov J, Nazaire M-D, Robinson J, Getz G, Lee W, Arman Aksoy B, Ciriello G, Taylor BS, Dresdner G, Gao J, Gross B, Seshan VE, Ladanyi M, Reva B, Sinha R, Onur Sumer S, Weinhold N, Schultz N, Shen R, Sander C, Ng S, Ma S, Zhu J, Radenbaugh A, Stuart JM, Benz CC, Yau C, Haussler D, Spellman PT, Wilkerson MD, Parker JS, Hoadley KA, Kimes PK, Neil Hayes D, Perou CM, Broom BM, Wang J, Lu Y, Kwok Shing Ng P, Diao L, Averett Byers L, Liu W, Heymach JV, Amos CI, Weinstein JN, Akbani R, Mills GB, Curley E, Paulauskis J, Lau K, Morris S, Shelton T, Mallery D, Gardner J, Penny R, Saller C, Tarvin K, Richards WG, Cerfolio R, Bryant A, Raymond DP, Pennell NA, Farver C, Czerwinski C, Huelsenbeck-Dill L, Iacocca M, Petrelli N, Rabeno B, Brown J, Bauer T, Dolzhanskiy O, Potapova O, Rotin D, Voronina O, Nemirovich-Danchenko E, Fedosenko KV, Gal A, Behera M, Ramalingam SS, Sica G, Flieder D, Boyd J, Weaver J, Kohl B, Huy Quoc Thinh D, Sandusky G, Juhl H, The Cancer Genome Atlas Research N, Disease analysis working g, Genome sequencing centres: The E, Edythe LBI, Washington University in St L, Baylor College of M, Genome characterization centres: Canada's Michael Smith Genome Sciences Centre BCCA, The E, Edythe LBI, Harvard Medical SB, Women's Hospital MDACC, University of North Carolina CH, University of K, The USCJHUECC, Genome data analysis centres: The E, Edythe LBI, Memorial Sloan-Kettering Cancer C,

University of California SCBI, Oregon H, Sciences U, The University of Texas MDACC, Biospecimen core resource: International Genomics C, Tissue source sites: Analytical Biological Service I, Brigham, Women's H, University of Alabama at B, Cleveland C, Christiana C, Cureline, Emory U, Fox Chase Cancer C, Ilsbio, Indiana U, Indivumed, John Flynn H. Comprehensive molecular profiling of lung adenocarcinoma. Nature. 2014;511(7511):543-50. doi: 10.1038/nature13385.

163. Berkers Celia R, Maddocks Oliver DK, Cheung Eric C, Mor I, Vousden Karen H. Metabolic Regulation by p53 Family Members. Cell metabolism. 2013;18(5):617-33. doi: https://doi.org/10.1016/j.cmet.2013.06.019.

164. Ortiz-Prado E, Dunn JF, Vasconez J, Castillo D, Viscor G. Partial pressure of oxygen in the human body: a general review. Am J Blood Res. 2019;9(1):1-14. Epub 2019/03/23. PubMed PMID: 30899601; PMCID: PMC6420699.

165. Albenberg L, Esipova TV, Judge CP, Bittinger K, Chen J, Laughlin A, Grunberg S, Baldassano RN, Lewis JD, Li H, Thom SR, Bushman FD, Vinogradov SA, Wu GD. Correlation between intraluminal oxygen gradient and radial partitioning of intestinal microbiota. Gastroenterology. 2014;147(5):1055-63 e8. Epub 2014/07/22. doi: 10.1053/j.gastro.2014.07.020. PubMed PMID: 25046162; PMCID: PMC4252572.

166. Shay JE, Celeste Simon M. Hypoxia-inducible factors: crosstalk between inflammation and metabolism. Semin Cell Dev Biol. 2012;23(4):389-94. Epub 2012/04/25. doi: 10.1016/j.semcdb.2012.04.004. PubMed PMID: 22525300.

167. McGettrick AF, O'Neill LAJ. The Role of HIF in Immunity and Inflammation. Cell metabolism. 2020;32(4):524-36. Epub 2020/08/28. doi: 10.1016/j.cmet.2020.08.002. PubMed PMID: 32853548.

168. Schofield CJ, Ratcliffe PJ. Signalling hypoxia by HIF hydroxylases. Biochem Biophys Res Commun. 2005;338(1):617-26. Epub 2005/09/06. doi: 10.1016/j.bbrc.2005.08.111. PubMed PMID: 16139242.

169. Semenza GL. HIF-1 mediates metabolic responses to intratumoral hypoxia and oncogenic mutations. The Journal of clinical investigation. 2013;123(9):3664-71. Epub 2013/09/04. doi: 10.1172/JCI67230. PubMed PMID: 23999440; PMCID: PMC3754249.

170. Furuta GT, Turner JR, Taylor CT, Hershberg RM, Comerford K, Narravula S, Podolsky DK, Colgan SP. Hypoxia-inducible factor 1-dependent induction of intestinal trefoil factor protects barrier function during hypoxia. The Journal of experimental medicine. 2001;193(9):1027-34. Epub 2001/05/09. doi: 10.1084/jem.193.9.1027. PubMed PMID: 11342587; PMCID: PMC2193432.

171. Xie L, Xue X, Taylor M, Ramakrishnan SK, Nagaoka K, Hao C, Gonzalez FJ, Shah YM. Hypoxia-inducible factor/MAZ-dependent induction of caveolin-1 regulates colon permeability through suppression of occludin, leading to hypoxia-induced inflammation. Mol Cell Biol. 2014;34(16):3013-23. Epub 2014/06/04. doi: 10.1128/MCB.00324-14. PubMed PMID: 24891620; PMCID: PMC4135598.

172. Manresa MC, Taylor CT. Hypoxia Inducible Factor (HIF) Hydroxylases as Regulators of Intestinal Epithelial Barrier Function. Cell Mol Gastroenterol Hepatol. 2017;3(3):303-15. Epub 2017/05/04. doi: 10.1016/j.jcmgh.2017.02.004. PubMed PMID: 28462372; PMCID: PMC5404106.

173. Gilsing AM, Fransen F, de Kok TM, Goldbohm AR, Schouten LJ, de Bruine AP, van Engeland M, van den Brandt PA, de Goeij AF, Weijenberg MP. Dietary heme iron and the risk of colorectal cancer with specific mutations in KRAS and APC. Carcinogenesis. 2013;34(12):2757-66. Epub 2013/08/29. doi: 10.1093/carcin/bgt290. PubMed PMID: 23983135.

174. Chun SY, Johnson C, Washburn JG, Cruz-Correa MR, Dang DT, Dang LH. Oncogenic KRAS modulates mitochondrial metabolism in human colon cancer cells by inducing HIF-1alpha and HIF-2alpha target genes. Mol Cancer. 2010;9:293. Epub 2010/11/16. doi: 10.1186/1476-4598-9-293. PubMed PMID: 21073737; PMCID: PMC2999617.

175. Zeng M, Kikuchi H, Pino MS, Chung DC. Hypoxia activates the K-ras proto-oncogene to stimulate angiogenesis and inhibit apoptosis in colon cancer cells. PloS one. 2010;5(6):e10966. Epub 2010/06/10. doi: 10.1371/journal.pone.0010966. PubMed PMID: 20532039; PMCID: PMC2881039.

176. Richard DE, Berra E, Gothie E, Roux D, Pouyssegur J. p42/p44 mitogen-activated protein kinases phosphorylate hypoxia-inducible factor 1alpha (HIF-1alpha) and enhance the transcriptional activity of HIF-1. The Journal of biological chemistry. 1999;274(46):32631-7. Epub 1999/11/07. doi: 10.1074/jbc.274.46.32631. PubMed PMID: 10551817.

177. Mylonis I, Chachami G, Samiotaki M, Panayotou G, Paraskeva E, Kalousi A, Georgatsou E, Bonanou S, Simos G. Identification of MAPK phosphorylation sites and their role in the localization and activity of hypoxia-inducible factor-1alpha. The Journal of biological chemistry. 2006;281(44):33095-106. Epub 2006/09/07. doi: 10.1074/jbc.M605058200. PubMed PMID: 16954218.

178. Kikuchi H, Pino MS, Zeng M, Shirasawa S, Chung DC. Oncogenic KRAS and BRAF differentially regulate hypoxia-inducible factor-1alpha and -2alpha in colon cancer. Cancer research. 2009;69(21):8499-506. Epub 2009/10/22. doi: 10.1158/0008-5472.CAN-09-2213. PubMed PMID: 19843849; PMCID: PMC2811371.

179. Dang DT, Chen F, Gardner LB, Cummins JM, Rago C, Bunz F, Kantsevoy SV, Dang LH. Hypoxia-inducible factor-1alpha promotes nonhypoxia-mediated proliferation in colon cancer cells and xenografts. Cancer research. 2006;66(3):1684-936. Epub 2006/02/03. doi: 10.1158/0008-5472.CAN-05-2887. PubMed PMID: 16452228.

180. Taylor M, Qu A, Anderson ER, Matsubara T, Martin A, Gonzalez FJ, Shah YM. Hypoxia-inducible factor-2alpha mediates the adaptive increase of intestinal ferroportin during iron deficiency in mice. Gastroenterology. 2011;140(7):2044-55. Epub

2011/03/23. doi: 10.1053/j.gastro.2011.03.007. PubMed PMID: 21419768; PMCID: PMC3109109.

181. Schwartz AJ, Das NK, Ramakrishnan SK, Jain C, Jurkovic MT, Wu J, Nemeth E, Lakhal-Littleton S, Colacino JA, Shah YM. Hepatic hepcidin/intestinal HIF-2alpha axis maintains iron absorption during iron deficiency and overload. The Journal of clinical investigation. 2019;129(1):336-48. Epub 2018/10/24. doi: 10.1172/JCI122359. PubMed PMID: 30352047; PMCID: PMC6307944.

182. Xue X, Ramakrishnan SK, Weisz K, Triner D, Xie L, Attili D, Pant A, Gyorffy B, Zhan M, Carter-Su C, Hardiman KM, Wang TD, Dame MK, Varani J, Brenner D, Fearon ER, Shah YM. Iron Uptake via DMT1 Integrates Cell Cycle with JAK-STAT3 Signaling to Promote Colorectal Tumorigenesis. Cell metabolism. 2016;24(3):447-61. Epub 2016/08/23. doi: 10.1016/j.cmet.2016.07.015. PubMed PMID: 27546461; PMCID: PMC5023486.

183. Xue X, Taylor M, Anderson E, Hao C, Qu A, Greenson JK, Zimmermann EM, Gonzalez FJ, Shah YM. Hypoxia-inducible factor-2alpha activation promotes colorectal cancer progression by dysregulating iron homeostasis. Cancer research. 2012;72(9):2285-93. Epub 2012/03/16. doi: 10.1158/0008-5472.CAN-11-3836. PubMed PMID: 22419665; PMCID: PMC3342485.

184. Stockwell BR, Jiang X. The Chemistry and Biology of Ferroptosis. Cell Chem Biol. 2020;27(4):365-75. Epub 2020/04/16. doi: 10.1016/j.chembiol.2020.03.013. PubMed PMID: 32294465; PMCID: PMC7204503.

185. Stockwell BR, Jiang X, Gu W. Emerging Mechanisms and Disease Relevance of Ferroptosis. Trends in cell biology. 2020;30(6):478-90. Epub 2020/05/16. doi: 10.1016/j.tcb.2020.02.009. PubMed PMID: 32413317; PMCID: PMC7230071.

186. Stockwell BR, Friedmann Angeli JP, Bayir H, Bush AI, Conrad M, Dixon SJ, Fulda S, Gascon S, Hatzios SK, Kagan VE, Noel K, Jiang X, Linkermann A, Murphy ME, Overholtzer M, Oyagi A, Pagnussat GC, Park J, Ran Q, Rosenfeld CS, Salnikow K, Tang D, Torti FM, Torti SV, Toyokuni S, Woerpel KA, Zhang DD. Ferroptosis: A Regulated Cell Death Nexus Linking Metabolism, Redox Biology, and Disease. Cell. 2017;171(2):273-85. Epub 2017/10/07. doi: 10.1016/j.cell.2017.09.021. PubMed PMID: 28985560; PMCID: PMC5685180.

187. Hui S, Cowan AJ, Zeng X, Yang L, TeSlaa T, Li X, Bartman C, Zhang Z, Jang C, Wang L, Lu W, Rojas J, Baur J, Rabinowitz JD. Quantitative Fluxomics of Circulating Metabolites. Cell metabolism. 2020;32(4):676-88 e4. Epub 2020/08/14. doi: 10.1016/j.cmet.2020.07.013. PubMed PMID: 32791100; PMCID: PMC7544659.

188. Hui S, Ghergurovich JM, Morscher RJ, Jang C, Teng X, Lu W, Esparza LA, Reya T, Le Z, Yanxiang Guo J, White E, Rabinowitz JD. Glucose feeds the TCA cycle via circulating lactate. Nature. 2017;551(7678):115-8. doi: 10.1038/nature24057.

189. Jang C, Hui S, Zeng X, Cowan AJ, Wang L, Chen L, Morscher RJ, Reyes J, Frezza C, Hwang HY, Imai A, Saito Y, Okamoto K, Vaspoli C, Kasprenski L, Zsido GA, 2nd, Gorman JH, 3rd, Gorman RC, Rabinowitz JD. Metabolite Exchange between Mammalian Organs Quantified in Pigs. Cell metabolism. 2019;30(3):594-606 e3. Epub 2019/07/02. doi: 10.1016/j.cmet.2019.06.002. PubMed PMID: 31257152; PMCID: PMC6726553.

190. Li JT, Yin M, Wang D, Wang J, Lei MZ, Zhang Y, Liu Y, Zhang L, Zou SW, Hu LP, Zhang ZG, Wang YP, Wen WY, Lu HJ, Chen ZJ, Su D, Lei QY. BCAT2-mediated BCAA catabolism is critical for development of pancreatic ductal adenocarcinoma. Nat Cell Biol. 2020;22(2):167-74. Epub 2020/02/08. doi: 10.1038/s41556-019-0455-6. PubMed PMID: 32029896.

191. Zhu Z, Achreja A, Meurs N, Animasahun O, Owen S, Mittal A, Parikh P, Lo TW, Franco-Barraza J, Shi J, Gunchick V, Sherman MH, Cukierman E, Pickering AM, Maitra A, Sahai V, Morgan MA, Nagrath S, Lawrence TS, Nagrath D. Tumour-reprogrammed stromal BCAT1 fuels branched-chain ketoacid dependency in stromal-rich PDAC tumours. Nat Metab. 2020;2(8):775-92. Epub 2020/07/23. doi: 10.1038/s42255-020-0226-5. PubMed PMID: 32694827; PMCID: PMC7438275.

192. Nelson BS, Lin L, Kremer DM, Sousa CM, Cotta-Ramusino C, Myers A, Ramos J, Gao T, Kovalenko I, Wilder-Romans K, Dresser J, Davis M, Lee HJ, Nwosu ZC, Campit S, Mashadova O, Nicolay BN, Tolstyka ZP, Halbrook CJ, Chandrasekaran S, Asara JM, Crawford HC, Cantley LC, Kimmelman AC, Wahl DR, Lyssiotis CA. Tissue of origin dictates GOT1 dependence and confers synthetic lethality to radiotherapy. Cancer Metab. 2020;8(1):1. Epub 2020/01/08. doi: 10.1186/s40170-019-0202-2. PubMed PMID: 31908776; PMCID: PMC6941320.

193. Chowdhry S, Zanca C, Rajkumar U, Koga T, Diao Y, Raviram R, Liu F, Turner K, Yang H, Brunk E, Bi J, Furnari F, Bafna V, Ren B, Mischel PS. NAD metabolic dependency in cancer is shaped by gene amplification and enhancer remodelling. Nature. 2019;569(7757):570-5. Epub 2019/04/26. doi: 10.1038/s41586-019-1150-2. PubMed PMID: 31019297; PMCID: PMC7138021.

194. Lyssiotis CA, Kimmelman AC. Metabolic Interactions in the Tumor Microenvironment. Trends Cell Biol. 2017;27(11):863-75. Epub 2017/07/25. doi: 10.1016/j.tcb.2017.06.003. PubMed PMID: 28734735; PMCID: PMC5814137.

195. Schwörer S, Vardhana SA, Thompson CB. Cancer Metabolism Drives a Stromal Regenerative Response. Cell Metab. 2019;29(3):576-91. Epub 2019/02/19. doi: 10.1016/j.cmet.2019.01.015. PubMed PMID: 30773467; PMCID: PMC6692899.

196. Olenchock BA, Rathmell JC, Vander Heiden MG. Biochemical Underpinnings of Immune Cell Metabolic Phenotypes. Immunity. 2017;46(5):703-13. Epub 2017/05/18. doi: 10.1016/j.immuni.2017.04.013. PubMed PMID: 28514672; PMCID: PMC5660630.

197. Leone RD, Powell JD. Metabolism of immune cells in cancer. Nature reviews Cancer. 2020;20(9):516-31. Epub 2020/07/08. doi: 10.1038/s41568-020-0273-y. PubMed PMID: 32632251.

198. Buck MD, Sowell RT, Kaech SM, Pearce EL. Metabolic Instruction of Immunity. Cell. 2017;169(4):570-86. Epub 2017/05/06. doi: 10.1016/j.cell.2017.04.004. PubMed PMID: 28475890; PMCID: PMC5648021.

199. Chang CH, Qiu J, O'Sullivan D, Buck MD, Noguchi T, Curtis JD, Chen Q, Gindin M, Gubin MM, van der Windt GJ, Tonc E, Schreiber RD, Pearce EJ, Pearce EL. Metabolic Competition in the Tumor Microenvironment Is a Driver of Cancer Progression. Cell. 2015;162(6):1229-41. Epub 2015/09/01. doi: 10.1016/j.cell.2015.08.016. PubMed PMID: 26321679; PMCID: PMC4864363.

200. Andrejeva G, Rathmell JC. Similarities and Distinctions of Cancer and Immune Metabolism in Inflammation and Tumors. Cell metabolism. 2017;26(1):49-70. Epub 2017/07/07. doi: 10.1016/j.cmet.2017.06.004. PubMed PMID: 28683294; PMCID: PMC5555084.

201. MacCarthy-Morrogh L, Martin P. The hallmarks of cancer are also the hallmarks of wound healing. Sci Signal. 2020;13(648):eaay8690. Epub 2020/09/10. doi: 10.1126/scisignal.aay8690. PubMed PMID: 32900881.

202. Tape CJ, Ling S, Dimitriadi M, McMahon KM, Worboys JD, Leong HS, Norrie IC, Miller CJ, Poulogiannis G, Lauffenburger DA, Jorgensen C. Oncogenic KRAS Regulates Tumor Cell Signaling via Stromal Reciprocation. Cell. 2016;165(4):910-20. Epub 2016/04/19. doi: 10.1016/j.cell.2016.03.029. PubMed PMID: 27087446; PMCID: PMC4868820.

203. di Magliano MP, Logsdon CD. Roles for KRAS in pancreatic tumor development and progression. Gastroenterology. 2013;144(6):1220-9. Epub 2013/04/30. doi: 10.1053/j.gastro.2013.01.071. PubMed PMID: 23622131; PMCID: PMC3902845.

204. Georges LM, Verset L, Zlobec I, Demetter P, De Wever O. Impact of the Microenvironment on Tumour Budding in Colorectal Cancer. Adv Exp Med Biol. 2018;1110:101-11. Epub 2019/01/10. doi: 10.1007/978-3-030-02771-1_7. PubMed PMID: 30623368.

205. Abe Y, Tanaka N. The Hedgehog Signaling Networks in Lung Cancer: The Mechanisms and Roles in Tumor Progression and Implications for Cancer Therapy. Biomed Res Int. 2016;2016:7969286. Epub 2017/01/21. doi: 10.1155/2016/7969286. PubMed PMID: 28105432; PMCID: PMC5220431.

206. Lee KE, Spata M, Bayne LJ, Buza EL, Durham AC, Allman D, Vonderheide RH, Simon MC. Hif1a Deletion Reveals Pro-Neoplastic Function of B Cells in Pancreatic Neoplasia. Cancer Discov. 2016;6(3):256-69. Epub 2015/12/31. doi: 10.1158/2159-8290.CD-15-0822. PubMed PMID: 26715642; PMCID: PMC4783189.

207. Pylayeva-Gupta Y, Das S, Handler JS, Hajdu CH, Coffre M, Koralov SB, Bar-Sagi D. IL35-Producing B Cells Promote the Development of Pancreatic Neoplasia. Cancer Discov. 2016;6(3):247-55. Epub 2015/12/31. doi: 10.1158/2159-8290.CD-15-0843. PubMed PMID: 26715643; PMCID: PMC5709038.

208. DeNardo DG, Barreto JB, Andreu P, Vasquez L, Tawfik D, Kolhatkar N, Coussens LM. CD4(+) T cells regulate pulmonary metastasis of mammary carcinomas by enhancing protumor properties of macrophages. Cancer cell. 2009;16(2):91-102. Epub 2009/08/04. doi: 10.1016/j.ccr.2009.06.018. PubMed PMID: 19647220; PMCID: PMC2778576.

209. Dey P, Li J, Zhang J, Chaurasiya S, Strom A, Wang H, Liao WT, Cavallaro F, Denz P, Bernard V, Yen EY, Genovese G, Gulhati P, Liu J, Chakravarti D, Deng P, Zhang T, Carbone F, Chang Q, Ying H, Shang X, Spring DJ, Ghosh B, Putluri N, Maitra A, Wang YA, DePinho RA. Oncogenic KRAS-Driven Metabolic Reprogramming in Pancreatic Cancer Cells Utilizes Cytokines from the Tumor Microenvironment. Cancer Discov. 2020;10(4):608-25. Epub 2020/02/13. doi: 10.1158/2159-8290.CD-19-0297. PubMed PMID: 32046984; PMCID: PMC7125035.

210. Cascone T, McKenzie JA, Mbofung RM, Punt S, Wang Z, Xu C, Williams LJ, Wang Z, Bristow CA, Carugo A, Peoples MD, Li L, Karpinets T, Huang L, Malu S, Creasy C, Leahey SE, Chen J, Chen Y, Pelicano H, Bernatchez C, Gopal YNV, Heffernan TP, Hu J, Wang J, Amaria RN, Garraway LA, Huang P, Yang P, Wistuba, II, Woodman SE, Roszik J, Davis RE, Davies MA, Heymach JV, Hwu P, Peng W. Increased Tumor Glycolysis Characterizes Immune Resistance to Adoptive T Cell Therapy. Cell metabolism. 2018;27(5):977-87 e4. Epub 2018/04/10. doi: 10.1016/j.cmet.2018.02.024. PubMed PMID: 29628419; PMCID: PMC5932208.

211. Zhang D, Wang Y, Shi Z, Liu J, Sun P, Hou X, Zhang J, Zhao S, Zhou BP, Mi J. Metabolic reprogramming of cancer-associated fibroblasts by IDH3alpha downregulation. Cell Rep. 2015;10(8):1335-48. Epub 2015/03/04. doi: 10.1016/j.celrep.2015.02.006. PubMed PMID: 25732824.

212. Halestrap AP. The monocarboxylate transporter family--Structure and functional characterization. IUBMB Life. 2012;64(1):1-9. Epub 2011/12/02. doi: 10.1002/iub.573. PubMed PMID: 22131303.

213. Halestrap AP, Wilson MC. The monocarboxylate transporter family--role and regulation. IUBMB Life. 2012;64(2):109-19. Epub 2011/12/14. doi: 10.1002/iub.572. PubMed PMID: 22162139.

214. Hutcheson J, Balaji U, Porembka MR, Wachsmann MB, McCue PA, Knudsen ES, Witkiewicz AK. Immunologic and Metabolic Features of Pancreatic Ductal Adenocarcinoma Define Prognostic Subtypes of Disease. Clinical cancer research : an official journal of the American Association for Cancer Research. 2016;22(14):3606-17. Epub 2016/02/10. doi: 10.1158/1078-0432.CCR-15-1883. PubMed PMID: 26858311; PMCID: PMC4947442.

215. Colegio OR, Chu NQ, Szabo AL, Chu T, Rhebergen AM, Jairam V, Cyrus N, Brokowski CE, Eisenbarth SC, Phillips GM, Cline GW, Phillips AJ, Medzhitov R. Functional polarization of tumour-associated macrophages by tumour-derived lactic acid. Nature. 2014;513(7519):559-63. Epub 2014/07/22. doi: 10.1038/nature13490. PubMed PMID: 25043024; PMCID: PMC4301845.

216. Fischer K, Hoffmann P, Voelkl S, Meidenbauer N, Ammer J, Edinger M, Gottfried E, Schwarz S, Rothe G, Hoves S, Renner K, Timischl B, Mackensen A, Kunz-Schughart L, Andreesen R, Krause SW, Kreutz M. Inhibitory effect of tumor cell-derived lactic acid on human T cells. Blood. 2007;109(9):3812-9. Epub 2007/01/27. doi: 10.1182/blood-2006-07-035972. PubMed PMID: 17255361.

217. Harmon C, Robinson MW, Hand F, Almuaili D, Mentor K, Houlihan DD, Hoti E, Lynch L, Geoghegan J, O'Farrelly C. Lactate-Mediated Acidification of Tumor Microenvironment Induces Apoptosis of Liver-Resident NK Cells in Colorectal Liver Metastasis. Cancer immunology research. 2019;7(2):335-46. Epub 2018/12/20. doi: 10.1158/2326-6066.CIR-18-0481. PubMed PMID: 30563827.

218. Zhao Y, Zhao X, Chen V, Feng Y, Wang L, Croniger C, Conlon RA, Markowitz S, Fearon E, Puchowicz M, Brunengraber H, Hao Y, Wang Z. Colorectal cancers utilize glutamine as an anaplerotic substrate of the TCA cycle in vivo. Scientific Reports. 2019;9(1):19180. doi: 10.1038/s41598-019-55718-2.

219. Sugiura A, Rathmell JC. Metabolic Barriers to T Cell Function in Tumors. Journal of immunology (Baltimore, Md : 1950). 2018;200(2):400-7. doi: 10.4049/jimmunol.1701041. PubMed PMID: 29311381.

220. Smith C, Chang MY, Parker KH, Beury DW, DuHadaway JB, Flick HE, Boulden J, Sutanto-Ward E, Soler AP, Laury-Kleintop LD, Mandik-Nayak L, Metz R, Ostrand-Rosenberg S, Prendergast GC, Muller AJ. IDO is a nodal pathogenic driver of lung cancer and metastasis development. Cancer Discov. 2012;2(8):722-35. Epub 2012/07/24. doi: 10.1158/2159-8290.CD-12-0014. PubMed PMID: 22822050; PMCID: PMC3677576.

221. Hsu YL, Hung JY, Chiang SY, Jian SF, Wu CY, Lin YS, Tsai YM, Chou SH, Tsai MJ, Kuo PL. Lung cancer-derived galectin-1 contributes to cancer associated fibroblast-mediated cancer progression and immune suppression through TDO2/kynurenine axis. Oncotarget. 2016;7(19):27584-98. Epub 2016/04/07. doi: 10.18632/oncotarget.8488. PubMed PMID: 27050278; PMCID: PMC5053673.

222. Brandacher G, Perathoner A, Ladurner R, Schneeberger S, Obrist P, Winkler C, Werner ER, Werner-Felmayer G, Weiss HG, Gobel G, Margreiter R, Konigsrainer A, Fuchs D, Amberger A. Prognostic value of indoleamine 2,3-dioxygenase expression in colorectal cancer: effect on tumor-infiltrating T cells. Clinical cancer research : an official journal of the American Association for Cancer Research. 2006;12(4):1144-51. Epub 2006/02/21. doi: 10.1158/1078-0432.CCR-05-1966. PubMed PMID: 16489067.

223. Witkiewicz AK, Costantino CL, Metz R, Muller AJ, Prendergast GC, Yeo CJ, Brody JR. Genotyping and expression analysis of IDO2 in human pancreatic cancer: a novel, active target. J Am Coll Surg. 2009;208(5):781-9. doi: 10.1016/j.jamcollsurg.2008.12.018. PubMed PMID: 19476837.

224. Holmgaard RB, Zamarin D, Li Y, Gasmi B, Munn DH, Allison JP, Merghoub T, Wolchok JD. Tumor-Expressed IDO Recruits and Activates MDSCs in a Treg-Dependent Manner. Cell Rep. 2015;13(2):412-24. Epub 2015/09/29. doi: 10.1016/j.celrep.2015.08.077. PubMed PMID: 26411680; PMCID: PMC5013825.

225. Sadik A, Somarribas Patterson LF, Öztürk S, Mohapatra SR, Panitz V, Secker PF, Pfänder P, Loth S, Salem H, Prentzell MT, Berdel B, Iskar M, Faessler E, Reuter F, Kirst I, Kalter V, Foerster KI, Jäger E, Guevara CR, Sobeh M, Hielscher T, Poschet G, Reinhardt A, Hassel JC, Zapatka M, Hahn U, von Deimling A, Hopf C, Schlichting R, Escher BI, Burhenne J, Haefeli WE, Ishaque N, Böhme A, Schäuble S, Thedieck K, Trump S, Seiffert M, Opitz CA. IL4I1 Is a Metabolic Immune Checkpoint that Activates the AHR and Promotes Tumor Progression. Cell. 2020;182(5):1252-70.e34. doi: https://doi.org/10.1016/j.cell.2020.07.038.

226. Szefel J, Danielak A, Kruszewski WJ. Metabolic pathways of L-arginine and therapeutic consequences in tumors. Advances in Medical Sciences. 2019;64(1):104-10. doi: https://doi.org/10.1016/j.advms.2018.08.018.

227. Chaudhri VK, Salzler GG, Dick SA, Buckman MS, Sordella R, Karoly ED, Mohney R, Stiles BM, Elemento O, Altorki NK, McGraw TE. Metabolic alterations in lung cancer-associated fibroblasts correlated with increased glycolytic metabolism of the tumor. Mol Cancer Res. 2013;11(6):579-92. Epub 2013/03/12. doi: 10.1158/1541-7786.MCR-12-0437-T. PubMed PMID: 23475953; PMCID: PMC3686965.

228. Sousa CM, Biancur DE, Wang X, Halbrook CJ, Sherman MH, Zhang L, Kremer D, Hwang RF, Witkiewicz AK, Ying H, Asara JM, Evans RM, Cantley LC, Lyssiotis CA, Kimmelman AC. Pancreatic stellate cells support tumour metabolism through autophagic alanine secretion. Nature. 2016;536(7617):479-83. Epub 2016/08/12. doi: 10.1038/nature19084. PubMed PMID: 27509858; PMCID: PMC5228623.

229. Zhao H, Yang L, Baddour J, Achreja A, Bernard V, Moss T, Marini JC, Tudawe T, Seviour EG, San Lucas FA, Alvarez H, Gupta S, Maiti SN, Cooper L, Peehl D, Ram PT, Maitra A, Nagrath D. Tumor microenvironment derived exosomes pleiotropically modulate cancer cell metabolism. Elife. 2016;5:e10250. Epub 2016/02/28. doi: 10.7554/eLife.10250. PubMed PMID: 26920219; PMCID: PMC4841778.

230. Banh RS, Biancur DE, Yamamoto K, Sohn ASW, Walters B, Kuljanin M, Gikandi A, Wang H, Mancias JD, Schneider RJ, Pacold ME, Kimmelman AC. Neurons Release Serine to Support mRNA Translation in Pancreatic Cancer. Cell. 2020. Epub 2020/11/04. doi: 10.1016/j.cell.2020.10.016. PubMed PMID: 33142117.

231. Manzo T, Prentice BM, Anderson KG, Raman A, Schalck A, Codreanu GS, Nava Lauson CB, Tiberti S, Raimondi A, Jones MA, Reyzer M, Bates BM, Spraggins JM,

Patterson NH, McLean JA, Rai K, Tacchetti C, Tucci S, Wargo JA, Rodighiero S, Clise-Dwyer K, Sherrod SD, Kim M, Navin NE, Caprioli RM, Greenberg PD, Draetta G, Nezi L. Accumulation of long-chain fatty acids in the tumor microenvironment drives dysfunction in intrapancreatic CD8+ T cells. Journal of Experimental Medicine. 2020;217(8). doi: 10.1084/jem.20191920.

232. Litvak Y, Byndloss MX, Baumler AJ. Colonocyte metabolism shapes the gut microbiota. Science (New York, NY). 2018;362(6418). Epub 2018/12/01. doi: 10.1126/science.aat9076. PubMed PMID: 30498100; PMCID: PMC6296223.

233. Kaiko GE, Ryu SH, Koues OI, Collins PL, Solnica-Krezel L, Pearce EJ, Pearce EL, Oltz EM, Stappenbeck TS. The Colonic Crypt Protects Stem Cells from Microbiota-Derived Metabolites. Cell. 2016;165(7):1708-20. Epub 2016/06/07. doi: 10.1016/j.cell.2016.05.018. PubMed PMID: 27264604; PMCID: PMC5026192.

234. Leinwand J, Miller G. Regulation and modulation of antitumor immunity in pancreatic cancer. Nat Immunol. 2020;21(10):1152-9. Epub 2020/08/19. doi: 10.1038/s41590-020-0761-y. PubMed PMID: 32807942.

235. Pushalkar S, Hundeyin M, Daley D, Zambirinis CP, Kurz E, Mishra A, Mohan N, Aykut B, Usyk M, Torres LE, Werba G, Zhang K, Guo Y, Li Q, Akkad N, Lall S, Wadowski B, Gutierrez J, Kochen Rossi JA, Herzog JW, Diskin B, Torres-Hernandez A, Leinwand J, Wang W, Taunk PS, Savadkar S, Janal M, Saxena A, Li X, Cohen D, Sartor RB, Saxena D, Miller G. The Pancreatic Cancer Microbiome Promotes Oncogenesis by Induction of Innate and Adaptive Immune Suppression. Cancer Discov. 2018;8(4):403-16. Epub 2018/03/24. doi: 10.1158/2159-8290.Cd-17-1134. PubMed PMID: 29567829; PMCID: PMC6225783.

236. Jin C, Lagoudas GK, Zhao C, Bullman S, Bhutkar A, Hu B, Ameh S, Sandel D, Liang XS, Mazzilli S, Whary MT, Meyerson M, Germain R, Blainey PC, Fox JG, Jacks T. Commensal Microbiota Promote Lung Cancer Development via γδ T Cells. Cell. 2019;176(5):998-1013.e16. Epub 2019/02/05. doi: 10.1016/j.cell.2018.12.040. PubMed PMID: 30712876; PMCID: PMC6691977.

237. Smith PM, Howitt MR, Panikov N, Michaud M, Gallini CA, Bohlooly YM, Glickman JN, Garrett WS. The microbial metabolites, short-chain fatty acids, regulate colonic Treg cell homeostasis. Science (New York, NY). 2013;341(6145):569-73. Epub 2013/07/06. doi: 10.1126/science.1241165. PubMed PMID: 23828891; PMCID: PMC3807819.

238. Tsay JJ, Wu BG, Badri MH, Clemente JC, Shen N, Meyn P, Li Y, Yie TA, Lhakhang T, Olsen E, Murthy V, Michaud G, Sulaiman I, Tsirigos A, Heguy A, Pass H, Weiden MD, Rom WN, Sterman DH, Bonneau R, Blaser MJ, Segal LN. Airway Microbiota Is Associated with Upregulation of the PI3K Pathway in Lung Cancer. Am J Respir Crit Care Med. 2018;198(9):1188-98. Epub 2018/06/05. doi: 10.1164/rccm.201710-2118OC. PubMed PMID: 29864375; PMCID: PMC6221574.

239. Segal LN, Clemente JC, Tsay JC, Koralov SB, Keller BC, Wu BG, Li Y, Shen N, Ghedin E, Morris A, Diaz P, Huang L, Wikoff WR, Ubeda C, Artacho A, Rom WN,

Sterman DH, Collman RG, Blaser MJ, Weiden MD. Enrichment of the lung microbiome with oral taxa is associated with lung inflammation of a Th17 phenotype. Nat Microbiol. 2016;1:16031. Epub 2016/08/31. doi: 10.1038/nmicrobiol.2016.31. PubMed PMID: 27572644; PMCID: PMC5010013.

240. McNabney SM, Henagan TM. Short Chain Fatty Acids in the Colon and Peripheral Tissues: A Focus on Butyrate, Colon Cancer, Obesity and Insulin Resistance. Nutrients. 2017;9(12). Epub 2017/12/13. doi: 10.3390/nu9121348. PubMed PMID: 29231905; PMCID: PMC5748798.

241. Viale A, Pettazzoni P, Lyssiotis CA, Ying H, Sanchez N, Marchesini M, Carugo A, Green T, Seth S, Giuliani V, Kost-Alimova M, Muller F, Colla S, Nezi L, Genovese G, Deem AK, Kapoor A, Yao W, Brunetto E, Kang Y, Yuan M, Asara JM, Wang YA, Heffernan TP, Kimmelman AC, Wang H, Fleming JB, Cantley LC, DePinho RA, Draetta GF. Oncogene ablation-resistant pancreatic cancer cells depend on mitochondrial function. Nature. 2014;514(7524):628-32. Epub 2014/08/15. doi: 10.1038/nature13611. PubMed PMID: 25119024; PMCID: PMC4376130.

242. Hou P, Kapoor A, Zhang Q, Li J, Wu CJ, Li J, Lan Z, Tang M, Ma X, Ackroyd JJ, Kalluri R, Zhang J, Jiang S, Spring DJ, Wang YA, DePinho RA. Tumor Microenvironment Remodeling Enables Bypass of Oncogenic KRAS Dependency in Pancreatic Cancer. Cancer Discov. 2020;10(7):1058-77. Epub 2020/04/29. doi: 10.1158/2159-8290.Cd-19-0597. PubMed PMID: 32341020; PMCID: PMC7334087.

243. Kapoor A, Yao W, Ying H, Hua S, Liewen A, Wang Q, Zhong Y, Wu CJ, Sadanandam A, Hu B, Chang Q, Chu GC, Al-Khalil R, Jiang S, Xia H, Fletcher-Sananikone E, Lim C, Horwitz GI, Viale A, Pettazzoni P, Sanchez N, Wang H, Protopopov A, Zhang J, Heffernan T, Johnson RL, Chin L, Wang YA, Draetta G, DePinho RA. Yap1 activation enables bypass of oncogenic Kras addiction in pancreatic cancer. Cell. 2014;158(1):185-97. Epub 2014/06/24. doi: 10.1016/j.cell.2014.06.003. PubMed PMID: 24954535; PMCID: PMC4109295.

244. Tanaka N, Lin JJ, Li C, Ryan MB, Zhang J, Kiedrowski LA, Michel AG, Syed MU, Fella KA, Sakhi M, Baiev I, Juric D, Gainor JF, Klempner SJ, Lennerz JK, Siravegna G, Bar-Peled L, Hata AN, Heist RS, Corcoran RB. Clinical acquired resistance to KRASG12C inhibition through a novel KRAS switch-II pocket mutation and polyclonal alterations converging on RAS-MAPK reactivation. Cancer Discovery. 2021:candisc.0365.2021. doi: 10.1158/2159-8290.CD-21-0365.

245. Muzumdar MD, Chen P-Y, Dorans KJ, Chung KM, Bhutkar A, Hong E, Noll EM, Sprick MR, Trumpp A, Jacks T. Survival of pancreatic cancer cells lacking KRAS function. Nature Communications. 2017;8(1):1090. doi: 10.1038/s41467-017-00942-5.

246. Chen P-Y, Muzumdar MD, Dorans KJ, Robbins R, Bhutkar A, del Rosario A, Mertins P, Qiao J, Schafer AC, Gertler F, Carr S, Jacks T. Adaptive and Reversible Resistance to Kras Inhibition in Pancreatic Cancer Cells. Cancer research. 2018;78(4):985. doi: 10.1158/0008-5472.CAN-17-2129.

247. Janes MR, Zhang J, Li L-S, Hansen R, Peters U, Guo X, Chen Y, Babbar A, Firdaus SJ, Darjania L, Feng J, Chen JH, Li S, Li S, Long YO, Thach C, Liu Y, Zarieh A, Ely T, Kucharski JM, Kessler LV, Wu T, Yu K, Wang Y, Yao Y, Deng X, Zarrinkar PP, Brehmer D, Dhanak D, Lorenzi MV, Hu-Lowe D, Patricelli MP, Ren P, Liu Y. Targeting KRAS Mutant Cancers with a Covalent G12C-Specific Inhibitor. Cell. 2018;172(3):578-89.e17. doi: https://doi.org/10.1016/j.cell.2018.01.006.

248. Yao W, Rose JL, Wang W, Seth S, Jiang H, Taguchi A, Liu J, Yan L, Kapoor A, Hou P, Chen Z, Wang Q, Nezi L, Xu Z, Yao J, Hu B, Pettazzoni PF, Ho IL, Feng N, Ramamoorthy V, Jiang S, Deng P, Ma GJ, Den P, Tan Z, Zhang SX, Wang H, Wang YA, Deem AK, Fleming JB, Carugo A, Heffernan TP, Maitra A, Viale A, Ying H, Hanash S, DePinho RA, Draetta GF. Syndecan 1 is a critical mediator of macropinocytosis in pancreatic cancer. Nature. 2019;568(7752):410-4. Epub 2019/03/29. doi: 10.1038/s41586-019-1062-1. PubMed PMID: 30918400; PMCID: PMC6661074.

249. Shackelford DB, Abt E, Gerken L, Vasquez DS, Seki A, Leblanc M, Wei L, Fishbein MC, Czernin J, Mischel PS, Shaw RJ. LKB1 inactivation dictates therapeutic response of non-small cell lung cancer to the metabolism drug phenformin. Cancer cell. 2013;23(2):143-58. Epub 2013/01/29. doi: 10.1016/j.ccr.2012.12.008. PubMed PMID: 23352126; PMCID: PMC3579627.

250. Liu Y, Marks K, Cowley GS, Carretero J, Liu Q, Nieland TJF, Xu C, Cohoon TJ, Gao P, Zhang Y, Chen Z, Altabef AB, Tchaicha JH, Wang X, Choe S, Driggers EM, Zhang J, Bailey ST, Sharpless NE, Hayes DN, Patel NM, Janne PA, Bardeesy N, Engelman JA, Manning BD, Shaw RJ, Asara JM, Scully R, Kimmelman A, Byers LA, Gibbons DL, Wistuba II, Heymach JV, Kwiatkowski DJ, Kim WY, Kung AL, Gray NS, Root DE, Cantley LC, Wong K-K. Metabolic and Functional Genomic Studies Identify Deoxythymidylate Kinase as a Target in LKB1-Mutant Lung Cancer. Cancer Discovery. 2013;3(8):870. doi: 10.1158/2159-8290.CD-13-0015.

251. LeBoeuf SE, Wu WL, Karakousi TR, Karadal B, Jackson SR, Davidson SM, Wong K-K, Koralov SB, Sayin VI, Papagiannakopoulos T. Activation of Oxidative Stress Response in Cancer Generates a Druggable Dependency on Exogenous Non-essential Amino Acids. Cell metabolism. 2020;31(2):339-50.e4. doi: https://doi.org/10.1016/j.cmet.2019.11.012.

252. Sherman MH, Yu RT, Engle DD, Ding N, Atkins AR, Tiriac H, Collisson EA, Connor F, Van Dyke T, Kozlov S, Martin P, Tseng TW, Dawson DW, Donahue TR, Masamune A, Shimosegawa T, Apte MV, Wilson JS, Ng B, Lau SL, Gunton JE, Wahl GM, Hunter T, Drebin JA, O'Dwyer PJ, Liddle C, Tuveson DA, Downes M, Evans RM. Vitamin D receptor-mediated stromal reprogramming suppresses pancreatitis and enhances pancreatic cancer therapy. Cell. 2014;159(1):80-93. Epub 2014/09/27. doi: 10.1016/j.cell.2014.08.007. PubMed PMID: 25259922; PMCID: PMC4177038.

253. Yan Y, Chen X, Wang X, Zhao Z, Hu W, Zeng S, Wei J, Yang X, Qian L, Zhou S, Sun L, Gong Z, Xu Z. The effects and the mechanisms of autophagy on the cancer-

associated fibroblasts in cancer. Journal of Experimental & Clinical Cancer Research. 2019;38(1):171. doi: 10.1186/s13046-019-1172-5.

254. Dalin S, Sullivan MR, Lau AN, Grauman-Boss B, Mueller HS, Kreidl E, Fenoglio S, Luengo A, Lees JA, Vander Heiden MG, Lauffenburger DA, Hemann MT. Deoxycytidine Release from Pancreatic Stellate Cells Promotes Gemcitabine Resistance. Cancer Res. 2019;79(22):5723-33. Epub 2019/09/06. doi: 10.1158/0008-5472.Can-19-0960. PubMed PMID: 31484670; PMCID: PMC7357734.

255. Halbrook CJ, Pontious C, Kovalenko I, Lapienyte L, Dreyer S, Lee HJ, Thurston G, Zhang Y, Lazarus J, Sajjakulnukit P, Hong HS, Kremer DM, Nelson BS, Kemp S, Zhang L, Chang D, Biankin A, Shi J, Frankel TL, Crawford HC, Morton JP, Pasca di Magliano M, Lyssiotis CA. Macrophage-Released Pyrimidines Inhibit Gemcitabine Therapy in Pancreatic Cancer. Cell metabolism. 2019;29(6):1390-9 e6. Epub 2019/03/05. doi: 10.1016/j.cmet.2019.02.001. PubMed PMID: 30827862; PMCID: PMC6602533.

256. Ribas A, Wolchok JD. Cancer immunotherapy using checkpoint blockade. Science (New York, NY). 2018;359(6382):1350-5. Epub 2018/03/24. doi: 10.1126/science.aar4060. PubMed PMID: 29567705; PMCID: PMC7391259.

257. Cristescu R, Mogg R, Ayers M, Albright A, Murphy E, Yearley J, Sher X, Liu XQ, Lu H, Nebozhyn M, Zhang C, Lunceford JK, Joe A, Cheng J, Webber AL, Ibrahim N, Plimack ER, Ott PA, Seiwert TY, Ribas A, McClanahan TK, Tomassini JE, Loboda A, Kaufman D. Pan-tumor genomic biomarkers for PD-1 checkpoint blockade–based immunotherapy. Science (New York, NY). 2018;362(6411):eaar3593. doi: 10.1126/science.aar3593.

258. Brahmer JR, Tykodi SS, Chow LQM, Hwu W-J, Topalian SL, Hwu P, Drake CG, Camacho LH, Kauh J, Odunsi K, Pitot HC, Hamid O, Bhatia S, Martins R, Eaton K, Chen S, Salay TM, Alaparthy S, Grosso JF, Korman AJ, Parker SM, Agrawal S, Goldberg SM, Pardoll DM, Gupta A, Wigginton JM. Safety and Activity of Anti–PD-L1 Antibody in Patients with Advanced Cancer. New England Journal of Medicine. 2012;366(26):2455-65. doi: 10.1056/NEJMoa1200694.

259. Leone RD, Zhao L, Englert JM, Sun I-M, Oh M-H, Sun I-H, Arwood ML, Bettencourt IA, Patel CH, Wen J, Tam A, Blosser RL, Prchalova E, Alt J, Rais R, Slusher BS, Powell JD. Glutamine blockade induces divergent metabolic programs to overcome tumor immune evasion. Science (New York, NY). 2019:eaav2588. doi: 10.1126/science.aav2588.

260. Ma EH, Verway MJ, Johnson RM, Roy DG, Steadman M, Hayes S, Williams KS, Sheldon RD, Samborska B, Kosinski PA, Kim H, Griss T, Faubert B, Condotta SA, Krawczyk CM, DeBerardinis RJ, Stewart KM, Richer MJ, Chubukov V, Roddy TP, Jones RG. Metabolic Profiling Using Stable Isotope Tracing Reveals Distinct Patterns of Glucose Utilization by Physiologically Activated CD8(+) T Cells. Immunity.

2019;51(5):856-70.e5. Epub 2019/11/21. doi: 10.1016/j.immuni.2019.09.003. PubMed PMID: 31747582.

261. Balmer ML, Ma EH, Thompson AJ, Epple R, Unterstab G, Lötscher J, Dehio P, Schürch CM, Warncke JD, Perrin G, Woischnig AK, Grählert J, Löliger J, Assmann N, Bantug GR, Schären OP, Khanna N, Egli A, Bubendorf L, Rentsch K, Hapfelmeier S, Jones RG, Hess C. Memory CD8(+) T Cells Balance Pro- and Anti-inflammatory Activity by Reprogramming Cellular Acetate Handling at Sites of Infection. Cell metabolism. 2020;32(3):457-67.e5. Epub 2020/08/02. doi: 10.1016/j.cmet.2020.07.004. PubMed PMID: 32738204.

262. Hellmann MD, Nathanson T, Rizvi H, Creelan BC, Sanchez-Vega F, Ahuja A, Ni A, Novik JB, Mangarin LMB, Abu-Akeel M, Liu C, Sauter JL, Rekhtman N, Chang E, Callahan MK, Chaft JE, Voss MH, Tenet M, Li X-M, Covello K, Renninger A, Vitazka P, Geese WJ, Borghaei H, Rudin CM, Antonia SJ, Swanton C, Hammerbacher J, Merghoub T, McGranahan N, Snyder A, Wolchok JD. Genomic Features of Response to Combination Immunotherapy in Patients with Advanced Non-Small-Cell Lung Cancer. Cancer cell. 2018;33(5):843-52.e4. Epub 2018/04/12. doi: 10.1016/j.ccell.2018.03.018. PubMed PMID: 29657128.

263. Skoulidis F, Goldberg ME, Greenawalt DM, Hellmann MD, Awad MM, Gainor JF, Schrock AB, Hartmaier RJ, Trabucco SE, Gay L, Ali SM, Elvin JA, Singal G, Ross JS, Fabrizio D, Szabo PM, Chang H, Sasson A, Srinivasan S, Kirov S, Szustakowski J, Vitazka P, Edwards R, Bufill JA, Sharma N, Ou SI, Peled N, Spigel DR, Rizvi H, Aguilar EJ, Carter BW, Erasmus J, Halpenny DF, Plodkowski AJ, Long NM, Nishino M, Denning WL, Galan-Cobo A, Hamdi H, Hirz T, Tong P, Wang J, Rodriguez-Canales J, Villalobos PA, Parra ER, Kalhor N, Sholl LM, Sauter JL, Jungbluth AA, Mino-Kenudson M, Azimi R, Elamin YY, Zhang J, Leonardi GC, Jiang F, Wong KK, Lee JJ, Papadimitrakopoulou VA, Wistuba, II, Miller VA, Frampton GM, Wolchok JD, Shaw AT, Jänne PA, Stephens PJ, Rudin CM, Geese WJ, Albacker LA, Heymach JV. STK11/LKB1 Mutations and PD-1 Inhibitor Resistance in KRAS-Mutant Lung Adenocarcinoma. Cancer Discov. 2018;8(7):822-35. Epub 2018/05/19. doi: 10.1158/2159-8290.Cd-18-0099. PubMed PMID: 29773717; PMCID: PMC6030433.

264. Rizvi H, Sanchez-Vega F, La K, Chatila W, Jonsson P, Halpenny D, Plodkowski A, Long N, Sauter JL, Rekhtman N, Hollmann T, Schalper KA, Gainor JF, Shen R, Ni A, Arbour KC, Merghoub T, Wolchok J, Snyder A, Chaft JE, Kris MG, Rudin CM, Socci ND, Berger MF, Taylor BS, Zehir A, Solit DB, Arcila ME, Ladanyi M, Riely GJ, Schultz N, Hellmann MD. Molecular Determinants of Response to Anti-Programmed Cell Death (PD)-1 and Anti-Programmed Death-Ligand 1 (PD-L1) Blockade in Patients With Non-Small-Cell Lung Cancer Profiled With Targeted Next-Generation Sequencing. J Clin Oncol. 2018;36(7):633-41. Epub 2018/01/18. doi: 10.1200/jco.2017.75.3384. PubMed PMID: 29337640; PMCID: PMC6075848.

265. Arbour KC, Jordan E, Kim HR, Dienstag J, Yu HA, Sanchez-Vega F, Lito P, Berger M, Solit DB, Hellmann M, Kris MG, Rudin CM, Ni A, Arcila M, Ladanyi M, Riely GJ. Effects of Co-occurring Genomic Alterations on Outcomes in Patients with

KRAS-Mutant Non–Small Cell Lung Cancer. Clinical Cancer Research. 2018;24(2):334. doi: 10.1158/1078-0432.CCR-17-1841.

266. Halbrook CJ, Pasca di Magliano M, Lyssiotis CA. Tumor cross-talk networks promote growth and support immune evasion in pancreatic cancer. Am J Physiol Gastrointest Liver Physiol. 2018;315(1):G27-G35. Epub 2018/03/16. doi: 10.1152/ajpgi.00416.2017. PubMed PMID: 29543507; PMCID: PMC6109710.

267. Yamamoto K, Venida A, Yano J, Biancur DE, Kakiuchi M, Gupta S, Sohn ASW, Mukhopadhyay S, Lin EY, Parker SJ, Banh RS, Paulo JA, Wen KW, Debnath J, Kim GE, Mancias JD, Fearon DT, Perera RM, Kimmelman AC. Autophagy promotes immune evasion of pancreatic cancer by degrading MHC-I. Nature. 2020;581(7806):100-5. doi: 10.1038/s41586-020-2229-5.

268. Zhu XG, Chudnovskiy A, Baudrier L, Prizer B, Liu Y, Ostendorf BN, Yamaguchi N, Arab A, Tavora B, Timson R, Heissel S, de Stanchina E, Molina H, Victora GD, Goodarzi H, Birsoy K. Functional Genomics In Vivo Reveal Metabolic Dependencies of Pancreatic Cancer Cells. Cell metabolism. 2020. doi: https://doi.org/10.1016/j.cmet.2020.10.017.

1.8 Figures

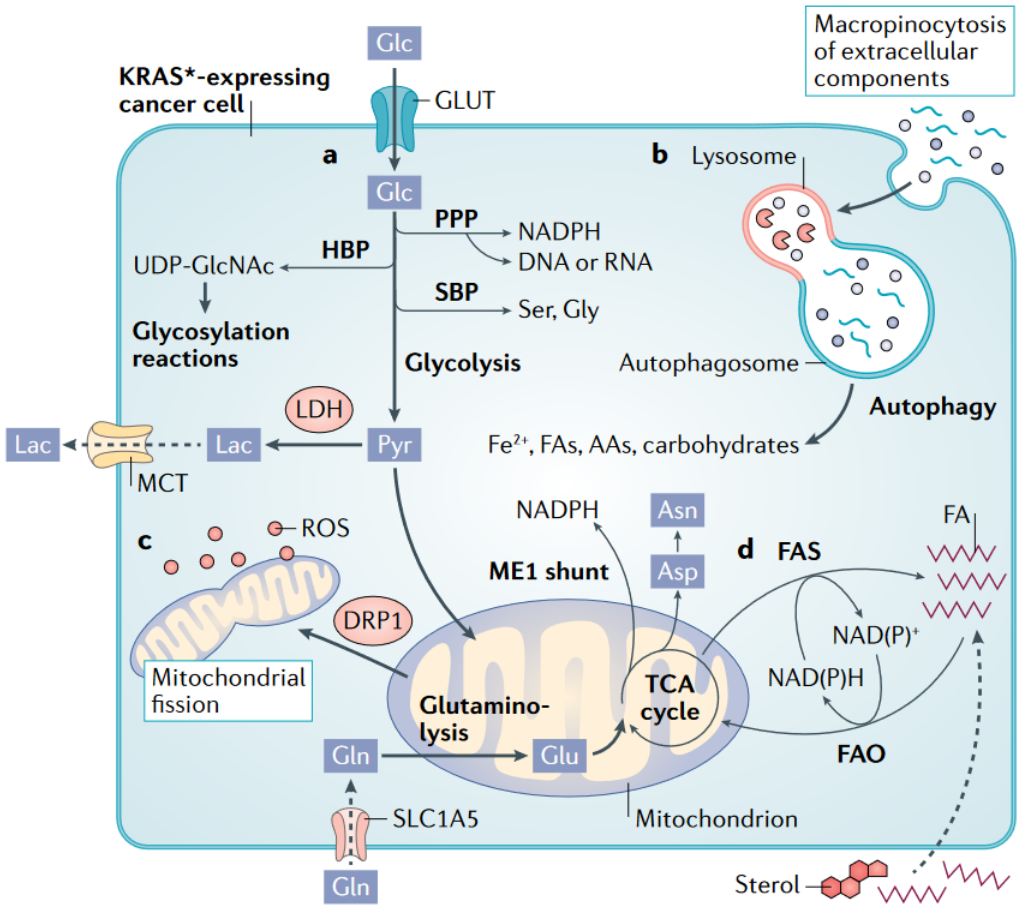

Figure 1-1 KRAS* rewires cancer cell metabolism.

a) Glucose (Glc) transport via glucose transporters (GLUTs) and flux through glycolysis is upregulated to provide intermediates for branching biosynthetic pathways. The hexosamine biosynthetic pathway (HBP) produces uridine diphosphate N-acetylglucosamine (UDP-GlcNAc) for glycosylation. The two arms of the pentose phosphate pathway (PPP) generate nicotinamide adenine dinucleotide phosphate (NADPH) as well as ribose bases for nucleotide synthesis. Flux through the serine biosynthesis pathway (SBP) generates the amino acids serine (Ser) and glycine (Gly). To maintain redox balance, increased expression of lactate dehydrogenase (LDH) converts pyruvate (Pyr) to lactate (Lac), which is transported out of the cell via monocarboxylate transporters (MCTs) to sustain glycolysis. Pyruvate also contributes carbon to the TCA cycle in mitochondria. Glutamine (Gln) is imported by SLC1A5 and converted to glutamate (Glu) by glutaminase 1 (GLS1) and fuels the tricarboxylic acid (TCA) cycle. KRAS* diverts TCA cycle intermediates through malic enzyme 1 (ME1) for NADPH production, as well as synthesis of amino acids like aspartate (Asp) and asparagine (Asn). **b)** KRAS* cells are dependent on nutrient scavenging pathways, such as macropinocytosis and autophagy, whereby free biosynthetic precursors are released for utilization by cancer cells. **c)** KRAS* regulates mitochondrial dynamics through DRP1 to fine tune mitochondrial fission and maintain optimal reactive oxygen species (ROS) levels for signaling while avoiding toxicity. **d)** Depending on intracellular redox state, KRAS* cells employ fatty acid synthesis (FAS) to regenerate NADP+ and synthesize lipids or fatty acid oxidation (FAO), whereby lipids are used for energy and NADPH production.

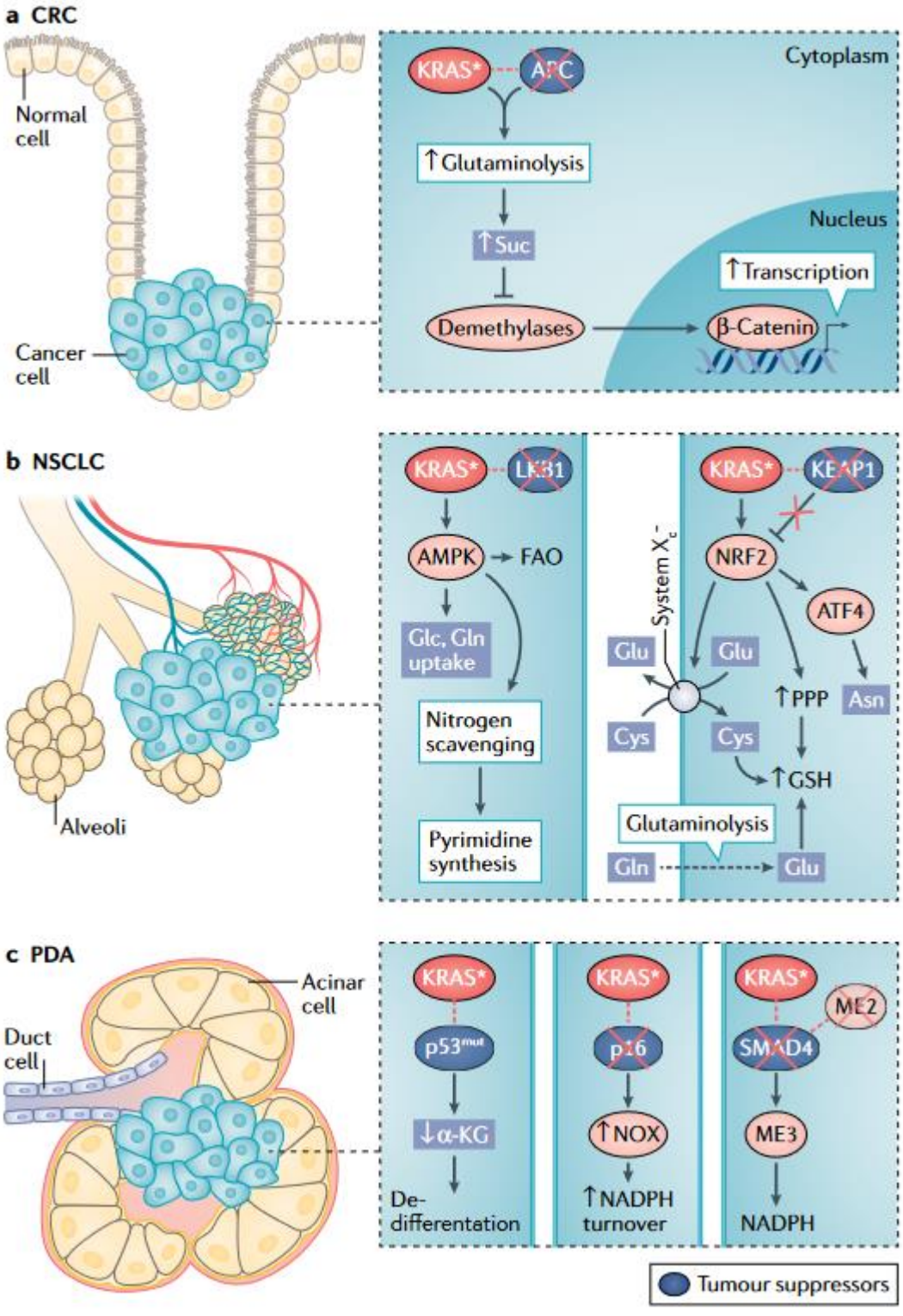

Figure 1-2 KRAS* synergizes with co-occurring mutations to direct metabolism.

a) In CRC, KRAS*-mediated glutamine (Gln) catabolism increases levels of the TCA cycle intermediate succinate (Suc), which inhibits the activity of α-ketoglutarate (αKG)-dependent demethylases.

Hypermethylation of Wnt pathway target genes promotes their expression and cooperates with β-catenin transcriptional activity for maximal activation downstream of APC loss. **b)** In NSCLC, aberrant activity of adenosine monophosphate kinase (AMPK), due to loss of liver kinase B1 (LKB1), increases fatty acid oxidation (FAO) and uptake of glucose (Glc) and Gln (left). Scavenging of ammonia from the urea cycle supplies nitrogen needed for pyrimidine synthesis. Loss of Kelch-like ECH-associated protein 1 (KEAP1) activates the nuclear factor erythroid 2-related factor 2 (NRF2) antioxidant transcriptional program. Increased glutamate (Glu) production from Gln through glutaminolysis is exchanged for extracellular cystine (cysteine dimer; Cys-Cys) through system X_C^-, which is also upregulated by NRF2. Cys is incorporated into glutathione (GSH) for protection from ROS. NRF2 also stimulates production of GSH through the pentose phosphate pathway (PPP) and regulates asparagine (Asn) production through activating transcription 4 (ATF) activity (right). **c)** In PDA, mutations to p53 ($p53^{mut}$) lead to reduced αKG levels and impaired demethylase activity, affecting epigenetic programs and cell state (left). Loss of the tumor suppressor p16 leads to increased NADH-oxidase (NOX) expression and activity which is important for NADPH turnover and redox balance (middle). Loss of the SMAD4 genetic locus coincides with loss of malic enzyme 2 (ME2), rendering cells dependent on compensatory ME3 activity for NADPH production (right).

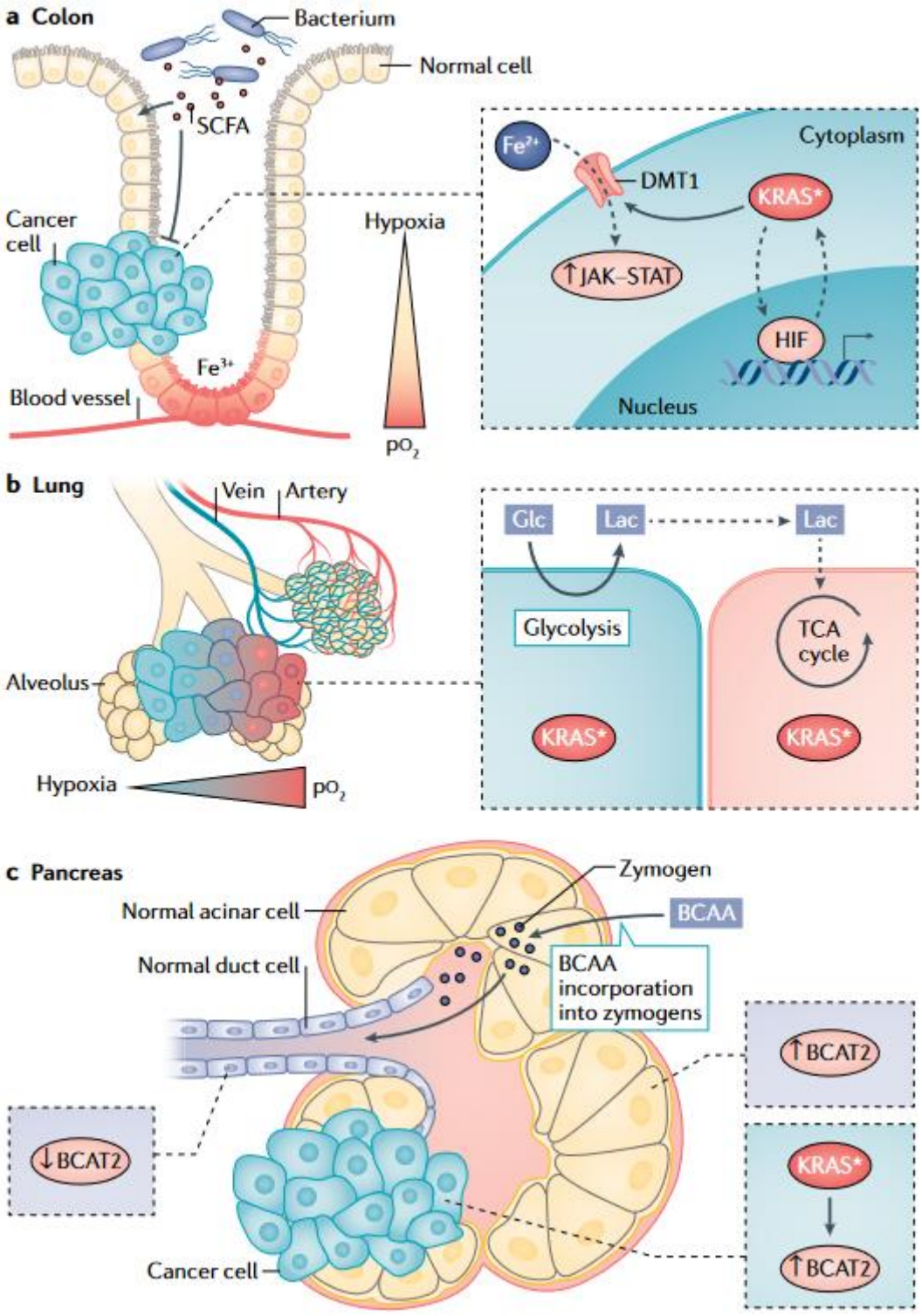

Figure 1-3 Tissue specific metabolism hijacked by KRAS*.

a) Hypoxic gradients in the colon stabilize hypoxia inducible factors (HIF) in normal colonocytes, which can then cooperate with KRAS* following transformation. The hypoxic lumen also promotes colonization by short-chain fatty acid (SCFA)-producing bacteria. SCFAs are used by heathy colon cells for fuel and

are prohibitive for development of colon tumors. Normal colonocytes are essential for iron (Fe^{3+}) absorption, and iron (Fe^{2+}) uptake through divalent metal transporter (DMT1) is utilized by KRAS* colon cancer cells to drive pro-tumorigenic JAK/STAT signalling. **b)** Normal lung epithelial cells demonstrate high glucose uptake and export of lactate. In NSCLC, KRAS* cancer cells located far from a blood vessel in hypoxia utilize glycolysis and produce lactate which can be taken up by tumor cells nearer to the blood vessel and utilized for oxidative respiration. **c)** Zymogen-producing acinar cells are branched-chain amino acid (BCAA)-avid to obtain building blocks for peptides and digestive enzymes and display elevated branched-chain amino acid transaminase 2 (BCAT2) expression, while BCAT2 levels are lower in normal ductal cells. During transformation by KRAS*, acinar cells dedifferentiate into ductal cells and progress to PDA. KRAS* stabilizes and increases BCAT2 expression in cancer cells, demonstrating how the duct-like PDA cells retain acinar cell metabolic programs.

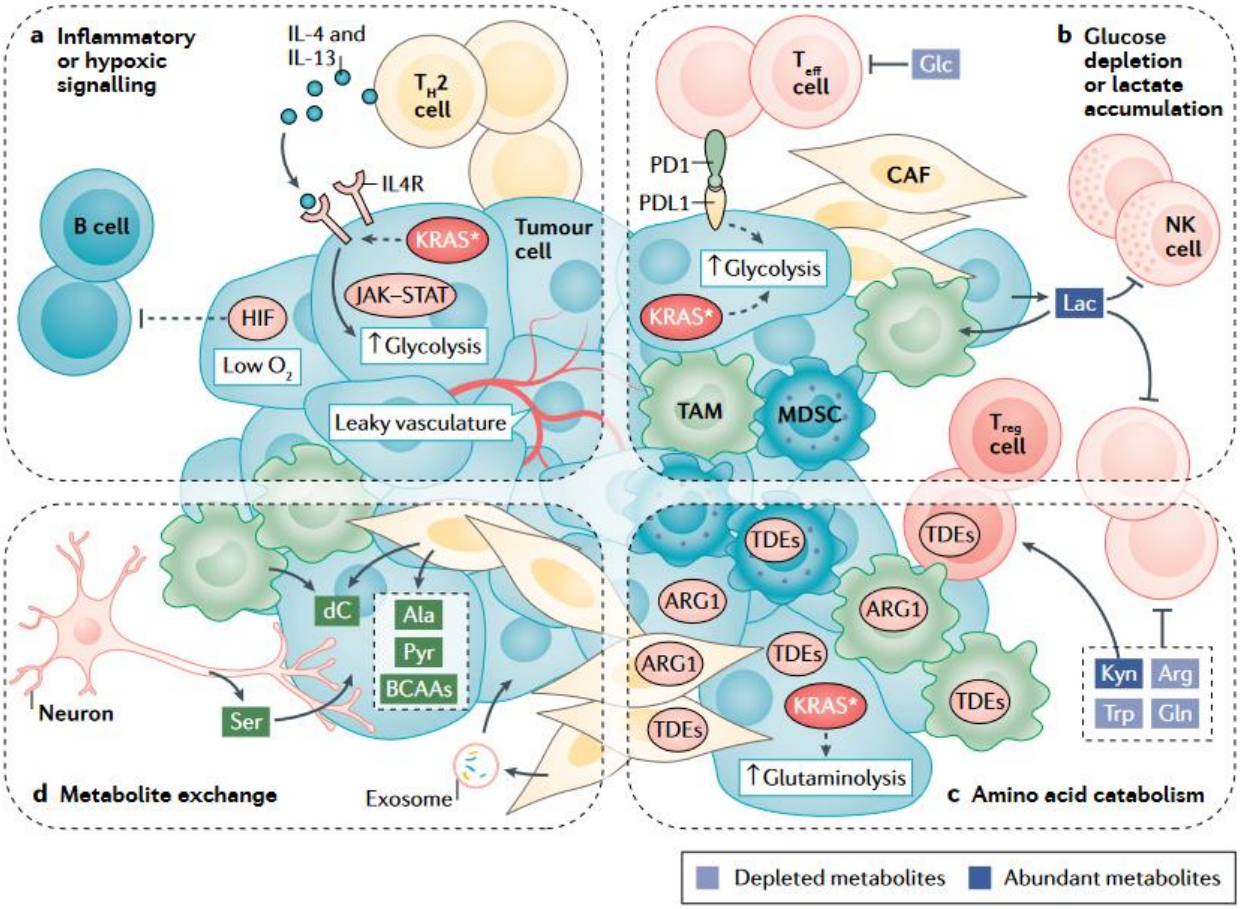

Figure 1-4 Interactions in the KRAS* TME.

A) T helper 2 (Th2) cells in the TME release type I cytokines. KRAS* increases expression of their receptors on the surface of cancer cells. Downstream signaling through JAK/STAT activates MYC to increase expression of glycolytic enzymes. Hypoxia-inducible factor (HIF) activity excludes B cells from the TME. **B)** Glucose (Glc) is required by effector T (Teff) cells to mount an anti-tumor immune response, yet Glc is depleted due to elevated glycolysis in KRAS*-expressing cancer cells and cancer-associated fibroblasts (CAFs). Expression of programmed death ligand 1 (PDL1) on cancer cells and binding with its PD1 receptor on Teff cells also stimulates glycolysis in cancer cells. Increased lactate (Lac) released into extracellular space by cancer cells and taken up by other cells further inhibits glycolysis in Teff cells and natural killer (NK) cells, while polarizing macrophages to a tumor-associated macrophage (TAM) state. **C)** Elevated glutaminolysis and glutamine (Gln) uptake in KRAS* cells depletes Gln, which is required by Teff cells. Expression of tryptophan degrading enzymes (TDEs) on regulatory T cells (Tregs),CAFs,TAMs, and cancer cells degrades tryptophan (Trp) into its derivative kynurenine (Kyn) which promotes Treg activity. KRAS* cancer cells are auxotrophic for arginine and express arginase 1 (ARG1) to break down arginine (Arg) in the TME. ARG1 is also expressed on CAFs and TAMs. **D)** Induction of autophagy in CAFs increases release of alanine (Ala) for uptake and use by cancer cells. CAFs also release pyruvate (Pyr), branched-chain amino acids (BCAAs), and metabolite-filled exosomes to support dysregulated KRAS* metabolism in cancer cells. Deoxycytidine (dC) released from CAFs and TAMs is taken up by cancer cells and blunts chemotherapy efficacy. Innervating neurons release serine (Ser) to support protein translation in cancer cells under Ser deprivation.

Chapter 2 – Hyaluronic Acid Fuels Pancreatic Cancer Cell Growth†

2.1 Introduction

As discussed in Chapter 1, PDA is one of the deadliest human cancers with no clinically effective treatment options(1). PDA is characterized by an intense fibroinflammatory stroma, poor vascularity, deregulated nutrient levels, and rich deposition of extracellular matrix components. To survive and proliferate in this nutrient dysregulated tumor microenvironment, the oncogenic driver in PDA, KRAS*, facilitates the rewiring of PDA metabolism(2-5).

One example of this, which has been demonstrated in previous work(6) and introduced in Chapter 1, is the effect of KRAS* on the activity of the hexosamine biosynthesis pathway (HBP). Signaling downstream of KRAS* results in upregulated expression of *Gfpt1*, which encodes glutamine-fructose 6-phosphate amidotransferase 1 (GFAT1). The HBP is an evolutionarily conserved pathway that integrates glucose, glutamine, fatty acid, and nucleotide metabolism to generate the final product uridine diphosphate N-acetylglucosamine (UDP-GlcNAc). UDP-GlcNAc is a crucial donor molecule for glycosylation and O-GlcNAcylation, two essential post-translational modifications required for cellular structure, signaling, and survival(7). The HBP is the

† This chapter consists of a published primary article: Kim PK*, Halbrook CJ*, **Kerk SA***, Radyk M, Wisner S, Kremer DM, Sajjakulnukit P, Andren A, Hou SW, Trivedi A, Thurston G, Anand A, Yan L, Salamanca-Cardona L, Welling SD, Zhang L, Pratt MR, Keshari KR, Ying H, Lyssiotis CA. Hyaluronic acid fuels pancreatic cancer cell growth. ***Elife***. 2021 Dec 24;10:e62645. doi: 10.7554/eLife.62645. PMID: 34951587; PMCID: PMC8730721.
*these authors contributed equally

only pathway able to generate UDP-GlcNAc *de novo*. Because the HBP integrates nutrients from several major macromolecular classes to produce UDP-GlcNAc, it predictably functions as a nutrient sensing mechanism for available energy within a cell(8). Indeed, numerous studies across cancer subtypes have demonstrated how HBP activity is enhanced to support tumor survival and growth(9-12) and even immune evasion through alteration of extracellular glycosylation content(13).

A compendium of studies during the last decade have revealed that PDA cells fuel their aberrant metabolic programs through nutrient scavenging(6, 14-18). Mechanisms include sustained activation of intracellular recycling pathways (e.g. autophagy), the upregulation of nutrient transporter expression (e.g. carbohydrate, lipid, and amino acid transporters), and the activation of extracellular nutrient scavenging pathways (e.g. macropinocytosis). Further, PDA cells also participate in metabolic crosstalk and nutrient acquisition with non-cancerous cells in the tumor microenvironment (TME), such as cancer-associated fibroblasts (CAFs) and tumor-associated macrophages (TAMs)(19-23). A notable example is the observation that PDA cells can directly obtain nutrients from the CAF-derived extracellular matrix (ECM), such as collagen(18). Taken together, elucidating the interaction of PDA cells with different cell populations and ECM components will be instrumental for delineating deregulated PDA metabolism and improving therapeutic strategies.

A major structural component of the TME is hyaluronic acid (HA), a hydrophilic glycosaminoglycan. HA is ubiquitously present in human tissue, especially in skin, connective tissue, and joints, and it is richly abundant in pancreatic tumors(24). HA is thought to be primarily deposited by CAFs and, to some extent, by PDA cells(25, 26).

HA avidly retains water, which is responsible for both its lubricating properties and, in PDA tumors, the supraphysiological pressure that impairs vascularity and limits drug penetrance(27, 28). An aspect of HA biology that has not previously been studied is its potential role as a nutrient. This is surprising given that HA is a carbohydrate polymer whose monomeric unit is a disaccharide of glucuronic acid and N-acetyl-glucosamine (GlcNAc).

Herein, we set forth to determine the utility of targeting the HBP in PDA. We found that GFAT1 was required for cell survival in vitro. In marked contrast, GFAT1 knockout tumors readily grew in vivo. Based on this observation, we hypothesized that GlcNAc-containing components of the TME could bypass the HBP in vivo by way of the GlcNAc salvage pathway. We demonstrate that HA can be metabolized by PDA cells to support survival and proliferation by refilling the HBP. In sum, our study identifies HA as a novel nutrient source in PDA and contributes to a growing body of data illuminating the important role of the TME in cancer metabolism.

2.2 Results

2.2.1 Pancreatic cancer cells require de novo HBP fidelity in vitro but not in vivo

Previously, we found that mutant Kras transcriptionally activates *Gfpt1* expression downstream of MAPK signaling in a murine model of PDA to facilitate HBP activity(6). GFAT1 catalyzes the reaction that generates glucosamine 6-phosphate and glutamate from fructose 6-phosphate and glutamine **(Fig. 2-1A)**. In another previous study we demonstrated that PDA cells are dependent on glutamine anaplerosis for proliferation(29). Thus, we hypothesized that inhibiting GFAT1 in PDA would have the

simultaneous benefit of blocking two major metabolic pathways that support PDA proliferation, thereby providing a considerable therapeutic window.

Our previous results targeting GFAT1 in murine cells with shRNA yielded insufficient knockdown to draw a conclusion as to its necessity in PDA(6). Thus, here we used CRISPR/Cas9 to knockout GFAT1 from three established human PDA cell lines: HPAC, TU8988T, and MiaPaCa2. During selection, the pooled polyclonal populations were grown in GlcNAc, which bypasses GFAT1 via the GlcNAc salvage pathway **(Fig. 2-1A)**. This supplement was included to minimize metabolic rewiring within the selected populations.

The GFAT1 knockout lines had differential response to GlcNAc withdrawal. Among the three GFAT1 knockout cell lines, only the HPAC line exhibited a marked reduction in cell number, consistent with loss of viability, in the 4 days following GlcNAc withdrawal (**Fig. 2-2A**). The impact on proliferation was similarly reflected in decrease of the UDP-GlcNAc pool, which was analyzed using liquid chromatography-coupled tandem mass spectrometry (LC-MS/MS) (**Fig. 2-2B**). Consistent with the proliferative phenotypes across lines, the HPAC line also had a significantly smaller UDP-GlcNAc pool than that of either MiaPaCa2 or 8988T cells (**Fig. 2-2C**). Cellular O-GlcNAcylation of the proteome was also measured by immunoblot three days after GlcNAc withdrawal. Again, consistent with the LC-MS/MS analysis, O-GlcNAc expression was significantly reduced in HPAC but was maintained in TU8988T (**Fig. 2-2D**).

The data from TU8988T and MiaPaca2 were similar to those from our earlier studies(6), and thus we posited that knockout of GFAT1 was incomplete. As such, we subsequently generated clonal cell lines from the pooled populations. This analysis

revealed that the degree of GFAT1 knockout varied by cell line and by clone, and this correlated with differential growth and sensitivity to GlcNAc withdrawal *in vitro* (**Fig. 2-2E,F**). Clones for each cell line without detectable GFAT1 expression **(Fig. 2-1B)** were further validated by sequencing and were subsequently used to examine the role of the HBP without interference from GFAT1 proficient cells.

Using our genomically-sequenced and bona fide GFAT1 knockout clonal lines, we found that GFAT1 knockout led to an abolishment of colony formation **(Fig. 2-1C)** and potently impaired proliferation **(Fig. 2-1D, Fig. 2-2G**) in all three PDA cell lines in vitro. We then moved these cells into *in vivo* tumor models. Surprisingly, when either the pooled or the clonal knockout lines were implanted into the flanks of immunocompromised mice, they readily formed tumors that were comparable to their wild type counterparts in terms of weight and volume (**Fig. 2-1E,F** and **Fig. 2-2H**). Similar results were obtained for GFAT1 knockout clonal lines implanted orthotopically into the pancreas (**Fig. 2-1G**). Of note, while clearly capable of forming tumors, the GFAT1 knockout clonal lines grown in the pancreas were smaller than the wild type tumors at endpoint. The marked discrepancy in phenotype between *in vitro* and *in vivo* settings led us to hypothesize that GFAT1 knockout clones were scavenging nutrients from the TME to refill the HBP, which enabled their survival and tumor growth.

2.2.2 Conditioned media rescues proliferation of GFAT1 knockout PDA cells

To test our scavenging hypothesis, we generated conditioned media (CM) from CAFs, the most abundant stromal cell type in the pancreatic TME(30, 31). When GFAT1 knockout clones were incubated in patient-derived CAF CM, we observed a significant, albeit modest, rescue in colony formation (**Fig. 2-3A,B**). Unexpectedly, we observed a

more robust, dose-dependent rescue of colony formation in GFAT1 knockout cells with CM from wild type TU8988T cells (**Fig. 2-3C-F** and **Fig. 2-4A**). Similarly, CM from wild type HPAC and MiaPaCa2 cells was able to partially rescue proliferation of a subset of GFAT1 knockout clones (**Fig. 2-3G** and **Fig. 2-4B,C**).

To begin to identify the rescue factors in the CM, we subjected the CM to boiling or repeated cycles of freezing and thawing (F/T). In each of these conditions, both the CAF and the PDA CM retained the ability to support colony formation in GFAT1 knockout cells (**Fig. 2-3A-D**). These results suggested the relevant factor(s) did not require tertiary structure. Additionally, we observed that the rescue activity of the CM was dose dependent (**Fig. 2-3E-G** and **Fig. 2-4A-C**).

As GlcNAc was used to establish our GFAT1 knockout lines, we first quantitated the GlcNAc concentration in the CM by mass spectrometry. GlcNAc dose response curves demonstrated that millimolar quantities of GlcNAc (>0.625mM) were required to rescue colony formation of GFAT1 knockout PDA cells (**Fig. 2-3H** and **Fig. 2-4D**). By contrast, LC-MS/MS quantification of GlcNAc in the CM revealed that it was in the low micromolar range (**Fig. 2-3I**), several orders of magnitude below the millimolar doses of exogenous GlcNAc required to maintain proliferation (**Fig. 2-3H** and **Fig. 2-4D**). These results illustrated that free GlcNAc was not the relevant molecule in the CM mediating rescue. This led us to consider alternate possibilities, including GlcNAc-containing components of the TME.

2.2.3 Hyaluronic acid rescues GFAT1 knockout PDA cells

GlcNAc is a widely utilized molecule as a structural component of the extracellular matrix, a modification of various lipid species, and a post-translational

modification on proteins(32, 33). Thus, we hypothesized that GlcNAc was released into CM as a component part of a lipid, protein, or glycosaminoglycan polymer, and that this mediated rescue of *GFAT1* knockout. To test this, we first applied necrotic cellular debris from the murine hematopoietic FL5.12 cell line(34) to GFAT1 knockout cells grown at clonal density. The necrotic cellular debris contains the full complement of biomolecules, including GlcNAc-containing proteins and lipids. Necrotic cell debris was unable to rescue GFAT1 knockout across our cell line panel (**Fig. 2-6A-F**). Next, we tested if glycosaminoglycan carbohydrate polymers could mediate rescue of GFAT1 knockout, in a matter akin to CM. High dose heparin was not able to rescue colony formation in GFAT1 knockout cells (**Fig. 2-6A-F**). In contrast, 78 kDa HA provided a modest but significant rescue (**Fig. 2-5A,B**).

HA is a carbohydrate polymer and an extracellular matrix component that is abundant in the PDA tumor microenvironment(24). The monomeric form of HA is a repeating disaccharide consisting of glucuronic acid and GlcNAc. HA polymer length, often described by its molecular weight (MW), has important impacts on its biological activity. In non-pathological settings, newly synthesized HA is predominantly high molecular weight (HMW; >1000kDa)(35). However, in tumors and tumor interstitial fluid, there is a significantly elevated level of low molecular weight (LMW; 10-250kDa) and oligo-HA (o-HA; <10kDa)(36, 37). Consistent with the rescue of colony formation in GFAT1 knockout cells, LMW HA (78 kDa) was also able to rescue total proteome O-GlcNAc levels, as assessed by western blot (**Fig. 2-5C-E**).

Cancer cells have been reported to uptake HA via macropinocytosis(38). Thus, a possible explanation for the modest rescue could be low macropinocytosis activity.

However, in PDA, mutant Kras drives macropinocytosis(14), and quantitation of macropinocytotic activity with a fluorescent dextran-based assay revealed that our three PDA cell lines exhibited considerable macropinocytosis (**Fig. 2-6G**). Similarly, following HA uptake using a fluorescently-conjugated HA (HA-FITC) revealed GFAT1 proficient and GFAT1 knockout cells readily take up HA (**Fig. 2-5F, Fig. 2-6H**).

This led us to hypothesize that the rate limiting step is not HA entry into cells, but rather, the cleavage of HA into smaller fragments. Consistent with this hypothesis, utilizing hyaluronidase to break down LMW HA enhanced the rescue of colony formation (**Fig. 2-5G**). Of note, hyaluronidase was heat-inactivated after it was used to cleave HA (i.e. before its application to GFAT1 knockout cells; **Fig. 2-6I**), as hyaluronidase has been reported to directly impact cellular metabolism(39). Next, we tracked the rescue of proliferation using HA of varying size: LMW HA (60kDa) and o-HA (5kDa). This analysis revealed that HA-mediated rescue, as measured through proliferation quantification, was considerably higher for o-HA than for LMW HA, and comparable to PDA CM (**Fig. 2-5H,I and Fig. 2-7A-D**).

To relate these studies back to our CM rescue studies, we employed an enzyme-linked immunosorbent assay (ELISA) to quantitate HA in the PDA and CAF CM (**Fig. 2-7E**). CAF CM contained considerably more HA than PDA CM, consistent with the known role for fibroblasts in the production of HA (**Fig. 2-7F**). However, we found that the lower limit of detection for the ELISA was ~50kDA HA. Indeed, we demonstrated this by digesting 10mM HA, CAF CM, or PDA CM with HAase. Post-digestion, we are unable to detect appreciable levels of HA (**Fig. 2-7F,G**). These results illustrate the CAF

CM produces more high molecular weight HA, which we posit explains its limited rescue of GFAT1 knockout in vitro.

HA is produced by the family of HA synthases (HAS), which can be inhibited in vitro with the tool compound 4-methylumbelliferone (4-MU)(40). To determine if HA is the relevant metabolite in wildtype PDA CM facilitating rescue of GFAT1 knockout, we first treated wildtype PDA cells with a range of 4-MU doses. Cell proliferation was followed to assess off-target toxicity and HA in CM was quantitated using the HA ELISA. Of note, while PDA cells produce much less detectable HA than CAFs, they do produce a sufficient amount so as to analyze 4-MU activity (**Fig. 2-7F**). Indeed, we demonstrated that 4-MU dose dependently blocked HA release into CM (**Fig. 2-8A**) while also exhibiting proliferative defects at the highest concentration tested (**Fig. 2-8B-D**). Application of CM from 4-MU-treated wildtype PDA cells in GFAT1 rescue assays revealed that the reduction in HA content paralleled the decrease in CM rescue activity in GFAT1 knockout cells (**Fig. 2-8E**). These collective in vitro studies illustrate that HA can rescue the proliferation of GFAT1 knockout cells and strongly suggest that HA is the relevant factor mediating the rescue activity of PDA CM. However, while we believe these collective results are convincing, detection and quantitation of o-HA in PDA CM will be required to draw a definitive conclusion.

To relate this work back to our tumor studies (**Fig. 2-1E-G**), we probed for HA content in tumor slices by immunohistochemical detection of HA binding protein (HABP) (41). We stained normal pancreas as the negative control (note: positive staining of vasculature) and a murine pancreatic tumor as a positive control (**Fig. 2-8F**). We then stained 10 tumor slices from GFAT1 proficient and deficient tumors from the

subcutaneous and the orthotopic models. Blinded scoring using a 0-3 scale (**Fig. 2-8G**) revealed more HA in the subcutaneous than orthotopic setting (**Fig. 2-8H**). Tumor genotype did not influence HABP levels in the subcutaneous model, whereas there was a marked reduction in HABP staining in the orthotopic GFAT1 knockout tumors (**Fig. 2-8H**). First, these data demonstrate that HA is available to PDA tumors in these models. Further, they suggest that the difference in growth of GFAT1 knockout tumors in the orthotopic model compared to subcutaneous, as observed in Fig.1-1E-G, may result from less HA availability.

2.2.4 Hyaluronic acid rescues GFAT1 null PDA via the GlcNAc salvage pathway

The GlcNAc salvage pathway bypasses GFAT1 by catalyzing the phosphorylation of GlcNAc to GlcNAc-6-phsophate, in a reaction mediated by N-acetyl-glucosamine kinase (NAGK). This GlcNAc-6-phosphate is subsequently converted into UDP-GlcNAc (**Fig. 2-1A**). Therefore, we hypothesized that the carbohydrate polymer HA, which is 50% GlcNAc, fuels the HBP via the GlcNAc salvage pathway through NAGK. To test this, we employed the same CRISPR/Cas9 strategy to target NAGK (**Fig. 2-9A**). Knockout of NAGK in parental TU8988T and MiaPaCa2 cell lines had no impact on colony formation, while reducing the colony forming capacity of HPAC cells (**Fig. 2-9B,C**). These results correlated with the elevated expression of NAGK in wild type HPAC cells (**Fig. 2-9D**). Of note, NAGK knockout did not result in up-regulation of GFAT1 (**Fig. 2-9A**), which could have suggested a compensatory metabolic rewiring. Next, we targeted NAGK in our GFAT1 knockout clones. GFAT1/NAGK double knockout cells were generated in media containing N-acetyl-galactosamine (GalNAc), an isomer of GlcNAc. Supplementation with GalNAc enables bypass of both the *de*

novo HBP and the GlcNAc salvage pathway, by way of the Leloir pathway(42), to support UDP-GalNAc and ultimately UDP-GlcNAc biogenesis (**Fig. 2-9E**). In this way, we were again able to select viable lines while avoiding the selection of those with unpredictable metabolic adaptations.

The GalNAc dose response for GFAT1 knockout clones was comparable to that of GlcNAc (**Fig. 2-3H**), demonstrating that they are indeed viable in GalNAc (**Fig. 2-9F, Fig. 2-10H**). Although NAGK expression was efficiently knocked down in our pooled populations (**Fig. 2-9G**), we again selected for clones in the TU8988T cell line in order to minimize the effect of NAGK-proficient clones persisting in the bulk population. From among these, we selected four GFAT1/NAGK clones and tracked their proliferation upon rescue with varying sizes of HA, GalNAc, or PDA CM. These were compared relative to wild type TU8988T cells and the GFAT1 knockout line. In stark contrast to the GFAT1 knockout line, LMW HA, o-HA and PDA CM was unable to rescue GFAT1/NAGK double knockout lines (**Fig. 2-9H-K, Fig. 2-10A-F**). Similar results were obtained in the MiaPaCa2 cell line (**Fig. 2-10G-J**).

Finally, we used LC/MS-MS to assess HBP metabolite levels and western blotting to follow proteome O-GlcNAcylation in the GFAT1 and GFAT1/NAGK double knockout cells. HA or PDA CM rescue of GFAT1 knockout cells restores UDP-GlcNAc pools and proteome O-GlcNAcylation, and this was blocked by knocking out NAGK (**Fig. 2-9L,M and Fig. 2-10K-N**). These results illustrate that HA rescue requires NAGK and the GlcNAc salvage pathway, consistent with the idea that HA-derived GlcNAc fuels UDP-GlcNAc biosynthesis upon GFAT1 knockout. Altogether, our data implicate HA as

a novel nutrient for PDA, where HA regulates PDA metabolism by refueling the HBP via the GlcNAc salvage pathway. This supports PDA survival and proliferation (**Fig. 2-9N**).

2.3 Discussion

The HBP is activated in a KRAS*-dependent manner in PDA via transcriptional regulation of *Gfpt1*(6), and it is similarly elevated in numerous cancers to provide a diverse set of functions, including the regulation of proliferation, survival, angiogenesis, and metastasis(10). As such, we and others have proposed that the HBP may provide a selective vulnerability for cancer therapy, with GFAT1 as an attractive therapeutic target(6, 11, 43, 44). Of note, GFAT2 is a homolog of GFAT1, and it too has been implicated as a drug target with context and tissue-specific functions(45, 46). We did not pursue GFAT2 in this study because it was neither regulated by KRAS* nor basally expressed in the models employed herein.

Several pan glutamine-deamidase inhibitors (e.g. azaserine and 6-diazo-5-oxo-L-norleucine), which potently suppress GFAT activity, have demonstrated anti-tumor activity *in vitro* and *in vivo* in PDA and other cancers(47, 48). However, because these drugs are not specific to the HBP, it has not been clear what impact GFAT-specific inhibition had on these phenotypes. As such, we took a genetic approach to knock out GFAT1 to elucidate the role of the HBP in PDA. In the PDA models tested, we found that GFAT1 knockout was not compatible with PDA cell proliferation *in vitro,* unless the media were supplemented with GlcNAc or GalNAc (**Fig. 2-1C,D** and **Fig. 2-9F**). However, these same cells readily formed tumors *in vivo* in subcutaneous and orthotopic models (**Fig. 2-1E-G**).

The stark discrepancy in phenotypes led us to hypothesize that the TME was providing the means to bypass GFAT1. Indeed, we found that denatured conditioned media from CAFs and wild type PDA cells were able to rescue viability in GFAT1 knockout PDA cells, implicating a molecule(s) without tertiary structure (**Fig. 2-3**). By examining several GlcNAc-containing candidates, we discovered a previously unknown role of HA as a nutrient source for PDA (**Fig. 2-5,8**). Of note, despite identifying that wild type PDA cells can produce HA, it is not our intention to indicate that HA in PDA tumors was deposited by the cancer cells. For example, HA is abundantly deposited in GFAT1 knockout subcutaneous PDA tumors (**Fig. 2-8H**). Rather, we found that wild type PDA CM could rescue the proliferation of GFAT1 knockout PDA cells in vitro, and we utilized this as a tool to study the process. The constellation of cell types in the pancreatic TME that produce/deposit/process HA is an area of active investigation. Either way, in sum we report that HA can refill the HBP via the GlcNAc salvage pathway to support PDA survival and proliferation.

HA is traditionally regarded as a structural component in physiology(49). In addition to this role, a wealth of studies have ascribed other functions to HA. For example, HA can activate cell-cell contact-mediated signal transduction through CD44 and/or receptor for HA-mediated motility (RHAMM)(50). The signaling activity/function of HA depends on its MW(49, 51). Similarly, a recent study illustrated that breakdown of the HA matrix with hyaluronidase enabled the interaction between growth factors and growth factor receptors(39). This promoted glucose metabolism, cellular proliferation, and migration. The role of HA in GFAT1 knockout PDA cells described herein is likely independent of its structural and signaling functions, given that we observe considerably

greater rescue with o-HA (**Fig. 2-5H,I**), a form of HA that is not traditionally considered for these purposes. Together with the increased rescue by o-HA, several additional experiments also suggested that intracellular catabolism of high molecular weight HA impedes its use as a fuel. Namely, while high molecular weight HA-FITC is readily captured by PDA cells (**Fig. 2-5F**), HAase catabolism of HA potentiates rescue of GFAT1 (**Fig. 2-5G**).

Our study introduces a novel role to HA as a fuel for PDA tumor growth (**Fig. 2-5H,I**), further highlighting the significance and biological complexity of this predominant glycosaminoglycan. Additionally, our study suggests that NAGK, through which HA-mediated GlcNAc presumably refuels the HBP in vivo, may be an attractive therapeutic target for PDA. Indeed, a recent study demonstrated that NAGK knockout in PDA impairs tumor growth in vivo, while only exhibiting a modest impact on cellular proliferation in vitro(52). These results are consistent with our observations that the GlcNAc salvage pathway is used to fill UDP-GlcNAc pools with HA-derived GlcNAc (**Fig. 2-9N**). Our study also contributes to a growing body of data illuminating unexpected nutrient sources in the TME that support cancer metabolism(14, 15, 17-22, 53), and this raises the possibility that other glycosaminoglycans may be similarly scavenged.

Due to its extremely hydrophilic nature, HA retains water and acts as a cushioning agent in tissue homeostasis and biomechanical integrity(49). In PDA, HA is a predominant component of the TME, and its water-retaining property is one of the main drivers of the supraphysiological intratumoral pressure(54). This pressure can exceed 10-fold that observed in the normal pancreas, and, as a result, tumor vasculature

collapses (41, 55, 56). The limited access to circulation impairs nutrient and oxygen delivery, and it has been proposed that this is a critical impediment to tumoral drug delivery(57). Indeed, in animal models, breakdown of the HA matrix with a therapeutic hyaluronidase (PEGPH20) reduces intratumoral pressure, restores circulation, which facilitates drug delivery, and thereby improves response to chemotherapy(41, 56). Based on these promising observations, PEGPH20 was tested in clinical trials alongside standard of care chemotherapy. Despite the successes in the preclinical models, PEGPH20 did not extend PDA patient survival(58).

The discrepancy between the clinical response to PEGPH20 and the preclinical data remains an active area of investigation and may concern the myriad additional roles of HA. For example, the HA matrix may be necessary to restrain tumor dissemination, as was shown for CAF depletion studies in PDA(59-62). Thus, the benefits afforded by enhanced drug penetration facilitated by PEGPH20 may be negated by this side effect. Along these lines, HA degradation may also enhance tumor metabolism and growth. This could occur through growth factor signaling-dependent(39) as well as signaling-independent pathways, like the GlcNAc salvage pathway described herein. In contrast, reduction in the HA content of tumors also facilitates T cell invasion(48), which may complement immunotherapy approaches, a concept that would be hindered by immunosuppressive chemotherapies. Given the conflicting roles of HA in tumor restraint and tumor growth, considerable work remains to be done to determine the most effective way to exploit this feature of pancreatic cancer.

2.4 Materials and Methods

Cell Culture

MiaPaCa2 (ATCC Cat# CRM-CRL-1420, RRID:CVCL_0428) and HPAC (ATCC Cat# CRL-2119, RRID:CVCL_3517) were obtained from ATCC. TU8988T (DSMZ Cat# ACC-162, RRID:CVCL_1847) was obtained from DSMZ. Patient-derived CAFs(63) were a generous gift from Rosa Hwang, and FL5.12 cells were a generous gift from Dr. Aimee Edinger. All cells were routinely checked for mycoplasma contamination with MycoAlert PLUS (Lonza) and validated for authenticity annually by STR profiling. Cells were maintained in standard high glucose DMEM without pyruvate (Gibco) supplemented with 10% fetal bovine serum (FBS; Corning). GFAT1 null PDA were cultured in standard media supplemented with 10mM GlcNAc (Sigma). GFAT1 null NAGK knockout PDA were cultured in standard media supplemented with 10mM GalNAc (Sigma). Low nutrient media was made with DMEM without glucose, glutamine and pyruvate (Gibco). Glucose, glutamine, and FBS were added to the final concentration of 1.25mM, 0.2mM and 1%, respectively. FL5.12 cells were maintained in RPMI 1640 (Gibco) supplemented with 10% FBS, 10mM HEPES (Sigma), 55μM β-mercaptoethanol (Sigma), antibiotics, 2mM glutamine, and 500 pg/mL recombinant murine IL-3 (Peprotech 213-13).

Generation of CRISPR/Cas9 knockout clones

GFAT1 and NAGK knockout PDA cell lines were generated using CRISPR/Cas9 method described previously (22). Overlapping oligonucleotides (Feng Zhang lab human GeCKOv2 CRISPR knockout pooled library; Addgene #1000000048) were annealed to generate sgRNA targeting GFAT1 or NAGK. sgRNA was cloned directly

into the overhangs of PX459 V2.0 vector (Feng Zhang lab; Addgene plasmid #62988) that was digested with BbsI. The resulting CRISPR/Cas9 plasmid was transformed into chemically competent Stbl3 cells, miniprepped for plasmid DNA, and sequence-verified. sgRNA oligonucleotide pairs for GFAT1(11) and NAGK are as follows: GFAT1 (sg1 Fwd 5′-CACCgCTTCAGAGACTGGAGTACAG-3′; sg1 Rev 5′-AAACCTGTACTCCAGTCTCTGAAGc-3′) and NAGK (sg1 Fwd 5'-CACCgTAGGGGAGGCACACGATCCG; sg1 Rev 5'-AAACCGGATCGTGTGCCTCCCCTAc-3'; sg2 Fwd 5'-CACCgGCCTAGGGCCTATCTCTGAG-3'; sg2 Rev 5'-AAACCTCAGAGATAGGCCCTAGGCc-3'). Human PDA were transiently transfected using Lipofectamine 3000 according to the manufacturer's instructions. Cells were selected with puromycin in the presence of GlcNAc (GFAT1 knockout bulk population) or GalNAc (GFAT1 NAGK double knockout bulk population). To select clones, polyclonal pools were seeded into 96-well plates at a density of 1 cell per well. Individual clones were expanded and verified via western blot and Sanger sequencing. TU8988T clone B9 has a 10 base pair (bp) and a 1bp deletion in GFAT1; TU8988T clone D10 has 2 different 1bp deletions in GFAT1; MiaPaCa2 clone M12 has 2 different 1bp deletions in GFAT1; HPAC clone H1 has a 187bp deletion in GFAT1; HPAC clone H7 has a 187bp deletion in GFAT1.

Conditioned media

Conditioned media was generated by culturing cells in 15 cm^2 plates (25mL growth media/plate) for 72 hours at 37°C, 5% CO_2, so that they reached ~90% confluence. The media were then filtered through a 0.45μm polyethersulfone membrane (VWR). Boiled

conditioned media was warmed to 100°C for 15 minutes. Freeze-thaw conditioned media were initially stored at -80°C and were thawed in a 37°C water bath on the day of the experiment. As indicated, fresh growth media were added to the conditioned media at the ratios indicated to avoid nutrient/metabolite exhaustion.

Colony formation and proliferation assays

For colony formation assays, cells were plated in a 6-well plate in biological triplicate at 500 cells/well in 2 mL of media and grown for 9-12 days. For proliferation assays, 5000 cells/well were plated. At end point, assays were fixed with 100% methanol for 10 minutes and stained with 0.5% crystal violet solution for 15 minutes. Relative colony formation was quantitated manually in a blinded fashion. Proliferation was quantified by removing the dye with 10% acetic acid and measuring OD595.

CyQUANT viability assay

Cells were seeded in 96-well black wall, clear bottom plates at 1000 cells/well in 50µL of media and incubated at 37°C, 5% CO_2 for indicated time points. At each time point, media was aspirated and plates were stored at -80°C. Proliferation was determined by CyQUANT (Invitrogen) according to the manufacturer's instructions. SpectraMax M3 Microplate reader (Molecular Devices) was used to measure fluorescence.

IncuCyte S3: Real-time, live-cell proliferation assay

1000 cells were seeded per well in a 96-well plate and incubated at 37°C, 5% CO_2 for cells to equilibrate. The next day, media were aspirated, washed once with PBS, and replaced with different media as indicated. Proliferation was measured on IncuCyte S3 using phase object confluence as a readout.

HA-FITC Uptake Experiments

TU8988T cells (WT, B9-GFAT1KO, D10-GFAT1KO), and BxPC3 cells were seeded in 6-well plates with DMEM + 10% FBS + GlcNAc. The next day, cells were rinsed with PBS and the media was switched to DMEM + 10% FBS. The following day, cells were seeded on a chamber slide and grown in DMEM + 10% FBS. MiaPaCa2 cells (WT, M12-GFAT1KO) were treated similarly and were seeded in 6-well plates with DMEM + 10% FBS + GlcNAc. The next day, cells were rinsed with PBS and seeded on a chamber slide in DMEM + 10% FBS.

After one day in chamber slides, the media was removed, cells were rinsed with PBS, and cells were incubated with HA-FITC media for one hour at 37°C (or 1 min at 37°C as a negative control). After incubation, cells were rinsed and fixed with 10% formalin for 15 minutes at room temp. Wells were rinsed three times with PBS + 0.3% BSA and cells were blocked for one hour at room temperature with PBS + 1% BSA. Cells were incubated overnight at 4°C with Mouse anti-panCK (Cytokeratin, DAKO M3515, [1:100]) in PBS + 1% BSA. The following day, cells were rinsed three times with PBS + 0.3% BSA and incubated 1 hour at room temperature with an anti-mouse Alexa fluor secondary antibody (Invitrogen) in PBS + 1% BSA. Following incubation, cells were rinsed and mounted with ProLong Gold Antifade Mountant with DAPI (Invitrogen). Olympus BX53F microscope, Olympus DP80 digital camera, and CellSens Standard software were used for imaging and 6 representative images were taken per cell line and condition. Uptake index was calculated using the Analyze Particles feature in ImageJ after automatic thresholding. The cell outlines and regions of interest were

determined using panCK expression and HA-FITC particles were measured. HA-FITC particle area was plotted as a percent of total cell area.

HA ELISA

An HA ELISA kit (cat no. DY3614, R&D Systems) was used to determine the concentration of HA in all the different conditioned media samples as per manufacturer's instructions.

Metabolite sample preparation

Intracellular metabolite fractions were prepared from cells grown in 6-well plates. The media was aspirated, and cells were incubated with cold (−80°C) 80% methanol (1mL/well) on dry ice for 10 minutes. Then, the wells were scraped with a cell scraper and transferred to 1.5mL tubes on dry ice. To measure GlcNAc concentration in different conditioned media, 0.8mL of ice-cold 100% methanol was added to 0.2mL of conditioned media, and the mixture was incubated on dry ice for 10 minutes.
After incubation of cell or media fractions on dry ice, the tubes were centrifuged at 15,000rpm for 10 minutes at 4°C to pellet the insoluble material, and the supernatant was collected in a fresh 1.5mL tube. Metabolite levels of intercellular fractions were normalized to the protein content of a parallel sample, and all samples were lyophilized on a SpeedVac, and re-suspended in a 50:50 mixture of methanol and water in HPLC vials for LC-MS/MS analysis.

Liquid chromatography-coupled mass spectrometry

To detect UDP-GlcNAc, the Shimadzu NEXERA integrated UHPLC system with a LC30AD pump, SIL30AC autosampler, CTO30A column oven, CBM20A controller was

coupled with the AB Sciex TripleTOF 5600 MS system with DuoSpray ion source. All calibrations and operations were under control of Analyst TF 1.7.1. Calibrations of TOF-MS and TOF-MS/MS were achieved through reference APCI source of SCEIX calibration solution. A high throughput LC method of 8 min with flowrate of 0.4 ml/min with a Supelco Ascentis Express HILIC (75 mm X 3.0 mm, 2.7 µm). Solvent A was made of 20 mM ammonium acetate of 95% water and 5% acetonitrile at pH 9.0. Solvent B was 95% acetonitrile and 5% water. LC gradient 0.0-0.5 min 90% B, 3 min 50% B, 4.10 min 1% B, 5.5 min 1% B, 5.6 min 90% B, 6.5 min 90% B, 8 min stopping. Key parameters on the MS were the CE and CE spread of -35ev, 15ev. Data were compared to a reference standard. Data processing was performed by Sciex PeakView, MasterView, LibraryView and MQ software tools and ChemSpider database.

To measure GlcNAc concentration in the various conditioned media, we utilized an Agilent Technologies Triple Quad 6470 LC/MS system consisting of 1290 Infinity II LC Flexible Pump (Quaternary Pump), 1290 Infinity II Multisampler, 1290 Infinity II Multicolumn Thermostat with 6 port valve and 6470 triple quad mass spectrometer. Agilent Masshunter Workstation Software LC/MS Data Acquisition for 6400 Series Triple Quadrupole MS with Version B.08.02 is used for compound optimization and sample data acquisition.

A GlcNAc standard was used to establish parameters, against which conditioned media were analyzed. For LC, an Agilent ZORBAX RRHD Extend-C18, 2.1 × 150 mm, 1.8 um and ZORBAX Extend Fast Guards for UHPLC were used in the separation. LC gradient profile is: at 0.25 ml/min, 0-2.5 min, 100% A; 7.5 min, 80% A and 20% C; 13 min 55% A and 45% C; 20 min, 1% A and 99% C; 24 min, 1% A and 99% C; 24.05 min, 1% A and

99% D; 27 min, 1% A and 99% D; at 0.8 ml/min, 27.5-31.35 min, 1% A and 99% D; at 0.6 ml/min, 31.50 min, 1% A and 99% D; at 0.4 ml/min, 32.25-39.9 min, 100% A; at 0.25 ml/min, 40 min, 100% A. Column temp is kept at 35 ºC, samples are at 4 ºC, injection volume is 2 µl. Solvent A is 97% water and 3% methanol 15 mM acetic acid and 10 mM tributylamine at pH of 5. Solvent C is 15 mM acetic acid and 10 mM tributylamine in methanol. Washing Solvent D is acetonitrile. LC system seal washing solvent 90% water and 10% isopropanol, needle wash solvent 75% methanol, 25% water.

6470 Triple Quad MS is calibrated with ESI-L Low concentration Tuning mix. Source parameters: Gas temp 150 ºC, Gas flow 10 l/min, Nebulizer 45 psi, Sheath gas temp 325 ºC, Sheath gas flow 12 l/min, Capillary -2000 V, Delta EMV -200 V. Dynamic MRM scan type is used with 0.07 min peak width, acquisition time is 24 min. Delta retention time of plus and minus 1 min, fragmentor of 40 eV and cell accelerator of 5 eV are incorporated in the method.

Xenograft studies

Animal experiments were conducted in accordance with the Office of Laboratory Animal Welfare and approved by the Institutional Animal Care and Use Committees of the University of Michigan. NOD-SCID gamma (NSG) mice (Jackson Laboratory), 6-10 weeks old of both sexes, were maintained in the facilities of the Unit for Laboratory Animal Medicine (ULAM) under specific pathogen-free conditions. Protocol#: PRO00008877.

Wild type TU8988T and two verified GFAT1 null clones (B9 and D10) were trypsinized and suspended at 1:1 ratio of DMEM (Gibco, 11965-092) cell suspension to Matrigel (Corning, 354234). 150-200µL were used per injection. Orthotopic tumors were

established by injecting 0.5 x 10^6 cells in 50µL of 1:1 DMEM to Matrigel mixture. The experiment lasted five weeks. For subcutaneous xenograft studies with the pooled populations or validated clones, tumors were established with 5 x 10^6 cells in 200µL of 1:1 DMEM to Matrigel mixture.

Tumor size was measured with digital calipers two times per week. Tumor volume (V) was calculated as V = 1/2(length x width^2). At endpoint, final tumor volume and mass were measured prior to processing. Tissue was snap-frozen in liquid nitrogen then stored at −80°C.

Western blot analysis

After SDS-PAGE, proteins were transferred to PVDF membrane, blocked with 5% milk, and incubated with primary antibody overnight at 4°C. The membranes were washed with TBST, incubated with the appropriate horseradish peroxidase-conjugated secondary antibody for 1hr and visualized on Bio-Rad imager with enhanced chemiluminescence detection system or exposed on radiographic film.

Immunohistochemistry on subcutaneous and orthotopic tumors

Subcutaneous and orthotopic tumors were fixed in Z-fix overnight, paraffin embedded, and sectioned onto slides. Sections were deparaffinized in xylene, rehydrated, and blocked with 2.5% BSA prior to incubation with biotinylated HABP antibody (Calbiochem #385911, [1:200]) overnight at 4°C. Vector Laboratories Vectastain Elite ABC-HRP Kit (PK-6100) and Vector Laboratories DAB Substrate Kit (SK-4100) were used for peroxidase detection of HABP signal.

Histological Scoring

HABP-stained tumors, normal pancreas tissue (negative control), and transformed pancreas tissue from KC mice (positive control) were processed and stained for HABP as described above. Ten representative 20x images from each group were scored blinded based on HABP staining. Staining was scored on the following scale: 0, no staining; 1, minimal staining; 2, moderate to strong staining in at least 20% of cells; 3, strong staining in at least 50% of cells.

Antibodies

The following antibodies were used in this study: VINCULIN (Cell Signaling 13901), ACTIN (Santa Cruz sc-47778), GAPDH (Cell Signaling 5174), GFAT1 (Abcam 125069), NAGK (Atlas Antibodies HPA035207), O-GlcNAc (Abcam 2735), panCK (Cytokeratin, DAKO M3515), biotinylated HABP (Calbiochem 385911), secondary anti-mouse-HRP (Cell Signaling 7076), and secondary anti-rabbit-HRP (Cell Signaling 7074).

Detection and quantification of macropinocytosis

The macropinocytosis index was measured as previously described(64). In brief, cells were seeded on the coverslips in 24-well plate for 24 hours and serum-starved for 18 h. Cells were incubated with 1mg/ml high molecular weight TMR–dextran (Fina Biosolutions) in serum-free medium for 30 min at 37 °C. Cells were then washed 5 times with cold DPBS and fixed in 4% polyformaldehyde for 15 min. The coverslips were mounted onto slides using DAKO Mounting Medium (DAKO) in which nuclei were stained with DAPI. At least six images were captured for each sample using an Olympus FV1000 confocal microscope and analyzed using the particle analysis feature

in ImageJ (NIH). The micropinocytosis index for each field was calculated as follow: Macropinocytosis Index = (total particle area/total cell area) × 100%.

Hyaluronic acid, hyaluronidase, and heparin

Heparin was obtained from Sigma (H3393). Oligo HA (5kDa) was obtained from Lifecore Biomedical. Two different LMW HA were used in this study: 78 kDa HA (Pure Health solutions) and 60kDa HA (Lifecore Biomedical). To make 10mM oligo- or LMW HA media, HA was added slowly into high glucose DMEM without pyruvate, stirred for two hours at room temperature, and filtered through 0.20μm polyethersulfone membrane. FBS was added to a final concentration of 10%.

Hyaluronidase (Sigma H3506) treatment was performed as follows: 10mM LMW HA media and control media (DMEM + 10% FBS) were incubated with hyaluronidase, according to manufacturer's instructions, overnight in a 37°C water bath. The next day, media were boiled for 15 minutes to denature hyaluronidase. The resulting media were mixed 1:1 with fresh growth media to avoid effects of nutrient/metabolite exhaustion.

Preparation of necrotic FL5.12 cells

Necrotic FL5.12 cells were prepared as described previously(34). Cells were washed three times with PBS, cultured in the FL5.12 media without IL-3 (100 million cells/mL) for 72 hours. The necrotic cells were spun down at 13,000 rpm for 10 minutes at 4°C, and the pellets were stored at -80°C until use.

Statistical analysis

Statistics were performed using GraphPad Prism 8. Groups of two were analyzed with two-tailed students t test. Groups of more than two were analyzed with one-way ANOVA

Tukey post-hoc test. All error bars represent mean with standard deviation. A *P* value of less than 0.05 was considered statistically significant. All group numbers and explanation of significant values are presented within the figure legends.

2.5 References

1. Siegel RL, Miller KD, Jemal A. Cancer statistics, 2020. CA: A Cancer Journal for Clinicians. 2020;70(1):7-30. doi: 10.3322/caac.21590.

2. Halbrook CJ, Lyssiotis CA. Employing Metabolism to Improve the Diagnosis and Treatment of Pancreatic Cancer. Cancer Cell. 2017;31(1):5-19. doi: 10.1016/j.ccell.2016.12.006. PubMed PMID: 28073003.

3. Perera RM, Bardeesy N. Pancreatic Cancer Metabolism: Breaking It Down to Build It Back Up. Cancer Discov. 2015;5(12):1247-61. doi: 10.1158/2159-8290.CD-15-0671. PubMed PMID: 26534901; PMCID: PMC4687899.

4. Ying H, Dey P, Yao W, Kimmelman AC, Draetta GF, Maitra A, DePinho RA. Genetics and biology of pancreatic ductal adenocarcinoma. Genes Dev. 2016;30(4):355-85. doi: 10.1101/gad.275776.115. PubMed PMID: 26883357; PMCID: PMC4762423.

5. Kerk SA, Papagiannakopoulos T, Shah YM, Lyssiotis CA. Metabolic networks in mutant KRAS-driven tumours: tissue specificities and the microenvironment. Nat Rev Cancer. 2021;21(8):510-25. Epub 2021/07/11. doi: 10.1038/s41568-021-00375-9. PubMed PMID: 34244683.

6. Ying H, Kimmelman AC, Lyssiotis CA, Hua S, Chu GC, Fletcher-Sananikone E, Locasale JW, Son J, Zhang H, Coloff JL, Yan H, Wang W, Chen S, Viale A, Zheng H, Paik JH, Lim C, Guimaraes AR, Martin ES, Chang J, Hezel AF, Perry SR, Hu J, Gan B, Xiao Y, Asara JM, Weissleder R, Wang YA, Chin L, Cantley LC, DePinho RA. Oncogenic Kras maintains pancreatic tumors through regulation of anabolic glucose metabolism. Cell. 2012;149(3):656-70. doi: 10.1016/j.cell.2012.01.058. PubMed PMID: 22541435; PMCID: PMC3472002.

7. Akella NM, Ciraku L, Reginato MJ. Fueling the fire: emerging role of the hexosamine biosynthetic pathway in cancer. BMC Biol. 2019;17(1):52-. doi: 10.1186/s12915-019-0671-3. PubMed PMID: 31272438.

8. Wellen KE, Lu C, Mancuso A, Lemons JMS, Ryczko M, Dennis JW, Rabinowitz JD, Coller HA, Thompson CB. The hexosamine biosynthetic pathway couples growth factor-induced glutamine uptake to glucose metabolism. Genes Dev. 2010;24(24):2784-99. Epub 2010/11/24. doi: 10.1101/gad.1985910. PubMed PMID: 21106670.

9. Paszek MJ, DuFort CC, Rossier O, Bainer R, Mouw JK, Godula K, Hudak JE, Lakins JN, Wijekoon AC, Cassereau L, Rubashkin MG, Magbanua MJ, Thorn KS, Davidson MW, Rugo HS, Park JW, Hammer DA, Giannone G, Bertozzi CR, Weaver VM. The cancer glycocalyx mechanically primes integrin-mediated growth and survival. Nature. 2014;511(7509):319-25. doi: 10.1038/nature13535. PubMed PMID: 25030168; PMCID: PMC4487551.

10. Akella NM, Ciraku L, Reginato MJ. Fueling the fire: emerging role of the hexosamine biosynthetic pathway in cancer. BMC Biol. 2019;17(1):52. doi: 10.1186/s12915-019-0671-3. PubMed PMID: 31272438; PMCID: PMC6610925.

11. Walter LA, Lin YH, Halbrook CJ, Chuh KN, He L, Pedowitz NJ, Batt AR, Brennan CK, Stiles BL, Lyssiotis CA, Pratt MR. Inhibiting the Hexosamine Biosynthetic Pathway Lowers O-GlcNAcylation Levels and Sensitizes Cancer to Environmental Stress. Biochemistry. 2019. doi: 10.1021/acs.biochem.9b00560. PubMed PMID: 31625393; PMCID: PMC7231633.

12. Yang C, Peng P, Li L, Shao M, Zhao J, Wang L, Duan F, Song S, Wu H, Zhang J, Zhao R, Jia D, Zhang M, Wu W, Li C, Rong Y, Zhang L, Ruan Y, Gu J. High expression of GFAT1 predicts poor prognosis in patients with pancreatic cancer. Sci Rep. 2016;6:39044. doi: 10.1038/srep39044. PubMed PMID: 27996048; PMCID: PMC5172351.

13. Lee HH, Wang YN, Xia W, Chen CH, Rau KM, Ye L, Wei Y, Chou CK, Wang SC, Yan M, Tu CY, Hsia TC, Chiang SF, Chao KSC, Wistuba, II, Hsu JL, Hortobagyi GN, Hung MC. Removal of N-Linked Glycosylation Enhances PD-L1 Detection and Predicts Anti-PD-1/PD-L1 Therapeutic Efficacy. Cancer Cell. 2019;36(2):168-78 e4. doi: 10.1016/j.ccell.2019.06.008. PubMed PMID: 31327656; PMCID: PMC6793936.

14. Commisso C, Davidson SM, Soydaner-Azeloglu RG, Parker SJ, Kamphorst JJ, Hackett S, Grabocka E, Nofal M, Drebin JA, Thompson CB, Rabinowitz JD, Metallo CM, Vander Heiden MG, Bar-Sagi D. Macropinocytosis of protein is an amino acid supply route in Ras-transformed cells. Nature. 2013;497(7451):633-7. doi: 10.1038/nature12138. PubMed PMID: 23665962; PMCID: PMC3810415.

15. Kamphorst JJ, Nofal M, Commisso C, Hackett SR, Lu W, Grabocka E, Vander Heiden MG, Miller G, Drebin JA, Bar-Sagi D, Thompson CB, Rabinowitz JD. Human pancreatic cancer tumors are nutrient poor and tumor cells actively scavenge extracellular protein. Cancer Res. 2015;75(3):544-53. Epub 2015/02/04. doi: 10.1158/0008-5472.CAN-14-2211. PubMed PMID: 25644265; PMCID: PMC4316379.

16. Yang S, Wang X, Contino G, Liesa M, Sahin E, Ying H, Bause A, Li Y, Stommel JM, Dell'antonio G, Mautner J, Tonon G, Haigis M, Shirihai OS, Doglioni C, Bardeesy N, Kimmelman AC. Pancreatic cancers require autophagy for tumor growth. Genes Dev. 2011;25(7):717-29. doi: 10.1101/gad.2016111. PubMed PMID: 21406549; PMCID: PMC3070934.

17. Davidson SM, Jonas O, Keibler MA, Hou HW, Luengo A, Mayers JR, Wyckoff J, Del Rosario AM, Whitman M, Chin CR, Condon KJ, Lammers A, Kellersberger KA, Stall BK, Stephanopoulos G, Bar-Sagi D, Han J, Rabinowitz JD, Cima MJ, Langer R, Vander Heiden MG. Direct evidence for cancer-cell-autonomous extracellular protein catabolism in pancreatic tumors. Nat Med. 2017;23(2):235-41. doi: 10.1038/nm.4256. PubMed PMID: 28024083; PMCID: PMC5407288.

18. Olivares O, Mayers JR, Gouirand V, Torrence ME, Gicquel T, Borge L, Lac S, Roques J, Lavaut MN, Berthezène P, Rubis M, Secq V, Garcia S, Moutardier V, Lombardo D, Iovanna JL, Tomasini R, Guillaumond F, Vander Heiden MG, Vasseur S. Collagen-derived proline promotes pancreatic ductal adenocarcinoma cell survival under nutrient limited conditions. Nat Commun. 2017;8:16031. Epub 2017/07/08. doi: 10.1038/ncomms16031. PubMed PMID: 28685754; PMCID: PMC5504351 remaining authors declare no competing financial interests.

19. Sousa CM, Biancur DE, Wang X, Halbrook CJ, Sherman MH, Zhang L, Kremer D, Hwang RF, Witkiewicz AK, Ying H, Asara JM, Evans RM, Cantley LC, Lyssiotis CA, Kimmelman AC. Pancreatic stellate cells support tumour metabolism through autophagic alanine secretion. Nature. 2016;536(7617):479-83. Epub 2016/08/10. doi: 10.1038/nature19084. PubMed PMID: 27509858.

20. Dalin S, Sullivan MR, Lau AN, Grauman-Boss B, Mueller HS, Kreidl E, Fenoglio S, Luengo A, Lees JA, Vander Heiden MG, Lauffenburger DA, Hemann MT. Deoxycytidine Release from Pancreatic Stellate Cells Promotes Gemcitabine Resistance. Cancer Res. 2019;79(22):5723-33. Epub 2019/09/06. doi: 10.1158/0008-5472.Can-19-0960. PubMed PMID: 31484670; PMCID: PMC7357734.

21. Halbrook CJ, Pontious C, Kovalenko I, Lapienyte L, Dreyer S, Lee HJ, Thurston G, Zhang Y, Lazarus J, Sajjakulnukit P, Hong HS, Kremer DM, Nelson BS, Kemp S, Zhang L, Chang D, Biankin A, Shi J, Frankel TL, Crawford HC, Morton JP, Pasca di Magliano M, Lyssiotis CA. Macrophage-Released Pyrimidines Inhibit Gemcitabine Therapy in Pancreatic Cancer. Cell Metab. 2019;29(6):1390-9 e6. doi: 10.1016/j.cmet.2019.02.001. PubMed PMID: 30827862; PMCID: PMC6602533.

22. Zhu Z, Achreja A, Meurs N, Animasahun O, Owen S, Mittal A, Parikh P, Lo TW, Franco-Barraza J, Shi J, Gunchick V, Sherman MH, Cukierman E, Pickering AM, Maitra A, Sahai V, Morgan MA, Nagrath S, Lawrence TS, Nagrath D. Tumour-reprogrammed stromal BCAT1 fuels branched-chain ketoacid dependency in stromal-rich PDAC tumours. Nat Metab. 2020. doi: 10.1038/s42255-020-0226-5. PubMed PMID: 32694827.

23. Lyssiotis CA, Kimmelman AC. Metabolic Interactions in the Tumor Microenvironment. Trends Cell Biol. 2017;27(11):863-75. Epub 2017/07/25. doi: 10.1016/j.tcb.2017.06.003. PubMed PMID: 28734735; PMCID: PMC5814137.

24. Theocharis AD, Tsara ME, Papageorgacopoulou N, Karavias DD, Theocharis DA. Pancreatic carcinoma is characterized by elevated content of hyaluronan and chondroitin sulfate with altered disaccharide composition. Biochim Biophys Acta.

2000;1502(2):201-6. Epub 2000/10/21. doi: 10.1016/s0925-4439(00)00051-x. PubMed PMID: 11040445.

25. Goossens P, Rodriguez-Vita J, Etzerodt A, Masse M, Rastoin O, Gouirand V, Ulas T, Papantonopoulou O, Van Eck M, Auphan-Anezin N, Bebien M, Verthuy C, Vu Manh TP, Turner M, Dalod M, Schultze JL, Lawrence T. Membrane Cholesterol Efflux Drives Tumor-Associated Macrophage Reprogramming and Tumor Progression. Cell Metab. 2019;29(6):1376-89.e4. Epub 2019/04/02. doi: 10.1016/j.cmet.2019.02.016. PubMed PMID: 30930171.

26. Mahlbacher V, Sewing A, Elsässer HP, Kern HF. Hyaluronan is a secretory product of human pancreatic adenocarcinoma cells. Eur J Cell Biol. 1992;58(1):28-34. Epub 1992/06/01. PubMed PMID: 1644063.

27. Jacobetz MA, Chan DS, Neesse A, Bapiro TE, Cook N, Frese KK, Feig C, Nakagawa T, Caldwell ME, Zecchini HI, Lolkema MP, Jiang P, Kultti A, Thompson CB, Maneval DC, Jodrell DI, Frost GI, Shepard HM, Skepper JN, Tuveson DA. Hyaluronan impairs vascular function and drug delivery in a mouse model of pancreatic cancer. Gut. 2013;62(1):112. doi: 10.1136/gutjnl-2012-302529.

28. Provenzano PP, Cuevas C, Chang AE, Goel VK, Von Hoff DD, Hingorani SR. Enzymatic targeting of the stroma ablates physical barriers to treatment of pancreatic ductal adenocarcinoma. Cancer cell. 2012;21(3):418-29. doi: 10.1016/j.ccr.2012.01.007. PubMed PMID: 22439937.

29. Son J, Lyssiotis CA, Ying H, Wang X, Hua S, Ligorio M, Perera RM, Ferrone CR, Mullarky E, Shyh-Chang N, Kang Y, Fleming JB, Bardeesy N, Asara JM, Haigis MC, DePinho RA, Cantley LC, Kimmelman AC. Glutamine supports pancreatic cancer growth through a KRAS-regulated metabolic pathway. Nature. 2013;496(7443):101-5. Epub 2013/03/29. doi: 10.1038/nature12040. PubMed PMID: 23535601; PMCID: PMC3656466.

30. Zhang Y, Crawford HC, Pasca di Magliano M. Epithelial-Stromal Interactions in Pancreatic Cancer. Annual review of physiology. 2019;81:211-33. Epub 2018/11/13. doi: 10.1146/annurev-physiol-020518-114515. PubMed PMID: 30418798.

31. Neesse A, Bauer CA, Ohlund D, Lauth M, Buchholz M, Michl P, Tuveson DA, Gress TM. Stromal biology and therapy in pancreatic cancer: ready for clinical translation? Gut. 2019;68(1):159-71. Epub 2018/09/05. doi: 10.1136/gutjnl-2018-316451. PubMed PMID: 30177543.

32. Moussian B. The role of GlcNAc in formation and function of extracellular matrices. Comp Biochem Physiol B Biochem Mol Biol. 2008;149(2):215-26. doi: 10.1016/j.cbpb.2007.10.009. PubMed PMID: 18032081.

33. Bond MR, Hanover JA. A little sugar goes a long way: the cell biology of O-GlcNAc. J Cell Biol. 2015;208(7):869-80. doi: 10.1083/jcb.201501101. PubMed PMID: 25825515; PMCID: PMC4384737.

34. Kim SM, Nguyen TT, Ravi A, Kubiniok P, Finicle BT, Jayashankar V, Malacrida L, Hou J, Robertson J, Gao D, Chernoff J, Digman MA, Potma EO, Tromberg BJ, Thibault P, Edinger AL. PTEN Deficiency and AMPK Activation Promote Nutrient Scavenging and Anabolism in Prostate Cancer Cells. Cancer Discov. 2018;8(7):866-83. doi: 10.1158/2159-8290.CD-17-1215. PubMed PMID: 29572236; PMCID: PMC6030497.

35. Monslow J, Govindaraju P, Puré E. Hyaluronan - a functional and structural sweet spot in the tissue microenvironment. Front Immunol. 2015;6:231. Epub 2015/06/02. doi: 10.3389/fimmu.2015.00231. PubMed PMID: 26029216; PMCID: PMC4432798.

36. Schmaus A, Klusmeier S, Rothley M, Dimmler A, Sipos B, Faller G, Thiele W, Allgayer H, Hohenberger P, Post S, Sleeman JP. Accumulation of small hyaluronan oligosaccharides in tumour interstitial fluid correlates with lymphatic invasion and lymph node metastasis. Br J Cancer. 2014;111(3):559-67. Epub 2014/06/18. doi: 10.1038/bjc.2014.332. PubMed PMID: 24937668; PMCID: PMC4119989.

37. Lv H, Yu G, Sun L, Zhang Z, Zhao X, Chai W. Elevate level of glycosaminoglycans and altered sulfation pattern of chondroitin sulfate are associated with differentiation status and histological type of human primary hepatic carcinoma. Oncology. 2007;72(5-6):347-56. Epub 2008/01/12. doi: 10.1159/000113145. PubMed PMID: 18187957.

38. Greyner HJ, Wiraszka T, Zhang LS, Petroll WM, Mummert ME. Inducible macropinocytosis of hyaluronan in B16-F10 melanoma cells. Matrix Biol. 2010;29(6):503-10. Epub 2010/07/06. doi: 10.1016/j.matbio.2010.06.004. PubMed PMID: 20600893.

39. Sullivan WJ, Mullen PJ, Schmid EW, Flores A, Momcilovic M, Sharpley MS, Jelinek D, Whiteley AE, Maxwell MB, Wilde BR, Banerjee U, Coller HA, Shackelford DB, Braas D, Ayer DE, de Aguiar Vallim TQ, Lowry WE, Christofk HR. Extracellular Matrix Remodeling Regulates Glucose Metabolism through TXNIP Destabilization. Cell. 2018;175(1):117-32 e21. doi: 10.1016/j.cell.2018.08.017. PubMed PMID: 30197082; PMCID: PMC6151140.

40. Nagy N, Kuipers HF, Frymoyer AR, Ishak HD, Bollyky JB, Wight TN, Bollyky PL. 4-methylumbelliferone treatment and hyaluronan inhibition as a therapeutic strategy in inflammation, autoimmunity, and cancer. Front Immunol. 2015;6:123. doi: 10.3389/fimmu.2015.00123. PubMed PMID: 25852691; PMCID: PMC4369655.

41. Provenzano PP, Cuevas C, Chang AE, Goel VK, Von Hoff DD, Hingorani SR. Enzymatic targeting of the stroma ablates physical barriers to treatment of pancreatic ductal adenocarcinoma. Cancer Cell. 2012;21(3):418-29. doi: 10.1016/j.ccr.2012.01.007. PubMed PMID: 22439937; PMCID: PMC3371414.

42. Termini JM, Silver ZA, Connor B, Antonopoulos A, Haslam SM, Dell A, Desrosiers RC. HEK293T cell lines defective for O-linked glycosylation. PLoS One.

2017;12(6):e0179949. doi: 10.1371/journal.pone.0179949. PubMed PMID: 28654657; PMCID: PMC5487050.

43. Guillaumond F, Leca J, Olivares O, Lavaut MN, Vidal N, Berthezene P, Dusetti NJ, Loncle C, Calvo E, Turrini O, Iovanna JL, Tomasini R, Vasseur S. Strengthened glycolysis under hypoxia supports tumor symbiosis and hexosamine biosynthesis in pancreatic adenocarcinoma. Proc Natl Acad Sci U S A. 2013;110(10):3919-24. doi: 10.1073/pnas.1219555110. PubMed PMID: 23407165; PMCID: PMC3593894.

44. Lucena MC, Carvalho-Cruz P, Donadio JL, Oliveira IA, de Queiroz RM, Marinho-Carvalho MM, Sola-Penna M, de Paula IF, Gondim KC, McComb ME, Costello CE, Whelan SA, Todeschini AR, Dias WB. Epithelial Mesenchymal Transition Induces Aberrant Glycosylation through Hexosamine Biosynthetic Pathway Activation. J Biol Chem. 2016;291(25):12917-29. doi: 10.1074/jbc.M116.729236. PubMed PMID: 27129262; PMCID: PMC4933211.

45. Kim J, Lee HM, Cai F, Ko B, Yang C, Lieu EL, Muhammad N, Rhyne S, Li K, Haloul M, Gu W, Faubert B, Kaushik AK, Cai L, Kasiri S, Marriam U, Nham K, Girard L, Wang H, Sun X, Kim J, Minna JD, Unsal-Kacmaz K, DeBerardinis RJ. The hexosamine biosynthesis pathway is a targetable liability in KRAS/LKB1 mutant lung cancer. Nat Metab. 2020;2(12):1401-12. doi: 10.1038/s42255-020-00316-0. PubMed PMID: 33257855; PMCID: PMC7744327.

46. Zhang W, Bouchard G, Yu A, Shafiq M, Jamali M, Shrager JB, Ayers K, Bakr S, Gentles AJ, Diehn M, Quon A, West RB, Nair V, van de Rijn M, Napel S, Plevritis SK. GFPT2-Expressing Cancer-Associated Fibroblasts Mediate Metabolic Reprogramming in Human Lung Adenocarcinoma. Cancer Res. 2018;78(13):3445-57. doi: 10.1158/0008-5472.CAN-17-2928. PubMed PMID: 29760045; PMCID: PMC6030462.

47. Leone RD, Zhao L, Englert JM, Sun IM, Oh MH, Sun IH, Arwood ML, Bettencourt IA, Patel CH, Wen J, Tam A, Blosser RL, Prchalova E, Alt J, Rais R, Slusher BS, Powell JD. Glutamine blockade induces divergent metabolic programs to overcome tumor immune evasion. Science. 2019;366(6468):1013-21. doi: 10.1126/science.aav2588. PubMed PMID: 31699883; PMCID: PMC7023461.

48. Sharma NS, Gupta VK, Garrido VT, Hadad R, Durden BC, Kesh K, Giri B, Ferrantella A, Dudeja V, Saluja A, Banerjee S. Targeting tumor-intrinsic hexosamine biosynthesis sensitizes pancreatic cancer to anti-PD1 therapy. J Clin Invest. 2020;130(1):451-65. doi: 10.1172/JCI127515. PubMed PMID: 31613799; PMCID: PMC6934212.

49. Toole BP. Hyaluronan: from extracellular glue to pericellular cue. Nat Rev Cancer. 2004;4(7):528-39. doi: 10.1038/nrc1391. PubMed PMID: 15229478.

50. Misra S, Hascall VC, Markwald RR, Ghatak S. Interactions between Hyaluronan and Its Receptors (CD44, RHAMM) Regulate the Activities of Inflammation and Cancer. Front Immunol. 2015;6:201. doi: 10.3389/fimmu.2015.00201. PubMed PMID: 25999946; PMCID: PMC4422082.

51. Vigetti D, Viola M, Karousou E, De Luca G, Passi A. Metabolic control of hyaluronan synthases. Matrix Biol. 2014;35:8-13. doi: 10.1016/j.matbio.2013.10.002. PubMed PMID: 24134926.

52. Campbell S, Mesaros C, Izzo L, Affronti H, Noji M, Schaffer BE, Tsang T, Sun K, Trefely S, Kruijning S, Blenis J, Blair IA, Wellen KE. Glutamine deprivation triggers NAGK-dependent hexosamine salvage. Elife. 2021;10. doi: 10.7554/eLife.62644. PubMed PMID: 34844667.

53. Jayashankar V, Edinger AL. Macropinocytosis confers resistance to therapies targeting cancer anabolism. Nature Communications. 2020;11(1):1121. doi: 10.1038/s41467-020-14928-3.

54. DuFort CC, DelGiorno KE, Hingorani SR. Mounting Pressure in the Microenvironment: Fluids, Solids, and Cells in Pancreatic Ductal Adenocarcinoma. Gastroenterology. 2016;150(7):1545-57 e2. doi: 10.1053/j.gastro.2016.03.040. PubMed PMID: 27072672; PMCID: PMC4957812.

55. DuFort CC, DelGiorno KE, Carlson MA, Osgood RJ, Zhao C, Huang Z, Thompson CB, Connor RJ, Thanos CD, Scott Brockenbrough J, Provenzano PP, Frost GI, Michael Shepard H, Hingorani SR. Interstitial Pressure in Pancreatic Ductal Adenocarcinoma Is Dominated by a Gel-Fluid Phase. Biophys J. 2016;110(9):2106-19. doi: 10.1016/j.bpj.2016.03.040. PubMed PMID: 27166818; PMCID: PMC4939548.

56. Jacobetz MA, Chan DS, Neesse A, Bapiro TE, Cook N, Frese KK, Feig C, Nakagawa T, Caldwell ME, Zecchini HI, Lolkema MP, Jiang P, Kultti A, Thompson CB, Maneval DC, Jodrell DI, Frost GI, Shepard HM, Skepper JN, Tuveson DA. Hyaluronan impairs vascular function and drug delivery in a mouse model of pancreatic cancer. Gut. 2013;62(1):112-20. doi: 10.1136/gutjnl-2012-302529. PubMed PMID: 22466618; PMCID: PMC3551211.

57. Olive KP, Jacobetz MA, Davidson CJ, Gopinathan A, McIntyre D, Honess D, Madhu B, Goldgraben MA, Caldwell ME, Allard D, Frese KK, Denicola G, Feig C, Combs C, Winter SP, Ireland-Zecchini H, Reichelt S, Howat WJ, Chang A, Dhara M, Wang L, Ruckert F, Grutzmann R, Pilarsky C, Izeradjene K, Hingorani SR, Huang P, Davies SE, Plunkett W, Egorin M, Hruban RH, Whitebread N, McGovern K, Adams J, Iacobuzio-Donahue C, Griffiths J, Tuveson DA. Inhibition of Hedgehog signaling enhances delivery of chemotherapy in a mouse model of pancreatic cancer. Science. 2009;324(5933):1457-61. doi: 10.1126/science.1171362. PubMed PMID: 19460966; PMCID: PMC2998180.

58. Van Cutsem E, Tempero MA, Sigal D, Oh DY, Fazio N, Macarulla T, Hitre E, Hammel P, Hendifar AE, Bates SE, Li CP, Hingorani SR, de la Fouchardiere C, Kasi A, Heinemann V, Maraveyas A, Bahary N, Layos L, Sahai V, Zheng L, Lacy J, Park JO, Portales F, Oberstein P, Wu W, Chondros D, Bullock AJ, Investigators H. Randomized Phase III Trial of Pegvorhyaluronidase Alfa With Nab-Paclitaxel Plus Gemcitabine for

Patients With Hyaluronan-High Metastatic Pancreatic Adenocarcinoma. J Clin Oncol. 2020:JCO2000590. doi: 10.1200/JCO.20.00590. PubMed PMID: 32706635.

59. Helms E, Onate MK, Sherman MH. Fibroblast Heterogeneity in the Pancreatic Tumor Microenvironment. Cancer Discov. 2020;10(5):648-56. doi: 10.1158/2159-8290.CD-19-1353. PubMed PMID: 32014869.

60. Lee JJ, Perera RM, Wang H, Wu DC, Liu XS, Han S, Fitamant J, Jones PD, Ghanta KS, Kawano S, Nagle JM, Deshpande V, Boucher Y, Kato T, Chen JK, Willmann JK, Bardeesy N, Beachy PA. Stromal response to Hedgehog signaling restrains pancreatic cancer progression. Proc Natl Acad Sci U S A. 2014;111(30):E3091-100. doi: 10.1073/pnas.1411679111. PubMed PMID: 25024225; PMCID: PMC4121834.

61. Ozdemir BC, Pentcheva-Hoang T, Carstens JL, Zheng X, Wu CC, Simpson TR, Laklai H, Sugimoto H, Kahlert C, Novitskiy SV, De Jesus-Acosta A, Sharma P, Heidari P, Mahmood U, Chin L, Moses HL, Weaver VM, Maitra A, Allison JP, LeBleu VS, Kalluri R. Depletion of Carcinoma-Associated Fibroblasts and Fibrosis Induces Immunosuppression and Accelerates Pancreas Cancer with Reduced Survival. Cancer Cell. 2015;28(6):831-3. doi: 10.1016/j.ccell.2015.11.002. PubMed PMID: 28843279.

62. Rhim AD, Oberstein PE, Thomas DH, Mirek ET, Palermo CF, Sastra SA, Dekleva EN, Saunders T, Becerra CP, Tattersall IW, Westphalen CB, Kitajewski J, Fernandez-Barrena MG, Fernandez-Zapico ME, Iacobuzio-Donahue C, Olive KP, Stanger BZ. Stromal elements act to restrain, rather than support, pancreatic ductal adenocarcinoma. Cancer Cell. 2014;25(6):735-47. doi: 10.1016/j.ccr.2014.04.021. PubMed PMID: 24856585; PMCID: PMC4096698.

63. Hwang RF, Moore T, Arumugam T, Ramachandran V, Amos KD, Rivera A, Ji B, Evans DB, Logsdon CD. Cancer-associated stromal fibroblasts promote pancreatic tumor progression. Cancer research. 2008;68(3):918-26. doi: 10.1158/0008-5472.CAN-07-5714. PubMed PMID: 18245495.

64. Commisso C, Flinn RJ, Bar-Sagi D. Determining the macropinocytic index of cells through a quantitative image-based assay. Nature Protocols. 2014;9(1):182-92. doi: 10.1038/nprot.2014.004.

2.6 Figures

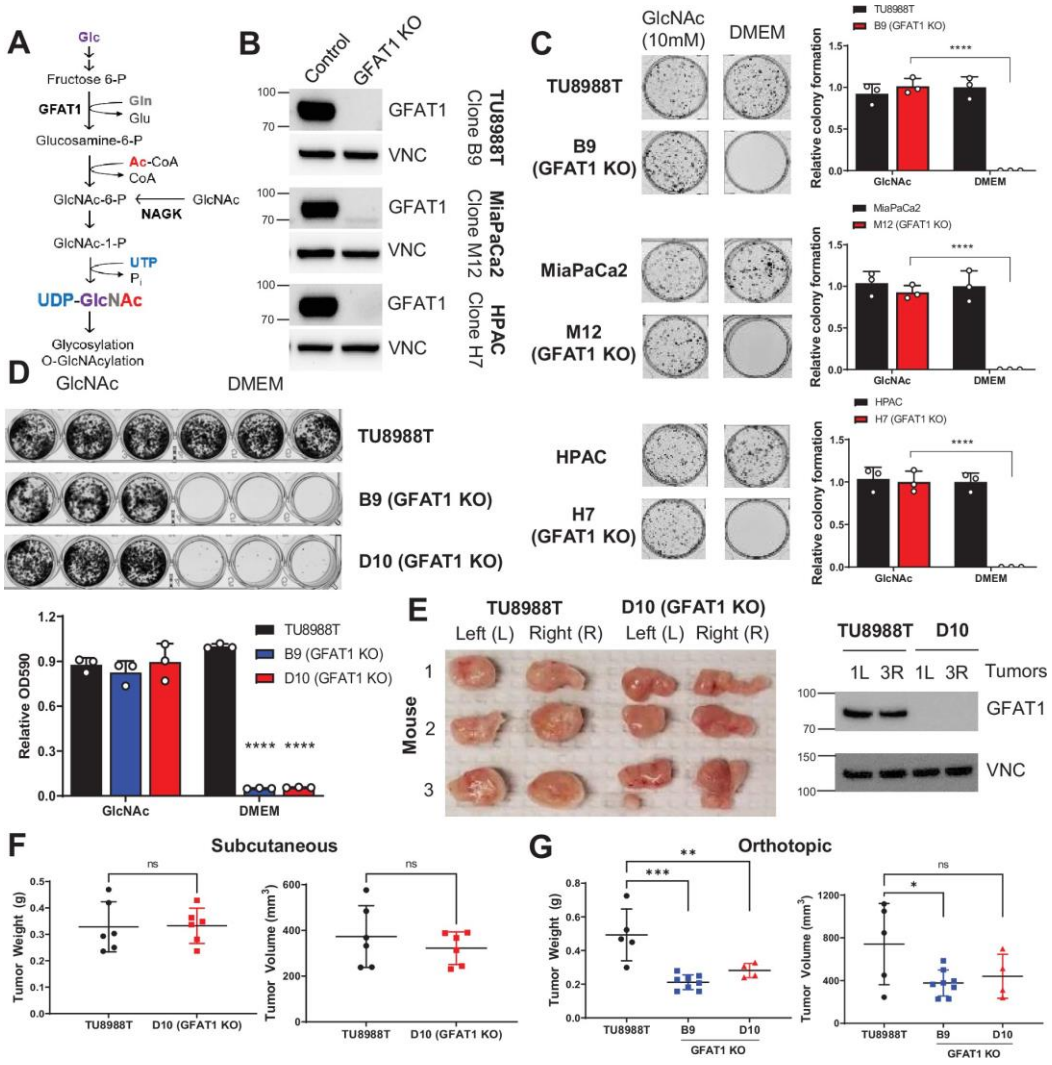

Figure 2-1 PDA requires de novo hexosamine biosynthetic pathway fidelity in vitro but not in vivo.

(**A**) Schematic overview of the hexosamine biosynthetic pathway (HBP) and the nutrient inputs. Ac-CoA, acetyl-coenzyme A; GFAT1, glutamine fructose 6-phosphate amidotransferase 1; Glc, glucose; GlcNAc, N-acetyl-glucosamine; Gln, glutamine; Glu, glutamate; NAGK, N-acetyl-glucosamine kinase; P_i, inorganic phosphorus; UTP, uridine-triphosphate. (**B**) Western blot of GFAT1 and loading control VINCULIN (VNC) from validated CRISPR/Cas9 knockout TU8988T, MiaPaca2, and HPAC clones and their control (non-targeted sgRNA). (**C**) Representative wells from a colony-forming assay in parental and clonally-derived GFAT1 knockout cell lines grown in base media (DMEM) or base media supplemented with 10mM GlcNAc. Data quantitated at right, n=3. (**D**) Proliferation assay in parental and two GFAT1 knockout clonal TU8988T cell lines. Representative wells are presented above data quantitated by crystal violet extraction and measured by optical density (OD) at 590nm, n=3. (**E**) Tumors from parental TU8988T (n=6) and GFAT1 knockout clone D10 (n=6) grown subcutaneously in immunocompromised mice. Accompanying western blot for GFAT1 and VNC loading control from representative tumor lysates. (**F**) Tumor volume and tumor weight from samples in **E**. (**G**) Tumor volume and tumor weight from parental TU8988T (n=5) and GFAT1 knockout clones B9 (n=8) and D10 (n=4) implanted and grown orthotopically in the pancreas of immunocompromised mice. Error bars represent mean ± SD. n.s., non-significant; *P < 0.05; ** P <0.01; *** P <0.001; **** P <0.0001.

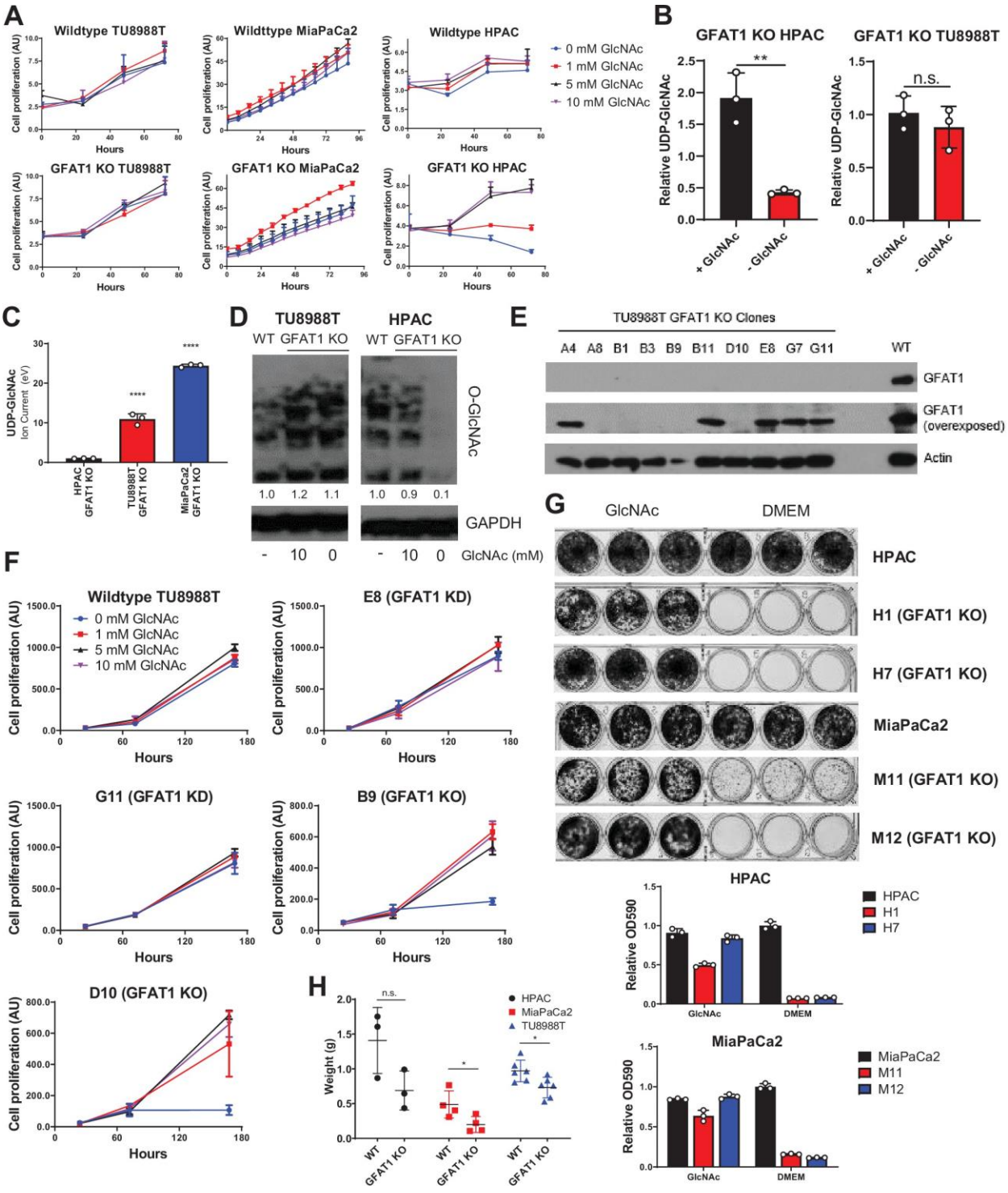

Figure 2-2 Additional characterization of GFAT1 knockout PDA populations and clonal lines.

(**A**) Proliferation kinetics of parental PDA cell lines and corresponding pooled populations of GFAT1 knockout cells supplemented with varying concentrations of GlcNAc (n=3). Cell quantity was assessed by Cyquant (DNA intercalating dye) and plotted in absorbance units (AU). (**B,C**) UDP-GlcNAc levels measured by liquid chromatography-coupled tandem mass spectrometry (LC-MS/MS) in (**B**) TU8988T and HPAC GFAT1 knockout lines in the presence or absence of 10 mM GlcNAc for 3 days, presented as

relative abundance (n=3), and (**C**) TU8988T, HPAC, and MiaPaCa2 GFAT1 knockout cells grown without GlcNAc for 3 days (n=3), presented as relative ion abundance. (**D**) Western blot of proteome O-GlcNAc and loading control GAPDH in parental and GFAT1 knockout TU8988T and HPAC. GFAT1 knockout lines were grown in the presence or absence of 10mM GlcNAc for 3 days. (**E**) Western blot for GFAT1, at short and long exposure, and ACTIN loading control in a panel of clonal cell lines selected from the pooled population of GFAT1 knockout TU8988T cells. (**F**) Proliferation kinetics of parental TU8988T (GFAT1 WT) and clonal cell lines E8, G11, B9, and D10 selected from the pooled GFAT1 knockout population supplemented with varying concentrations of GlcNAc (n=3). Clones correspond to those in the western blot in **E**. Cell quantity was assessed by cell titer glo and plotted in relative fluorescent units (RFU). (**G**) Representative wells from proliferation assay in parental and two GFAT1 knockout clonal HPAC and MiaPaCa2 cell lines. At bottom, data are quantitated by crystal violet extraction and measurement of optical density (OD) at 590nm, n=3. (**H**) Tumors from parental (n=3) and GFAT1 knockout (n=3) HPAC; parental (n=4) and GFAT1 knockout (n=4) MiaPaCa2; and parental (n=6) and GFAT1 knockout (n=6) TU8988T cell lines grown subcutaneously in immunocompromised mice. Error bars represent mean ± SD. n.s., non-significant; *$P < 0.05$; ** $P < 0.01$; **** $P < 0.0001$.

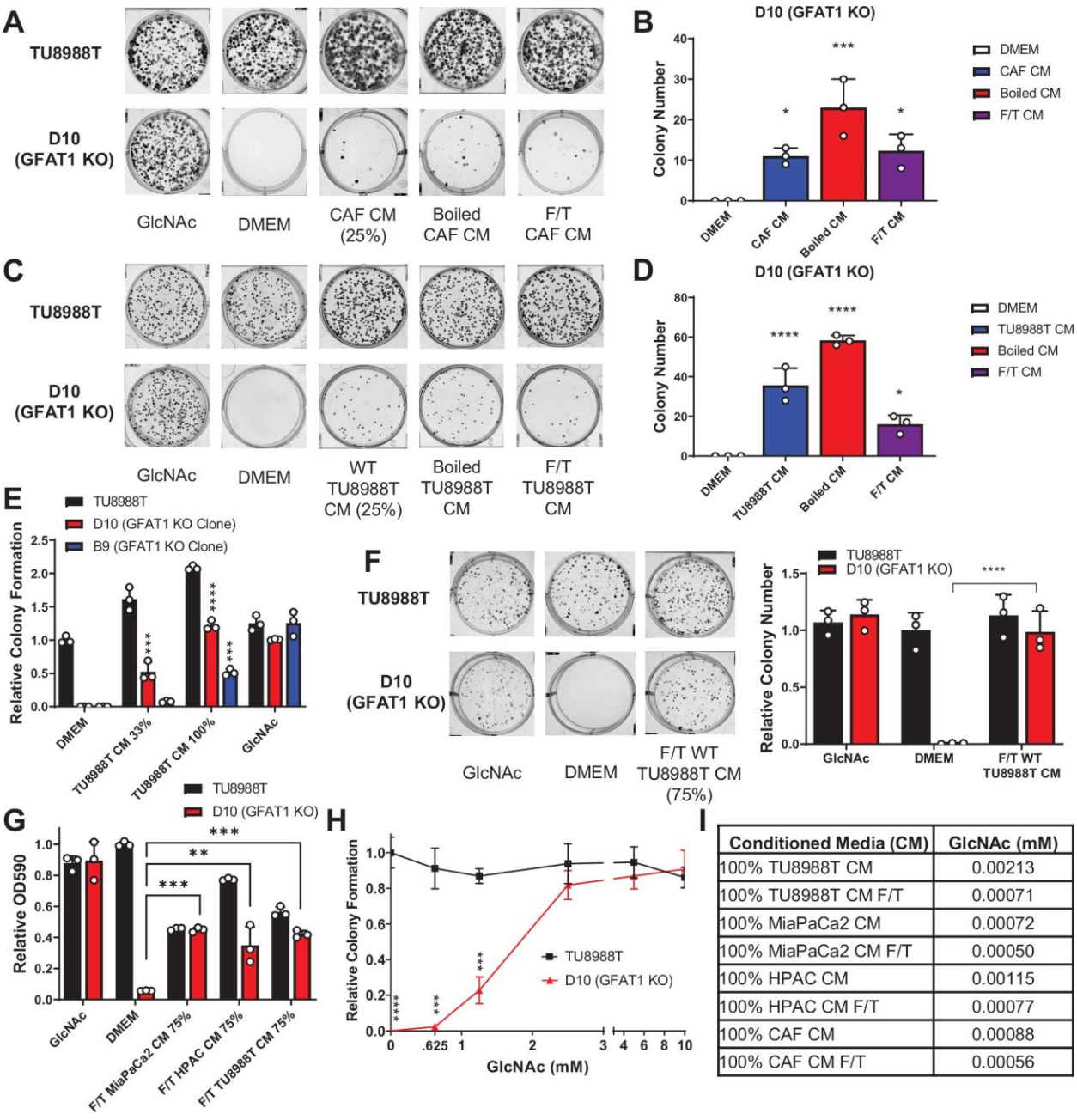

Conditioned Media (CM)	GlcNAc (mM)
100% TU8988T CM	0.00213
100% TU8988T CM F/T	0.00071
100% MiaPaCa2 CM	0.00072
100% MiaPaCa2 CM F/T	0.00050
100% HPAC CM	0.00115
100% HPAC CM F/T	0.00077
100% CAF CM	0.00088
100% CAF CM F/T	0.00056

Figure 2-3 Conditioned media from CAFs and wild type PDA cells support proliferation of GFAT1 knockout cells**.**

(**A**) Representative wells from a colony-forming assay in parental TU8988T and GFAT1 knockout clonal line D10 in 10mM GlcNAc, base media (DMEM), or base media supplemented 1:3 (25%) with cancer associated fibroblast (CAF) conditioned media (CM), boiled CAF CM, or CAF CM subject to freeze-thaw (F/T). (**B**) Quantitation of colonies from data in **A** (n=3). (**C**) Representative wells from a colony-forming assay in parental TU8988T and GFAT1 knockout clonal line D10 in 10mM GlcNAc, DMEM, or base media supplemented 1:3 (25%) with CM from wild type TU8988T cells, boiled TU8988T CM, or TU8988T CM subject to F/T. (**D**) Quantitation of colonies from data in **C** (n=3). (**E**) Quantitation of colony forming assay data of parental and GFAT1 knockout clonal TU8988T lines in base media, positive control GlcNAc, wild type TU8988T CM diluted 1:2 (33%) or used directly (100%) (n=3). (**F**) Representative wells and quantitation of colony forming assay data of parental and GFAT1 knockout clonal TU8988T lines in

base media, positive control GlcNAc, and wild type TU8988T CM subject to F/T and diluted 3:1 (75%) (n=3). (**G**) Quantitation of colony forming assay data of parental and GFAT1 knockout clonal TU8988T lines in base media, positive control GlcNAc, or wild type TU8988T, HPAC, or MiaPaCa2 CM subject to F/T and diluted 3:1 (75%) (n=3). (**H**) GlcNAc dose response curve presented as relative colony number for parental and GFAT1 knockout TU8988T cells (n=3). (**I**) Mean of absolute quantitation of GlcNAc in various CM by LC-MS/MS (n=3). Error bars represent mean ± SD. *P < 0.05; ** P <0.01; *** P <0.001; **** P <0.0001.

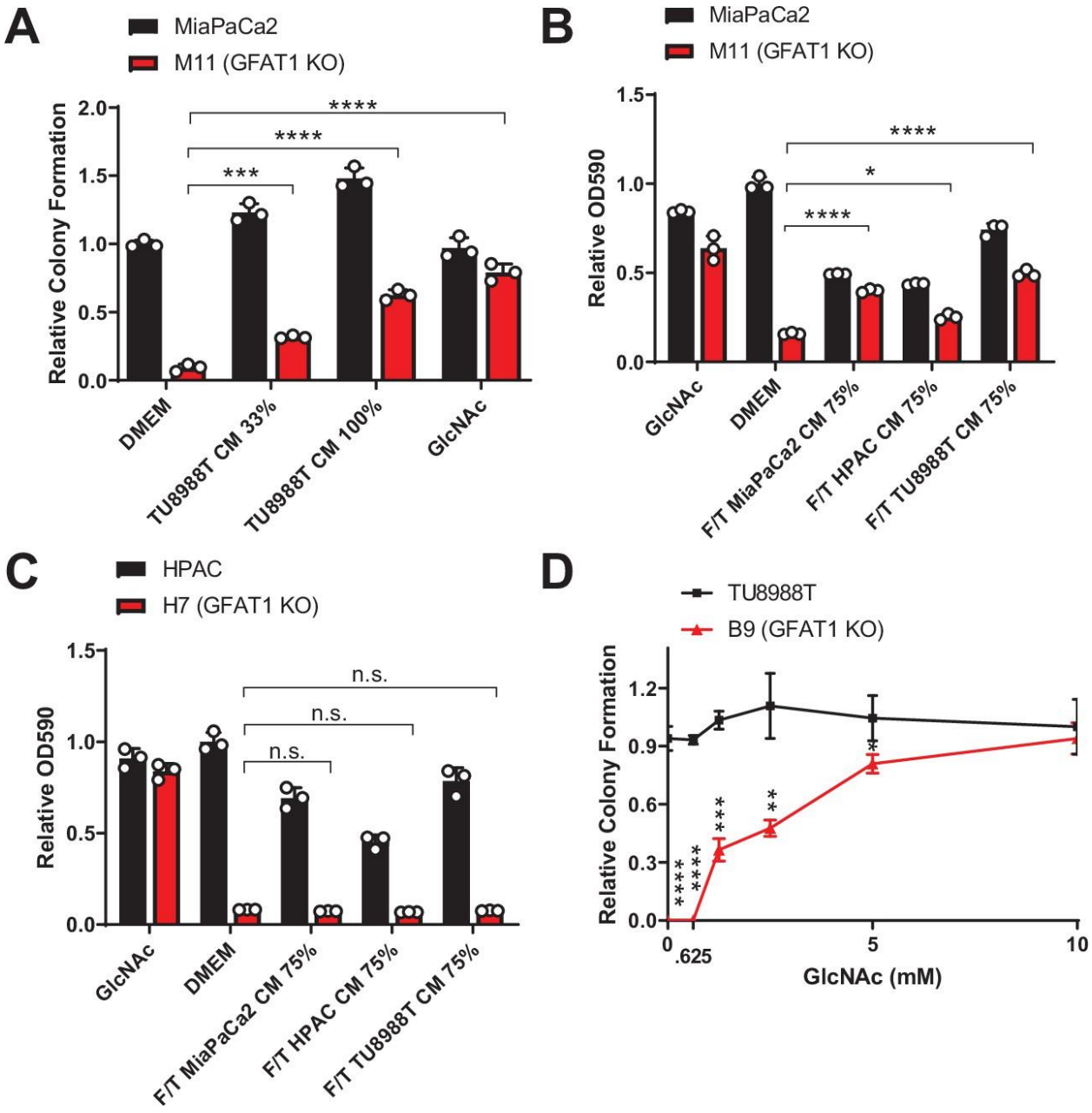

Figure 2-4 Rescue activity of conditioned media and GlcNAc in GFAT1 knockout cells.

(**A**) Quantitation of colony forming assay data of parental MiaPaCa2 and GFAT1 knockout clonal line M11 in base media (DMEM), positive control GlcNAc, wild type TU8988T CM diluted 1:2 (33%) or used directly (100%) (n=3). (**B,C**) Quantitation of proliferation assay data of (**B**) parental MiaPaCa2 and GFAT1 knockout clonal line M11 and (**C**) parental HPAC and GFAT1 knockout clonal line H7 in base media (DMEM), positive control GlcNAc, or wild type TU8988T, HPAC, or MiaPaCa2 CM diluted 3:1 (75%) that was subjected to freeze-thaw (F/T) (n=3). Data represent crystal violet extracted from cells at endpoint and measured by optical density (OD) at 590nm. (**D**) GlcNAc dose response curve presented as relative colony number for parental TU8988T cells and GFAT1 knockout clonal line B9 (n=3). Error bars represent mean ± SD. n.s., non-significant; *P < 0.05; ** P <0.01; *** P <0.001; **** P <0.0001.

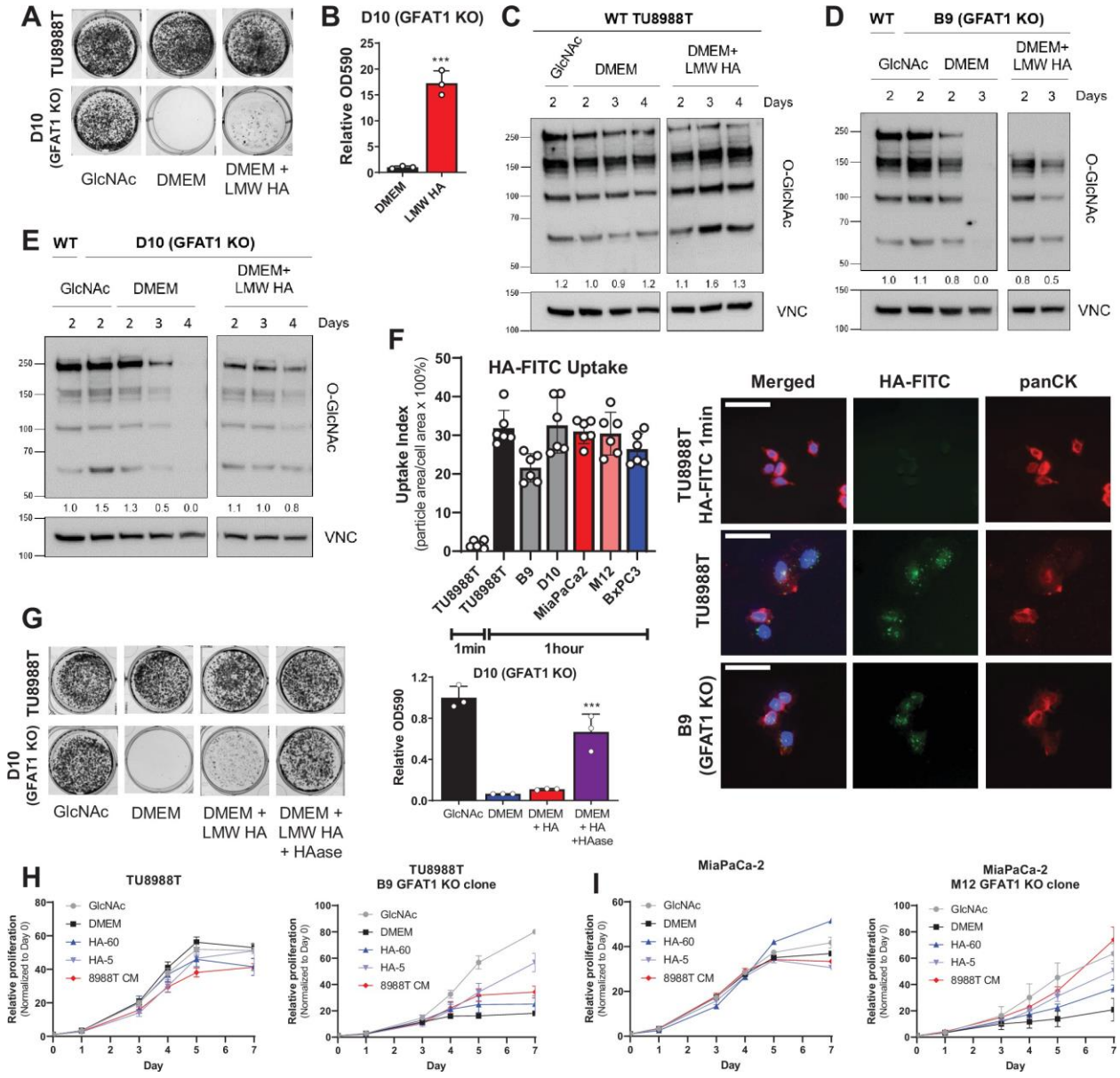

Figure 2-5 Hyaluronic acid rescues GFAT1 knockout PDA cells.

(**A**) Representative wells from a colony-forming assay in parental and clonally-derived GFAT1 knockout TU8988T cell lines grown in base media (DMEM), positive control GlcNAc (10mM), or low molecular weight (LMW) hyaluronic acid (78kDa HA, 10mM). (**B**) Quantitation of data from **A** (n=3). (**C**) Western blot of proteome O-GlcNAc and loading control VINCULIN (VNC) in parental TU8988T cells grown in base media (DMEM) plus GlcNAc or LMW HA for the indicated time points. Band density was quantitated, normalized to control, and presented below the blot. (**D,E**) Western blot of proteome O-GlcNAc and loading control VNC in GFAT1 knockout clonal lines (**D**) B9 and (**E**) D10 in base media (DMEM) plus GlcNAc or LMW HA for the indicated time points. Wild type (WT) TU8988T included as control. Band density was quantitated, normalized to control, and presented below the blot. (**F**) Quantitation of HA-FITC uptake in wild type (TU8988T, MiaPaCa2, BxPC3) and GFAT1 knockout clones (B9, D10, M12) presented as percent total particle area over total cell area at 1 minute or 1 hour; n=6 frames per condition. Cell area was calculated by staining for pan-cytokeratin (panCK). At right, representative images. Scale bar, 50 µm. (**G**) Representative wells of a proliferation assay in parental TU8988T and GFAT1 knockout clonal line D10 grown in base media (DMEM), positive control GlcNAc (10mM), or base

media supplemented 1:1 with boiled LMW HA (10mM) with and without pre-digestion with hyaluronidase (HAase). At endpoint, cells are stained with crystal violet, and the stain was then extracted and quantitated by OD at 590nm (n=3). (**H,I**) Proliferation time course, as measured on the Incucyte, of (**H**) TU8988T and (**I**) MiaPaCa parental and GFAT1 knockout cells in base media (DMEM), positive control (GlcNAc), 60 kDa HA (LMW HA), 5 kDa HA (o-HA), or wild type TU8988T CM (n=3). Error bars represent mean ± SD. *** *P* <0.001.

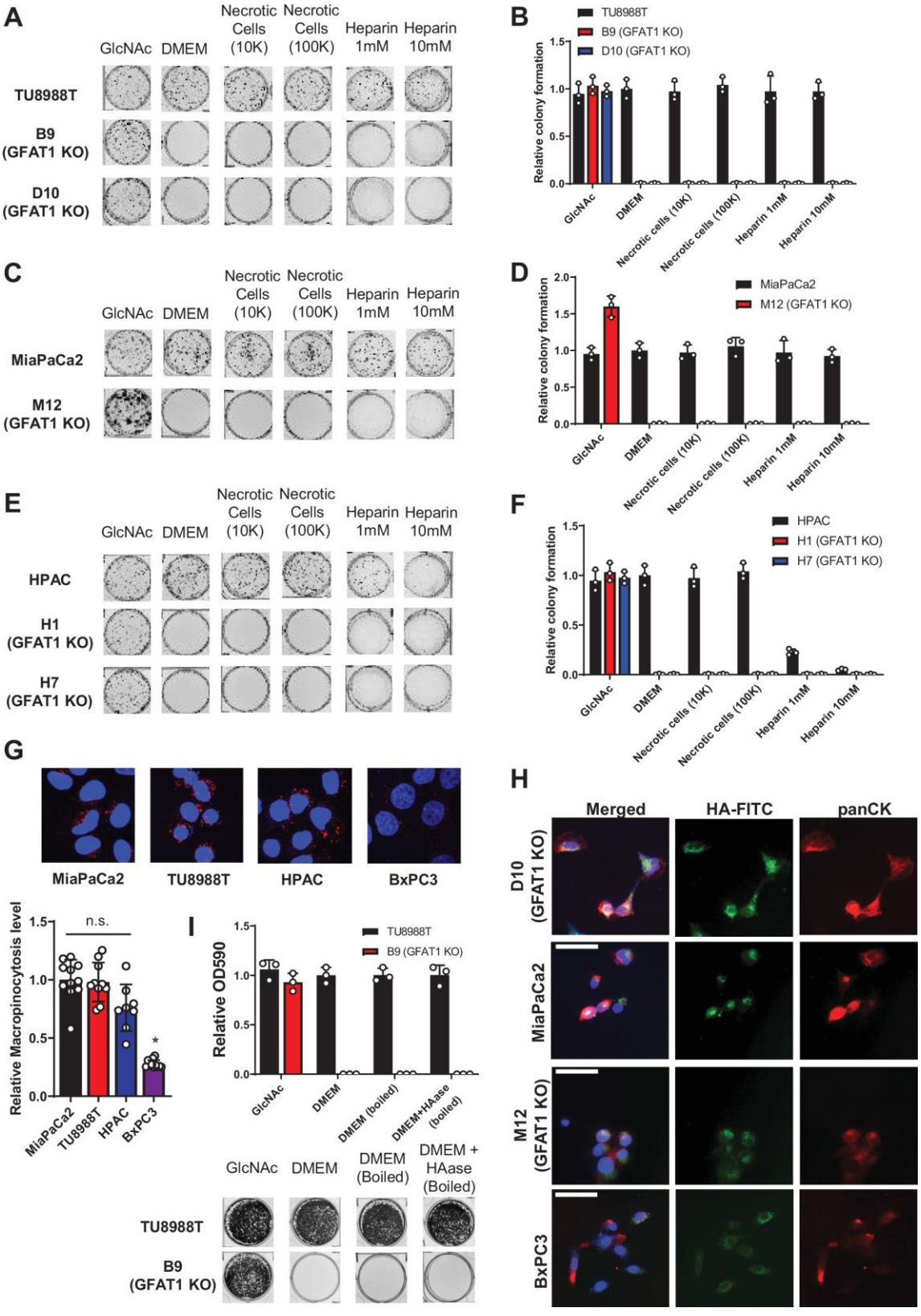

Figure 2-6 Characterization of macropinocytosis and glycosaminoglycan rescue activity in PDA and GFAT1 knockout cells.

(**A-F**) Representative colony formation assays and their quantitation following treatment with two concentrations of heparin or necrotic cell debris that contain complete cellular contents, relative to base media (DMEM) and positive control GlcNAc in (**A,B**) parental and GFAT1 knockout TU8988T, (**C,D**) parental and GFAT1 knockout MiaPaCa2, and (**E,F**) parental and GFAT1 knockout HPAC. (**G**) Immunostaining images of intracellular fluorescently-tagged dextran (red) engulfed by macropinocytosis in PDA cell lines. Nuclear DAPI staining in blue. Quantitation of macropinocytotic index presented at bottom for n=6 wells per biological replicate (n=3). (**H**) Representative images for the data presented in Figure 3F. HA-FITC is presented in green with pan-cytokeratin (panCK) in red. Nuclear staining with DAPI in blue. Scale bar, 50 μm. (**I**) Quantitated data are presented above representative wells from a proliferation assay in parental TU8988T and GFAT1 knockout clone B9 in 10mM GlcNAc, base media (DMEM), base media supplemented 1:1 with boiled DMEM, or base media supplemented 1:1 with boiled HAase-treated DMEM. Quantitated data represent crystal violet extracted from cells at endpoint and measured by optical density (OD) at 590nm (n=3). Error bars represent mean ± SD. n.s., non-significant; *$P < 0.05$.

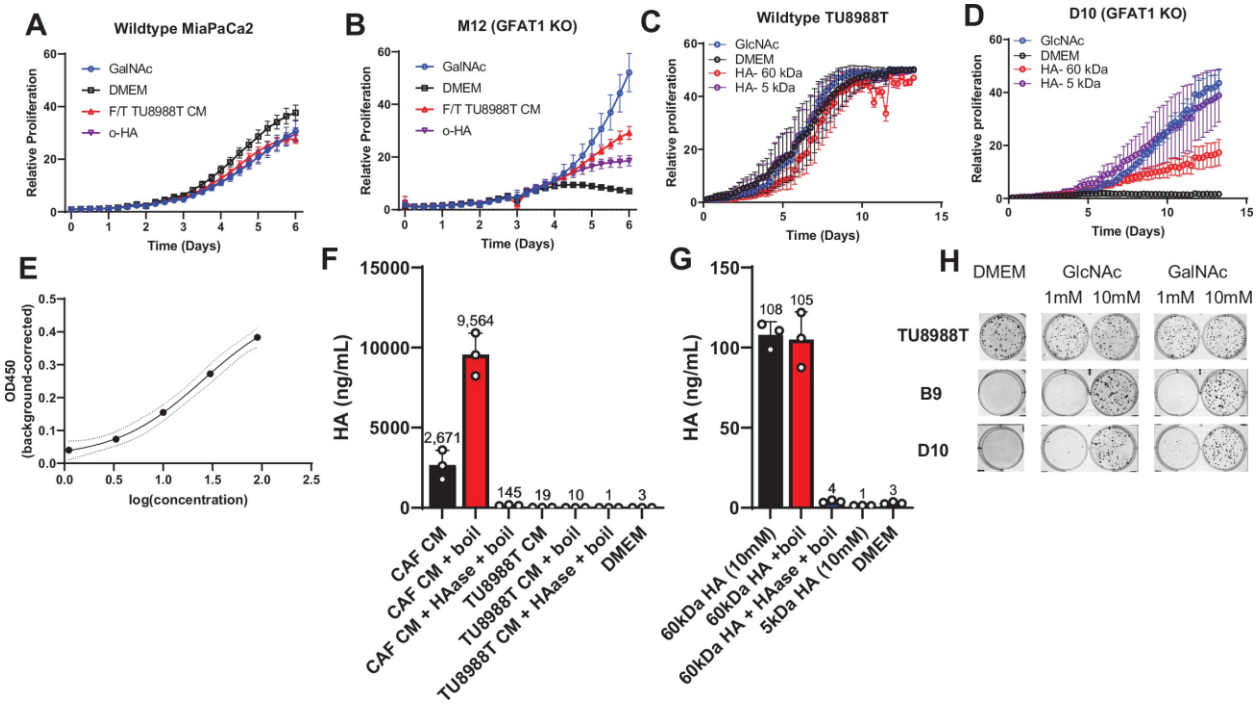

Figure 2-7 Analysis of hyaluronic acid formulation on GFAT1 rescue and composition in conditioned media.

(**A,B**) Proliferation time course of (**A**) parental MiaPaCa2 and (**B**) GFAT1 knockout cells in base media (DMEM), positive control (GlcNAc), 5 kDa HA (o-HA), or wild type TU8988T conditioned media (CM) subject to freeze thaw (F/T) (n=3). (**C,D**) Proliferation time course of (**C**) parental TU8988T and (**D**) GFAT1 knockout cells in base media (DMEM), positive control (GlcNAc), 60 kDa HA (LMW HA), or 5 kDa HA (o-HA).(**E**) Dynamic range of HA detection by ELISA, employed to quantitate HA. (**F**) HA content in cancer associated fibroblast (CAF) and wildtype TU8988T CM, that treated with HAase, and that treated with boiled HAase, relative to DMEM alone negative control. (**G**) Detection of 10mM 60kDa and 5kDa HA standard and 60kDa standard treated with HAase, as well as that treated with boiled HAase, relative to DMEM alone negative control. (**H**) Representative wells from colony formation assays in parental and GFAT1 knockout clonal TU8988T cell lines in base media (DMEM), positive control GlcNAc, and N-acetyl-galactosamine (GalNAc). Quantitated data are presented in **Fig. 2-5F**. Error bars represent mean ± SD.

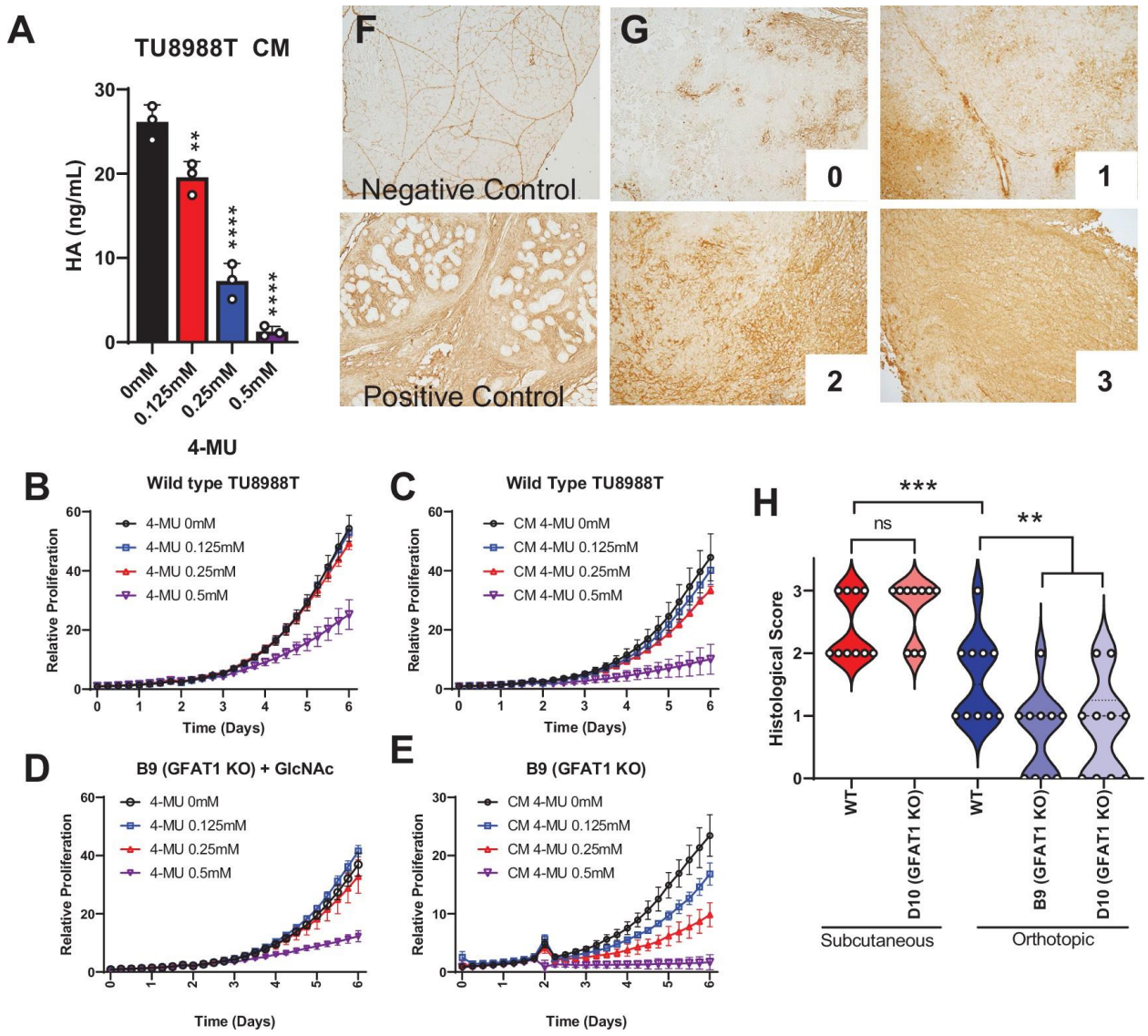

Figure 2-8 Hyaluronic acid in conditioned media rescues GFAT1 knockout.

(A) Quantification of HA in CM from wildtype TU8988T cells treated with varying doses of 4-MU (n=3). **(B-E)** Proliferation time course of (B,C) wild type TU8988T and (D,E) GFAT1 knockout TU8988T grown (B,D) directly in varying concentrations of 4-MU or (C,E) in CM from wild type TU8988T cells exposed to 4-MU during media conditioning. GFAT1 knockout cells in (D) were propagated in GlcNAc to maintain viability (n=3 for all cell lines and conditions). **(F)** HABP staining of normal murine pancreas (negative control) and a murine pancreatic tumor (positive control). **(G)** Representative images for HABP staining classification used in H. **(H)** 10 representative slides from wildtype (WT) and GFAT1 knockout subcutaneous and orthotopic tumors (Figure 1F,G) were stained and blindly scored using the classification metric in G (n=10). Error bars represent mean ± SD. *P < 0.05; ** P <0.01; *** P <0.001; **** P <0.0001.

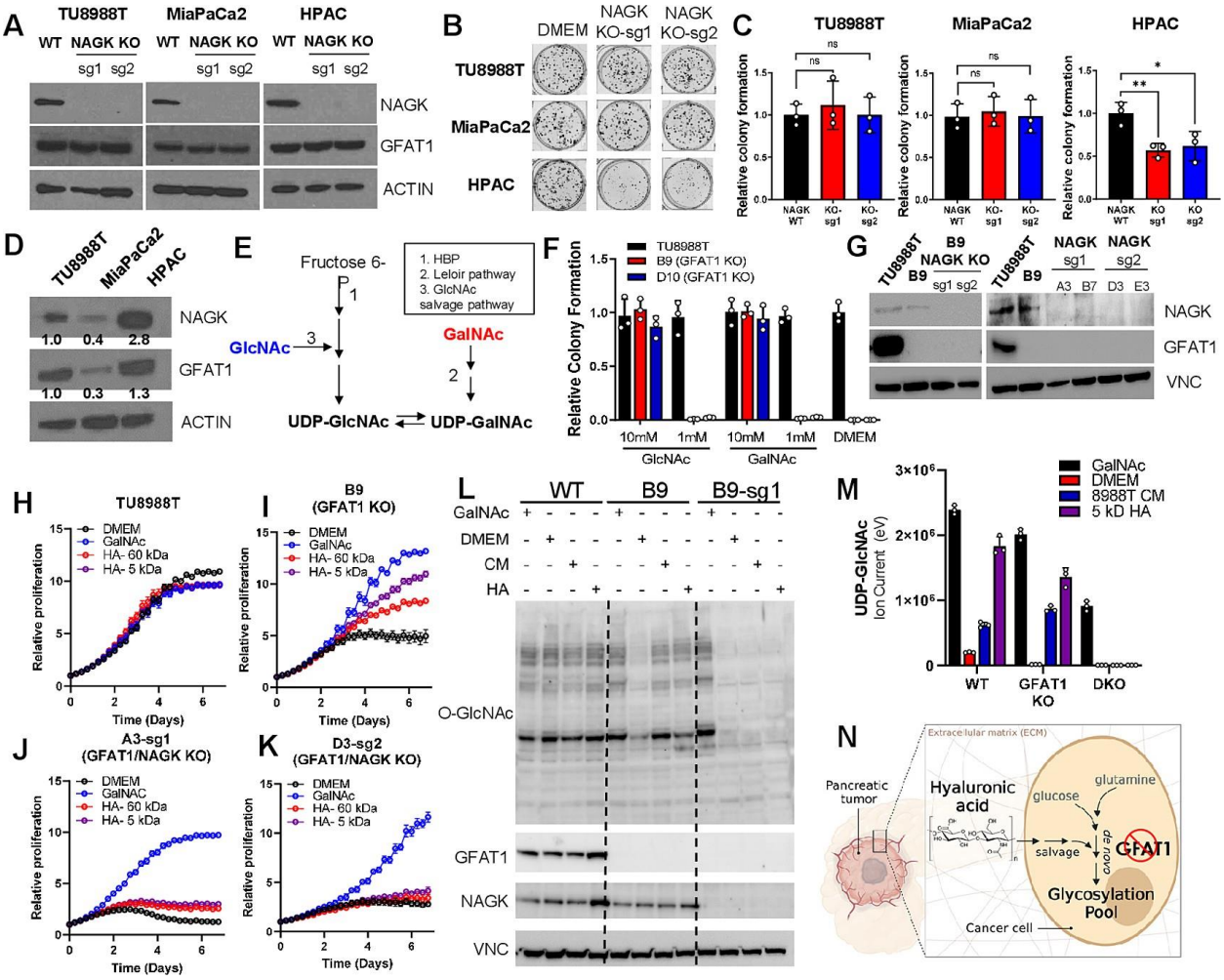

Figure 2-9 Hyaluronic acid-derived GlcNAc rescues GFAT1 loss via the GlcNAc salvage pathway.

(**A**) Western blot of NAGK, GFAT1, and ACTIN loading control from TU8988T, MiaPaCa2, and HPAC parental (wild type, WT) and NAGK knockout (KO) populations. NAGK was knocked out using two independent sgRNAs (sg1, sg2). (**B**) Representative wells from a colony forming assay for parental and NAGK knockout lines. (**C**) Quantitation of colony forming assay data in **B** (n=3). (**D**) Western blot for NAGK, GFAT1, and loading control ACTIN in parental PDA cell lines. Band density was quantitated, normalized to control, and presented below the blot. (**E**) Schematic overview of the Leloir pathway of galactose catabolism integrated with the HBP and GlcNAc salvage pathway. (**F**) Quantitated data from colony formation assays in parental and GFAT1 knockout clonal TU8988T cell lines in base media (DMEM), positive control GlcNAc, and N-acetyl-galactosamine (GalNAc) (n=3) (**G**) Western blot for GFAT1, NAGK, and loading control VINCULIN (VNC) in parental TU8988T and HPAC, GFAT1 knockout clones, and GFAT/NAGK double targeted lines. (**H-K**) Proliferation time course of (**H,I**) parental TU8988T and GFAT1 knockout line B9 in base media, GalNAc positive control, 60 kDa HA, or 5 kDa HA; (**J,K**) GFAT1/NAGK double targeted clones in base media, GalNAc positive control, 60 kDa HA, or 5 kDa HA (n=3). (**L**) Western blot for proteome O-GlcNAcylation (O-GlcNAc), GFAT1, NAGK, and VCN in parental (WT), GFAT1 knockout (B9) and GFAT1/NAGK double knockout (B9-sg1) TU8988T cells treated with 10mM GalNAc, DMEM, CM or o-HA. (**M**) LC-MS/MS analysis of UDP-GlcNAc from the samples in **L** (n=3). (**N**) Schematic overview of the HA metabolism through the GlcNAc salvage pathway to fuel glycosylation in GFAT1 knockout PDA. Error bars represent mean ± SD. n.s., non-significant; **P* < 0.05; ** *P* <0.01.

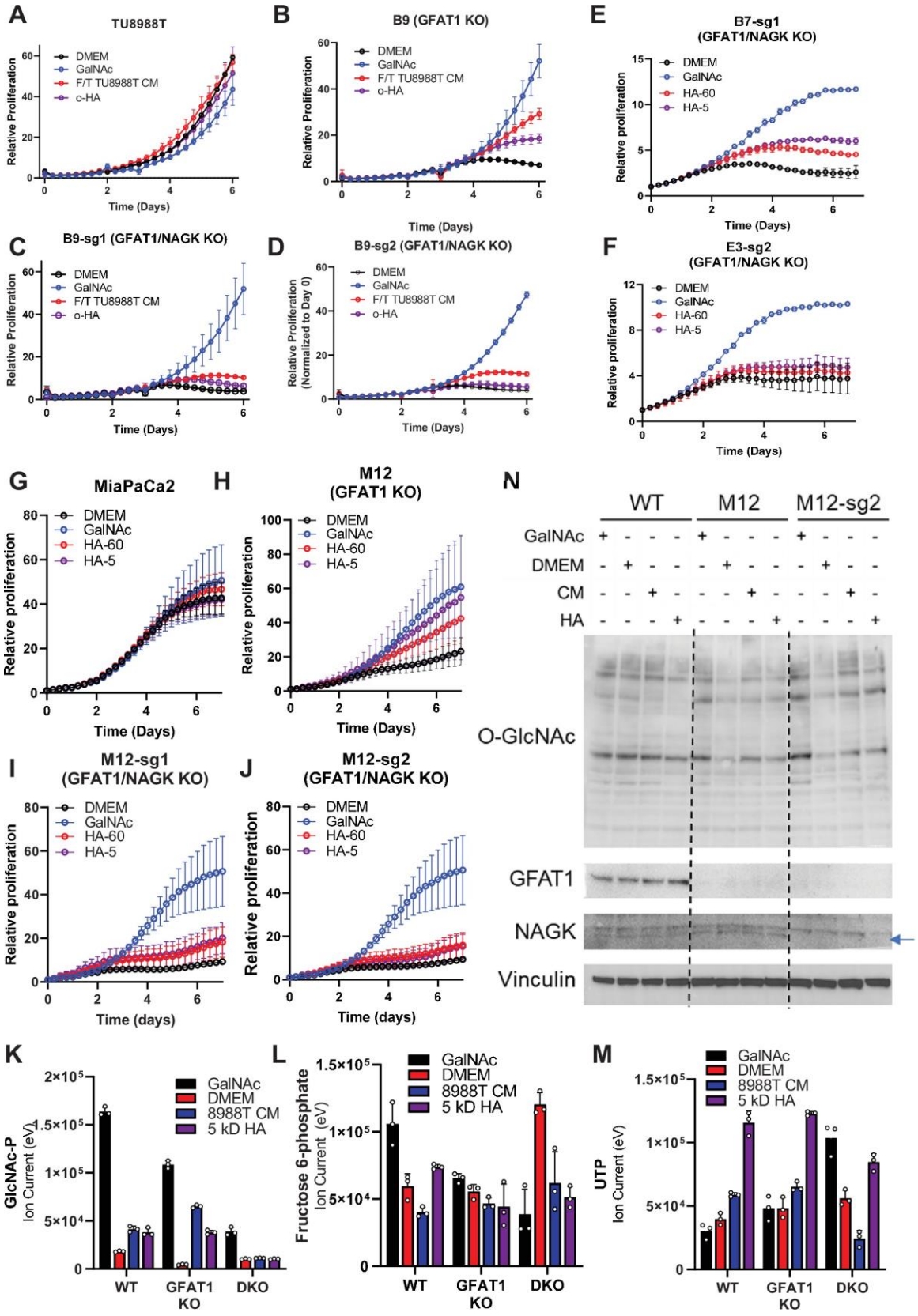

Figure 2-10 Additional characterization of HA rescue in GFAT1/NAGK double knockout cell lines.

(**A-D**) Proliferation time course of (**A**) parental TU8988T, (**B**) GFAT1 knockout cells, and (**C,D**) two GFAT1/NAGK double knockout cell lines in base media (DMEM), positive control (GlcNAc), 5 kDa HA (o-HA), or wild type TU8988T conditioned media (CM) subject to freeze thaw (F/T) (n=3). (**E,F**) Proliferation time course of two additional GFAT1/NAGK double knockout cells lines from main text **Figure 5H-K** in base media (DMEM), positive control (GalNAc), 5 kDa HA (o-HA), or 60kDa HA (n=3). (**G-J**) Proliferation time course of (**G**) wildtype MiaPaCa2, (**H**) GFAT1 knockout line M12, and (**I,J**) GFAT1/NAGK double knockout cells in base media, GalNAc positive control, 60 kDa HA, or 5 kDa o-HA (n=3). (**K-M**) LC-MS/MS analysis of (**K**) GlcNAc-phosphate (GlcNAc-P), (**L**) fructose 6-phosphate, and (**M**) uridine triphosphate from the samples in **Fig. 2-5L** (n=3). (**N**) Western blot for proteome O-GlcNAcylation (O-GlcNAc), GFAT1, NAGK, and VCN in parental (WT), GFAT1 knockout (M12) and GFAT1/NAGK double knockout MiaPaCa2 cells treated with 10mM GalNAc, DMEM, CM or o-HA. The NAGK band appears below a non-specific band, as indicated by the blue arrow. Error bars represent mean ± SD.

Chapter 3 – GOT2 in Cancer Metabolism‡

3.1 Background

Tumors rewire cellular metabolism to sustain aberrant growth and survival(1-3). Cancer cells do not create new metabolic pathways, but rather re-purpose inherent metabolic tendencies of the cells and tissues of origin(4). Thus, understanding cellular metabolism under homeostatic conditions can provide insight into the metabolic underpinnings of cancer cells. Furthermore, unique aspects of cancer metabolism present vulnerabilities that can be exploited therapeutically without disrupting non-malignant cell function(5).

Here, we discuss these concepts through the lens of glutamate-oxaloacetate transaminase 2 (GOT2), a mitochondrial enzyme that has recently garnered considerable interest in cancer metabolism. GOT2 is a mitochondrial aminotransferase that reversibly produces aspartate and α-ketoglutarate from glutamate and oxaloacetate. GOT2 is most well known as a member of the malate-aspartate shuttle (MAS), a cytosolic-mitochondrial pathway that transfers reducing equivalents into the mitochondria to support oxidative phosphorylation(6). In addition to, and as a part of this function, GOT2 also participates in several critical metabolic functions: nucleotide synthesis, redox homeostasis, fueling the tricarboxylic acid (TCA) cycle, fatty acid

‡ This chapter consists of an invited review currently under revision: **Kerk SA**, Garcia-Bermudez J, Birsoy K, Sherman MH, Shah YM, Lyssiotis CA. Spotlight on GOT2 in Cancer. ***OncoTargets and Therapy***.

transport, nitrogen balance, and sulfur catabolism **(Fig.1)**. The following sections will dissect how each of these GOT2-related pathways have been investigated under both cellular homeostasis and cancer metabolism.

3.2 Metabolic functions of GOT2

3.2.1 Aspartate requirement for nucleotide synthesis

The deregulated cell growth and division in cancer cells imposes significant requirements for RNA and DNA. Perhaps the most well-studied product of the GOT2-catalyzed reaction is the amino acid aspartate, which is a rate-limiting metabolite for cancer cells due to its contribution of both carbon and nitrogen to nucleotide synthesis (7-10) **(Fig.1c)**. In vitro studies demonstrated that aspartate supplementation rescued loss of GOT2 in pancreatic cancer cells. In vivo, however, pancreatic tumors overcome loss of GOT2 by acquisition of aspartate from the tumor microenvironment using macropinocytosis (11). In acute myelogenous leukemia, disruption of vitamin B6 synthesis, a co-factor in the GOT2 reaction, disrupted aspartate synthesis and impaired cancer cell growth. Supplementation with aspartate was sufficient to rescue decreased GOT2 activity due to chemical and genetic inhibition of the vitamin B6 pathway(12). Furthermore, GOT2 expression is increased in triple negative breast cancer and overexpression of GOT2 in these cells increased intracellular aspartate levels and promoted proliferation(13, 14). Interestingly, VHL-deficient clear-cell renal clear cell renal carcinoma tumors have decreased expression of GOT2(15, 16), suggesting alternative strategies to generate or acquire aspartate, like macropinocytosis, though those mechanisms remain to be identified.

Aspartate has also been reported to play important roles in metabolism in healthy cells. For example, chondrocytes depend on GOT2-derived aspartate for differentiation and to carry out bone remodeling functions(17). Similarly, perturbations in hematopoietic stem cells (HSCs) that elevate intracellular aspartate levels, such as overexpression of the mitochondrial aspartate transporter or deletion of GOT1, the cytosolic isoform that consumes aspartate, boosted HSC number and activity. Deletion of both GOT1 and GOT2 was lethal for HSCs as they were unable to synthesize nucleotides or another product of aspartate metabolism, the amino acid asparagine(18).

3.2.2 Redox balance

Disruption of the MAS induces ‘reductive stress’, characterized by increased levels of NADH that interfere with redox sensitive metabolic pathways. Patients with germline loss-of-function GOT2 variants present with neurological defects including epilepsy, and fibroblasts derived from these patients demonstrated impaired serine biosynthesis (a redox coupled pathway). Proper function could be restored through supplementation with serine or pyruvate, the latter being a metabolite that accepts electrons from NADH to resolve reductive stress(19). Similarly, in vitro studies in pancreatic cancer demonstrated that loss of GOT2 induced reductive stress due to NADH accumulation, which was alleviated through NADH oxidizing mechanisms(20). Furthermore, impaired mitochondrial metabolism and reduced expression of GOT2 in neurons have been identified in several neurological pathologies (21, 22) (23) (24) (24). This suggests that GOT2 is involved in sustaining oxidative metabolism to generate energy for highly active neuronal subtypes. Dietary, chemical, or genetic interventions

that alleviate reductive stress could be effective therapies for defects in the MAS, including GOT2 inactivation(25).

Maintenance of NADPH/NADP+ pools is also essential to protect cells against damaging levels of reactive oxygen species (ROS). In ischemic hearts, hypoxia inducible factor 1α expression, the primary cellular factor involved in the hypoxic response, is inversely correlated with GOT2 expression and coincides with a concomitant increase in glutathione (GSH), a tripeptide of glycine, glutamate, and cysteine and the most abundant endogenous antioxidant (26). GOT2 consumes glutamate, therefore downregulation of GOT2 expression may lead to an increased availability of glutamate for production of GSH.

In cancer cells the maintenance of a redox state that supports sustained proliferation is paramount. Because the MAS sustains redox balance between the cytosol and the mitochondria, its activity is modulated in various cancer types. For instance, a rewired MAS in PDAC fuels production of NADPH through malic enzyme 1 (ME1) in the cytosol to regenerate GSH and protect cells from ROS(27). Several enzymes in this pathway are overexpressed in pancreatic tumors compared to normal pancreas(28). Loss of GOT2 also induced senescence mediated by decreased NADPH synthesis and ROS accumulation(29). Furthermore, inhibition of glutamine breakdown (or glutaminolysis) coupled with therapies that generated ROS induced redox catastrophe in pancreatic cancer cells both in vitro and in vivo(28). Conversely, in hepatocellular carcinoma , GOT2 is downregulated in response to insulin signaling(30), resulting in increased glutamate availability for GSH synthesis(31).

3.2.3 The dysregulated cancer TCA cycle

The net activity of the MAS does not consume carbon or nitrogen. However, when provided substrates in excess of MAS activity, GOT2 can generate surplus α-ketoglutarate and aspartate. The aspartate can be used as a biosynthetic precursor, as described above. Production of α-ketoglutarate from GOT2 provides a major carbon input that sustains anaplerotic TCA cycling in proliferating cells **(Fig.1e)**. When functioning in this mode, the TCA cycle generates both the reducing equivalents needed to produce energy as well as provide biosynthetic precursors(32). Pancreatic cancer cells in culture utilize glutamine-derived α-ketoglutarate through GOT2 as the primary anaplerotic input to support biosynthesis and proliferation(27). Similarly, GOT2 overexpression in diffuse large B cell lymphoma drives elevated glutaminolysis to support anaplerosis through α-ketoglutarate production(33).

The ratios of TCA cycle intermediates have also been implicated in cell fate(32). For example, paragangliomas and pheochromocytomas, rare neurological tumors, are unique in that they harbor loss of function mutations in the MAS components MDH2, SLC25A11, and a gain of function mutation in GOT2(34). Indeed, a whole-exome sequencing study of 11 patients revealed a patient with a germline GOT2 gain of function mutation, while two other tumors had increased GOT2 activity(35). This increased GOT2 activity elevated both the succinate/fumarate ratio and the available aspartate, due to increased anaplerosis(35, 36). Epigenetic modifying enzymes, such as histone and DNA demethylases, consume α-ketoglutarate and produce succinate. Therefore, while the TCA cycle is important for biosynthesis and energy production, it is necessary to consider how disruption of the α-ketoglutarate/succinate ratio through

increased GOT2 activity has broader implications on cell state and differentiation programs in these and other tumors, as well as in normal physiology.

3.3 Emerging GOT2 pathways in cancer

GOT2 has been reported to have additional functions, outside of the classical roles described above, such as fatty acid binding, cysteine/sulfur breakdown, and nitrogen balance **(Fig.1b,d,f)**. For example, several studies have proposed GOT2 is a plasma membrane-bound fatty acid binding protein and have provided the alternate protein name FABPpm. In this role, GOT2/FABPpm is responsible for the import of free fatty acids under conditions of cellular stress, organ injury, or fatty acid accumulation, potentially influencing fatty acid oxidation(37-46). Despite considerable literature examining the role of GOT2 as a plasma-membrane bound fatty acid transporter in several tissues, this capacity has only recently been examined in cancer. One provocative study confirmed GOT2 as a fatty acid binding protein in pancreatic cancer(47). GOT2 free fatty acid binding activity in syngeneic allografts in immune competent mice promoted anti-inflammatory PPARδ activity, ultimately blocking cytotoxic T cell infiltration, and promoting tumor growth(47). These findings indicate more remains to be investigated regarding the role of GOT2 in fatty acid metabolism in cancer.

GOT2 is also involved in nitrogen balance through production/consumption of the non-essential amino acids aspartate and glutamate. Regarding aspartate, it can enter the urea cycle, the primary mechanism by which cells either recycle or dispose of nitrogen. Human patients with inborn errors of GOT2 metabolism displayed dysregulated levels of serum ammonia(19, 25). As such, further work is needed to

identify mechanisms by which GOT2 is involved in removing toxic levels of ammonia or recovering nitrogen for incorporation into amino acids and nucleotides.

In colorectal cancer, GOT2 is essential in nitrogen balance through production of amino acids and the urea cycle via a HIF1a-SOX12-GOT2 axis that drives asparagine production from aspartate. Inhibition of this pathway impairs cell growth(48). Additionally, in Kaposi's sarcoma-associated herpesvirus cells, GOT2-derived nitrogen is essential for both nucleotide and amino acid production(49). Cells detoxify ammonia through the urea cycle and aspartate incorporation is a critical node in fueling this cycle. Cancer cells often cells downregulate urea cycle enzymes to maintain aspartate pools for nucleotide production(50). However, how cancer cells tune aspartate flux between the urea cycle or nucleotide synthesis remains unclear.

Promiscuous GOT2 transaminase activity has also been proposed to act on cysteinesulfinate to produce 3-sulfinylpyruvate, which is further catabolized to sulfur dioxide and pyruvate, presenting a potential link between GOT2 and taurine biosynthesis(51). Downregulation of GOT2 and the sulfur dioxide pathway is also implicated in myocardial injury(52). Furthermore, serum levels of GOT2 correlated with increased cardiovascular disease (45), and this was proposed to be due to increased sulfur dioxide production. This pathway has not yet been evaluated in cancer cells.

3.4 GOT2 in the tumor microenvironment

Tumors are dynamic pseudo-organs in which malignant and non-transformed cell types work in concert to support growth and survival(53, 54). As such, the metabolism of immune and stromal cells can have a strong influence on cancer cells(55). Aside from its myriad functions in cancer cells, GOT2 is also expressed, and potentially

important, in several of these non-cancer tumor cells. For instance, in an autochthonous model of pancreatic tumorigenesis with loss of Got2, while immunohistochemistry (IHC) confirmed knockdown of Got2 in transformed, epithelial lesions, the surrounding stroma retained strong expression of Got2(20). Indeed, single-cell RNA-sequencing of mouse and human pancreatic tumors also detected significant GOT2 expression in several compartments including macrophages, fibroblasts, T cells, and endothelial cells(56). Furthermore, CAR-T cells engineered to express GOT2 demonstrated enhanced cytotoxic activity against liver cancer both in vitro and in vivo(57). An in-silico analysis of clear cell renal carcinoma detected GOT2 expression in both immune and stromal cell types(16). In sum, these findings suggest that understanding the role of GOT2 in the tumor as whole is important when evaluating GOT2 as a potential target in cancer.

3.5 Key considerations when interrogating cancer metabolism

Cumulatively, the body of work involving GOT2 highlights several key points in tumor metabolism. First, cancer cells exhibit dynamic metabolism to support malignant functions. Second, the metabolic pathways utilized by cancer cells are dictated by tissue of origin, genomic profile, environmental nutrient composition, and external signaling. Third, investigating cancer metabolism in the proper context is essential for identifying therapeutically tractable targets.

A major challenge in targeting cancer metabolism is the ability of cancer cells to rapidly adapt to metabolic pathway blockade(58). As it relates to the MAS, GOT2 inhibition leads to an elevated NADH/NAD+ ratio, and this reductive stress is detrimental to rapidly proliferating cells. Several essential metabolic pathways depend on this ratio, and NADH accumulation decreases flux through these pathways. Yet,

while loss of GOT2 in PDAC cell lines led to reductive stress and impaired proliferation, xenograft tumors grew unimpeded in the absence of GOT2. It was discovered that pancreatic cancer-associated fibroblasts (CAFs) release sufficient pyruvate to ameliorate NADH accumulation through reduction to lactate(20) **(Fig.2A)**. In addition to alleviating reductive stress, PDAC cells can acquire aspartate through macropinocytosis in the absence of GOT2 **(Fig.2A)**. PDAC tumors are rich in extracellular matrix with a prominent stromal compartment secreting numerous proteins. These proteins can be non-specifically scavenged and broken down into their amino acid components to replenish aspartate pools in the absence of GOT2 in vivo(11). Additionally, GOT1 can compensate for the loss of GOT2, and double GOT1/GOT2 knockout slowed pancreatic cancer xenograft growth(11) **(Fig.2A)**. Lastly, a recent study has demonstrated how the MAS can reverse its direction to correct mitochondrial redox imbalance imposed by inhibition of the (ETC)(59). Collectively, these studies emphasize both cell-intrinsic and -extrinsic mechanisms can compensate for loss of GOT2.

The tissue of origin plays a critical role in the tumor-promoting or -restraining function of GOT2 in cancer metabolism (4). For instance, in HCC, downregulation of GOT2 is associated with more aggressive disease and worse outcomes. Indeed, overexpressing GOT2 in HCC cell lines restrains tumor growth. One potential explanation is that loss of GOT2 increases pools of the GOT2 substrate glutamate, increasing its incorporation in glutathione(31) **(Fig.2B)**. Conversely, in PDAC GOT2 is part of the rewired MAS utilized to synthesize NADPH and reduce glutathione(27). Perhaps, tumors arising in the liver versus the pancreas utilize distinct pathways for

glutathione production, which then dictate whether GOT2 expression is detrimental or beneficial for tumor metabolism.

Lastly, the pre-clinical models utilized can influence metabolic findings, even in the same cancer type. Two studies found that loss of GOT2 in human pancreatic cancer cell lines in vitro impaired proliferation, while human xenografts in immunocompromised mice progressed unimpeded in the absence of GOT2. As discussed, cell-intrinsic rewiring and metabolic crosstalk within the TME could both contribute to this compensation(11, 20, 58). However, intriguingly, a third study reported the opposite phenotype. Loss of GOT2 had no effect on in vitro cellular proliferation but significantly inhibited the growth of murine syngeneic allografts in immunocompetent mice. GOT2 loss induced cytotoxic T cell infiltration due to decreased fatty acid binding and PPARδ signaling in cancer cells, which was absent in the models using human PDAC cells in immunocompromised mice(47) **(Fig.2C)**. To complicate matters further, deletion of Got2 in an autochthonous model of pancreatic tumorigenesis did not affect the number or severity of lesions (20). However, these two studies compared rapidly growing, established allografts to gradually developing neoplastic lesions. Future work examining the role of GOT2 in advanced mouse models that more accurately recapitulate human disease are warranted to fully understand the role of GOT2 in pancreatic cancer. Even still, differences between mouse and human tissue will have to be considered. In sum, the model systems used to investigate metabolism can impact cancer metabolism, and careful study across several model systems is needed to accurately assess the metabolic vulnerabilities within a cancer type.

3.6 References

1. DeBerardinis RJ, Chandel NS. Fundamentals of cancer metabolism. Sci Adv. 2016;2(5):e1600200. Epub 2016/07/08. doi: 10.1126/sciadv.1600200. PubMed PMID: 27386546; PMCID: PMC4928883.

2. Pavlova NN, Thompson CB. The Emerging Hallmarks of Cancer Metabolism. Cell Metab. 2016;23(1):27-47. Epub 2016/01/16. doi: 10.1016/j.cmet.2015.12.006. PubMed PMID: 26771115; PMCID: PMC4715268.

3. Vander Heiden MG, Cantley LC, Thompson CB. Understanding the Warburg effect: the metabolic requirements of cell proliferation. Science. 2009;324(5930):1029-33. Epub 2009/05/23. doi: 10.1126/science.1160809. PubMed PMID: 19460998; PMCID: PMC2849637.

4. Kerk SA, Papagiannakopoulos T, Shah YM, Lyssiotis CA. Metabolic networks in mutant KRAS-driven tumours: tissue specificities and the microenvironment. Nat Rev Cancer. 2021;21(8):510-25. Epub 2021/07/11. doi: 10.1038/s41568-021-00375-9. PubMed PMID: 34244683.

5. Vander Heiden MG. Targeting cancer metabolism: a therapeutic window opens. Nature reviews Drug discovery. 2011;10(9):671-84. Epub 2011/09/01. doi: 10.1038/nrd3504. PubMed PMID: 21878982.

6. Borst P. The malate-aspartate shuttle (Borst cycle): How it started and developed into a major metabolic pathway. IUBMB Life. 2020;72(11):2241-59. Epub 2020/09/12. doi: 10.1002/iub.2367. PubMed PMID: 32916028; PMCID: PMC7693074.

7. Birsoy K, Wang T, Chen WW, Freinkman E, Abu-Remaileh M, Sabatini DM. An Essential Role of the Mitochondrial Electron Transport Chain in Cell Proliferation Is to Enable Aspartate Synthesis. Cell. 2015;162(3):540-51. Epub 2015/08/02. doi: 10.1016/j.cell.2015.07.016. PubMed PMID: 26232224; PMCID: PMC4522279.

8. Garcia-Bermudez J, Baudrier L, La K, Zhu XG, Fidelin J, Sviderskiy VO, Papagiannakopoulos T, Molina H, Snuderl M, Lewis CA, Possemato RL, Birsoy K. Aspartate is a limiting metabolite for cancer cell proliferation under hypoxia and in tumours. Nat Cell Biol. 2018;20(7):775-81. Epub 2018/06/27. doi: 10.1038/s41556-018-0118-z. PubMed PMID: 29941933; PMCID: PMC6030478.

9. Sullivan LB, Gui DY, Hosios AM, Bush LN, Freinkman E, Vander Heiden MG. Supporting Aspartate Biosynthesis Is an Essential Function of Respiration in Proliferating Cells. Cell. 2015;162(3):552-63. Epub 2015/08/02. doi: 10.1016/j.cell.2015.07.017. PubMed PMID: 26232225; PMCID: PMC4522278.

10. Sullivan LB, Luengo A, Danai LV, Bush LN, Diehl FF, Hosios AM, Lau AN, Elmiligy S, Malstrom S, Lewis CA, Vander Heiden MG. Aspartate is an endogenous metabolic limitation for tumour growth. Nat Cell Biol. 2018;20(7):782-8. Epub

2018/06/27. doi: 10.1038/s41556-018-0125-0. PubMed PMID: 29941931; PMCID: PMC6051729.

11. Garcia-Bermudez J, Badgley MA, Prasad S, Baudrier L, Liu Y, La K, Soula M, Williams RT, Yamaguchi N, Hwang RF, Taylor LJ, de Stanchina E, Rostandy B, Alwaseem H, Molina H, Bar-Sagi D, Birsoy K. Adaptive stimulation of macropinocytosis overcomes aspartate limitation in cancer cells under hypoxia. Nature Metabolism. 2022. doi: 10.1038/s42255-022-00583-z.

12. Chen C-C, Li B, Millman SE, Chen C, Li X, Morris JP, Mayle A, Ho Y-J, Loizou E, Liu H, Qin W, Shah H, Violante S, Cross JR, Lowe SW, Zhang L. Vitamin B6 Addiction in Acute Myeloid Leukemia. Cancer Cell. 2020;37(1):71-84.e7.

13. He Y, Deng F, Zhao S, Zhong S, Zhao J, Wang D, Chen X, Zhang J, Hou J, Zhang W, Ding L, Tang J, Zhou Z. Analysis of miRNA-mRNA network reveals miR-140-5p as a suppressor of breast cancer glycolysis via targeting GLUT1. Epigenomics. 2019;11(9):1021-36. Epub 2019/06/12. doi: 10.2217/epi-2019-0072. PubMed PMID: 31184216.

14. Hong R, Zhang W, Xia X, Zhang K, Wang Y, Wu M, Fan J, Li J, Xia W, Xu F, Chen J, Wang S, Zhan Q. Preventing BRCA1/ZBRK1 repressor complex binding to the GOT2 promoter results in accelerated aspartate biosynthesis and promotion of cell proliferation. Mol Oncol. 2019;13(4):959-77. Epub 2019/02/05. doi: 10.1002/1878-0261.12466. PubMed PMID: 30714292; PMCID: PMC6441895.

15. Meléndez-Rodríguez F, Urrutia AA, Lorendeau D, Rinaldi G, Roche O, Böğürcü-Seidel N, Ortega Muelas M, Mesa-Ciller C, Turiel G, Bouthelier A, Hernansanz-Agustín P, Elorza A, Escasany E, Li QOY, Torres-Capelli M, Tello D, Fuertes E, Fraga E, Martínez-Ruiz A, Pérez B, Giménez-Bachs JM, Salinas-Sánchez AS, Acker T, Sánchez Prieto R, Fendt SM, De Bock K, Aragonés J. HIF1α Suppresses Tumor Cell Proliferation through Inhibition of Aspartate Biosynthesis. Cell Rep. 2019;26(9):2257-65.e4. Epub 2019/02/28. doi: 10.1016/j.celrep.2019.01.106. PubMed PMID: 30811976.

16. Ferreira WAS, de Oliveira EHC. Expression of GOT2 Is Epigenetically Regulated by DNA Methylation and Correlates with Immune Infiltrates in Clear-Cell Renal Cell Carcinoma. Curr Issues Mol Biol. 2022;44(6):2472-89. Epub 2022/06/24. doi: 10.3390/cimb44060169. PubMed PMID: 35735610; PMCID: PMC9222030.

17. Stegen S, Rinaldi G, Loopmans S, Stockmans I, Moermans K, Thienpont B, Fendt SM, Carmeliet P, Carmeliet G. Glutamine Metabolism Controls Chondrocyte Identity and Function. Dev Cell. 2020;53(5):530-44.e8. Epub 2020/05/30. doi: 10.1016/j.devcel.2020.05.001. PubMed PMID: 32470321.

18. Qi L, Martin-Sandoval MS, Merchant S, Gu W, Eckhardt M, Mathews TP, Zhao Z, Agathocleous M, Morrison SJ. Aspartate availability limits hematopoietic stem cell function during hematopoietic regeneration. Cell Stem Cell. 2021;28(11):1982-99.e8. Epub 2021/08/28. doi: 10.1016/j.stem.2021.07.011. PubMed PMID: 34450065; PMCID: PMC8571029.

19. van Karnebeek CDM, Ramos RJ, Wen XY, Tarailo-Graovac M, Gleeson JG, Skrypnyk C, Brand-Arzamendi K, Karbassi F, Issa MY, van der Lee R, Drögemöller BI, Koster J, Rousseau J, Campeau PM, Wang Y, Cao F, Li M, Ruiter J, Ciapaite J, Kluijtmans LAJ, Willemsen M, Jans JJ, Ross CJ, Wintjes LT, Rodenburg RJ, Huigen M, Jia Z, Waterham HR, Wasserman WW, Wanders RJA, Verhoeven-Duif NM, Zaki MS, Wevers RA. Bi-allelic GOT2 Mutations Cause a Treatable Malate-Aspartate Shuttle-Related Encephalopathy. American journal of human genetics. 2019;105(3):534-48. Epub 2019/08/20. doi: 10.1016/j.ajhg.2019.07.015. PubMed PMID: 31422819; PMCID: PMC6732527.

20. Kerk SA, Lin L, Myers AL, Sutton DJ, Andren A, Sajjakulnukit P, Zhang L, Zhang Y, Jiménez JA, Nelson BS, Chen B, Robinson A, Thurston G, Kemp SB, Steele NG, Hoffman MT, Wen HJ, Long D, Ackenhusen SE, Ramos J, Gao X, Nwosu ZC, Galban S, Halbrook CJ, Lombard DB, Piwnica-Worms DR, Ying H, Pasca di Magliano M, Crawford HC, Shah YM, Lyssiotis CA. Metabolic requirement for GOT2 in pancreatic cancer depends on environmental context. Elife. 2022;11. Epub 2022/07/12. doi: 10.7554/eLife.73245. PubMed PMID: 35815941; PMCID: PMC9328765.

21. Missailidis D, Sanislav O, Allan CY, Smith PK, Annesley SJ, Fisher PR. Dysregulated Provision of Oxidisable Substrates to the Mitochondria in ME/CFS Lymphoblasts. Int J Mol Sci. 2021;22(4). Epub 2021/03/07. doi: 10.3390/ijms22042046. PubMed PMID: 33669532; PMCID: PMC7921983.

22. Wesseling H, Chan MK, Tsang TM, Ernst A, Peters F, Guest PC, Holmes E, Bahn S. A combined metabonomic and proteomic approach identifies frontal cortex changes in a chronic phencyclidine rat model in relation to human schizophrenia brain pathology. Neuropsychopharmacology. 2013;38(12):2532-44. Epub 2013/08/15. doi: 10.1038/npp.2013.160. PubMed PMID: 23942359; PMCID: PMC3799075.

23. Gao Y, Mu J, Xu T, Linghu T, Zhao H, Tian J, Qin X. Metabolomic analysis of the hippocampus in a rat model of chronic mild unpredictable stress-induced depression based on a pathway crosstalk and network module approach. J Pharm Biomed Anal. 2021;193:113755. Epub 2020/11/16. doi: 10.1016/j.jpba.2020.113755. PubMed PMID: 33190083.

24. Honorat JA, Nakatsuji Y, Shimizu M, Kinoshita M, Sumi-Akamaru H, Sasaki T, Takata K, Koda T, Namba A, Yamashita K, Sanda E, Sakaguchi M, Kumanogoh A, Shirakura T, Tamura M, Sakoda S, Mochizuki H, Okuno T. Febuxostat ameliorates secondary progressive experimental autoimmune encephalomyelitis by restoring mitochondrial energy production in a GOT2-dependent manner. PLoS One. 2017;12(11):e0187215. Epub 2017/11/07. doi: 10.1371/journal.pone.0187215. PubMed PMID: 29107957; PMCID: PMC5673182 Pharma Ltd. The drug febuxostat used in the study was kindly provided by Teijin Pharma Ltd. This does not alter our adherence to PLoS One policies on sharing data and materials.

25. Bölsterli BK, Boltshauser E, Palmieri L, Spenger J, Brunner-Krainz M, Distelmaier F, Freisinger P, Geis T, Gropman AL, Häberle J, Hentschel J, Jeandidier B,

Karall D, Keren B, Klabunde-Cherwon A, Konstantopoulou V, Kottke R, Lasorsa FM, Makowski C, Mignot C, O'Gorman Tuura R, Porcelli V, Santer R, Sen K, Steinbrücker K, Syrbe S, Wagner M, Ziegler A, Zöggeler T, Mayr JA, Prokisch H, Wortmann SB. Ketogenic Diet Treatment of Defects in the Mitochondrial Malate Aspartate Shuttle and Pyruvate Carrier. Nutrients. 2022;14(17). Epub 2022/09/10. doi: 10.3390/nu14173605. PubMed PMID: 36079864; PMCID: PMC9460686.

26. Li K, Zheng Y, Wang X. The Potential Relationship Between HIF-1α and Amino Acid Metabolism After Hypoxic Ischemia and Dual Effects on Neurons. Frontiers in neuroscience. 2021;15:676553. Epub 2021/09/07. doi: 10.3389/fnins.2021.676553. PubMed PMID: 34483819; PMCID: PMC8416424.

27. Son J, Lyssiotis CA, Ying H, Wang X, Hua S, Ligorio M, Perera RM, Ferrone CR, Mullarky E, Shyh-Chang N, Kang Y, Fleming JB, Bardeesy N, Asara JM, Haigis MC, DePinho RA, Cantley LC, Kimmelman AC. Glutamine supports pancreatic cancer growth through a KRAS-regulated metabolic pathway. Nature. 2013;496(7443):101-5. Epub 2013/03/29. doi: 10.1038/nature12040. PubMed PMID: 23535601; PMCID: PMC3656466.

28. Chakrabarti G, Moore ZR, Luo X, Ilcheva M, Ali A, Padanad M, Zhou Y, Xie Y, Burma S, Scaglioni PP, Cantley LC, DeBerardinis RJ, Kimmelman AC, Lyssiotis CA, Boothman DA. Targeting glutamine metabolism sensitizes pancreatic cancer to PARP-driven metabolic catastrophe induced by ß-lapachone. Cancer Metab. 2015;3:12. Epub 2015/10/16. doi: 10.1186/s40170-015-0137-1. PubMed PMID: 26462257; PMCID: PMC4601138.

29. Yang S, Hwang S, Kim M, Seo SB, Lee JH, Jeong SM. Mitochondrial glutamine metabolism via GOT2 supports pancreatic cancer growth through senescence inhibition. Cell Death Dis. 2018;9(2):55. Epub 2018/01/21. doi: 10.1038/s41419-017-0089-1. PubMed PMID: 29352139; PMCID: PMC5833441.

30. Honma K, Kamikubo M, Mochizuki K, Goda T. Insulin-induced inhibition of gluconeogenesis genes, including glutamic pyruvic transaminase 2, is associated with reduced histone acetylation in a human liver cell line. Metabolism. 2017;71:118-24. Epub 2017/05/20. doi: 10.1016/j.metabol.2017.03.009. PubMed PMID: 28521864.

31. Li Y, Li B, Xu Y, Qian L, Xu T, Meng G, Li H, Wang Y, Zhang L, Jiang X, Liu Q, Xie Y, Cheng C, Sun B, Yu D. GOT2 Silencing Promotes Reprogramming of Glutamine Metabolism and Sensitizes Hepatocellular Carcinoma to Glutaminase Inhibitors. Cancer Res. 2022. Epub 2022/07/28. doi: 10.1158/0008-5472.Can-22-0042. PubMed PMID: 35895805.

32. Arnold PK, Finley LWS. Regulation and function of the mammalian tricarboxylic acid cycle. J Biol Chem. 2023;299(2):102838. Epub 2022/12/30. doi: 10.1016/j.jbc.2022.102838. PubMed PMID: 36581208; PMCID: PMC9871338.

33. Feist M, Schwarzfischer P, Heinrich P, Sun X, Kemper J, von Bonin F, Perez-Rubio P, Taruttis F, Rehberg T, Dettmer K, Gronwald W, Reinders J, Engelmann JC,

Dudek J, Klapper W, Trümper L, Spang R, Oefner PJ, Kube D. Cooperative STAT/NF-κB signaling regulates lymphoma metabolic reprogramming and aberrant GOT2 expression. Nat Commun. 2018;9(1):1514. Epub 2018/04/19. doi: 10.1038/s41467-018-03803-x. PubMed PMID: 29666362; PMCID: PMC5904148.

34. Buffet A, Burnichon N, Favier J, Gimenez-Roqueplo AP. An overview of 20 years of genetic studies in pheochromocytoma and paraganglioma. Best Pract Res Clin Endocrinol Metab. 2020;34(2):101416. Epub 2020/04/17. doi: 10.1016/j.beem.2020.101416. PubMed PMID: 32295730.

35. Remacha L, Comino-Méndez I, Richter S, Contreras L, Currás-Freixes M, Pita G, Letón R, Galarreta A, Torres-Pérez R, Honrado E, Jiménez S, Maestre L, Moran S, Esteller M, Satrústegui J, Eisenhofer G, Robledo M, Cascón A. Targeted Exome Sequencing of Krebs Cycle Genes Reveals Candidate Cancer-Predisposing Mutations in Pheochromocytomas and Paragangliomas. Clin Cancer Res. 2017;23(20):6315-24. Epub 2017/07/20. doi: 10.1158/1078-0432.Ccr-16-2250. PubMed PMID: 28720665.

36. Dwight T, Kim E, Novos T, Clifton-Bligh RJ. Metabolomics in the Diagnosis of Pheochromocytoma and Paraganglioma. Horm Metab Res. 2019;51(7):443-50. Epub 2019/07/16. doi: 10.1055/a-0926-3790. PubMed PMID: 31307108.

37. Heather LC, Cole MA, Lygate CA, Evans RD, Stuckey DJ, Murray AJ, Neubauer S, Clarke K. Fatty acid transporter levels and palmitate oxidation rate correlate with ejection fraction in the infarcted rat heart. Cardiovasc Res. 2006;72(3):430-7. Epub 2006/10/13. doi: 10.1016/j.cardiores.2006.08.020. PubMed PMID: 17034771.

38. Kalinowska A, Górski J, Harasim E, Harasiuk D, Bonen A, Chabowski A. Differential effects of chronic, in vivo, PPAR's stimulation on the myocardial subcellular redistribution of FAT/CD36 and FABPpm. FEBS Lett. 2009;583(15):2527-34. Epub 2009/07/15. doi: 10.1016/j.febslet.2009.07.008. PubMed PMID: 19596004.

39. Nie J, Ngokana LD, Kou J, Zhao Y, Tu J, Ji H, Tan P, Zhao T, Cao Y, Wu Z, Wang Q, Ren S, Xuan X, Huang H, Li Y, Liang H, Gao X, Zhou L. Low-dose ethanol intake prevents high-fat diet-induced adverse cardiovascular events in mice. Food Funct. 2020;11(4):3549-62. Epub 2020/04/10. doi: 10.1039/c9fo02645b. PubMed PMID: 32270151.

40. Han XX, Chabowski A, Tandon NN, Calles-Escandon J, Glatz JF, Luiken JJ, Bonen A. Metabolic challenges reveal impaired fatty acid metabolism and translocation of FAT/CD36 but not FABPpm in obese Zucker rat muscle. Am J Physiol Endocrinol Metab. 2007;293(2):E566-75. Epub 2007/05/24. doi: 10.1152/ajpendo.00106.2007. PubMed PMID: 17519284.

41. Chabowski A, Momken I, Coort SL, Calles-Escandon J, Tandon NN, Glatz JF, Luiken JJ, Bonen A. Prolonged AMPK activation increases the expression of fatty acid transporters in cardiac myocytes and perfused hearts. Mol Cell Biochem. 2006;288(1-2):201-12. Epub 2006/05/20. doi: 10.1007/s11010-006-9140-8. PubMed PMID: 16710744.

42. Holloway GP, Lally J, Nickerson JG, Alkhateeb H, Snook LA, Heigenhauser GJ, Calles-Escandon J, Glatz JF, Luiken JJ, Spriet LL, Bonen A. Fatty acid binding protein facilitates sarcolemmal fatty acid transport but not mitochondrial oxidation in rat and human skeletal muscle. J Physiol. 2007;582(Pt 1):393-405. Epub 2007/05/05. doi: 10.1113/jphysiol.2007.135301. PubMed PMID: 17478525; PMCID: PMC2075306.

43. Jeppesen J, Albers P, Luiken JJ, Glatz JF, Kiens B. Contractions but not AICAR increase FABPpm content in rat muscle sarcolemma. Mol Cell Biochem. 2009;326(1-2):45-53. Epub 2009/01/15. doi: 10.1007/s11010-008-0006-0. PubMed PMID: 19142713.

44. Nickerson JG, Alkhateeb H, Benton CR, Lally J, Nickerson J, Han XX, Wilson MH, Jain SS, Snook LA, Glatz JFC, Chabowski A, Luiken J, Bonen A. Greater transport efficiencies of the membrane fatty acid transporters FAT/CD36 and FATP4 compared with FABPpm and FATP1 and differential effects on fatty acid esterification and oxidation in rat skeletal muscle. J Biol Chem. 2009;284(24):16522-30. Epub 2009/04/22. doi: 10.1074/jbc.M109.004788. PubMed PMID: 19380575; PMCID: PMC2713524.

45. Sookoian S, Castaño GO, Scian R, Fernández Gianotti T, Dopazo H, Rohr C, Gaj G, San Martino J, Sevic I, Flichman D, Pirola CJ. Serum aminotransferases in nonalcoholic fatty liver disease are a signature of liver metabolic perturbations at the amino acid and Krebs cycle level. Am J Clin Nutr. 2016;103(2):422-34. Epub 2016/01/23. doi: 10.3945/ajcn.115.118695. PubMed PMID: 26791191.

46. Challa TD, Straub LG, Balaz M, Kiehlmann E, Donze O, Rudofsky G, Ukropec J, Ukropcova B, Wolfrum C. Regulation of De Novo Adipocyte Differentiation Through Cross Talk Between Adipocytes and Preadipocytes. Diabetes. 2015;64(12):4075-87. Epub 2015/09/06. doi: 10.2337/db14-1932. PubMed PMID: 26340931.

47. Abrego J, Sanford-Crane H, Oon C, Xiao X, Betts CB, Sun D, Nagarajan S, Diaz L, Sandborg H, Bhattacharyya S, Xia Z, Coussens LM, Tontonoz P, Sherman MH. A cancer cell-intrinsic GOT2-PPARd axis suppresses antitumor immunity. Cancer Discov. 2022. Epub 2022/07/28. doi: 10.1158/2159-8290.Cd-22-0661. PubMed PMID: 35894778.

48. Du F, Chen J, Liu H, Cai Y, Cao T, Han W, Yi X, Qian M, Tian D, Nie Y, Wu K, Fan D, Xia L. SOX12 promotes colorectal cancer cell proliferation and metastasis by regulating asparagine synthesis. Cell Death Dis. 2019;10(3):239. Epub 2019/03/13. doi: 10.1038/s41419-019-1481-9. PubMed PMID: 30858360; PMCID: PMC6412063.

49. Zhu Y, Li T, Ramos da Silva S, Lee JJ, Lu C, Eoh H, Jung JU, Gao SJ. A Critical Role of Glutamine and Asparagine γ-Nitrogen in Nucleotide Biosynthesis in Cancer Cells Hijacked by an Oncogenic Virus. mBio. 2017;8(4). Epub 2017/08/16. doi: 10.1128/mBio.01179-17. PubMed PMID: 28811348; PMCID: PMC5559638.

50. Missiaen R, Anderson NM, Kim LC, Nance B, Burrows M, Skuli N, Carens M, Riscal R, Steensels A, Li F, Simon MC. GCN2 inhibition sensitizes arginine-deprived

hepatocellular carcinoma cells to senolytic treatment. Cell Metab. 2022;34(8):1151-67.e7. Epub 2022/07/16. doi: 10.1016/j.cmet.2022.06.010. PubMed PMID: 35839757; PMCID: PMC9357184.

51. Jiang H, Stabler SP, Allen RH, Abman SH, Maclean KN. Altered hepatic sulfur metabolism in cystathionine β-synthase-deficient homocystinuria: regulatory role of taurine on competing cysteine oxidation pathways. Faseb j. 2014;28(9):4044-54. Epub 2014/06/04. doi: 10.1096/fj.14-253633. PubMed PMID: 24891521; PMCID: PMC5395733.

52. Liang Y, Liu D, Ochs T, Tang C, Chen S, Zhang S, Geng B, Jin H, Du J. Endogenous sulfur dioxide protects against isoproterenol-induced myocardial injury and increases myocardial antioxidant capacity in rats. Lab Invest. 2011;91(1):12-23. Epub 2010/08/25. doi: 10.1038/labinvest.2010.156. PubMed PMID: 20733562.

53. Lyssiotis CA, Kimmelman AC. Metabolic Interactions in the Tumor Microenvironment. Trends Cell Biol. 2017;27(11):863-75. Epub 2017/07/25. doi: 10.1016/j.tcb.2017.06.003. PubMed PMID: 28734735; PMCID: PMC5814137.

54. Li F, Simon MC. Cancer Cells Don't Live Alone: Metabolic Communication within Tumor Microenvironments. Dev Cell. 2020;54(2):183-95. Epub 2020/07/09. doi: 10.1016/j.devcel.2020.06.018. PubMed PMID: 32640203; PMCID: PMC7375918.

55. Schwörer S, Vardhana SA, Thompson CB. Cancer Metabolism Drives a Stromal Regenerative Response. Cell Metab. 2019;29(3):576-91. Epub 2019/02/19. doi: 10.1016/j.cmet.2019.01.015. PubMed PMID: 30773467; PMCID: PMC6692899.

56. Steele NG, Carpenter ES, Kemp SB, Sirihorachai VR, The S, Delrosario L, Lazarus J, Amir E-aD, Gunchick V, Espinoza C, Bell S, Harris L, Lima F, Irizarry-Negron V, Paglia D, Macchia J, Chu AKY, Schofield H, Wamsteker E-J, Kwon R, Schulman A, Prabhu A, Law R, Sondhi A, Yu J, Patel A, Donahue K, Nathan H, Cho C, Anderson MA, Sahai V, Lyssiotis CA, Zou W, Allen BL, Rao A, Crawford HC, Bednar F, Frankel TL, Pasca di Magliano M. Multimodal mapping of the tumor and peripheral blood immune landscape in human pancreatic cancer. Nature Cancer. 2020;1(11):1097-112. doi: 10.1038/s43018-020-00121-4.

57. Hickman TL, Choi E, Whiteman KR, Muralidharan S, Pai T, Johnson T, Parikh A, Friedman T, Gilbert M, Shen B, Barron L, McGinness KE, Ettenberg SA, Motz GT, Weiss GJ, Jensen-Smith A. BOXR1030, an anti-GPC3 CAR with exogenous GOT2 expression, shows enhanced T cell metabolism and improved anti-cell line derived tumor xenograft activity. PLoS One. 2022;17(5):e0266980. Epub 2022/05/05. doi: 10.1371/journal.pone.0266980. PubMed PMID: 35507536; PMCID: PMC9067639

58. Biancur DE, Paulo JA, Małachowska B, Quiles Del Rey M, Sousa CM, Wang X, Sohn ASW, Chu GC, Gygi SP, Harper JW, Fendler W, Mancias JD, Kimmelman AC. Compensatory metabolic networks in pancreatic cancers upon perturbation of glutamine metabolism. Nat Commun. 2017;8:15965. Epub 2017/07/04. doi: 10.1038/ncomms15965. PubMed PMID: 28671190; PMCID: PMC5500878 A.C.K. is an

inventor on patents pertaining to Kras regulated metabolic pathways, redox control pathways in pancreatic cancer, targeting GOT1 as a therapeutic approach and the autophagic control of iron metabolism. A.C.K is on the SAB of Cornerstone Pharmaceuticals. J.D.M. is an inventor on a patent pertaining to the autophagic control of iron metabolism. All other authors declare no competing financial interests.

59. Altea-Manzano P, Vandekeere A, Edwards-Hicks J, Roldan M, Abraham E, Lleshi X, Guerrieri AN, Berardi D, Wills J, Junior JM, Pantazi A, Acosta JC, Sanchez-Martin RM, Fendt S-M, Martin-Hernandez M, Finch AJ. Reversal of mitochondrial malate dehydrogenase 2 enables anaplerosis via redox rescue in respiration-deficient cells. Molecular Cell. 2022.

3.7 Figures

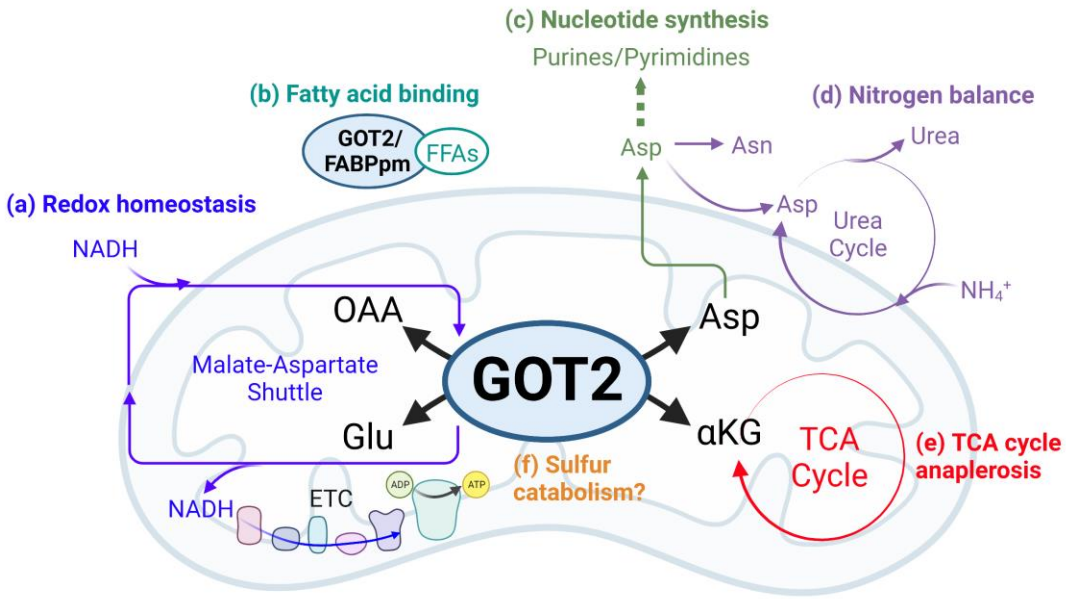

Figure 3-1 Cellular metabolism involving GOT2.

(a) As part of the malate-aspartate shuttle, GOT2 facilitates the transfer of electrons generated from cytosolic glucose oxidation and carried by membrane-impermeable NADH into the mitochondria, where NADH is regenerated and electrons are deposited into the ETC to drive ATP production through oxidative phosphorylation. **(b)** Cytosolic GOT2, also known as FABPpm, binds to free fatty acids with implications for FFA transport, oxidation, and signaling. **(c)** Asp produced by GOT2 provides carbon and nitrogen for synthesis of purine and pyrimidine nucleotide bases. **(d)** Asp from GOT2 is further utilized to synthesize the amino acid Asn and for incorporation into the urea cycle, which detoxifies cellular NH_4^+ through urea excretion or recycling of nitrogen for numerous anabolic pathways. **(e)** GOT2 fuels anabolic TCA cycling through production of the intermediate αKG. **(f)** Some evidence suggests promiscuous GOT2 activity is involved in the catabolism of sulfur-containing metabolites, though this mechanism remains to be thoroughly investigated.

GOT2, glutamate-oxaloacetate transaminase 2; OAA, oxaloacetate; Glu, glutamate; Asp, aspartate; αKG, α-ketoglutarate; NADH, reduced nicotinamide adenine dinucleotide; ETC, electron transport chain; ADP, adenosine diphosphate; ATP, adenosine triphosphate; FFA, free fatty acid; Asn, asparagine; NH_4^+, ammonium; TCA, tricarboxylic acid. Created with BioRender.com.

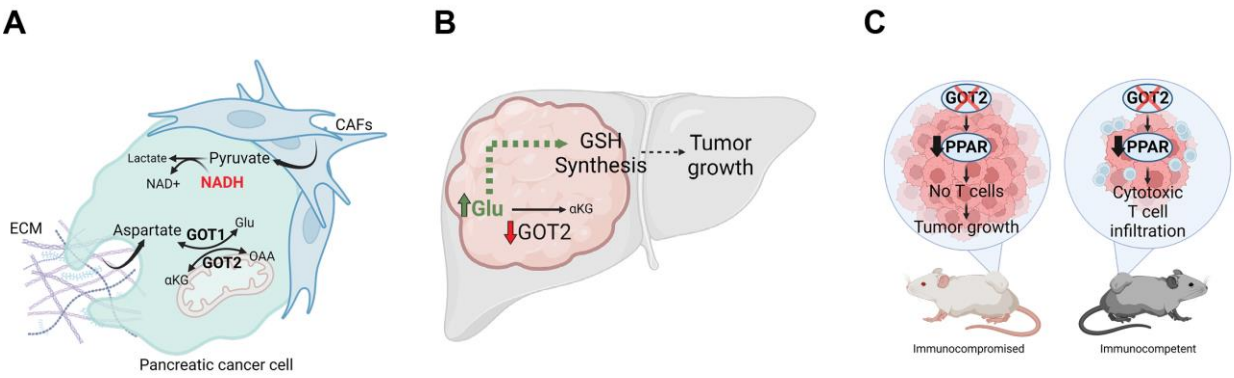

Figure 3-2 Context-specific GOT2 metabolism in cancer.

(A) Pancreatic cancer cells compensate for loss of GOT2 via several mechanisms. CAF- and environment-derived pyruvate can be utilized to reduce pyruvate to lactate and alleviate NADH accumulation. Aspartate can either be produced by compensatory cytosolic GOT1 activity or through macropinocytosis and breakdown of ECM components. **(B)** GOT2 is tumor promoting or restraining depending on tumor type. Hepatocellular carcinoma downregulates GOT2. This increases Glu availability for GSH synthesis and sustained tumor growth. **(C)** GOT2 impairment induces different phenotypes in immune competent or compromised mouse models. A decrease in PPARδ anti-inflammatory pathways caused by loss of GOT2 fatty acid binding activity lifts the blockade on cytotoxic T cells, leading to increased infiltration and cancer cell killing.

GOT2, glutamate-oxaloacetate transaminase 2; OAA, oxaloacetate; Glu, glutamate; αKG, α-ketoglutarate; NADH, reduced nicotinamide adenine dinucleotide; GSH, glutathione; PPAR, Peroxisome proliferator-activated receptor. Created with BioRender.com.

Chapter 4 – Metabolic Requirement for GOT2 in Pancreatic Cancer Depends on Environmental Context[§]

4.1 Introduction

Cancer cells depend on deregulated metabolic programs to meet energetic and biosynthetic demands(1-3). Metabolic therapies aim to preferentially target these dependencies(4). This approach has shown promise in preclinical models of pancreatic ductal adenocarcinoma (PDA) – one of the deadliest major cancers, notoriously resistant to anti-cancer therapies(5, 6). Pancreatic tumors are poorly vascularized and nutrient dysregulated(7). Therefore, cancer cells commandeer metabolic pathways to scavenge and utilize nutrients(6, 8). As I covered in Chapter 1, a wealth of recent literature has identified that this is mediated predominantly by mutant KRAS (KRAS*), the oncogenic driver in most pancreatic tumors(9-14). KRAS* has also been implicated in shaping the pancreatic tumor microenvironment (TME)(15, 16). PDA tumors exhibit a complex tumor microenvironment(17, 18) with metabolic interactions between malignant, stromal, and immune cells enabling and facilitating tumor progression(19). Recent successes in drug development have provided KRAS* selective inhibitors, and these are in various stages of preclinical and clinical testing. However, consistent with

[§] This chapter consists of a published primary article: **Kerk SA**, Lin L, Myers AL, Sutton DJ, Andren A, Sajjakulnukit P, Zhang L, Zhang Y, Jiménez JA, Nelson BS, Chen B, Robinson A, Thurston G, Kemp SB, Steele NG, Hoffman MT, Wen HJ, Long D, Ackenhusen SE, Ramos J, Gao X, Nwosu ZC, Galban S, Halbrook CJ, Lombard DB, Piwnica-Worms DR, Ying H, Pasca di Magliano M, Crawford HC, Shah YM, Lyssiotis CA. Metabolic requirement for GOT2 in pancreatic cancer depends on environmental context. ***Elife***. 2022 Jul 11;11:e73245. doi: 10.7554/eLife.73245. PMID: 35815941; PMCID: PMC9328765.

other targeted therapies, resistance inevitably occurs(20, 21). Therefore, disrupting downstream metabolic crosstalk mechanisms in PDA is a compelling combinatorial or alternative approach(22).

In support of this idea, previous work from our lab described that PDA cells are uniquely dependent on KRAS*-mediated rewiring of glutamine metabolism for protection against oxidative stress(11). Mitochondrial glutamate oxaloacetate transaminase 2 (GOT2) is implicated in this rewired metabolism in PDA. In Chapter 3, I discussed how in normal physiology, GOT2 functions in the malate-aspartate shuttle (MAS), a mechanism by which cells transfer reducing equivalents between the cytosol and mitochondria to balance the two independent NADH pools and maintain redox balance (**Fig. 4-1A**). PDA cells driven by KRAS* divert metabolites from the MAS and increase flux through malic enzyme 1 (ME1) to produce NADPH(11). Since this pathway is critical for PDA, we set out to evaluate GOT2 as a potential therapeutic target. Using metabolomics analyses and manipulation of the redox state in PDA cells, we discovered that loss of GOT2 in vitro induces intracellular NADH accumulation and reductive stress. These metabolic changes impair cellular growth, which can be rescued with chemical or genetic interventions that oxidize NADH. However, loss of GOT2 had no effect on tumor growth or initiation in immunocompromised or immunocompetent mouse models of PDA. Cancer cells utilize a complex cell-intrinsic rewiring and crosstalk with the TME to maintain redox homeostasis in vivo. These data emphasize an under-appreciated role for GOT2 in pancreatic tumor redox homeostasis and illustrate the differential biochemical pathways and metabolic plasticity deployed by cancer cells in vivo.

4.2 Results

4.2.1 Loss of GOT2 impairs PDA cell proliferation in vitro

To expand on our previous work studying GOT2 in PDA(11), and to evaluate GOT2 as a potential therapeutic target, we generated a panel of PDA cell lines with doxycycline-inducible expression of either a control non-targeting shRNA (shNT) or two independent shRNAs (sh1, sh2) targeting the *GOT2* transcript. Cells cultured in media containing doxycycline (+Dox) exhibited a marked decrease in GOT2 protein expression compared to cells cultured in media without doxycycline (-Dox) (**Fig. 4-1B; Fig. 4-2A**). This knockdown was specific for GOT2, relative to the cytosolic aspartate aminotransaminase GOT1 (**Fig. 4-2B**). Having validated GOT2 knockdown (KD), we tested the importance of GOT2 for cellular proliferation. In general, GOT2 KD in PDA cells impaired colony formation (**Fig. 4-1C,D; Fig. 4-2C**) and proliferation (**Fig. 4-2D**). Consistent with our previous report(11), GOT2 was not required for the proliferation of non-transformed pancreatic cell types (**Fig. 4-2E,F).**

Since GOT2 has several vital metabolic roles in a cell (**Fig. 4-1A**), the changes caused by decreased GOT2 expression in PDA cells were examined using liquid chromatography coupled tandem mass spectroscopy (LC-MS/MS). Numerous changes in the intracellular metabolome of GOT2 KD cells were observed (**Fig. 4-3A,B**). Of note, the products of the GOT2-catalyzed reaction, aspartate (Asp) and α-ketoglutarate (αKG), were decreased (**Fig. 4-1E**), and supplementation of these metabolites rescued growth of GOT2 KD (**Fig. 4-1F**). While these PDAC cell lines do not express Asp transporters, we confirmed that supraphysiological levels of Asp (20-fold excess) led to an increase in intracellular Asp (**Fig. 4-3C**). In addition to reduced αKG, there was a

disruption in TCA cycle intermediates, consistent with a role for GOT2 in facilitating glutamine anaplerosis (**Fig. 4-3D**).

4.2.2 GOT2 KD perturbs redox homeostasis in PDA cells

Aside from the expected decrease in Asp and αKG, and the perturbation of the TCA cycle, closer examination of the GOT2 KD metabolomics dataset revealed an impairment in glycolysis with a node at glyceraldehyde 3-phosphate dehydrogenase (GAPDH), indicative of NADH reductive stress (**Fig. 4-4A**). Examination of glycolytic rate via Seahorse Flux Analysis confirmed that glycolysis was indeed impaired in GOT2 KD cells (**Fig. 4-5A**). GAPDH reduces NAD+ to produce NADH, where a build-up of NADH product-inhibits GAPDH activity. Indeed, metabolite pools in upstream glycolysis and branch pathways like the pentose phosphate pathway are increased, and those in downstream glycolysis are decreased (**Fig. 4-4B**). In cultured PDA cells, the MAS transfers glycolytic reducing potential to drive the electron transport chain (ETC) and support the maintenance of cytosolic redox balance (**Fig. 4-1A**). We thus hypothesized that GOT2 KD interrupted this shuttle, preventing the proper transfer of electron potential in the form of NADH between these two compartments. In support of this, GOT2 KD increased the intracellular ratio of NADH to NAD+ (**Fig. 4-4C**).

NADH accumulation leads to reductive stress, which can be relieved if the cell has access to electron acceptors(23). Pyruvate is a notable metabolite in this regard, as it can accept electrons from NADH, producing lactate and regenerating NAD+, in a reaction catalyzed by lactate dehydrogenase (LDH). Therefore, we hypothesized that pyruvate could rescue the defect in cellular proliferation mediated by GOT2 KD. Indeed, culturing GOT2 KD cells in pyruvate rescued proliferation in a dose dependent manner

(**Fig. 4-4D,E; Fig. 4-5B**). Additionally, cells expressing a genetically-encoded, fluorescent ATP sensor indicated that ATP levels dropped with GOT2 KD and were restored with pyruvate supplementation (**Fig. 4-5C**), reflecting the link between TCA cycle activity, respiration, and oxidative phosphorylation. Furthermore, having identified a metabolite that permits in vitro proliferation of PDA cells without GOT2, we engineered CRISPR-Cas9 *GOT2* knock out (KO) cells for further investigation (**Fig. 4-5D**). In support of the data generated using the doxycycline-inducible shRNA, *GOT2* KO impaired colony formation of PDA cells, which was similarly restored through extracellular pyruvate supplementation (**Fig. 4-5E,F**).

α-ketobutyrate (αKB) is another electron acceptor that turns over NADH in a mechanism analogous to pyruvate but without entering downstream metabolism in the same fashion as pyruvate(24). αKB also rescued proliferation after GOT2 KD (**Fig. 4-4F; Fig. 4-5F**). This mechanism is dependent on NADH turnover, and not NAD+ synthesis, as the NAD+ precursor nicotinamide mononucleotide (NMN) failed to rescue GOT2 KD (**Fig. 4-5G**)

To test this further, GOT2 KD cells were engineered to express either doxycycline-inducible cytosolic or mitochondrial *Lactobacillus brevis* NADH oxidase (LbNOX), which uses molecular oxygen to oxidize NADH and produce water and NAD+ (**Fig. 4-6A**)(25, 26). Cytosolic LbNOX, but not mitochondrial LbNOX (mLbNOX), rescued proliferation of GOT2 KD cells (**Fig. 4-4G; Fig. 4-6B**). We confirmed the mLbNOX construct encoded a functional enzyme as defects in proliferation incurred by treatment with complex I inhibitor Piericidin could be rescued with mLbNOX as reported previously (**Fig. 4-6C**)(26). LbNOX reversed the increased NADH/NAD+ ratio induced

by GOT2 KD via an overall decrease in NADH levels (**Fig. 4-4H; Fig. 4-6D**). Further, the secreted pyruvate/lactate ratios in the media of LbNOX-expressing cells dramatically increased, indicating a resolution of the cytosolic NADH stress induced by GOT2 KD (**Fig. 4-6E,F**). Moreover, the metabolic defects observed following GOT2 KD were ameliorated by cytosolic LbNOX activity, including an increase in Asp and αKG, normalization of TCA cycle metabolites, and the release of the glycolytic block at GAPDH (**Fig. 4-6G**). The spatial control of the LbNOX system indicated that KD of mitochondrial GOT2 could be rescued by balancing the cytosolic NADH/NAD+ pool.

Next, we traced the metabolic fate of U13C-pyruvate in cells with GOT2 KD. Importantly, we also assessed the impact and metabolism of pyruvate in this system following inhibition of the mitochondrial pyruvate carrier (MPC) inhibitor UK5099, which blocks entry of pyruvate into the mitochondria. (**Fig. 4-4I**). Media containing equimolar unlabelled glucose and U13C-pyruvate was used to prevent dilution of the pyruvate label by unlabelled pyruvate generated via glycolysis from the high glucose concentration used in normal media. This media formulation had no impact on the pyruvate GOT2 KD rescue phenotype (**Fig. 4-7A**). In this experiment, roughly 50% of the intracellular pyruvate was labelled (**Fig. 4-4J**), in line with the other half of the unlabelled pyruvate coming from glucose, and most of the labelled pyruvate was converted to lactate (**Fig. 4-4K**). We observed modest labelling of citrate, aspartate, and alanine from pyruvate (**Fig. 4-7B-D**). While the labelled TCA cycle and branching pathway intermediates decreased dramatically with UK5099, this MPC inhibition had no effect on the pyruvate GOT2 KD rescue phenotype (**Fig. 4-7E**).

Both lactate and alanine can fuel oxidation via the TCA cycle(27, 28), and Asp is critical for nucleotide production. Pyruvate can be converted into all three of these metabolites, yet supplementation with exogenous lactate, alanine, or nucleoside bases failed to rescue GOT2 KD (**Fig. 4-7F-H**). These data collectively suggest a redox role for pyruvate-mediated rescue of GOT2 KD, as opposed to entering the mitochondria for ATP production or biosynthesis. These findings provide clear evidence using several orthogonal strategies that GOT2 KD results in accumulation of NADH pools and reductive stress in PDA cells.

4.2.3 GOT2 is not required for PDA tumor growth in vivo

To test the effect of GOT2 KD on in vivo tumor growth, PDA cell lines were injected subcutaneously into the flanks of immunocompromised (NOD *scid* gamma; NSG) mice. We allowed the tumors to establish for 7 days, after which the mice were fed normal chow or doxycycline chow *ad libitum*. Surprisingly, despite the inhibitory in vitro phenotype, and robust suppression of GOT2 expression in vivo, PDA tumors from five different cell lines grew unimpeded with GOT2 KD (**Fig. 4-8A,B; Fig. 4-9A,B**). Nuclear Ki67 staining confirmed that tumors lacking GOT2 were proliferative, and actually displayed a modest, but significant, increase in Ki67-positive nuclei (**Fig. 4-8C,D**). To further examine the role of GOT2 in the proper tissue context, PDA cells were injected orthotopically into the pancreas of NSG mice and tumors were allowed to establish for 7 days before feeding the mice regular or DOX chow. Similar to the flank model, GOT2 KD had no effect on the growth of orthotopic tumors (**Fig. 4-9C**). Having observed a discrepancy between in vitro and in vivo dependence on GOT2 for proliferation, the relative abundances of intracellular metabolites from flank tumors were

analyzed via LC-MS/MS to compare the metabolic changes between cell lines and tumors following loss of GOT2. While GOT2 KD induced some changes in tumor metabolite levels, the affected metabolic pathways were distinct from those observed in vitro, bearing in mind we were comparing homogenous cell lines with heterocellular xenografts (**Fig. 4-8E,F; Fig. 4-9D-F**). Asp abundance was significantly decreased, yet αKG levels remained constant (**Fig. 4-8E**), and TCA cycle intermediates were unaffected (**Fig. 4-9F**). This led us to initially hypothesize that PDA cells rewire their metabolism in vivo to maintain αKG levels when GOT2 is knocked down. However, upon examination of the expression of other αKG-producing enzymes in GOT2 KD tumors, we did not observe a compensatory increase in expression (**Fig. 4-9G**). Certainly, expression does not always dictate metabolic flux, but these data led us to adopt an alternative, cell-extrinsic hypothesis to explain the different in vitro and in vivo GOT2 KD phenotypes. Finally, the glycolytic signature indicative of NADH stress was not observed in the metabolomics analysis from flank GOT2 KD tumors, further illustrating the differential dependence on GOT2 in PDA in vitro and in vivo (**Fig. 4-8F**).

To evaluate the role of GOT2 in an immunocompetent model, we crossed the LSL-$Kras^{G12D}$;Ptf1a-Cre (KC) mouse with $Got2^{f/f}$ mice to generate a LSL-$Kras^{G12D}$;$Got2^{f/f}$;Ptf1a-Cre mouse (KC-Got2) (**Fig. 4-10A, Fig. 4-11A**). Loss of *Got2* had no observable effect on the architecture of the healthy, non-transformed pancreas (**Fig. 4-11B,C**). This is in support of our data demonstrating loss of GOT2 was not deleterious in human, non-malignant pancreatic cell types (**Fig. 4-2F**).

KC-Got2 and KC controls were aged to 3, 6, and 12 months, at which point pancreata were harvested. We confirmed loss of GOT2 in the epithelial compartment

via IHC (**Fig. 4-10B**). No differences were observed in the weights of pancreata between 3 month KC-Got2 and KC mice (**Fig. 4-10C**). Scoring the H&E stained tissues from these groups by a blinded pathologist revealed that KC-Got2 mice had a significantly greater percentage of healthy acinar cells compared to KC controls (**Fig. 4-10D,E**). However, no differences were observed in the percentages of acinar-ductal metaplasia or PanIN grade between KC-Got2 and KC mice (**Fig. 4-10E**). Additionally, we aged KC-Got2 mice to 6 months and compared the pancreata to matched 6 month KC historic controls, observing a slight decrease in weight for KC-Got2 pancreatic (**Fig. 4-10F,G**). A histological analysis by a blinded pathologist did not identify a difference in number or severity of lesions (**Fig. 4-10H**). In addition, both KC and KC-Got2 mice had progressed to carcinoma after aging for 1 year (**Fig. 4-10I,J)**. This suggests that loss of *Got2* does not affect the progression of PDA following transformation by oncogenic Kras.

4.2.4 Cancer-associated fibroblast conditioned media supports colony formation in GOT2 KD cells in vitro

Human PDA tumors develop a complex microenvironment composed of a tumor-promoting immune compartment, a robust fibrotic response consisting of diverse stromal cell types, and a dense extracellular matrix (ECM)(18). While the flank tumor milieu in immunocompromised mice is less complex than that of a human PDA tumor, α-smooth muscle actin (αSMA) staining revealed that activated mouse fibroblasts comprised a substantial portion of the microenvironment in tumors regardless of GOT2 status (**Fig. 4-13A**). Additionally, we and others have previously reported mechanisms by which CAFs in the stroma engage in cooperative metabolic crosstalk with pancreatic

cancer cells(28-30). So, we hypothesized that CAFs supported PDA metabolism following GOT2 KD. To investigate potential metabolic crosstalk in a simplified setting, PDA cells were cultured in vitro with conditioned media (CM) from human CAFs (hCAFs). In support of our hypothesis, hCAF CM promoted colony formation in PDA cells with GOT2 KD in a dose-dependent manner (**Fig. 4-12A,B; Fig. 4-13B**). Furthermore, hCAF CM displayed a more pronounced colony formation rescue phenotype compared to CM from tumor-educated macrophages (TEMs) or from PDA cells (**Fig. 4-13C**).

To begin to identify the factors in hCAF CM responsible for this effect, hCAF CM was boiled, filtered through a 3 kDa cut-off membrane, or subjected to cycles of freezing and thawing. In each of these conditions, hCAF CM supported colony formation in GOT2 KD cells, suggesting the relevant factor(s) was a metabolite (**Fig. 4-12C; Fig. 4-13D**). Therefore, the relative abundances of metabolites in hCAF CM were analyzed via LC-MS/MS (**Fig. 4-13E**). Interestingly, when the metabolites were ranked in order of relative abundance, compared to the media control, pyruvate was one of the most differentially abundant metabolites released by hCAFs into the conditioned media (**Fig. 4-12D**). Since we used pyruvate-free DMEM to culture hCAFs, to avoid overinterpreting this finding, we quantified the absolute concentration of pyruvate in hCAF CM at 250 µM, with some variability between batches (**Fig. 4-12E**). This is a physiologically relevant concentration of pyruvate in serum collected from mice harboring pancreatic tumors(31), and 250 µM pyruvate rescued GOT2 KD in vitro (**Fig. 4-12E**). Consistent with the idea of metabolite exchange, PDA cells cultured in hCAF CM had elevated levels of intracellular pyruvate (**Fig. 4-13F**).

In the in vivo flank model, mouse fibroblasts infiltrate the pancreatic xenografts and engage in crosstalk with cancer cells. Therefore, we tested whether our findings with hCAFs were also applicable in mouse cancer-associated fibroblasts (mCAFs). mCAFs isolated from a pancreatic flank xenograft in an NSG mouse also secreted pyruvate at similar levels to hCAFs in vitro (**Fig. 4-12E**). Further, mCAF CM promoted PDA colony formation following GOT2 KD (**Fig. 4-12F**, **Fig. 4-13G**). Since these mCAFs are the same CAFs encountered by PDA cells in our in vivo model, these data further support a mechanism by which CAFs compensate for loss of GOT2, by providing pyruvate to PDA cells lacking GOT2.

To better understand the production and release of pyruvate in CAFs, we traced glucose metabolism using uniformly carbon labeled (U13C)-Glucose and LC-MS metabolomics. We demonstrate that the pyruvate released by CAFs was produced from glucose (**Fig. 4-12G**), and, in support of previous studies(32, 33), these CAFs displayed labelling patterns indicative of glycolytic metabolism (**Fig. 4-12H**).

Aside from pyruvate, we also detected significantly elevated levels of Asp and αKG in CAF CM (**Fig. 4-13E**). Since these are metabolites produced by GOT2, we next asked whether they were present at sufficient concentrations in CAF CM to compensate for loss of GOT2 in vitro. However, we quantified Asp at 15 μM and αKG at 50 μM in CAF CM (**Fig. 4-14A**), well below the reported values from mouse serum(31). Furthermore, millimolar levels of Asp are required to impact intracellular levels, as PDA cell lines do not express an Asp transporter(34), and dimethyl-αKG must be used as αKG has limited membrane permeablility(35). Nevertheless, we tested the rescue activity of reported serum levels of Asp and αKG (50 μM and 500 μM, respectively)(31), again

utilizing the dimethyl-αKG, and compared this to serum levels of pyruvate (250 μM). Here we found that pyruvate rescued proliferation of GOT2 KD to a greater extent than the combination of Asp and αKG (**Fig. 4-14B**). Therefore, we conclude that pyruvate, and not Asp or αKG, is responsible for the GOT2 KD rescue activity of CAF CM in vitro.

Like GOT2 inhibition, it is well-established that inhibiting the activity of complex I of the ETC also results in an increase in NADH, which can be counteracted with extracellular pyruvate(23, 24, 26, 34). Therefore, since pyruvate is highly abundant in hCAF CM, we hypothesized that PDA cells cultured in hCAF CM would be protected from complex I inhibitors. Indeed, both hCAF CM and extracellular pyruvate conferred resistance to PDA cells against the complex I inhibitors rotenone, phenformin, and IACS-010759 (**Fig. 4-14C**)(36). This points to a potential mechanism by which the TME could affect sensitivity to complex I inhibition, though more in depth studies are needed to test this finding further.

4.2.5 Inhibiting pyruvate uptake and metabolism blocks rescue of GOT2 KD in vitro

According to our model, PDA cells are more vulnerable to GOT2 KD or complex I inhibitors in a pyruvate-depleted environment or if pyruvate uptake were blocked. Pyruvate can be transported by four MCT isoforms(37-39), and an analysis of the CCLE database suggests that PDA cell lines primarily express MCT1 and MCT4 (**Fig. 4-16A**). Since MCT1 has a higher affinity for pyruvate than MCT4(38), we decided to focus on MCT1 as the transporter by which PDA cells import pyruvate(40, 41). Indeed, PDA cells express significantly higher levels of MCT1, as compared to hCAFs (**Fig. 4-16B**). Similarly, examining expression of MCT1 from a recently published single cell analysis

of a murine syngeneic orthotopic pancreatic tumor(42) indicated that PDA cells express high levels of MCT1 (**Fig. 4-16C**).

Import/export of pyruvate and lactate through MCT1, as well as the intracellular redox state, is affected by extracellular concentrations of pyruvate and lactate. The absolute concentrations of pyruvate and lactate were measured in hCAF and mCAF CM to calculate the relative pyruvate/lactate ratio from in vitro GOT2 KD rescue experiments (**Fig. 4-15A**). In parallel, the absolute levels of pyruvate and lactate, and the relative ratio, were measured in tumor interstitial fluid (TIF) from flank xenografts and in serum from host mice (**Fig. 4-15B**). When the measured pyruvate and lactate levels from each of these permutations were added back to regular media, the pyruvate/lactate ratios mimicking CAF CM, serum, or TIF promoted the growth of GOT2 KD cells in vitro (**Fig. 4-15C**). These data indicate the pyruvate/lactate ratios in CAF CM in vitro and in the in vivo TME are favorable for pyruvate import, possibly through MCT1.

Therefore, we hypothesized that blocking pyruvate import through MCT1 would render cells vulnerable to GOT2 KD. The small molecule AZD3965 has specificity for MCT1 over MCT4(43-45), therefore GOT2 KD cells were cultured in pyruvate or hCAF CM in the presence of AZD3965. In support of our hypothesis, MCT1 chemical inhibition reduced the pyruvate and hCAF CM rescue of GOT2 KD (**Fig. 4-15D**).

For a genetic approach, MCT1 was knocked down in doxycycline-inducible GOT2 KD cells (**Fig. 4-16D,F**). MCT1 KD modestly slowed the growth of GOT2 KD cells cultured in pyruvate or hCAF CM (**Fig. 4-16E,G**). We reasoned that partial knockdown could explain why MCT1 KD had a more modest effect than chemical inhibition of MCT1. Therefore, we next generated MCT1 KO clones in GOT2 KD cells (**Fig. 4-15E**). Indeed,

MCT1 KO in GOT2 KD cells blocked pyruvate rescue (**Fig. 4-15F**). We also demonstrate that MCT1 inhibition was most effective at physiological levels of pyruvate (250 µM) (**Fig. 4-15F, Fig. 4-16H**). Furthermore, MCT1 KO cells cultured with U13C-pyruvate demonstrated reduced uptake of pyruvate, as measured by intracellular labelled pyruvate (**Fig. 4-15G**). Since pyruvate is rapidly imported and converted to lactate, the reduced pyruvate uptake was observed more clearly in dramatically reduced levels of labelled lactate in MCT1 KO cells (**Fig. 4-15G**). Lastly, MCT1 blockade was tested in combination with complex I inhibitors in PDA cells cultured in pyruvate or hCAF CM. AZD3965 also reversed the rescue activity of pyruvate or hCAF CM in PDA cells treated with IACS-010759 (**Fig. 4-16I**).

The reduction of pyruvate to lactate by lactate dehydrogenase (LDH) is the central mechanism in our model by which NAD+ is regenerated to support proliferation in GOT2 inhibited cells. Thus, we next asked whether inhibiting LDH activity could also prevent GOT2 KD rescue by pyruvate or hCAF CM. Our PDA cell lines highly expressed the LDHA isoform of LDH, as determined by western blotting (**Fig. 4-16J**). As such, we utilized the LDHA-specific chemical inhibitor FX11 in this study(46). In further support of our model, inhibiting LDHA with FX11 slowed the in vitro proliferation of GOT2 KD cells cultured in pyruvate or hCAF CM, relative to single agent controls (**Fig. 4-15H**, **Fig. 4-16K**).

Cumulatively, these data support an in vitro model whereby perturbation of mitochondrial metabolism with GOT2 KD or complex I inhibition disrupts redox balance in PDA cells. This can be restored through import of pyruvate from the extracellular environment and reduction to lactate to regenerate NAD+.

4.2.6 Metabolic plasticity in vivo supports adaptation to combined GOT2 KD and inhibition of pyruvate metabolism

This proposed in vitro mechanism suggests that the unhampered growth of GOT2 inhibited tumors (**Fig. 4-4A,B**) could be explained by uptake of pyruvate from the TME. In vitro, MCT1 KD had a modest effect on the proliferation of GOT2 KD cells cultured in pyruvate or hCAF CM. In contrast, we found that MCT1 KD had no effect on the growth of GOT2 KD subcutaneous xenografts (**Fig. 4-17A, B**). A caveat of this finding was the observed detectable levels of MCT1 at endpoint (**Fig. 4-17C,D**). However, MCT1 KO similarly did not impact the growth of GOT2 KD tumors in vivo, which is in stark contrast to the results observed in vitro whereby MCT1 KO blocked the rescue of colony formation in GOT2 KD cells by pyruvate (**Fig. 4-17E**). In these tumors, MCT1 was not detectable at endpoint and we did not observe a compensatory increase in MCT4 expression in either cell lines or xenografts with MCT1 KO (**Fig. 4-17F,G**). Similarly, administration of AZD3965 did not impact the growth of GOT2 KD xenografts, again contrasting our in vitro data showing strong blockade of GOT2 KD rescue by pyruvate or hCAF CM with MCT1 chemical inhibition (**Fig. 4-17E-G**). Lastly, unlike in vitro, FX11 had no effect on GOT2 KD growth in vivo (**Fig. 4-18A,B**).

4.3 Discussion

GOT2 is an essential component of the MAS(47), which we now demonstrate is required for redox homeostasis in PDA cells in vitro. Knockdown of GOT2 in vitro disrupts the MAS and renders PDA cells incapable of transferring reducing equivalents between the cytosol and mitochondria, leading to a cytosolic accumulation of NADH.

This predominantly impacts the rate of glycolysis, an NAD+-coupled pathway, with secondary impacts on mitochondrial metabolism, that together slow the proliferation of PDA cells in vitro. For instance, GOT2 feeds into the ME1 shunt, which we demonstrated previously also produces pyruvate and sustains intracellular NADPH levels(48). Extracellular supplementation of electron acceptors like pyruvate and αKB, or the expression of a cytosolic NADH oxidase, relieves this NADH reductive stress and the associated pathway feedback inhibition.

In striking contrast to the in vitro data presented herein, we also illustrate that GOT2 KD does not affect the growth of PDA tumors in vivo, potentially because electron acceptors in the tumor microenvironment can restore redox homeostasis. Indeed, pyruvate is present in mouse serum at 250 μM(31), a concentration which is sufficient to compensate for GOT2 KD in vitro. Furthermore, we also demonstrate that pancreatic CAFs release pyruvate in vitro, which can be utilized by PDA cells. This is supported by previous findings in CAFs from other cancers(49). Therefore, a source of pyruvate is available to PDA tumors, either from circulation or potentially from the CAFs.

This led us to hypothesize that blocking pyruvate uptake and metabolism would deprive PDA cells of a critical means to relieve the NADH stress mediated by GOT2 KD. In vitro, this hypothesis was supported by data illustrating that either inhibition of MCT1 or LDHA blocked the GOT2 KD rescue activity of pyruvate and CAF CM. However, this proved to be more complicated in vivo, as neither approach successfully sensitized tumors to GOT2 KD. We believe this could be explained by several mechanisms. First, previous work in KRAS*-driven non-small cell lung cancer (NSCLC) reported differential dependencies on glutaminolysis in vitro in cells lines versus in vivo in lung tumors.

Glutaminase inhibition was ineffective in vivo in these models as lung tumors primarily utilized glucose as a carbon source for the TCA cycle instead of glutamine. If this mechanism is active in our models, glucose, and not glutamine catabolism through GOT2, would fuel the TCA cycle. Second, while MCT4 has a lower affinity for pyruvate than MCT1, it can transport pyruvate(38). It is also highly expressed in the cell lines used here (**Fig. 4-17F,G**) and has been shown to confer resistance to cancer cells against MCT1 inhibition (50, 51). Thus, dual inhibition of MCT1 and MCT4 may be required to effectively block pyruvate uptake. Third, even with sufficient MCT blockade, PDA cells could still obtain pyruvate through other processes, such as macropinocytosis(7, 9). Fourth, while our study focuses on pyruvate, numerous circulating metabolites can function as electron acceptors and could relieve the intracellular accumulation of NADH if cancer cells are unable to import pyruvate(52). Fifth, reduction of pyruvate to lactate by LDH is not the only reaction by which NAD+ is regenerated. Recent studies have identified how serine pathway modulation, polyunsaturated fatty acid synthesis, and the glycerol-phosphate shunt all contribute to NADH turnover(53-55). Future work remains to assess these mechanisms in PDA cells in vivo and if they compensate for an impaired MAS (see Chapter 5). Nevertheless, our data emphasize that redox homeostasis is a vital aspect of cancer cell metabolism and is maintained through a complex web of intracellular compensatory pathways and extracellular interactions.

Aside from its broader role in redox balance, GOT2 is also a prominent source of aspartate in PDA cells, and we demonstrate that GOT2 inhibition dramatically decreases aspartate levels both in vitro and in vivo. Previous studies have shown that

aspartate availability is rate limiting in rapidly proliferating cells(24, 34, 56, 57). In our models, in contrast to physiological pyruvate concentrations simultaneous treatment with supraphysiological doses of both Asp and membrane-permeable dimethyl-αKG were required to provide a rescue of PDA cell proliferation in the absence of GOT2. Additionally, free Asp is available at low micromolar concentrations and has limited uptake capacity of PDA cells(31). Supplementation of physiologically relevant concentrations of Asp and αKG afforded a modest rescue compared to physiological pyruvate. Furthermore, exogenous protein supplementation with bovine serum albumin (BSA), another potential source for aspartate, failed to rescue GOT2 KD in vitro (**Fig. 4-18C**). While non-specific engulfment of extracellular matrix (ECM) via macropinocytosis in vivo could supply PDA cells with Asp (58), meeting a vital requirement for biosynthesis, we propose this does not address overall redox imbalance. Pyruvate, on the other hand, regenerates NAD+ allowing broader metabolic processes to resume, including Asp production and nucleotide biosynthesis. In support of this, recent work in myoblasts demonstrated that while complex I inhibition with piericidin increased the NADH/NAD+ ratio leading to depletion of Asp, adding Asp back to the system neither restored redox balance nor induced proliferation(59).

Our work also highlights the emerging metabolic role of cancer-associated fibroblasts (CAFs) in PDA. Recent studies have shown that CAFs engage in cooperative metabolic crosstalk with cancer cells in many different tumor types(19, 28, 29, 60, 61). We add to this body of literature by demonstrating that CAFs release pyruvate, which is taken up and utilized by PDA cells. However, much remains to be discovered about CAF metabolism how they contribute to redox homeostasis in tumors.

Some types of activated fibroblasts are known to be highly glycolytic(32, 33), an observation supported by our data. Yet the advent of single-cell RNA sequencing in murine and human pancreatic tumor models has led to a recent appreciation for the heterogeneity of CAFs(62-67). The newly identified iCAF, myCAF, and apCAF populations have distinct functions in a pancreatic tumor(62) and likely employ distinct metabolism to carry out these functions. Much more remains to be uncovered regarding competitive or cooperative interactions between PDA cells and the various CAF subpopulations, including which subtype(s) are responsible for pyruvate release (see Chapter 5).

Lastly, this work suggests that the role of the tumor microenvironment should be considered when targeting cancer metabolism. Indeed, approaches like disrupting the MAS shuttle via GOT2 KD or blocking complex I with small molecule inhibitors were less effective in vitro when PDA cells were cultured in supplemental pyruvate or CAF CM. These data are relevant since numerous mitochondrial inhibitors are currently in clinical trials against solid tumor types (NCT03291938, NCT03026517, NCT03699319, NCT02071862). Previous studies have also shown that complex I inhibitors are more effective in combination with AZD3965(68), a selective inhibitor of MCT1, though our work and others indicate that the status of other MCT isoforms should also be considered. Furthermore, the abundance of CAFs present in a tumor, as well as the level of circulating pyruvate in the patient, could predict outcomes for treatment with metabolic therapies that lead to redox imbalance. Targeting pancreatic cancer metabolism is an alluring approach, and a more detailed understanding of the metabolic

crosstalk occurring in a pancreatic tumor can shed light on potential resistance mechanisms and inform more effective metabolic therapies.

4.4 Materials and Methods

Cell culture

MIAPaCa-2, BxPC-3, Capan-1, Panc03.27, Panc10.05, PL45, and HPNE cell lines were obtained from ATCC. PaTu-8902, PaTu-8988T, and YAPC cells lines were obtained from DSMZ. UM6, UM19, UM28, UM32, UM53, and UM76 were generated from primary patient tumors at the University of Michigan. Human pancreatic stellate cells (hPSCs, also described here as hCAFs) were a generous gift from Rosa Hwang (69). Mouse cancer-associated fibroblasts (mCAFs) were isolated as described below. All cell lines were cultured in high-glucose Dubelcco's Modified Eagle Medium (DMEM, Gibco) without pyruvate and supplemented with 10% fetal bovine serum (FBS, Corning). 0.25% Trypsin (Gibco) was used to detach and passage cells. Cell lines were tested regularly for mycoplasma contamination using MycoAlert (Lonza). All cell lines in this study were validated for authentication using STR profiling via the University of Michigan Advanced Genomics Core. L-Aspartic acid (Sigma), dimethyl-α-ketoglutarate (Sigma), adenine (Sigma), guanine (Sigma), thymine (Sigma), cytosine (Sigma), sodium pyruvate (Invitrogen), α-ketobutyrate (Sigma), nicotinamide mononucleotide (NMN, Sigma), L-alanine (Sigma), and sodium lactate (Sigma) were used at the indicated concentrations. UK5099, AZD3965, and phenformin were purchased from Cayman chemical, Rotenone from Sigma, FX11 from MedChem Express, and IACS-010759 was generously provided by Dr. Giulio Draetta, University of Texas MD Anderson Cancer Center.

Doxy-inducible shGOT2 cells

The tet-pLKO-puro plasmid was obtained from Dmitri Wiederschain via Addgene (#21915). Oligonucleotides encoding sense and antisense shRNAs (shGOT2.1- TRCN0000034824, shGOT2.2- TRCN0000034825) targeting *GOT2* (NM_002080.4) were synthesized (Integrated DNA Technologies), annealed, and cloned at AgeI and EcoRI sites according to the Wiederschain Protocol(70). A tet-pLKO non-targeting control vector (shNT-CCGGCAACAAGATGAAGAGCACCAACTCGAGTTGGTGCTCTTCATCTTGTTGTTTTT) was constructed using the same strategy. Tet-pLKO-shGOT2 and tet-pLKO-shNT lentiviruses were produced by the University of Michigan Vector Core using purified plasmid DNA. Stable cell lines were generated through transduction with optimized viral titers and selection with 1.5 µg/mL puromycin for 7 days.

GOT2 or MCT1 knockout cells

GOT2 or *SLC16A1* (MCT1) knockout PDA cell lines were generated using a CRISPR-Cas9 method described previously(71). Briefly, sgRNA oligonucleotide pairs were obtained from the Human GeCKO Library (v2, 3/9/2015). For *GOT2* KO (sg1 (Fwd) 5'-CACCgAAGCTCACCTTGCGGACGCT-3', (Rev) 5'-AAACAGCGTCCGCAAGGTGAGCTTc; sg2 (Fwd) 5'-CACCgCGTTCTGCCTAGCGTCCGCA-3', (Rev) 5'-AAACTGCGGACGCTAGGCAGAACGc-3'), and for MCT1 KO (sg1 (Fwd) 5'-CACCgTGGGCCCGATTGGTCGCATG-3', (Rev) 5'-AAACCATGCGACCAATCGGGCCCAc; sg2 (Fwd) 5'-CACCgTTTCTACAAGAGGCGACCAT-3', (Rev) 5'-

AAACATGGTCGCCTCTTGTAGAAAc-3'), were cloned into the pSpCas9(BB)-2A-Puro plasmid (PX459, v2.0; Addgene, #62988), transfected in PDA cell lines, and selected in puromycin for 7 days. Cells were then seeded into 96 well plates at a density of 1 cell per well, and individual clones were expanded. *GOT2* KO cells were maintained in 1 mM pyruvate for this entire process. *GOT2* knockout was verified via Western blot. Cells transfected with the empty PX459 vector were used as controls.

MCT1 KD cells

Cells were transduced with 8 µg/mL polybrene and lentivirus containing the pGFP-C-shLenti plasmid (Origine, #TR30023) containing an shCTR sequence, shMCT1.1 [TL309405A (5′-GAGGAAGAGACCAGTATAGATGTTGCTGG-3′)], or shMCT1.2 [TL309405B (5′-ATCCAGCTCTGACCATGATTGGCAAGTAT-3′)]. These plasmids were a generous gift from Dr. Sean Morrison(45). The cells were then centrifuged at 1000xg for 60 minutes at room temperature. Transduced cells were then expanded and sorted on the MoFlo Astrios (Beckman-Coulter). GFP+ cells were collected and expanded before verification of MCT1 KD via Western blotting.

Transduction of LbNOX/mitoLbNOX: pINDUCER (Addgene, #44014) plasmids containing GFP, LbNOX, or mitoLbNOX were obtained from Dr. Haoqing Ying, MD Anderson. Plasmids were sequenced and transfected along with lentiviral packaging plasmids into HEK293FT cells with Lipofectamine 3000 (Thermo Fisher) per manufacturer's instructions. Virus was collected after 48 hours and filtered through a 0.2 µm filter. PaTu-8902 and MIAPaCa-2 iDox-shGOT2.1 cells were seeded in 6 well plates at 250,000 cells/well, transduced with the indicated vectors, and selected in G418 at 500 µg/mL for 7 days. Expression of Flag-tagged LbNOX or mitoLbNOX was confirmed

by Western blot with a Flag antibody after culturing cells in 1 µg/mL doxycycline for 3 days.

Luciferase-expressing cells

MIAPaCa-2 iDox-shGOT2.1 cells were transduced with the FUGW-FL (EF1a-luc-UBC6-EGFP) lentiviral vector constructed previously(72) and GFP+ cells were selected via flow cytometry. Luciferase activity was confirmed following transduction and selection with an in vitro luciferase assay and detection on a SpectraMax M3 Microplate reader (Molecular Devices).

ATP fluorescent sensor/Incucyte growth assays

PaTu-8902 and MIAPaCa-2 iDox-GOT2.1 cells were transduced with CytoATP or CytoATP non-binding control vectors using the CytoATP Lentivirus Reagent Kit (Sartorious, #4772) and polybrene transfection reagent (Thermo Fisher) and selected for 7 days in 2 µg/mL puromycin. For proliferation and rescue experiments, cells were incubated in an Incucyte (Sartorious) equipped with a Metabolism Optical Module, where the ratio of ATP binding was detected and normalized to the non-binding control cells. Proliferation rate was determined by the percent confluence detected in the phase channel of the Incucyte normalized to Day 0 for each condition.

Isolating mouse CAFs

UM2 subcutaneous xenografts from NSG mice were isolated and prepared in the laboratory of Dr. Diane Simeone, as reported previously(73), and single cell suspensions were plated and cultured *in vitro*. Mouse CAFs were separated from

human pancreatic UM2 cancer cells using the Mouse Cell Depletion Kit (MACS Miltenyi Biotec) according to the manufacturer's instructions.

Conditioned media

Conditioned media was generated by splitting cells at ~90% confluence in a 10 cm^2 plate into four 15 cm^2 plates containing a final volume of 27 mL of growth media, and incubating for 72 hours at 37°C, 5% CO_2. Afterward, the media was collected in 50 mL conical tubes, centrifuged at 1,000 rpm for 5 minutes to remove any detached cells or debris, and divided into fresh 15 mL conical tubes in 10 mL aliquots for long-term storage at -80°C. For all conditioned media experiments, unless indicated otherwise, growth media was mixed with conditioned media for a final ratio of 75% conditioned media to 25% fresh growth media.

For the experiments in Figure 5C and Figure 5-figure supplement 1D, conditioned media were manipulated as follows. For boiling, the conditioned media tubes were placed in a water bath at 100°C for 10 minutes. To filter out factors >3 kDa, the conditioned media were transferred to a 3 kDa filter (Millipore) and centrifuged at 15,000 rpm in 30-minute increments until all the conditioned media had passed through the filter. To expose the conditioned media to freeze-thaw cycles, the tubes containing the conditioned media were thawed for 30 minutes in a 60°C water bath, and then frozen at -80°C for 30 minutes. This was repeated two more times for a total of three freeze-thaw cycles.

Colony formation assays

Cells were seeded in 6 well plates at 200-400 cells per well in 2 mL of growth media and incubated overnight at 37°C, 5% CO_2. The next day, the growth media was

aspirated and fresh media containing the indicated compounds were added to the cells. Doxycycline was used at 1 µg/mL for all assays. For each assay, cells were incubated in the indicated conditions for 10 days, with the media and doxycycline changed every three days. After 10 days, the media was aspirated, the wells were washed once with PBS, and the cells were fixed in 100% methanol for 10 minutes. Next, the methanol was removed, and the cells were stained with 0.4% crystal violet for 10 minutes. Finally, the crystal violet was removed, the plates were washed under running water and dried on the benchtop overnight. The next day, images were taken of the plates with a Chemidoc BioRad imager and quantified using the ColonyArea plugin in ImageJ, as described previously(74).

Proliferation assays

Cells were pre-treated for 3 days with 1 µg/mL doxycycline before seeding in 96 well plates at 1,000 cells/well in 80 µL of media and incubated overnight at 37°C, 5% CO_2. The next day, 150 µL of the indicated treatment media was added to the appropriate wells, and the cells were incubated for 6-7 more days, with a media change on day 3. Cell proliferation was determined by live cell imaging for the duration of the assay, or using CyQUANT (Invitrogen) at endpoint according to the manufacturer's instructions, and detecting fluorescence on a SpectraMax M3 Microplate reader (Molecular Devices).

Glycolytic rate assay

PaTu-8902 iDox-shGOT2.1 cells that had been cultured in 1 µg/mL doxycycline for 3 days were seeded at $2x10^4$ cells/well in 80 µl/well of normal growth media in an Agilent XF96 V3 PS Cell Culture Microplate (Agilent). To achieve an even distribution of cells within wells, plates were incubated on the bench top at room temperature for 1 hour

before incubating at 37ºC, 5% CO_2 overnight. To hydrate the XF96 FluxPak (Agilent), 200 µL/well of sterile water was added and the entire cartridge was incubated at 37ºC, CO_2-free incubator overnight. The following day, one hour prior to running the assay, 60 µL of media was removed, and the cells were washed twice with 200 µL/well of assay medium (XF DMEM Base Medium, pH 7.4 containing 25 mM Glucose and 4 mM Glutamine; Agilent). After washing, 160 µL/well of assay medium was added to the cell culture plate for a final volume of 180 µL/well. Cells were then incubated at 37ºC, in a CO_2-free incubator until analysis. In parallel, one hour prior to the assay, water from the FluxPak hydration was exchanged for 200 µL/well of XF Calibrant 670 (Agilent) and the cartridge was returned to 37ºC, CO_2-free incubator until analysis. Rotenone/Antimycin (50 µM, Agilent) and 2DG (500 mM, Agilent) were re-constituted in assay medium to make the indicated stock concentrations. 20 µL of rotenone/antimycin was loaded into Port A for each well of the FluxPak and 22 µL of 2DG into Port B, for a final concentration of 0.5 µM and 50 mM, respectively. The Glycolytic Rate Assay was conducted on an XF96 Extracellular Flux Analyzer (Agilent) and PER was calculated using Wave 2.6 software (Agilent). Following the assay, PER was normalized to cell number with the CyQUANT NF Cell Proliferation Assay (Invitrogen) according to manufacturer's instructions.

Protein lysates

Cell lines cultured in 6 well plates in vitro were washed with ice-cold PBS on ice and incubated in 250 µL of RIPA buffer (Sigma) containing protease (Roche) and phosphatase (Sigma) inhibitors on ice for 10 minutes. Next, cells were scraped with a pipet tip, and the resulting lysate was transferred to a 1.5 mL tube also on ice. The

lysate was centrifuged at 15,000 rpm for 10 minutes at 4°C. After, the supernatant was transferred to a fresh 1.5 mL tube and stored at -80°C.

In vivo tumor tissue was placed in a 1.5 mL tube containing a metal ball and 300 µL RIPA buffer with protease and phosphatase inhibitors. The tissue was homogenized using a tissue lyser machine. Then, the resulting lysate was centrifuged at 15,000 rpm for 10 minutes at 4°C. After, the supernatant was transferred to a fresh 1.5 mL tube and stored at -80°C.

Western blotting

Protein levels were determined using a BCA assay (Thermo Fisher), according to manufacturer's instructions. Following quantification, the necessary volume of lysate containing 30 µg of protein was added to a mixture of loading dye (Invitrogen) and reducing agent (Invitrogen) and incubated at 90°C for 5 minutes. Next, the lysate was separated on a 4-12% Bis-Tris gradient gel (Invitrogen) along with a protein ladder (Invitrogen) at 150 V until the dye reached the bottom of the gel (about 90 minutes). Then, the protein was transferred to a methanol-activated PVDF membrane (Millipore) at 25 V for 1 hour. After that, the membrane was blocked in 5% blocking reagent (Biorad) dissolved in TBS-T on a plate rocked for >1 hour. The membrane was then incubated overnight at 4°C rocking in the indicated primary antibody diluted in blocking buffer. The next day, the primary antibody was removed, and the membrane was washed 3 times in TBS-T rocking for 5 minutes. Then, the membrane was incubated for 1 hour rocking at room temperature in the appropriate secondary antibody diluted in TBS-T. Finally, the membrane was washed as before, and incubated in Clarity ECL reagent (Biorad) according to manufacturer's instructions before imaging on a Biorad

Chemidoc. The following primary antibodies were used in this study: GOT2 (Atlas, HPA018139), GOT1 (Abcam, ab171939), GLUD1 (Abcam, ab166618), IDH1 (Cell Signaling, 3997S), MCT1 (Abcam, ab85021), MCT4 (Sigma, AB3316P), anti-Flag (Sigma, F3165), Vinculin (Cell Signaling, 13901S), LDHA (Cell Signaling, 3582), LDHB (Abcam, ab53292), and the anti-rabbit-HRP secondary antibody (Cell Signaling, 7074S)

Isolating polar metabolites

For intracellular metabolome analyses, cells were seeded at 10,000 cells in 2 mL of growth media per well of a 6 well plate and incubated overnight. The next day, the growth media was removed, and cells were incubated in media containing the indicated compounds for 6 days, with the media being changed every 3 days. On day 6, the media was removed, and the cells were fixed and metabolites extracted into 1 mL/well of ice-cold 80% methanol on dry ice for 10 minutes. Following the incubation, the wells were scraped with a pipet tip and transferred to a 1.5 mL tube on dry ice.

To analyze extracellular metabolomes, 0.8 mL of ice-cold 100% methanol was added to 0.2 mL of media, mixed well, and incubated on dry ice for 10 minutes.

Mouse serum and tumor interstitial fluid (TIF) were isolated and analyzed as described previously(31).

The tubes were then centrifuged at 15,000 rpm for 10 minutes at 4°C to pellet insoluble material, and the resulting metabolite supernatant was transferred to a fresh 1.5 mL tube. The metabolites were then dried on a SpeedVac until the methanol/water had evaporated, and the resulting pellet was re-suspended in a 50:50 mixture of methanol and water.

Snapshot metabolomics

Samples were run on an Agilent 1290 Infinity II LC -6470 Triple Quadrupole (QqQ) tandem mass spectrometer (MS/MS) system with the following parameters: Agilent Technologies Triple Quad 6470 LC-MS/MS system consists of the 1290 Infinity II LC Flexible Pump (Quaternary Pump), the 1290 Infinity II Multisampler, the 1290 Infinity II Multicolumn Thermostat with 6 port valve and the 6470 triple quad mass spectrometer. Agilent Masshunter Workstation Software LC/MS Data Acquisition for 6400 Series Triple Quadrupole MS with Version B.08.02 is used for compound optimization, calibration, and data acquisition.

Solvent A is 97% water and 3% methanol 15 mM acetic acid and 10 mM tributylamine at pH of 5. Solvent C is 15 mM acetic acid and 10 mM tributylamine in methanol. Washing Solvent D is acetonitrile. LC system seal washing solvent 90% water and 10% isopropanol, needle wash solvent 75% methanol, 25% water. GC-grade Tributylamine 99% (ACROS ORGANICS), LC/MS grade acetic acid Optima (Fisher Chemical), InfinityLab Deactivator additive, ESI–L Low concentration Tuning mix (Agilent Technologies), LC-MS grade solvents of water, and acetonitrile, methanol (Millipore), isopropanol (Fisher Chemical).

An Agilent ZORBAX RRHD Extend-C18, 2.1 × 150 mm and a 1.8 um and ZORBAX Extend Fast Guards for UHPLC are used in the separation. LC gradient profile is: at 0.25 ml/min, 0-2.5 min, 100% A; 7.5 min, 80% A and 20% C; 13 min 55% A and 45% C; 20 min, 1% A and 99% C; 24 min, 1% A and 99% C; 24.05 min, 1% A and 99% D; 27 min, 1% A and 99% D; at 0.8 ml/min, 27.5-31.35 min, 1% A and 99% D; at 0.6 ml/min, 31.50 min, 1% A and 99% D; at 0.4 ml/min, 32.25-39.9 min, 100% A; at 0.25 ml/min, 40

min, 100% A. Column temp is kept at 35 ºC, samples are at 4 ºC, injection volume is 2 µl.

6470 Triple Quad MS is calibrated with the Agilent ESI-L Low concentration Tuning mix. Source parameters: Gas temp 150 ºC, Gas flow 10 l/min, Nebulizer 45 psi, Sheath gas temp 325 ºC, Sheath gas flow 12 l/min, Capillary -2000 V, Delta EMV -200 V. Dynamic MRM scan type is used with 0.07 min peak width, acquisition time is 24 min. dMRM transitions and other parameters for each compounds are list in a separate sheets. Delta retention time of plus and minus 1 min, fragmentor of 40 eV and cell accelerator of 5 eV are incorporated in the method.

The MassHunter Metabolomics Dynamic MRM Database and Method was used for target identification. The QqQ data were pre-processed with Agilent MassHunter Workstation QqQ Quantitative Analysis Software (B0700). Each metabolite abundance level in each sample was divided by the median of all abundance levels across all samples for proper comparisons, statistical analyses, and visualizations among metabolites. Metabolites with values >1 are higher in the experimental conditions and metabolites with values <1 are lower in the experimental condition. The statistical significance test was done by a two-tailed t-test with a significance threshold level of 0.05.

Heatmaps were generated and data clustered using Morpheus Matrix Visualization and analysis tool (https://software.broadinstitute.org/morpheus).

Pathway analyses were conducted using MetaboAnalyst (https://www.metaboanalyst.ca).

U13C-Glucose, U13C-Pyruvate isotope tracing or glucose tracing

CAFs were seeded in 6 well plates at $2x10^5$ cells/well and incubated for 72 hours in growth media containing U13C-Glucose (Cambridge Isotope Laboratories). For pyruvate tracing, PaTu-8902 and MIAPaCa-2 iDox-shGOT2.1 cells were cultured in media containing 1 mM unlabelled glucose and 1 mM U13C-Pyruvate (Cambridge Isotope Laboratories) for 16 hours.

Polar metabolites were extracted from the media and cells according to the method described above. Isotope tracing experiments utilized the same chromatography as described in the Snapshot Metabolomics section, and were conducted on two instruments with the following parameters: Agilent Technologies Q-TOF 6530 LC/MS system consists of a 1290 Infinity II LC Flexible Pump (Quaternary Pump), 1290 Infinity II Multisampler, 1290 Infinity II Multicolumn Thermostat with 6 port valve and a 6530 Q-TOF mass spectrometer with a dual Assisted Jet Stream (AJI) ESI source. Agilent MassHunter Workstation Software LC/MS Data Acquisition for 6200 series TOF/6500 series Q-TOF Version B.09.00 Build 9.0.9044.a SP1 is used for calibration and data acquisition.

Agilent 6530 Q-TOF MS is calibrated with ESI-L Low Concentration Tuning mix. Source parameters: Gas temp 250 ºC, Gas flow 13 l/min, Nebulizer 35 psi, Sheath gas temp 325 º C, Sheath gas flow 12 l/min, Vcap 3500 V, Nozzle Voltage (V) 1500, Fragmentor 140, Skimmer1 65, OctopoleRFPeak 750. The MS acquisition mode is set in MS1 with mass range between 50-1200 da with collision energy of zero. The scan rate (spectra/sec) is set at 1 Hz. The LC-MS acquisition time is 18 min and total run time is

30 min. Reference masses are enabled with reference masses in negative mode of 112.9856 and 1033.9881 da.

Agilent Technologies 6545B Accurate-Mass Quadrupole Time of Flight (MS Q-TOF) LC/MS coupled with an Agilent 1290 Infinity II UHPLC. Agilent Masshunter Workstation Software LC/MS Data Acquisition for 6500 Series QTOF MS with Version 09.00, Build9.0.9044.0 was used for tuning, calibration, and data acquisition.

In negative mode, the UHPLC was configured with 1290 Infinity II LC Flexible Pump (Quaternary Pump),1290 Infinity II Multisampler, 1290 Infinity II Multicolumn Thermostat with 6 port valves. In negative scan mode, the Agilent G6545B Q-TOF MS with Dual AJD ESI Sources in centroid mode was configured with following parameters: Acquisition range: 50-1200 da at scan rate of 1 spectra/sec, Gas temp 250 ºC, Gas Flow 13 L/min, Nebulizer at 40 psi, Sheath Gas Heater 325 ºC, Sheath Gas Flow 12L/min, Capillary 3500 V, Nozzle Voltage 1000 V, Fragmentor 130 V, Skimmer1 60 V, Octopole RFPeak 750V, Collision 0 V, Auto Recalibration limit of detection 150 ppm with min height 1000 counts, Reference ions of two at 59.0139 and 980.0164 da.

Data processing was performed in Agilent MassHunter Workstation Profinder 10.0 Build 10.0.10062.0. Isotopologue distributions were derived from a compound standard library built in Agilent MassHunter PCDL (Personal Compound and Database Library) v7.0.

Xenograft studies

Animal experiments were conducted in accordance with the Office of Laboratory Animal Welfare and approved by the Institutional Animal Care and Use Committees (IACUC) of the University of Michigan. NOD scid gamma (NSG) mice (Jackson Laboratory) 6-10

weeks old of both sexes were maintained in the facilities of the Unit for Laboratory Animal Medicine (ULAM) under specific pathogen-free conditions.

Cells expressing doxycycline-inducible shNT or doxycycline-inducible shGOT2 were injected subcutaneously into both the left and right flanks of male and female NSG mice, with 1-4x10^6 cells in a mixture of 50 µL media and 50 µL Matrigel (Corning) per injection. Tumors were established for 7 days before mice were fed either normal chow or chow containing doxycycline (BioServ). Tumors were measured with calipers two times per week, and mice were euthanized once the tumors reached a diameter of 2 cm^3. Subcutaneous tumor volume (V) was calculated as V=1/2(length x $width^2$). At endpoint, the tumors were removed, and fragments were either snap frozen in liquid nitrogen and stored at -80°C or fixed in ZFix solution (Anatech) for histology.

Cells expressing doxycycline-inducible shGOT2 and luciferase were injected into the pancreas tail of NSG mice, with 200,000 cells in a mixture of 50 µL media and 50 µL Matrigel (Corning) per injection. Tumors were established for 7 days before mice were fed either normal chow or chow containing doxycycline (BioServ). Tumor progression was monitored by weekly intraperitoneal injections of luciferin (Promega) and bioluminescence imaging (BLI) on an IVIS SpectrumCT (Perkin Elmer). BLI was analyzed with Living Image software (PerkinElmer) At endpoint, the tumors were removed, and fragments were either snap frozen in liquid nitrogen and stored at -80°C or fixed in ZFix (Anatech) solution for histology.

AZD3965 or FX11 was dissolved in DMSO and stored at -80 ºC in aliquots. Each day, one aliquot was thaw and mixed with a 0.5% Hypromellose (Sigma), 0.2% tween80 (Sigma) solution such that the final DMSO concentration was 5%. Vehicle or AZD3965

was administered at 100 mg/kg by daily oral gavage. FX11 was administered at 2 mg/kg by daily intraperitoneal injection.

Histology

Tissues were processed using a Leica ASP300S tissue processor (Leica Microsystems). Paraffin-embedded tissues were sectioned at 4 μm and stained for specific target proteins using the Discovery Ultra XT autostainer (Ventana Medical Systems), with listed antibodies, and counterstained with Mayer's hematoxylin (Sigma). Hematoxylin and eosin (H&E) staining was performed using Mayer's hematoxylin solution and Eosin Y (Thermo Fisher). IHC slides were then scanned on a Pannoramic SCAN scanner (Perkin Elmer). Scanned images were quantified using algorithms provided from Halo software version 2.0 (Indica Labs). The following antibodies were used for IHC: Ki67 (1:1,000; Abcam, ab15580), αSMA (1:20,000; Abcam, ab5694), Got2 (1:500; Atlas, HPA018139).

KC-Got2$^{f/f}$ model

Mice containing loxP sites flanking exon 2 of the Got2 gene were generated by Ozgene. These mice were crossed to the LSL-Kras^{G12D};Ptf1a-Cre model(75). Tails from 3-week-old mice were collected at weaning and submitted to Transnetyx for genotyping. The following primers were used: Kras^{G12D} (Fw-GGCCTGCTGAAAATGACTGAGTATA, Rev-CTGTATCGTCAAGGCGCTCTT); Got2 WT (Fw-GCAGATTAAAACCACAAGGCCTGTA, Rev-ATGTTAAAATTGTCATCCCCTTGTGC); Got2 floxed (Fw-GCAGATTAAAACCACAAGGCCTGTA,Rev-AGAGAATAGGAACTTCGGAATAGGAACT); Cre (Fw-TTAATCCATATTGGCAGAACGAAAACG, Rev-CAGGCTAAGTGCCTTCTCTACA).

Statistics

Statistics were performed using Graph Pad Prism 8. Groups of 2 were analyzed with two-tailed students t test, groups greater than 2 were compared using one-way ANOVA analysis with Tukey post hoc test or two-way ANOVA with Dunnett's correction for multiple independent variables. All error bars represent mean with standard deviation, all group numbers and explanation of significant values are presented within the figure legends. Experiments were repeated at least twice to verify results.

Data availability

The mass spectrometry-based metabolomics data are available in Supplementary Table 1. Annotated raw blots are included for all westerns as Source Data Files.

All schematics and models were created using Biorender.com.

4.5 References

1. Pavlova NN, Thompson CB. The Emerging Hallmarks of Cancer Metabolism. Cell metabolism. 2016;23(1):27-47. doi: 10.1016/j.cmet.2015.12.006. PubMed PMID: 26771115.

2. Vander Heiden MG, DeBerardinis RJ. Understanding the Intersections between Metabolism and Cancer Biology. Cell. 2017;168(4):657-69. doi: 10.1016/j.cell.2016.12.039. PubMed PMID: 28187287; PMCID: PMC5329766.

3. Martínez-Reyes I, Chandel NS. Cancer metabolism: looking forward. Nature reviews Cancer. 2021. Epub 2021/07/18. doi: 10.1038/s41568-021-00378-6. PubMed PMID: 34272515.

4. Vander Heiden MG. Targeting cancer metabolism: a therapeutic window opens. Nature reviews Drug discovery. 2011;10(9):671-84. Epub 2011/09/01. doi: 10.1038/nrd3504. PubMed PMID: 21878982.

5. Ryan DP, Hong TS, Bardeesy N. Pancreatic Adenocarcinoma. New England Journal of Medicine. 2014;371(11):1039-49. doi: 10.1056/NEJMra1404198.

6. Halbrook CJ, Lyssiotis CA. Employing Metabolism to Improve the Diagnosis and Treatment of Pancreatic Cancer. Cancer Cell. 2017;31(1):5-19. doi: 10.1016/j.ccell.2016.12.006. PubMed PMID: 28073003.

7. Kamphorst JJ, Nofal M, Commisso C, Hackett SR, Lu W, Grabocka E, Vander Heiden MG, Miller G, Drebin JA, Bar-Sagi D, Thompson CB, Rabinowitz JD. Human pancreatic cancer tumors are nutrient poor and tumor cells actively scavenge extracellular protein. Cancer Res. 2015;75(3):544-53. Epub 2015/02/04. doi: 10.1158/0008-5472.CAN-14-2211. PubMed PMID: 25644265; PMCID: PMC4316379.

8. Encarnación-Rosado J, Kimmelman AC. Harnessing metabolic dependencies in pancreatic cancers. Nature reviews Gastroenterology & hepatology. 2021;18(7):482-92. Epub 2021/03/21. doi: 10.1038/s41575-021-00431-7. PubMed PMID: 33742165; PMCID: PMC8249349.

9. Commisso C, Davidson SM, Soydaner-Azeloglu RG, Parker SJ, Kamphorst JJ, Hackett S, Grabocka E, Nofal M, Drebin JA, Thompson CB, Rabinowitz JD, Metallo CM, Vander Heiden MG, Bar-Sagi D. Macropinocytosis of protein is an amino acid supply route in Ras-transformed cells. Nature. 2013;497(7451):633-7. doi: 10.1038/nature12138. PubMed PMID: 23665962; PMCID: PMC3810415.

10. Ying H, Kimmelman AC, Lyssiotis CA, Hua S, Chu GC, Fletcher-Sananikone E, Locasale JW, Son J, Zhang H, Coloff JL, Yan H, Wang W, Chen S, Viale A, Zheng H, Paik JH, Lim C, Guimaraes AR, Martin ES, Chang J, Hezel AF, Perry SR, Hu J, Gan B, Xiao Y, Asara JM, Weissleder R, Wang YA, Chin L, Cantley LC, DePinho RA. Oncogenic Kras maintains pancreatic tumors through regulation of anabolic glucose metabolism. Cell. 2012;149(3):656-70. doi: 10.1016/j.cell.2012.01.058. PubMed PMID: 22541435; PMCID: PMC3472002.

11. Son J, Lyssiotis CA, Ying H, Wang X, Hua S, Ligorio M, Perera RM, Ferrone CR, Mullarky E, Shyh-Chang N, Kang Ya, Fleming JB, Bardeesy N, Asara JM, Haigis MC, DePinho RA, Cantley LC, Kimmelman AC. Glutamine supports pancreatic cancer growth through a KRAS-regulated metabolic pathway. Nature. 2013;496:101. doi: 10.1038/nature12040

https://www.nature.com/articles/nature12040#supplementary-information.

12. Viale A, Pettazzoni P, Lyssiotis CA, Ying H, Sanchez N, Marchesini M, Carugo A, Green T, Seth S, Giuliani V, Kost-Alimova M, Muller F, Colla S, Nezi L, Genovese G, Deem AK, Kapoor A, Yao W, Brunetto E, Kang Y, Yuan M, Asara JM, Wang YA, Heffernan TP, Kimmelman AC, Wang H, Fleming JB, Cantley LC, DePinho RA, Draetta GF. Oncogene ablation-resistant pancreatic cancer cells depend on mitochondrial function. Nature. 2014;514(7524):628-32. doi: 10.1038/nature13611. PubMed PMID: 25119024; PMCID: PMC4376130.

13. Santana-Codina N, Roeth AA, Zhang Y, Yang A, Mashadova O, Asara JM, Wang X, Bronson RT, Lyssiotis CA, Ying H, Kimmelman AC. Oncogenic KRAS supports pancreatic cancer through regulation of nucleotide synthesis. Nat Commun.

2018;9(1):4945. doi: 10.1038/s41467-018-07472-8. PubMed PMID: 30470748; PMCID: PMC6251888.

14. Humpton TJ, Alagesan B, DeNicola GM, Lu D, Yordanov GN, Leonhardt CS, Yao MA, Alagesan P, Zaatari MN, Park Y, Skepper JN, Macleod KF, Perez-Mancera PA, Murphy MP, Evan GI, Vousden KH, Tuveson DA. Oncogenic KRAS Induces NIX-Mediated Mitophagy to Promote Pancreatic Cancer. Cancer Discov. 2019;9(9):1268-87. Epub 2019/07/03. doi: 10.1158/2159-8290.CD-18-1409. PubMed PMID: 31263025; PMCID: PMC6726540.

15. Tape CJ, Ling S, Dimitriadi M, McMahon KM, Worboys JD, Leong HS, Norrie IC, Miller CJ, Poulogiannis G, Lauffenburger DA, Jorgensen C. Oncogenic KRAS Regulates Tumor Cell Signaling via Stromal Reciprocation. Cell. 2016;165(4):910-20. doi: 10.1016/j.cell.2016.03.029. PubMed PMID: 27087446; PMCID: PMC4868820.

16. Kerk SA, Papagiannakopoulos T, Shah YM, Lyssiotis CA. Metabolic networks in mutant KRAS-driven tumours: tissue specificities and the microenvironment. Nat Rev Cancer. 2021;21(8):510-25. Epub 2021/07/11. doi: 10.1038/s41568-021-00375-9. PubMed PMID: 34244683.

17. Storz P, Crawford HC. Carcinogenesis of Pancreatic Ductal Adenocarcinoma. Gastroenterology. 2020. Epub 2020/03/23. doi: 10.1053/j.gastro.2020.02.059. PubMed PMID: 32199881.

18. Zhang Y, Crawford HC, Pasca di Magliano M. Epithelial-Stromal Interactions in Pancreatic Cancer. Annual review of physiology. 2019;81:211-33. Epub 2018/11/13. doi: 10.1146/annurev-physiol-020518-114515. PubMed PMID: 30418798.

19. Lyssiotis CA, Kimmelman AC. Metabolic Interactions in the Tumor Microenvironment. Trends in cell biology. 2017;27(11):863-75. Epub 2017/07/25. doi: 10.1016/j.tcb.2017.06.003. PubMed PMID: 28734735; PMCID: PMC5814137.

20. Janes MR, Zhang J, Li L-S, Hansen R, Peters U, Guo X, Chen Y, Babbar A, Firdaus SJ, Darjania L, Feng J, Chen JH, Li S, Li S, Long YO, Thach C, Liu Y, Zarieh A, Ely T, Kucharski JM, Kessler LV, Wu T, Yu K, Wang Y, Yao Y, Deng X, Zarrinkar PP, Brehmer D, Dhanak D, Lorenzi MV, Hu-Lowe D, Patricelli MP, Ren P, Liu Y. Targeting KRAS Mutant Cancers with a Covalent G12C-Specific Inhibitor. Cell. 2018;172(3):578-89.e17. doi: 10.1016/j.cell.2018.01.006.

21. Jänne PA, Riely GJ, Gadgeel SM, Heist RS, Ou SI, Pacheco JM, Johnson ML, Sabari JK, Leventakos K, Yau E, Bazhenova L, Negrao MV, Pennell NA, Zhang J, Anderes K, Der-Torossian H, Kheoh T, Velastegui K, Yan X, Christensen JG, Chao RC, Spira AI. Adagrasib in Non-Small-Cell Lung Cancer Harboring a KRAS(G12C) Mutation. N Engl J Med. 2022. Epub 2022/06/04. doi: 10.1056/NEJMoa2204619. PubMed PMID: 35658005.

22. Cox AD, Fesik SW, Kimmelman AC, Luo J, Der CJ. Drugging the undruggable RAS: Mission possible? Nat Rev Drug Discov. 2014;13(11):828-51. Epub 2014/10/18. doi: 10.1038/nrd4389. PubMed PMID: 25323927; PMCID: PMC4355017.

23. Gui DY, Sullivan LB, Luengo A, Hosios AM, Bush LN, Gitego N, Davidson SM, Freinkman E, Thomas CJ, Vander Heiden MG. Environment Dictates Dependence on Mitochondrial Complex I for NAD+ and Aspartate Production and Determines Cancer Cell Sensitivity to Metformin. Cell metabolism. 2016;24(5):716-27. Epub 2016/10/18. doi: 10.1016/j.cmet.2016.09.006. PubMed PMID: 27746050; PMCID: PMC5102768.

24. Sullivan LB, Gui DY, Hosios AM, Bush LN, Freinkman E, Vander Heiden MG. Supporting Aspartate Biosynthesis Is an Essential Function of Respiration in Proliferating Cells. Cell. 2015;162(3):552-63. Epub 2015/08/02. doi: 10.1016/j.cell.2015.07.017. PubMed PMID: 26232225; PMCID: PMC4522278.

25. Goodman RP, Markhard AL, Shah H, Sharma R, Skinner OS, Clish CB, Deik A, Patgiri A, Hsu YH, Masia R, Noh HL, Suk S, Goldberger O, Hirschhorn JN, Yellen G, Kim JK, Mootha VK. Hepatic NADH reductive stress underlies common variation in metabolic traits. Nature. 2020. Epub 2020/05/29. doi: 10.1038/s41586-020-2337-2. PubMed PMID: 32461692.

26. Titov DV, Cracan V, Goodman RP, Peng J, Grabarek Z, Mootha VK. Complementation of mitochondrial electron transport chain by manipulation of the NAD+/NADH ratio. Science. 2016;352(6282):231-5. Epub 2016/04/29. doi: 10.1126/science.aad4017. PubMed PMID: 27124460; PMCID: PMC4850741.

27. Hui S, Ghergurovich JM, Morscher RJ, Jang C, Teng X, Lu W, Esparza LA, Reya T, Le Z, Yanxiang Guo J, White E, Rabinowitz JD. Glucose feeds the TCA cycle via circulating lactate. Nature. 2017;551(7678):115-8. Epub 2017/10/19. doi: 10.1038/nature24057. PubMed PMID: 29045397; PMCID: PMC5898814.

28. Sousa CM, Biancur DE, Wang X, Halbrook CJ, Sherman MH, Zhang L, Kremer D, Hwang RF, Witkiewicz AK, Ying H, Asara JM, Evans RM, Cantley LC, Lyssiotis CA, Kimmelman AC. Pancreatic stellate cells support tumour metabolism through autophagic alanine secretion. Nature. 2016;536(7617):479-83. doi: 10.1038/nature19084. PubMed PMID: 27509858; PMCID: PMC5228623.

29. Zhao H, Yang L, Baddour J, Achreja A, Bernard V, Moss T, Marini JC, Tudawe T, Seviour EG, San Lucas FA, Alvarez H, Gupta S, Maiti SN, Cooper L, Peehl D, Ram PT, Maitra A, Nagrath D. Tumor microenvironment derived exosomes pleiotropically modulate cancer cell metabolism. Elife. 2016;5:e10250. doi: 10.7554/eLife.10250. PubMed PMID: 26920219; PMCID: PMC4841778.

30. Bertero T, Oldham WM, Grasset EM, Bourget I, Boulter E, Pisano S, Hofman P, Bellvert F, Meneguzzi G, Bulavin DV, Estrach S, Feral CC, Chan SY, Bozec A, Gaggioli C. Tumor-Stroma Mechanics Coordinate Amino Acid Availability to Sustain Tumor Growth and Malignancy. Cell metabolism. 2019;29(1):124-40.e10. Epub 2018/10/09. doi: 10.1016/j.cmet.2018.09.012. PubMed PMID: 30293773; PMCID: PMC6432652.

31. Sullivan MR, Danai LV, Lewis CA, Chan SH, Gui DY, Kunchok T, Dennstedt EA, Vander Heiden MG, Muir A. Quantification of microenvironmental metabolites in murine cancers reveals determinants of tumor nutrient availability. Elife. 2019;8. doi: 10.7554/eLife.44235. PubMed PMID: 30990168; PMCID: PMC6510537.

32. Zhang D, Wang Y, Shi Z, Liu J, Sun P, Hou X, Zhang J, Zhao S, Zhou BP, Mi J. Metabolic reprogramming of cancer-associated fibroblasts by IDH3alpha downregulation. Cell Reports. 2015;10(8):1335-48. Epub 2015/03/04. doi: 10.1016/j.celrep.2015.02.006. PubMed PMID: 25732824.

33. Lemons JMS, Feng X-J, Bennett BD, Legesse-Miller A, Johnson EL, Raitman I, Pollina EA, Rabitz HA, Rabinowitz JD, Coller HA. Quiescent Fibroblasts Exhibit High Metabolic Activity. PLOS Biology. 2010;8(10):e1000514. doi: 10.1371/journal.pbio.1000514.

34. Birsoy K, Wang T, Chen WW, Freinkman E, Abu-Remaileh M, Sabatini DM. An Essential Role of the Mitochondrial Electron Transport Chain in Cell Proliferation Is to Enable Aspartate Synthesis. Cell. 2015;162(3):540-51. Epub 2015/08/02. doi: 10.1016/j.cell.2015.07.016. PubMed PMID: 26232224; PMCID: PMC4522279.

35. Parker SJ, Encarnación-Rosado J, Hollinshead KER, Hollinshead DM, Ash LJ, Rossi JAK, Lin EY, Sohn ASW, Philips MR, Jones DR, Kimmelman AC. Spontaneous hydrolysis and spurious metabolic properties of α-ketoglutarate esters. Nat Commun. 2021;12(1):4905. Epub 2021/08/14. doi: 10.1038/s41467-021-25228-9. PubMed PMID: 34385458; PMCID: PMC8361106 on patents pertaining to KRAS-regulated metabolic pathways, redox control pathways in pancreatic cancer, targeting GOT1 as a therapeutic approach, and the autophagy control of iron metabolism. A.C.K. is on the SAB of Rafael/Cornerstone Pharmaceuticals. A.C.K. is a consultant for Deciphera and Abbvie. The other authors declare no competing interests.

36. Molina JR, Sun Y, Protopopova M, Gera S, Bandi M, Bristow C, McAfoos T, Morlacchi P, Ackroyd J, Agip A-NA, Al-Atrash G, Asara J, Bardenhagen J, Carrillo CC, Carroll C, Chang E, Ciurea S, Cross JB, Czako B, Deem A, Daver N, de Groot JF, Dong J-W, Feng N, Gao G, Gay J, Do MG, Greer J, Giuliani V, Han J, Han L, Henry VK, Hirst J, Huang S, Jiang Y, Kang Z, Khor T, Konoplev S, Lin Y-H, Liu G, Lodi A, Lofton T, Ma H, Mahendra M, Matre P, Mullinax R, Peoples M, Petrocchi A, Rodriguez-Canale J, Serreli R, Shi T, Smith M, Tabe Y, Theroff J, Tiziani S, Xu Q, Zhang Q, Muller F, DePinho RA, Toniatti C, Draetta GF, Heffernan TP, Konopleva M, Jones P, Di Francesco ME, Marszalek JR. An inhibitor of oxidative phosphorylation exploits cancer vulnerability. Nature Medicine. 2018;24(7):1036-46. doi: 10.1038/s41591-018-0052-4.

37. Halestrap AP. Monocarboxylic acid transport. Compr Physiol. 2013;3(4):1611-43. doi: 10.1002/cphy.c130008. PubMed PMID: 24265240.

38. Halestrap AP. The monocarboxylate transporter family--Structure and functional characterization. IUBMB Life. 2012;64(1):1-9. Epub 2011/12/02. doi: 10.1002/iub.573. PubMed PMID: 22131303.

39. Halestrap AP, Wilson MC. The monocarboxylate transporter family—Role and regulation. IUBMB Life. 2012;64(2):109-19. doi: 10.1002/iub.572.

40. Rao Y, Gammon S, Zacharias NM, Liu T, Salzillo T, Xi Y, Wang J, Bhattacharya P, Piwnica-Worms D. Hyperpolarized [1-(13)C]pyruvate-to-[1-(13)C]lactate conversion is rate-limited by monocarboxylate transporter-1 in the plasma membrane. Proceedings of the National Academy of Sciences of the United States of America. 2020;117(36):22378-89. Epub 2020/08/26. doi: 10.1073/pnas.2003537117. PubMed PMID: 32839325; PMCID: PMC7486767.

41. Rao Y, Gammon ST, Sutton MN, Zacharias NM, Bhattacharya P, Piwnica-Worms D. Excess exogenous pyruvate inhibits lactate dehydrogenase activity in live cells in an MCT1-dependent manner. Journal of Biological Chemistry. 2021;297(1). doi: 10.1016/j.jbc.2021.100775. PubMed PMID: 100775.

42. Steele NG, Carpenter ES, Kemp SB, Sirihorachai VR, The S, Delrosario L, Lazarus J, Amir E-aD, Gunchick V, Espinoza C, Bell S, Harris L, Lima F, Irizarry-Negron V, Paglia D, Macchia J, Chu AKY, Schofield H, Wamsteker E-J, Kwon R, Schulman A, Prabhu A, Law R, Sondhi A, Yu J, Patel A, Donahue K, Nathan H, Cho C, Anderson MA, Sahai V, Lyssiotis CA, Zou W, Allen BL, Rao A, Crawford HC, Bednar F, Frankel TL, Pasca di Magliano M. Multimodal mapping of the tumor and peripheral blood immune landscape in human pancreatic cancer. Nature Cancer. 2020;1(11):1097-112. doi: 10.1038/s43018-020-00121-4.

43. Polanski R, Hodgkinson CL, Fusi A, Nonaka D, Priest L, Kelly P, Trapani F, Bishop PW, White A, Critchlow SE, Smith PD, Blackhall F, Dive C, Morrow CJ. Activity of the monocarboxylate transporter 1 inhibitor AZD3965 in small cell lung cancer. Clin Cancer Res. 2014;20(4):926-37. Epub 2013/11/28. doi: 10.1158/1078-0432.Ccr-13-2270. PubMed PMID: 24277449; PMCID: PMC3929348.

44. Hong CS, Graham NA, Gu W, Espindola Camacho C, Mah V, Maresh EL, Alavi M, Bagryanova L, Krotee PAL, Gardner BK, Behbahan IS, Horvath S, Chia D, Mellinghoff IK, Hurvitz SA, Dubinett SM, Critchlow SE, Kurdistani SK, Goodglick L, Braas D, Graeber TG, Christofk HR. MCT1 Modulates Cancer Cell Pyruvate Export and Growth of Tumors that Co-express MCT1 and MCT4. Cell Reports. 2016;14(7):1590-601. Epub 02/11. doi: 10.1016/j.celrep.2016.01.057. PubMed PMID: 26876179.

45. Tasdogan A, Faubert B, Ramesh V, Ubellacker JM, Shen B, Solmonson A, Murphy MM, Gu Z, Gu W, Martin M, Kasitinon SY, Vandergriff T, Mathews TP, Zhao Z, Schadendorf D, DeBerardinis RJ, Morrison SJ. Metabolic heterogeneity confers differences in melanoma metastatic potential. Nature. 2020;577(7788):115-20. doi: 10.1038/s41586-019-1847-2.

46. Le A, Cooper CR, Gouw AM, Dinavahi R, Maitra A, Deck LM, Royer RE, Vander Jagt DL, Semenza GL, Dang CV. Inhibition of lactate dehydrogenase A induces oxidative stress and inhibits tumor progression. Proceedings of the National Academy of

Sciences of the United States of America. 2010;107(5):2037-42. Epub 2010/02/06. doi: 10.1073/pnas.0914433107. PubMed PMID: 20133848; PMCID: PMC2836706.

47. Borst P. The malate–aspartate shuttle (Borst cycle): How it started and developed into a major metabolic pathway. IUBMB Life. 2020;72(11):2241-59. doi: https://doi.org/10.1002/iub.2367.

48. Son J, Lyssiotis CA, Ying H, Wang X, Hua S, Ligorio M, Perera RM, Ferrone CR, Mullarky E, Shyh-Chang N, Kang Y, Fleming JB, Bardeesy N, Asara JM, Haigis MC, DePinho RA, Cantley LC, Kimmelman AC. Glutamine supports pancreatic cancer growth through a KRAS-regulated metabolic pathway. Nature. 2013;496(7443):101-5. Epub 2013/03/29. doi: 10.1038/nature12040. PubMed PMID: 23535601; PMCID: PMC3656466.

49. Sakamoto A, Kunou S, Shimada K, Tsunoda M, Aoki T, Iriyama C, Tomita A, Nakamura S, Hayakawa F, Kiyoi H. Pyruvate secreted from patient-derived cancer-associated fibroblasts supports survival of primary lymphoma cells. Cancer Sci. 2019;110(1):269-78. Epub 2018/11/15. doi: 10.1111/cas.13873. PubMed PMID: 30426593; PMCID: PMC6317936.

50. Bonglack EN, Messinger JE, Cable JM, Ch'ng J, Parnell KM, Reinoso-Vizcaíno NM, Barry AP, Russell VS, Dave SS, Christofk HR, Luftig MA. Monocarboxylate transporter antagonism reveals metabolic vulnerabilities of viral-driven lymphomas. Proceedings of the National Academy of Sciences of the United States of America. 2021;118(25). Epub 2021/06/24. doi: 10.1073/pnas.2022495118. PubMed PMID: 34161263.

51. Hong CS, Graham NA, Gu W, Espindola Camacho C, Mah V, Maresh EL, Alavi M, Bagryanova L, Krotee PAL, Gardner BK, Behbahan IS, Horvath S, Chia D, Mellinghoff IK, Hurvitz SA, Dubinett SM, Critchlow SE, Kurdistani SK, Goodglick L, Braas D, Graeber TG, Christofk HR. MCT1 Modulates Cancer Cell Pyruvate Export and Growth of Tumors that Co-express MCT1 and MCT4. Cell Rep. 2016;14(7):1590-601. doi: 10.1016/j.celrep.2016.01.057. PubMed PMID: 26876179; PMCID: PMC4816454.

52. Hui S, Cowan AJ, Zeng X, Yang L, TeSlaa T, Li X, Bartman C, Zhang Z, Jang C, Wang L, Lu W, Rojas J, Baur J, Rabinowitz JD. Quantitative Fluxomics of Circulating Metabolites. Cell metabolism. 2020;32(4):676-88 e4. Epub 2020/08/14. doi: 10.1016/j.cmet.2020.07.013. PubMed PMID: 32791100; PMCID: PMC7544659.

53. Yang L, Garcia Canaveras JC, Chen Z, Wang L, Liang L, Jang C, Mayr JA, Zhang Z, Ghergurovich JM, Zhan L, Joshi S, Hu Z, McReynolds MR, Su X, White E, Morscher RJ, Rabinowitz JD. Serine Catabolism Feeds NADH when Respiration Is Impaired. Cell metabolism. 2020;31(4):809-21.e6. doi: https://doi.org/10.1016/j.cmet.2020.02.017.

54. Kim W, Deik A, Gonzalez C, Gonzalez ME, Fu F, Ferrari M, Churchhouse CL, Florez JC, Jacobs SBR, Clish CB, Rhee EP. Polyunsaturated Fatty Acid Desaturation Is a Mechanism for Glycolytic NAD(+) Recycling. Cell metabolism. 2019;29(4):856-70 e7.

Epub 2019/01/29. doi: 10.1016/j.cmet.2018.12.023. PubMed PMID: 30686744; PMCID: PMC6447447.

55. Liu S, Fu S, Wang G, Cao Y, Li L, Li X, Yang J, Li N, Shan Y, Cao Y, Ma Y, Dong M, Liu Q, Jiang H. Glycerol-3-phosphate biosynthesis regenerates cytosolic NAD(+) to alleviate mitochondrial disease. Cell metabolism. 2021. Epub 2021/07/17. doi: 10.1016/j.cmet.2021.06.013. PubMed PMID: 34270929.

56. Sullivan LB, Luengo A, Danai LV, Bush LN, Diehl FF, Hosios AM, Lau AN, Elmiligy S, Malstrom S, Lewis CA, Vander Heiden MG. Aspartate is an endogenous metabolic limitation for tumour growth. Nature Cell Biology. 2018;20(7):782-8. Epub 2018/06/27. doi: 10.1038/s41556-018-0125-0. PubMed PMID: 29941931; PMCID: PMC6051729.

57. Garcia-Bermudez J, Baudrier L, La K, Zhu XG, Fidelin J, Sviderskiy VO, Papagiannakopoulos T, Molina H, Snuderl M, Lewis CA, Possemato RL, Birsoy K. Aspartate is a limiting metabolite for cancer cell proliferation under hypoxia and in tumours. Nature Cell Biology. 2018;20(7):775-81. doi: 10.1038/s41556-018-0118-z.

58. Garcia-Bermudez J, Badgley MA, Prasad S, Baudrier L, Liu Y, La K, Soula M, Williams RT, Yamaguchi N, Hwang RF, Taylor LJ, de Stanchina E, Rostandy B, Alwaseem H, Molina H, Bar-Sagi D, Birsoy K. Adaptive stimulation of macropinocytosis overcomes aspartate limitation in cancer cells under hypoxia. Nature Metabolism. 2022. doi: 10.1038/s42255-022-00583-z.

59. Mick E, Titov DV, Skinner OS, Sharma R, Jourdain AA, Mootha VK. Distinct mitochondrial defects trigger the integrated stress response depending on the metabolic state of the cell. eLife. 2020;9. Epub 2020/05/29. doi: 10.7554/eLife.49178. PubMed PMID: 32463360; PMCID: PMC7255802.

60. Sanford-Crane H, Abrego J, Sherman MH. Fibroblasts as Modulators of Local and Systemic Cancer Metabolism. Cancers (Basel). 2019;11(5). Epub 2019/05/07. doi: 10.3390/cancers11050619. PubMed PMID: 31058816; PMCID: PMC6562905.

61. Schworer S, Vardhana SA, Thompson CB. Cancer Metabolism Drives a Stromal Regenerative Response. Cell metabolism. 2019;29(3):576-91. Epub 2019/02/19. doi: 10.1016/j.cmet.2019.01.015. PubMed PMID: 30773467.

62. Elyada E, Bolisetty M, Laise P, Flynn WF, Courtois ET, Burkhart RA, Teinor JA, Belleau P, Biffi G, Lucito MS, Sivajothi S, Armstrong TD, Engle DD, Yu KH, Hao Y, Wolfgang CL, Park Y, Preall J, Jaffee EM, Califano A, Robson P, Tuveson DA. Cross-Species Single-Cell Analysis of Pancreatic Ductal Adenocarcinoma Reveals Antigen-Presenting Cancer-Associated Fibroblasts. Cancer Discov. 2019;9(8):1102-23. Epub 2019/06/15. doi: 10.1158/2159-8290.Cd-19-0094. PubMed PMID: 31197017; PMCID: PMC6727976.

63. Ohlund D, Handly-Santana A, Biffi G, Elyada E, Almeida AS, Ponz-Sarvise M, Corbo V, Oni TE, Hearn SA, Lee EJ, Chio, II, Hwang CI, Tiriac H, Baker LA, Engle DD,

Feig C, Kultti A, Egeblad M, Fearon DT, Crawford JM, Clevers H, Park Y, Tuveson DA. Distinct populations of inflammatory fibroblasts and myofibroblasts in pancreatic cancer. The Journal of experimental medicine. 2017;214(3):579-96. Epub 2017/02/25. doi: 10.1084/jem.20162024. PubMed PMID: 28232471; PMCID: PMC5339682.

64. Neuzillet C, Tijeras-Raballand A, Ragulan C, Cros J, Patil Y, Martinet M, Erkan M, Kleeff J, Wilson J, Apte M, Tosolini M, Wilson AS, Delvecchio FR, Bousquet C, Paradis V, Hammel P, Sadanandam A, Kocher HM. Inter- and intra-tumoural heterogeneity in cancer-associated fibroblasts of human pancreatic ductal adenocarcinoma. The Journal of pathology. 2019;248(1):51-65. Epub 2018/12/24. doi: 10.1002/path.5224. PubMed PMID: 30575030.

65. Hosein AN, Huang H, Wang Z, Parmar K, Du W, Huang J, Maitra A, Olson E, Verma U, Brekken RA. Cellular heterogeneity during mouse pancreatic ductal adenocarcinoma progression at single-cell resolution. JCI Insight. 2019;5. Epub 2019/07/25. doi: 10.1172/jci.insight.129212. PubMed PMID: 31335328.

66. Helms EJ, Berry MW, Chaw RC, DuFort CC, Sun D, Onate MK, Oon C, Bhattacharyya S, Sanford-Crane H, Horton W, Finan JM, Sattler A, Makar R, Dawson DW, Xia Z, Hingorani SR, Sherman MH. Mesenchymal Lineage Heterogeneity Underlies Nonredundant Functions of Pancreatic Cancer-Associated Fibroblasts. Cancer Discov. 2022;12(2):484-501. Epub 2021/09/23. doi: 10.1158/2159-8290.Cd-21-0601. PubMed PMID: 34548310; PMCID: PMC8831457.

67. Hutton C, Heider F, Blanco-Gomez A, Banyard A, Kononov A, Zhang X, Karim S, Paulus-Hock V, Watt D, Steele N, Kemp S, Hogg EKJ, Kelly J, Jackstadt RF, Lopes F, Menotti M, Chisholm L, Lamarca A, Valle J, Sansom OJ, Springer C, Malliri A, Marais R, Pasca di Magliano M, Zelenay S, Morton JP, Jørgensen C. Single-cell analysis defines a pancreatic fibroblast lineage that supports anti-tumor immunity. Cancer Cell. 2021;39(9):1227-44.e20. Epub 2021/07/24. doi: 10.1016/j.ccell.2021.06.017. PubMed PMID: 34297917; PMCID: PMC8443274.

68. Beloueche-Babari M, Wantuch S, Casals Galobart T, Koniordou M, Parkes HG, Arunan V, Chung YL, Eykyn TR, Smith PD, Leach MO. MCT1 Inhibitor AZD3965 Increases Mitochondrial Metabolism, Facilitating Combination Therapy and Noninvasive Magnetic Resonance Spectroscopy. Cancer Res. 2017;77(21):5913-24. Epub 2017/09/20. doi: 10.1158/0008-5472.CAN-16-2686. PubMed PMID: 28923861; PMCID: PMC5669455.

69. Hwang RF, Moore T, Arumugam T, Ramachandran V, Amos KD, Rivera A, Ji B, Evans DB, Logsdon CD. Cancer-associated stromal fibroblasts promote pancreatic tumor progression. Cancer research. 2008;68(3):918-26. Epub 2008/02/05. doi: 10.1158/0008-5472.Can-07-5714. PubMed PMID: 18245495; PMCID: PMC2519173.

70. Wiederschain D, Wee S, Chen L, Loo A, Yang G, Huang A, Chen Y, Caponigro G, Yao YM, Lengauer C, Sellers WR, Benson JD. Single-vector inducible lentiviral RNAi

system for oncology target validation. Cell Cycle. 2009;8(3):498-504. Epub 2009/01/30. doi: 10.4161/cc.8.3.7701. PubMed PMID: 19177017.

71. Ran FA, Hsu PD, Wright J, Agarwala V, Scott DA, Zhang F. Genome engineering using the CRISPR-Cas9 system. Nature protocols. 2013;8(11):2281-308. Epub 2013/10/26. doi: 10.1038/nprot.2013.143. PubMed PMID: 24157548; PMCID: PMC3969860.

72. Smith MC, Luker KE, Garbow JR, Prior JL, Jackson E, Piwnica-Worms D, Luker GD. CXCR4 regulates growth of both primary and metastatic breast cancer. Cancer Res. 2004;64(23):8604-12. Epub 2004/12/03. doi: 10.1158/0008-5472.Can-04-1844. PubMed PMID: 15574767.

73. Li C, Heidt DG, Dalerba P, Burant CF, Zhang L, Adsay V, Wicha M, Clarke MF, Simeone DM. Identification of pancreatic cancer stem cells. Cancer research. 2007;67(3):1030-7. Epub 2007/02/07. doi: 10.1158/0008-5472.Can-06-2030. PubMed PMID: 17283135.

74. Guzman C, Bagga M, Kaur A, Westermarck J, Abankwa D. ColonyArea: an ImageJ plugin to automatically quantify colony formation in clonogenic assays. PloS one. 2014;9(3):e92444. Epub 2014/03/22. doi: 10.1371/journal.pone.0092444. PubMed PMID: 24647355; PMCID: PMC3960247.

75. Hingorani SR, Petricoin EF, III, Maitra A, Rajapakse V, King C, Jacobetz MA, Ross S, Conrads TP, Veenstra TD, Hitt BA, Kawaguchi Y, Johann D, Liotta LA, Crawford HC, Putt ME, Jacks T, Wright CVE, Hruban RH, Lowy AM, Tuveson DA. Preinvasive and invasive ductal pancreatic cancer and its early detection in the mouse. Cancer cell. 2003;4(6):437-50. doi: 10.1016/S1535-6108(03)00309-X.

4.6 Figures

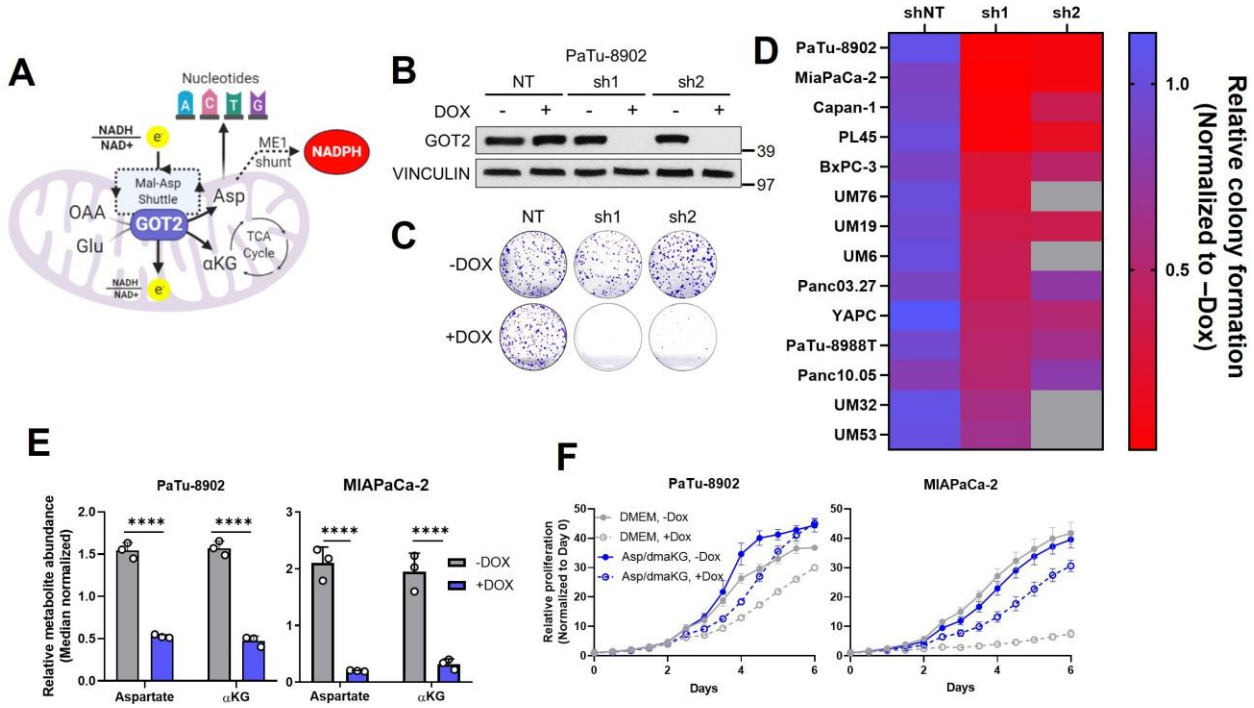

Figure 4-1 GOT2 KD impairs in vitro PDA proliferation.

A) The metabolic roles of mitochondrial glutamate-oxaloacetate transaminase 2 (GOT2). OAA=oxaloacetate, Glu=glutamate, Mal=malate, Asp=Aspartate, αKG=α-ketoglutarate, ME1=malic enzyme 1, TCA=tricarboxylic acid. **B)** Immunoblot of GOT2 and VINCULIN loading control in PaTu-8902 cells after 1 µg/mL doxycycline (DOX) induction of two independent GOT2 (sh1, sh2) and non-targeting (NT) shRNAs for 3 days. **C)** Representative images from colony formation assays in ishRNA PaTu-8902 cells -Dox (n=3) or +Dox (n=3). **D)** Heatmap summarizing the relative colony formation ishRNA PDA cell lines -Dox (n=3) or +Dox (n=3), normalized to -Dox for each indicated shRNA. Representative images from colony formation assays and western blots presented in Figure 1-figure supplement 1. **E)** Relative abundances of Asp and αKG in PaTu-8902 (left) and MIAPaCa-2 (right) ishGOT2.1 -Dox (n=3) or +Dox (n=3). **F)** Relative proliferation of PaTu-8902 (left) and MIAPaCa-2 (right) ishGOT2.1 -Dox (n=3) or +Dox (n=3) cultured in normal media (DMEM) or supplemented with 20 mM Asp and 1 mM dimethyl-αKG (dmαKG). For all panels, data represent mean ± SD. *p<0.05, **p<0.01, ***p<0.001, ****p<0.0001.

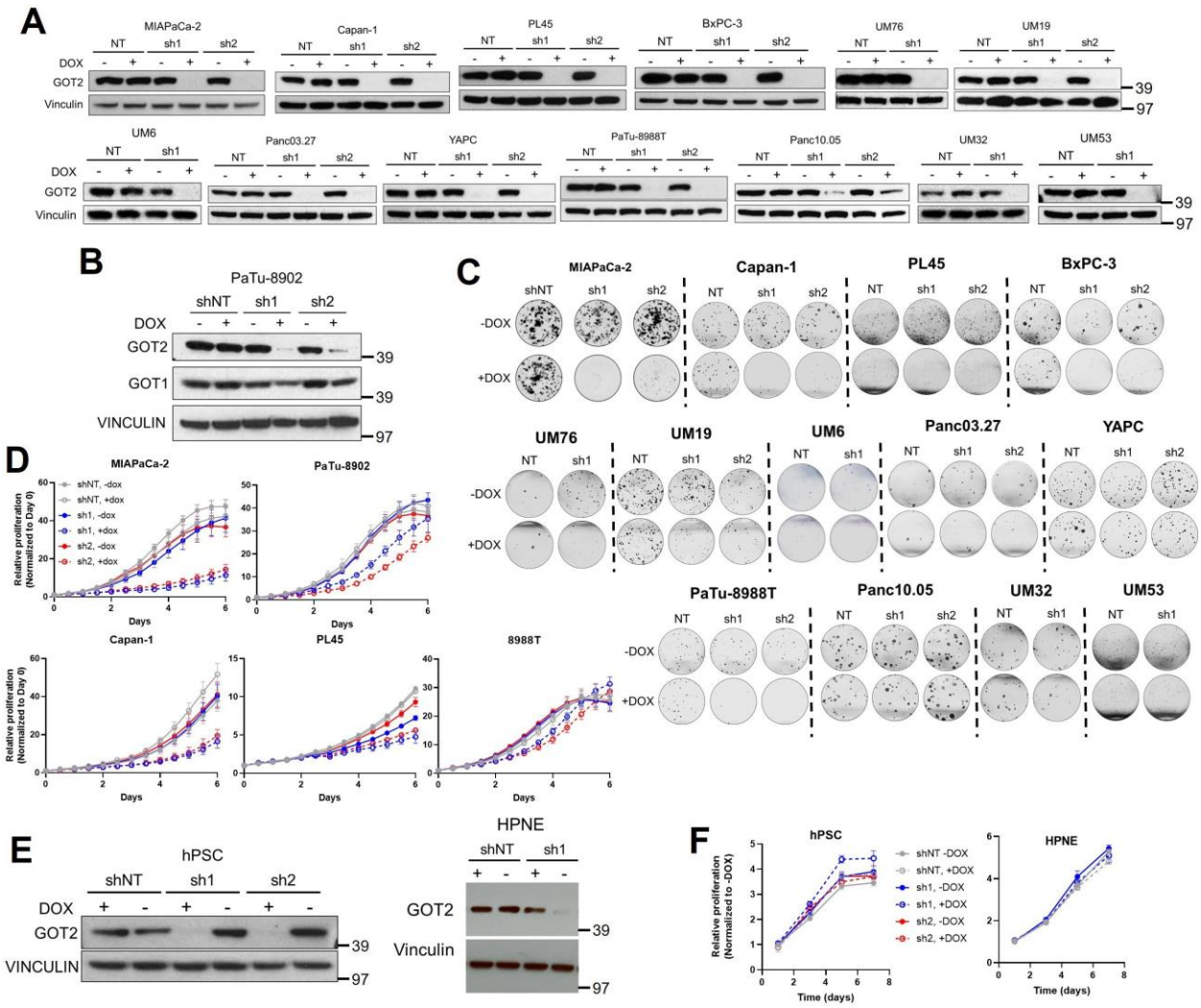

Figure 4-2 Validation of GOT2 KD and proliferation assays in PDA and normal cell lines

A) Immunoblots of GOT2 and VINCULIN loading control in PDA cell lines after 1 µg/mL doxycycline (Dox) induction of the indicated shRNAs (ishRNA) for 3 days. NT=non-targeting shRNA. Westerns for data in Figure 1D. B) Immunoblot of GOT1, GOT2, and VINCULIN in PaTu-8902 ishRNA -Dox or +Dox after 3 days. C) Representative images from colony formation assays in PDA ishRNA cell lines -Dox (n=3) or +Dox (n=3) for the data in Figure 1D. D) Relative proliferation of PDA ishRNA cell lines -Dox (n=3) or +Dox (n=3), normalized to Day 0 cell number for each condition. E) Immunoblots of GOT2 and VINCULIN in human cancer associated fibroblast cell line (hPSC) and human pancreatic nestin expressing cells (HPNE) ishRNA cells. F) Relative proliferation of hPSC (left) and HPNE (right) ishRNA -Dox (n=3) or +Dox (n=3). For all panels, data represent mean ± SD. *p<0.05, **p<0.01, ***p<0.001, ****p<0.0001.

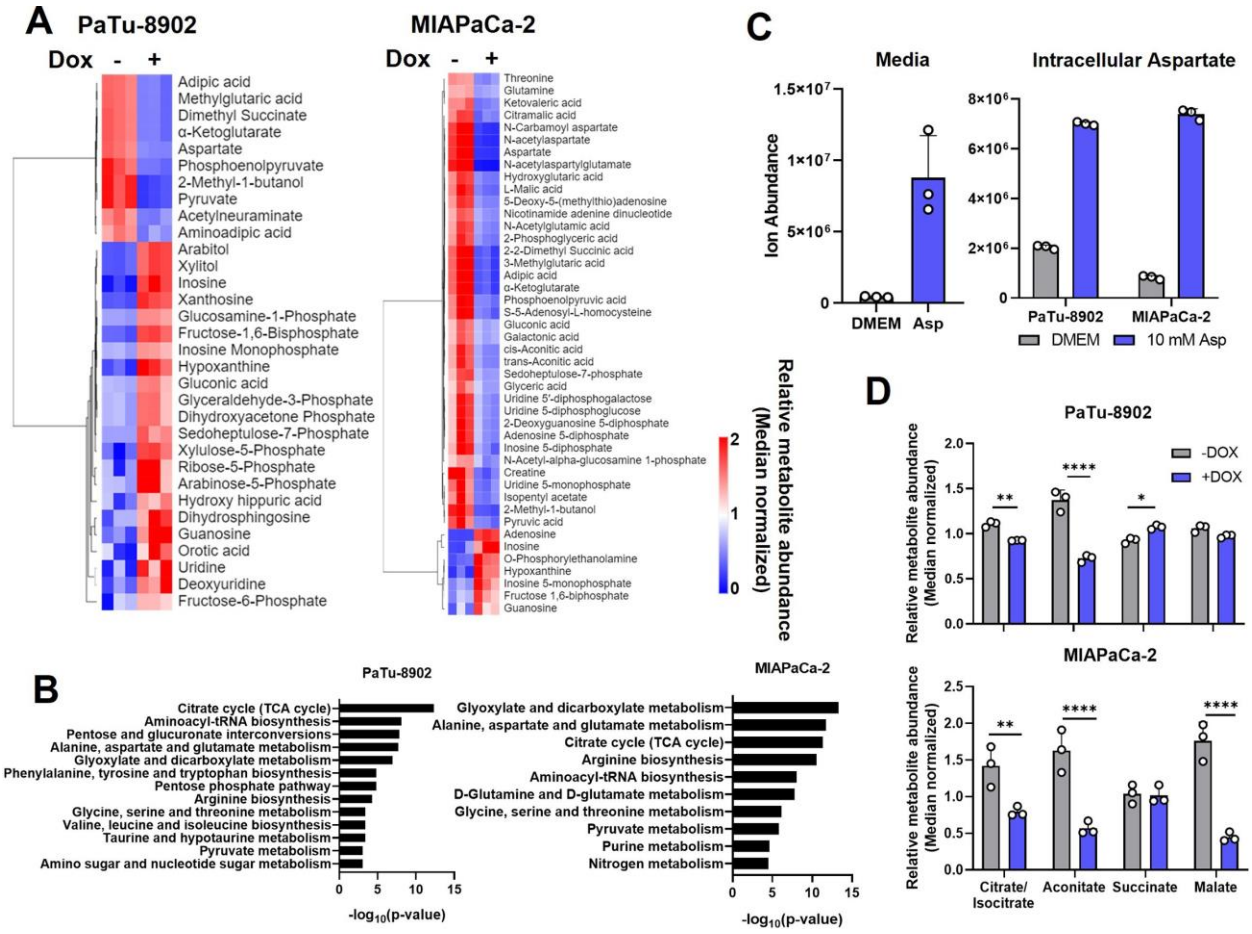

Figure 4-3 Metabolomic characterization of GOT2 KD in PDA cell lines

A) Heatmaps of the relative abundances of metabolites significantly ($p<0.05$) different between -Dox (n=3) and +Dox (n=3) PaTu-8902 (left) and MIAPaCa-2 (right) ishGOT2.1 cells. **B)** Metabolic pathway analysis of the data presented in A). **C)** Ion abundances of aspartate (Asp) in normal media or media with 10 mM Asp (left) and intracellular abundances in PaTu-8902 and MIAPaCa-2 cultured in normal media or media with 10 mM Asp (right). **D)** Relative abundances of TCA cycle metabolites in PaTu-8902 (top) or MIAPaCa-2 (bottom) ishGOT2.1 -Dox (n=3) or +Dox (n=3). For all panels, data represent mean ± SD. *$p<0.05$, **$p<0.01$, ***$p<0.001$, ****$p<0.0001$.

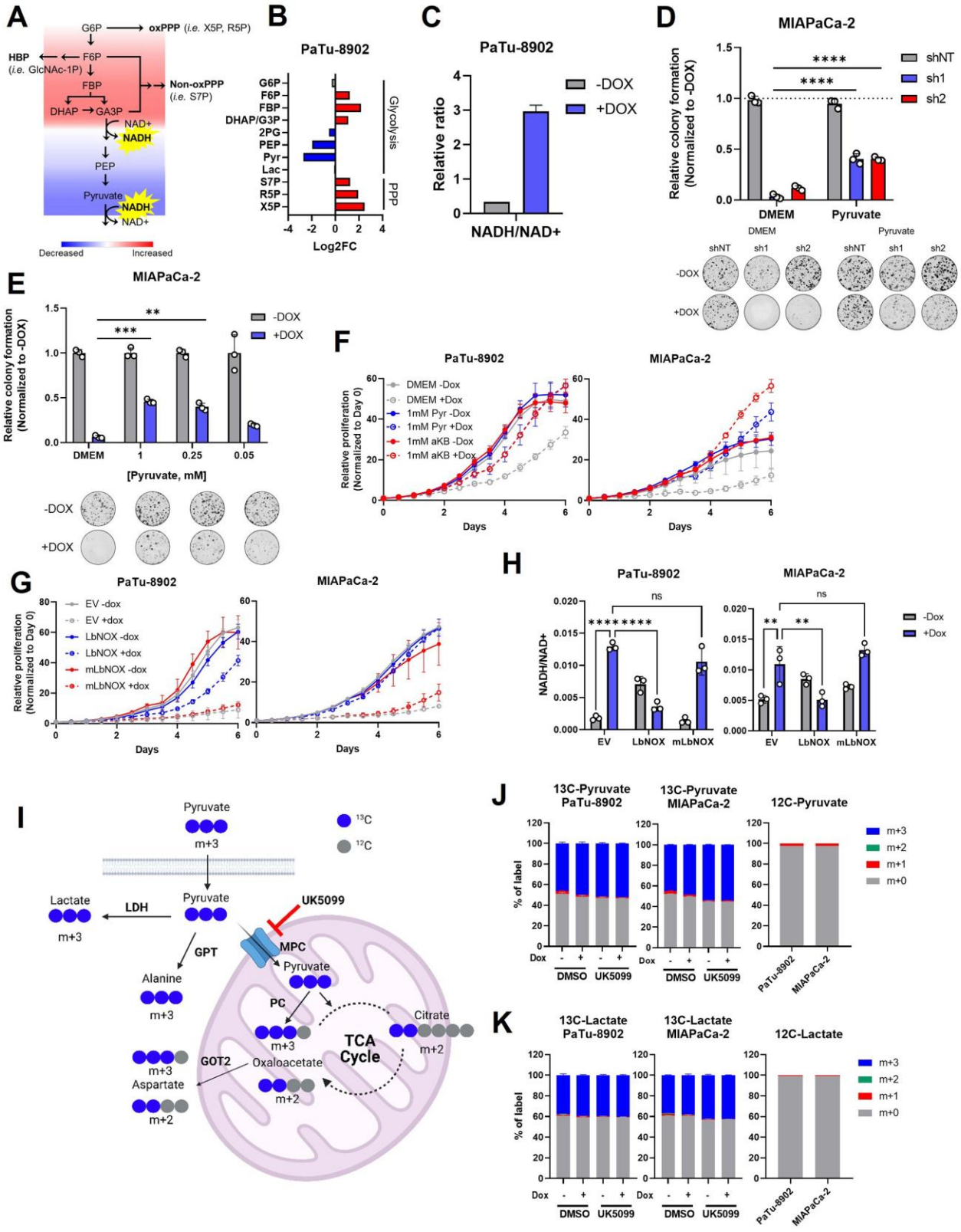

Figure 4-4 GOT2 KD induces reductive stress, which can be ameliorated by NADH turnover.

A) Schematic of glycolytic signature induced by GOT2 KD-mediated NADH build-up and reductive stress. G6P=glucose-6-phosphate, F6P=fructose-6-phosphate, FBP=fructose-1,6-bisphosphate, DHAP=dihydroxyacetone phosphate, GA3P=glyceraldehyde-3-phosphate, PEP=phosphoenol pyruvate, oxPPP=oxidative pentose phosphate pathway, Non-oxPPP=non-oxidative pentose phosphate pathway, X5P=xylulose-5-phosphate, R5P=ribose-5-phosphate, S7P=seduoheptulose-7-phosphate, HBP=hexosamine biosynthesis pathway, GlcNAc-1P=N-acetylglucosamine 1-phosphate. **B)** Relative fold changes in the indicated metabolites between PaTu-8902 ishGOT2.1 -Dox (n=3) and +Dox (n=3). 2PG=2-phosphoglycerate, Pyr=Pyruvate, Lac=Lactate. **C)** Relative NADH/NAD+ ratio in PaTu-8902 ishGOT2.1 -Dox (n=3) and +Dox (n=3). **D)** Relative colony formation of MIAPaCa-2 ishRNA -Dox (n=3) or +Dox (n=3) cultured in normal media (DMEM) or DMEM with 1 mM pyruvate, normalized to -Dox for each condition. **E)** Relative colony formation of MIAPaCa-2 ishGOT2.1 -Dox (n=3) or +Dox (n=3) cultured in normal media (DMEM) or DMEM with the indicated concentrations of pyruvate (mM), normalized to -Dox for each condition. **F)** Relative proliferation of PaTu-8902 (left) and MIAPaCa-2 (right) ishGOT2.1 -Dox (n=3) or +Dox (n=3) cultured in normal media (DMEM) or DMEM with 1 mM pyruvate (Pyr) or α-ketobutyrate (αKB), normalized to Day 0 for each condition. **G)** Relative proliferation of PaTu-8902 (left) and MIAPaCa-2 (right) ishGOT2.1 -Dox (n=3) or +Dox (n=3) expressing doxycycline-inducible empty vector (EV), cytosolic *Lactobacillus* NADH oxidase (LbNOX), or mitochondrial LbNOX (mLbNOX), normalized to Day 0 for each condition. **H)** Relative NADH/NAD+ ratio of PaTu-8902 (left) and MIAPaCa-2 (right) ishGOT2.1 -Dox (n=3) or +Dox (n=3) expressing EV, LbNOX, or mLbNOX. **I)** Schematic of 13C3-pyruvate into relevant metabolic pathways. 13C-carbon labels in blue, non-labeled carbon in gray. LDH=lactate dehydrogenase, GPT=glutamate-pyruvate transaminase, MPC=mitochondrial pyruvate carrier, PC=pyruvate carboxylase. **J-K)** Fractional labelling of intracellular pyruvate J) or lactate K) in PaTu-8902 and MIAPaCa-2 ishGOT2.1 -Dox (n=3) or +Dox (n=3) cultured in 1 mM 13C3-Pyruvate and treated with DMSO vehicle control or 5 μM UK5099 (MPC inhibitor). Unlabeled controls presented at right. For all panels, data represent mean ± SD. *p<0.05, **p<0.01, ***p<0.001, ****p<0.0001.

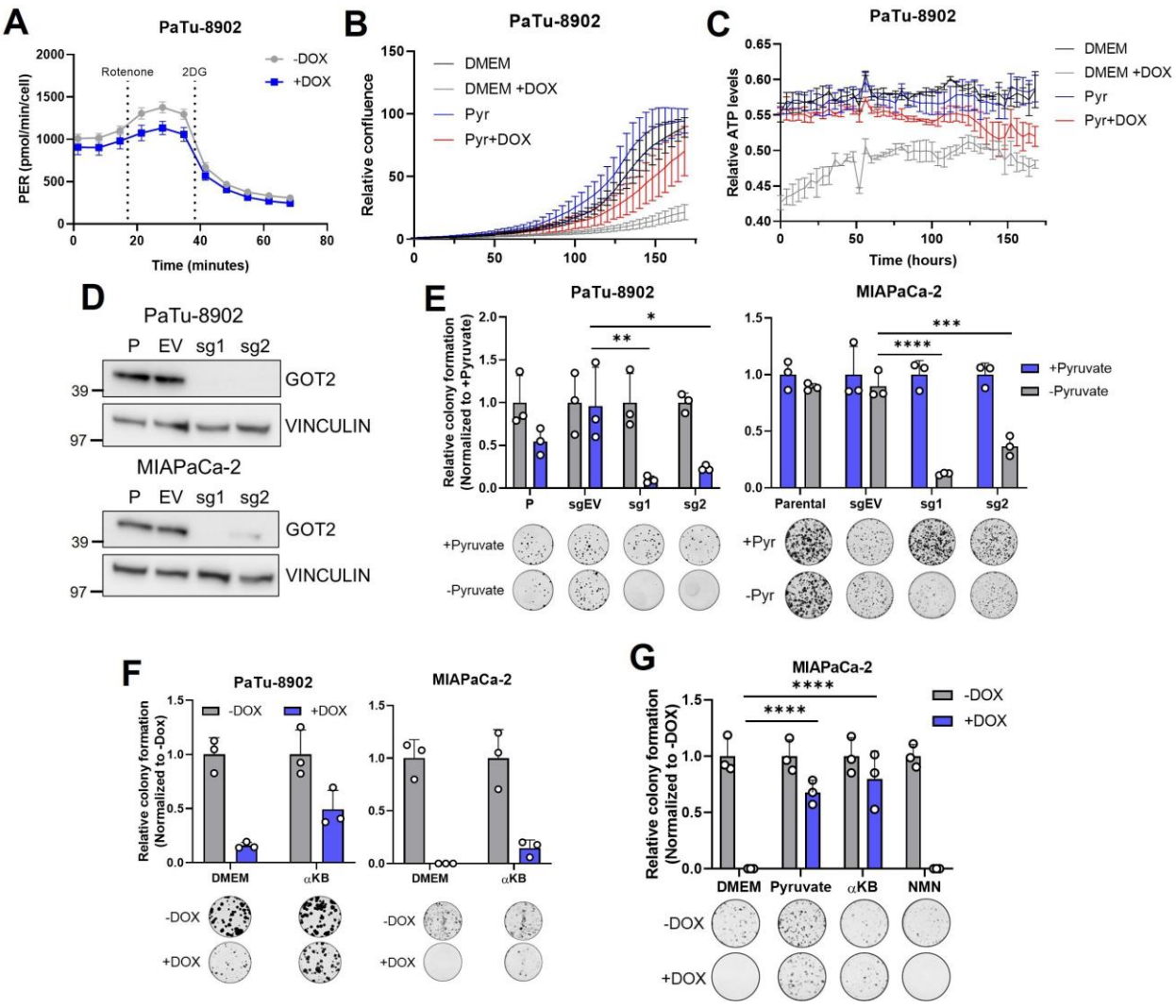

Figure 4-5 Further characterization of the role of GOT2 in redox stress.

A) Glycolytic rate assay showing the proton efflux rate (PER) of PaTu-8902 ishGOT2.1 -Dox (n=4) or +Dox (n=4). **B-C)** Relative proliferation B) and ATP levels C) of PaTu-8902 ishGOT2.1 -Dox (n=3) or +Dox (n=3) cultured in normal DMEM or DMEM with 1 mM pyruvate (Pyr). **D)** Immunoblots of GOT2 and VINCULIN loading control in PaTu-8902 (top) and MIAPaCa-2 (bottom) parental (P), empty vector (EV), or two sgRNAs targeting GOT2 (sg1, sg2). **E)** Relative colony formation of PaTu-8902 (left) and MIAPaCa-2 (right) P, EV, sgGOT2.1, or sgGOT2.2 cultured in normal DMEM (-Pyr, n=3) or DMEM with 1 mM pyruvate (+Pyr, n=3), normalized to +Pyr for each condition. **F)** Relative colony formation of PaTu-8902 (left) and MIAPaCa-2 (right) ishGOT2.1 -Dox (n=3) or +Dox (n=3) cultured in normal media (DMEM) or DMEM with 1 mM α-ketobutyrate (αKB), normalized to -Dox for each condition. **G)** Relative colony formation of MIAPaCa-2 ishGOT2.1 -Dox (n=3) or +Dox (n=3) cultured in normal media (DMEM) or DMEM with 1 mM pyruvate, αKB, or nicotinaminde mononucleotide (NMN), normalized to -Dox for each condition. For all panels, data represent mean ± SD. *p<0.05, **p<0.01, ***p<0.001, ****p<0.0001.

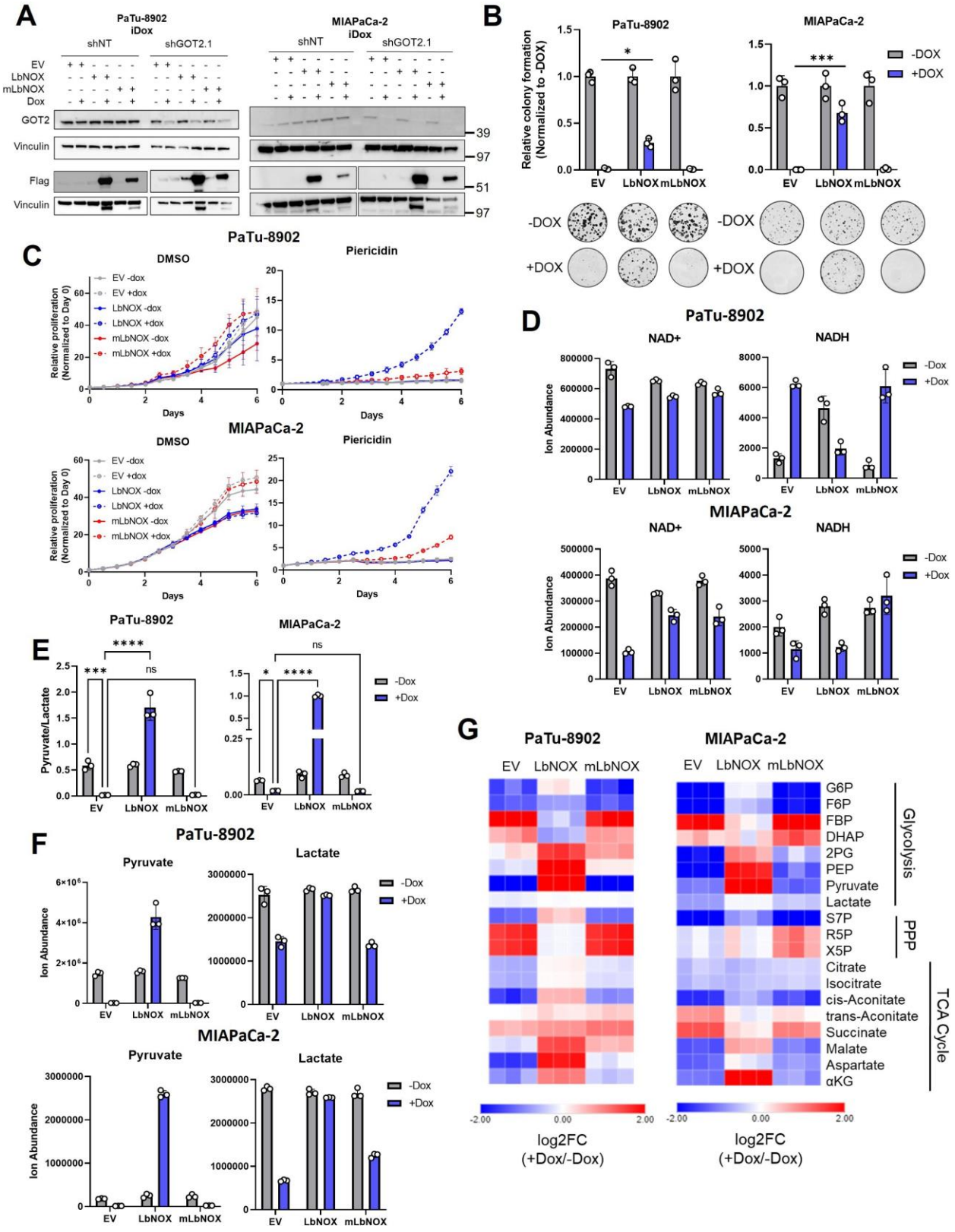

Figure 4-6 LbNOX relieves redox stress induced by GOT2 KD.

A) Immunoblots of GOT2, FLAG, and VINCULIN loading controls from PaTu-8902 (left) or MIAPaCa-2 (right) ishNT or GOT2.1 cells expressing doxycycline-inducible expression of empty vector (EV) or FLAG-tagged cytosolic *Lactobacillus* NADH oxidase (LbNOX) or mitochondrial LbNOX (mLbNOX). **B)** Relative colony formation of PaTu-8902 (left) and MIAPaCa-2 (right) ishGOT2.1 -Dox (n=3) or +Dox (n=3) expressing EV, LbNOX, or mLbNOX, normalized to -Dox for each condition. **C)** Relative proliferation of PaTu-8902 (top) and MIAPaCa-2 (bottom) ishNT -Dox (n=3) or +Dox (n=3) expressing EV, LbNOX, or mLbNOX and treated with DMSO vehicle control (left) or 1 μM piericidin (right), normalized to Day 0 for each condition. **D)** Ion abundances of NAD+ (left) and NADH (right) in PaTu-8902 (top) and MIAPaCa-2 (bottom) ishGOT2.1 -Dox (n=3) and +Dox (n=3). **E)** Relative extracellular pyruvate/lactate ratios in PaTu-8902 (left) and MIAPaCa-2 (right) ishGOT2.1 -Dox (n=3) and +Dox (n=3). **F)** Ion abundances of extracellular pyruvate (left) and lactate (right) in PaTu-8902 (top) and MIAPaCa-2 (bottom) ishGOT2.1 -Dox (n=3) and +Dox (n=3). **G)** Heatmap of log2 fold-changes in metabolite abundances between PaTu-8902 (left) and MIAPaCa-2 (right) ishGOT2.1 -Dox (n=3) and +Dox (n=3) expressing EV, LbNOX, or mLbNOX. G6P=glucose-6-phosphate, F6P=fructose-6-phosphate, FBP=fructose-1,6-bisphosphate, DHAP=dihydroxyacetone phosphate, 2PG=2-phosphoglycerate, PEP=phosphoenol pyruvate, X5P=xylulose-5-phosphate, R5P=ribose-5-phosphate, S7P=seduoheptulose-7-phosphate, αKG=α-ketoglutarate, PPP=pentose phosphate pathway. For all panels, data represent mean ± SD. *p<0.05, **p<0.01, ***p<0.001, ****p<0.0001.

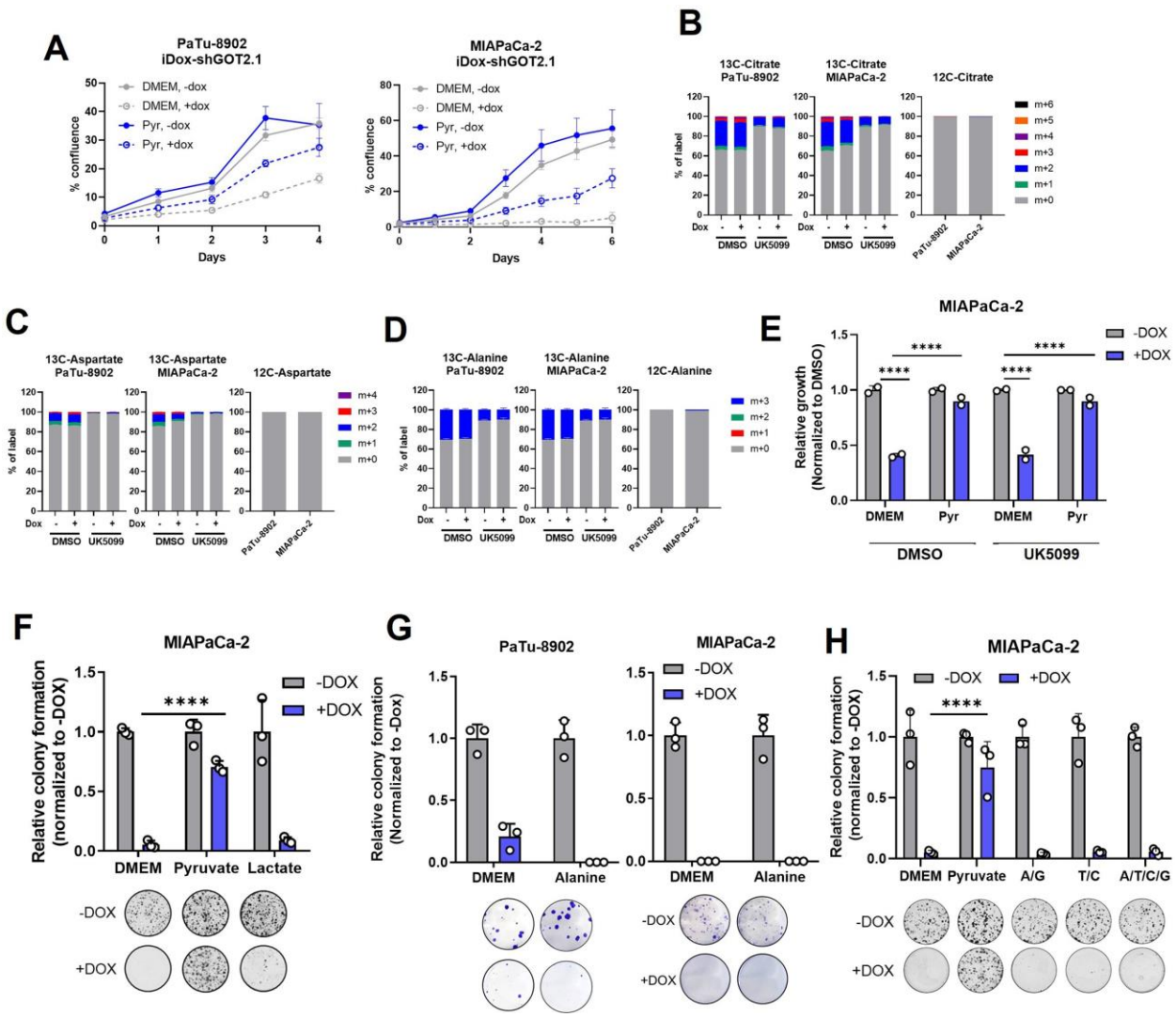

Figure 4-7 Isotope tracing of labelled pyruvate in GOT2 KD PDA cell lines.

A) Relative proliferation of PaTu-8902 (left) and MIAPaCa-2 (right) ishGOT2.1 -Dox (n=3) or +Dox (n=3) cultured in 1 mM Glucose DMEM with 1 mM pyruvate (Pyr) normalized to Day 0 for each condition. **B-D)** Fractional labelling of intracellular citrate B), aspartate C), or alanine D) from 13C3-Pyruvate (1 mM) in PaTu-8902 and MIAPaCa-2 ishGOT2.1 -Dox (n=3) or +Dox (n=3) treated with DMSO vehicle control or 5 µM UK5099 (MPC inhibitor). Unlabeled controls presented at right. **E)** Relative cell number of MIAPaCa-2 ishGOT2.1 -Dox (n=3) or +Dox (n=3) cultured in normal DMEM or DMEM with 1 mM Pyr, treated with DMSO vehicle control or 5 µM UK5099, normalized to DMSO for each condition. **F)** Relative colony formation of MIAPaCa-2 ishGOT2.1 -Dox (n=3) or +Dox (n=3) cultured in normal DMEM or DMEM with 1 mM Pyr or lactate (Lac), normalized to -Dox for each condition. **G)** Relative colony formation of PaTu-8902 (left) and MIAPaCa-2 (right) ishGOT2.1 -Dox (n=3) or +Dox (n=3) cultured in normal DMEM or DMEM with 1 mM alanine, normalized to -Dox for each condition. **H)** Relative colony formation of MIAPaCa-2 ishGOT2.1 -Dox (n=3) or +Dox (n=3) cultured in normal DMEM or DMEM with either 1 mM Pyr or 100 µM of the indicated combinations of adenine (A), guanine (G), thymidine (T), and cytidine (C), normalized to -Dox for each condition. For all panels, data represent mean ± SD. *p<0.05, **p<0.01, ***p<0.001, ****p<0.0001.

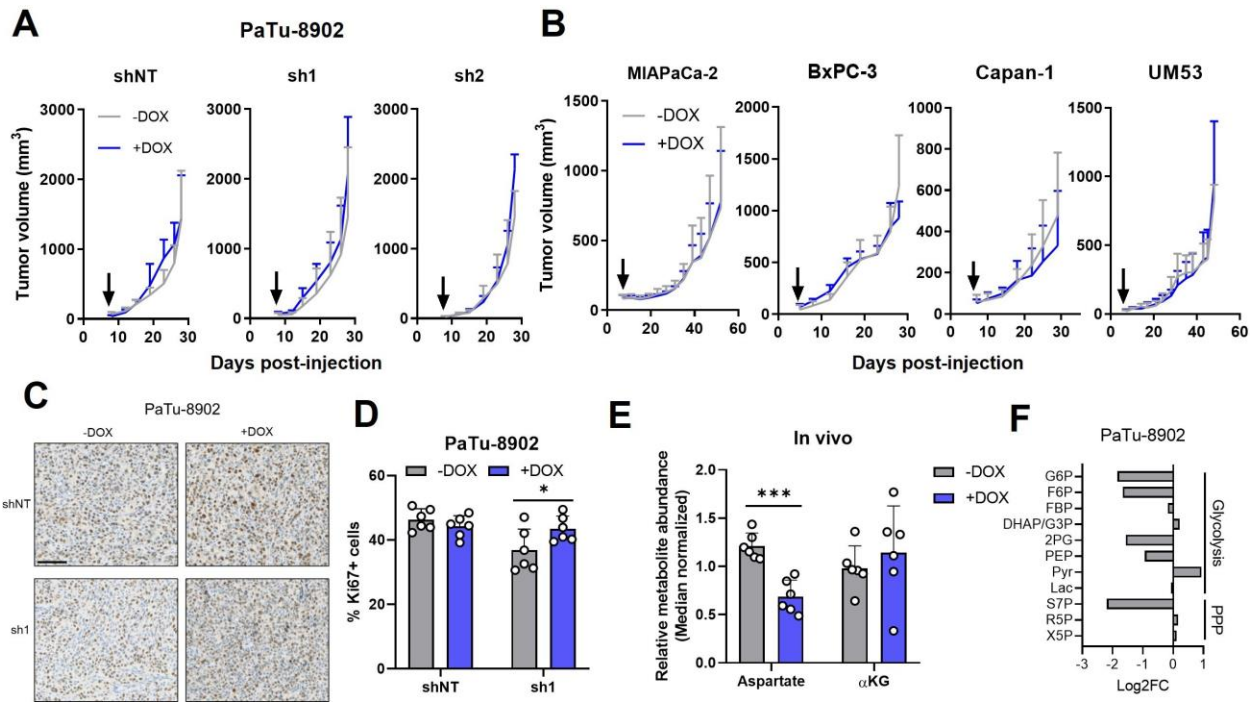

Figure 4-8 GOT2 is not required for in vivo growth of PDA xenografts.

A) Tumor volumes of PaTu-8902 ishRNA flank xenografts in NSG mice fed normal chow (-Dox, n=6) or doxycycline chow (+Dox, n=6). Arrows indicate administration of Dox chow 1 week after PDA cell injection. **B)** Tumor volumes of four additional PDA cell line ishGOT2.1 flank xenografts in NSG mice fed normal chow (-Dox, n=6) or doxycycline chow (+Dox, n=6). Arrows indicate administration of Dox chow 1 week after PDA cell injection. **C)** Immunohistochemistry (IHC) for Ki67 in flank xenograft tissue from PaTu-8902 ishRNA -Dox (n=6) or +Dox (n=6). **D)** Quantification of Ki67+ cells in tissue depicted in C). **E)** Relative abundances of Asp and αKG in PaTu-8902 ishGOT2.1 -Dox (n=6) or +Dox (n=6) flank xenografts. **F)** Relative fold changes in the indicated metabolites between PaTu-8902 ishGOT2.1 -Dox (n=6) and +Dox (n=6) flank xenografts. G6P=glucose-6-phosphate, F6P=fructose-6-phosphate, FBP=fructose-1,6-bisphosphate, DHAP=dihydroxyacetone phosphate, GA3P=glyceraldehyde-3-phosphate, 2PG=2-phosphoglycerate, PEP=phosphoenol pyruvate, Pyr=Pyruvate, Lac=Lactate, X5P=xylulose-5-phosphate, R5P=ribose-5-phosphate, S7P=seduoheptulose-7-phosphate, PPP=pentose phosphate pathway. For all panels, data represent mean ± SD. *p<0.05, **p<0.01, ***p<0.001, ****p<0.0001.

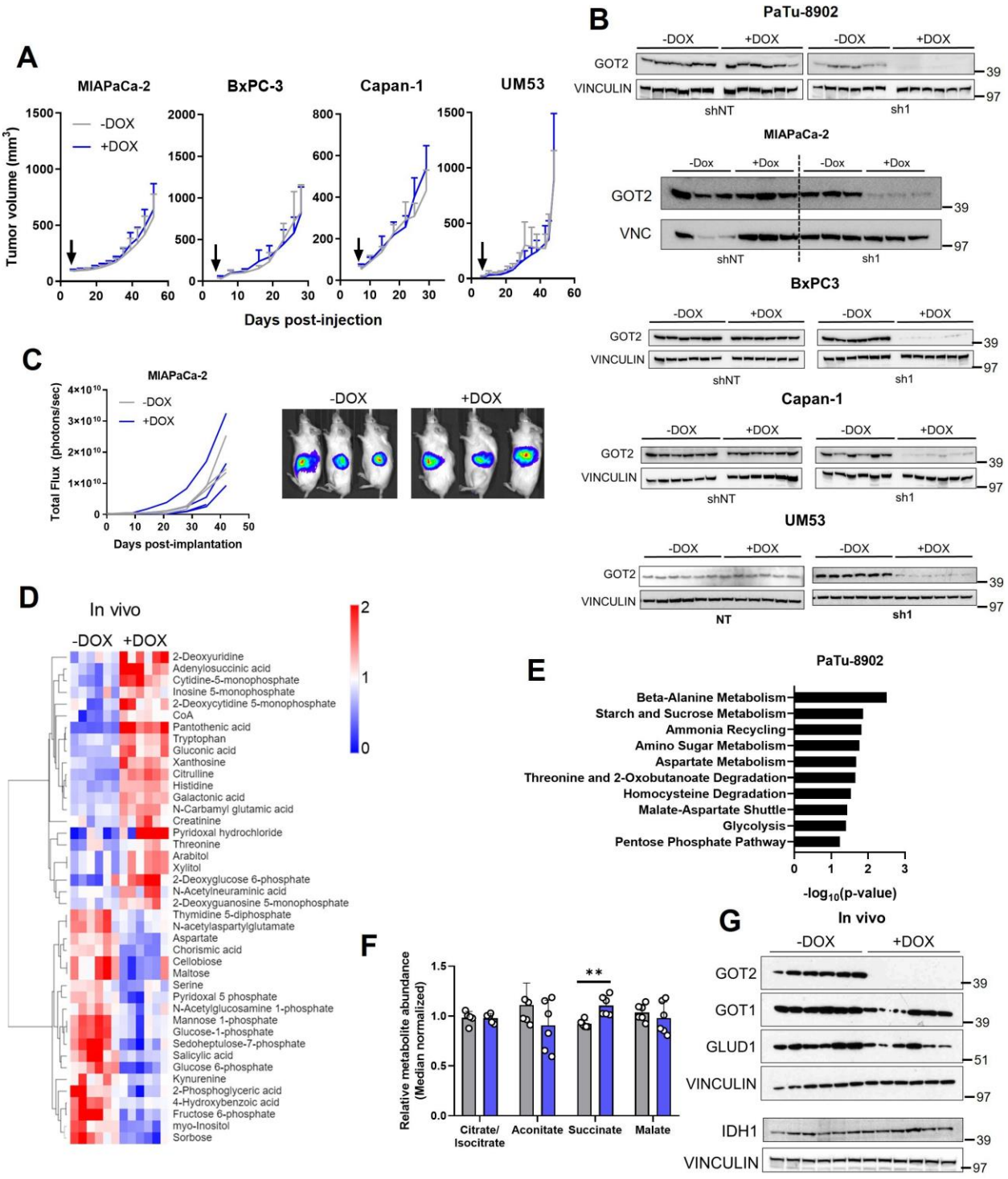

Figure 4-9 In vivo growth and metabolism of GOT2 KD PDA xenografts.

A) Tumor volumes of PDA cell line ishNT flank xenografts in NSG mice fed normal chow (-Dox, n=6) or doxycycline chow (+Dox, n=6). Arrows indicate administration of Dox chow 1 week after PDA cell injection. **B)** Immunoblots for GOT2 and VINCULIN loading control in PDA ishRNA -Dox or +Dox xenografts at endpoint. Each lane represents an independent xenograft. **C)** Bioluminescence of MIAPaCa-2 GFP-Luc ishGOT2.1 -Dox (n=3) or +Dox (n=3) orthotopic xenografts. **D)** Heatmaps of the

relative abundances of metabolites significantly ($p<0.05$) different between PaTu-8902 ishGOT2.1 -Dox (n=6) and +Dox (n=6) flank xenografts. **E)** Metabolic pathway analysis of the data presented in D). **F)** Relative abundances of TCA cycle metabolites in PaTu-8902 ishGOT2.1 -Dox (n=6) or +Dox (n=6) flank xenografts. **G)** Immunoblots for GOT2, GOT1, GLUD1, IDH1, and VINCULIN in PaTu-8902 ishGOT2.1 -Dox or +Dox flank xenografts at endpoint. For all panels, data represent mean ± SD. *$p<0.05$, **$p<0.01$, ***$p<0.001$, ****$p<0.0001$.

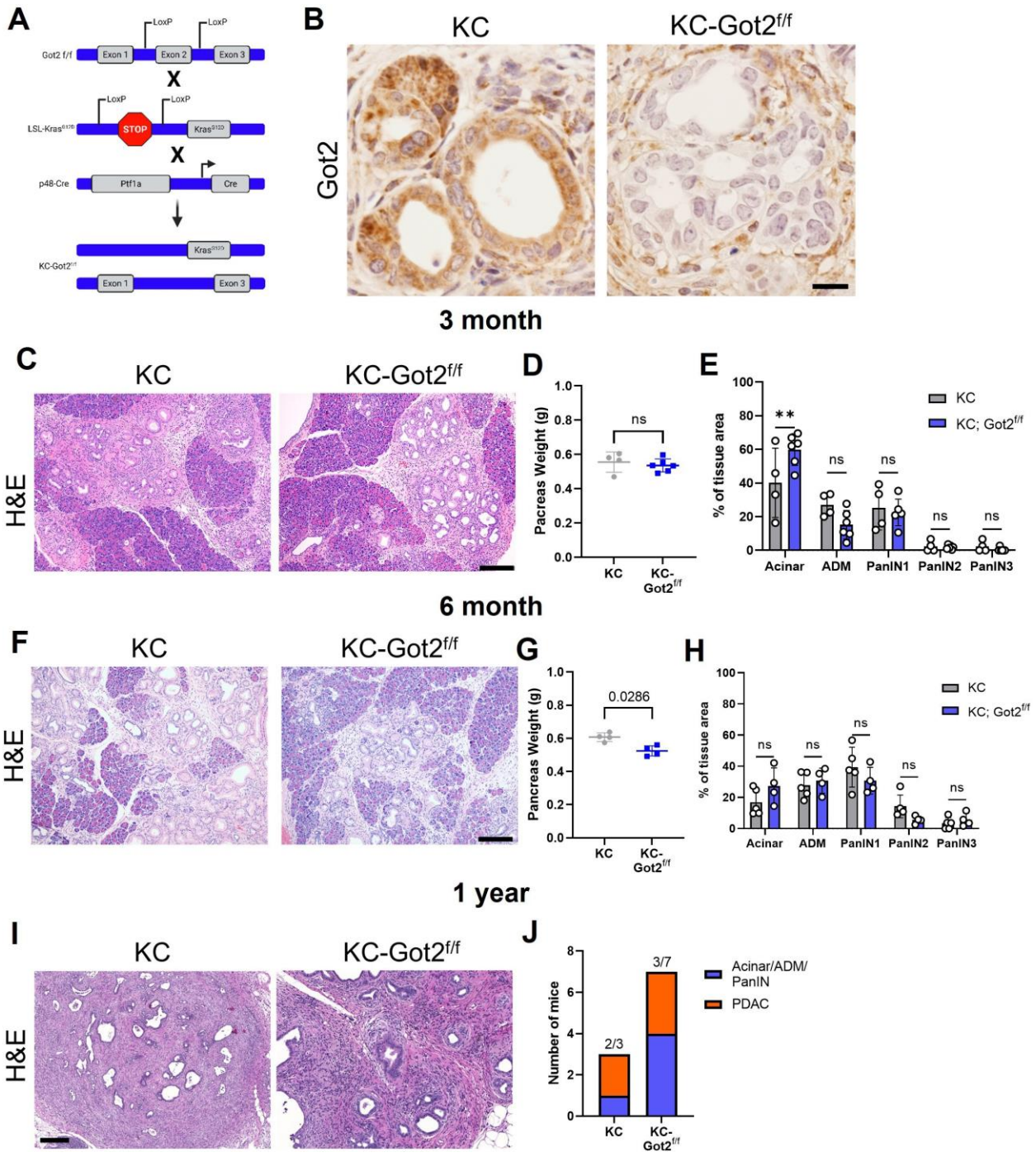

Figure 4-10 GOT2 deletion does not impact on PDA tumorigenesis in an autochthonous model.

A) Got2 deletion (floxed exon 2) with expression of mutant Kras (LSL-Kras^{G12D}) driven by epithelial pancreas-specific Cre recombinase (p48-Cre) on an immunocompetent (C57B/6) background (KC-Got2). **B)** Representative immunohistochemistry (IHC) for Got2 in pancreata from 3-month old KC-Got2 or age-matched KC historic controls. **C)** Pancreas weights of 3-month KC (n=4) or KC-Got2 (n=6) mice. **D)** Representative H&E staining of pancreata from 3-month KC (n=4) or KC-Got2 (n=6) mice. **E)** Quantitation of H&E staining from C) of tissue area with healthy acinar cells, acinar-ductal metaplasia (ADM), or pancreatic intraepithelial (PanIN) lesion severity. **F)** Representative H&E staining of pancreata from 6-

month KC (n=5) or KC-Got2 (n=4) mice. **G)** Pancreas weights of 6-month KC (n=4) or KC-Got2 (n=4) mice. **H)** Quantitation of H&E staining from F) of tissue area with healthy acinar cells, ADM, or PanIN lesion severity. **I)** Representative H&E staining of pancreata from 1-year KC (n=3) or KC-Got2 (n=7) mice. **J)** Number of KC or KC-Got2 tissue that had progressed to carcinoma at 1 year. For all panels, data represent mean ± SD. *p<0.05, **p<0.01, ***p<0.001, ****p<0.0001.

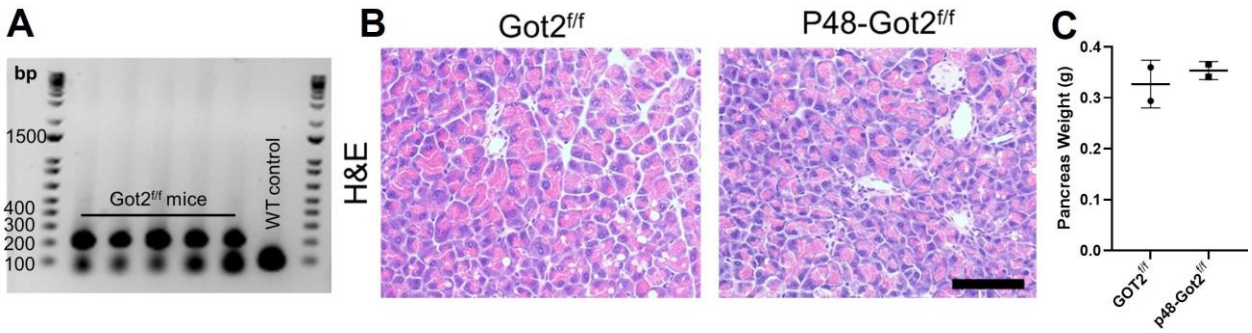

Figure 4-11 Got2 deletion has no effect on the normal mouse pancreas.

A) DNA gel showing representative genotyping of DNA isolated from tails of Got2$^{f/f}$ mice or wild type (WT) control. **B)** Representative H&E staining of pancreata from 3-month WT (Got2 f/f, n=2) or p48-Got2 f/f (n=2) mice. **C)** Pancreas weights of 3-month Got2 f/f (n=2) or p48-Got2 f/f (n=2) mice. For all panels, data represent mean ± SD. *p<0.05, **p<0.01, ***p<0.001, ****p<0.0001.

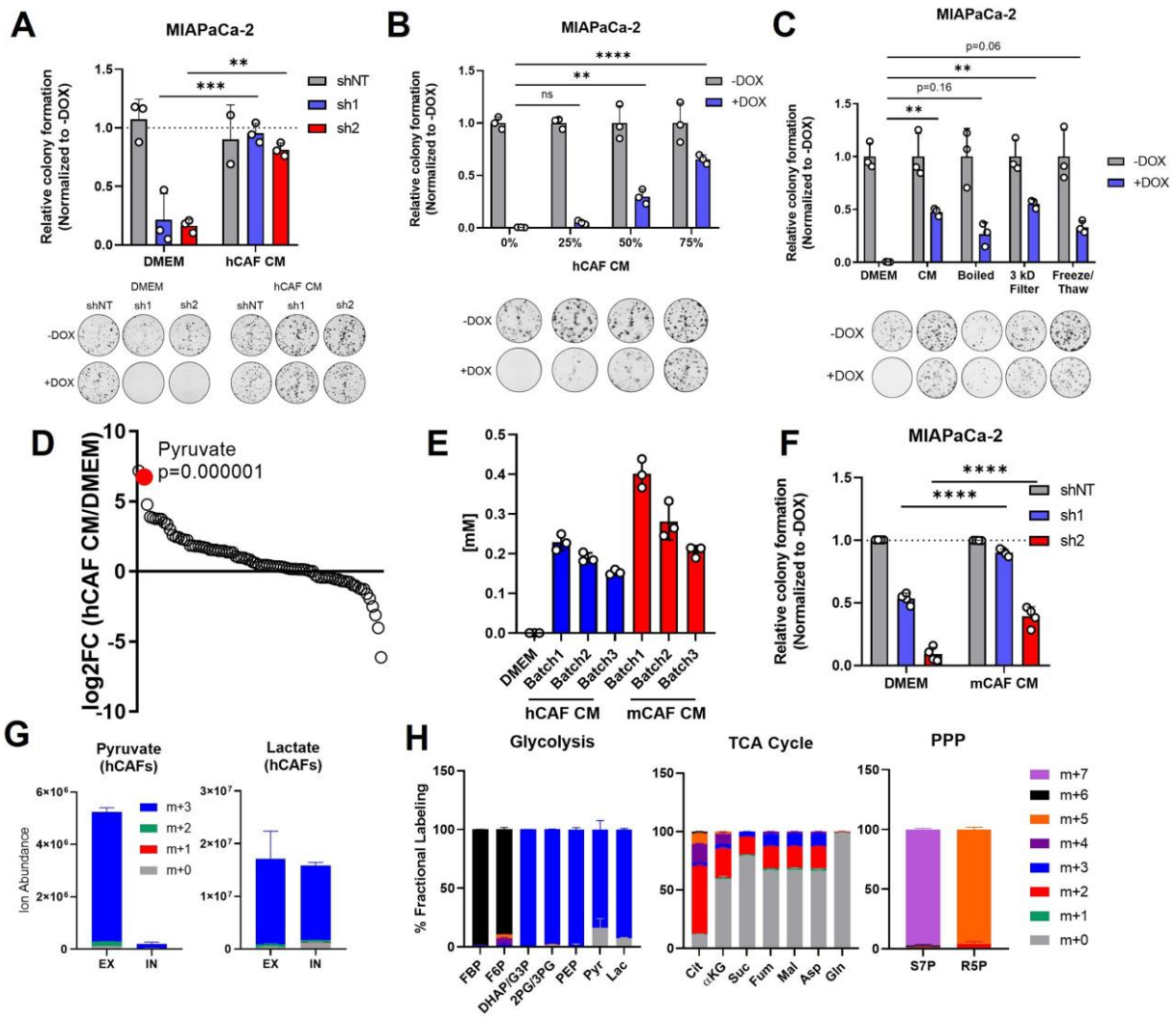

Figure 4-12 Pancreatic CAFs release pyruvate and compensate for loss of GOT2 in vitro.

A) Relative colony formation of MIAPaCa-2 ishGOT2.1 -Dox (n=3) or +Dox (n=3) cultured in normal media (DMEM) or human CAF (hCAF) CM generated after 72 hours of conditioning, normalized to -Dox for each condition. **B)** Relative colony formation of MIAPaCa-2 ishGOT2.1 -Dox (n=3) or +Dox (n=3) cultured in DMEM or indicated dilutions of hCAF CM, normalized to -Dox for each condition. **C)** Relative colony formation of MIAPaCa-2 ishGOT2.1 -Dox (n=3) or +Dox (n=3) cultured in DMEM, Mock-treated hCAF CM, boiled, 3 kDa filtered, or that subjected to freeze/thaw cycles. Data normalized to -Dox for each condition. **D)** Ranked log2 fold changes of metabolite abundances in hCAF CM compared to pyruvate-free normal DMEM. **E)** Absolute quantitation of pyruvate concentrations (mM) in three independently generated batches of hCAF or mouse CAF (mCAF) CM, including a pyruvate-free DMEM control. **F)** Relative colony formation of MIAPaCa-2 ishGOT2.1 -Dox (n=3) or +Dox (n=3) cultured in normal media (DMEM) or mCAF CM, normalized to -Dox for each condition. **G)** Ion abundance of extracellular (EX) or intracellular (IN) pyruvate (left) or lactate (right) isotopologues from hCAFs cultured with 25 mM 13C6-Glucose. **H)** Fractional labelling of intracellular glycolysis (left), TCA cycle (middle), and pentose phosphate pathway (PPP, right) metabolites in hCAFs cultured with 25 mM 13C6-Glucose. F6P=fructose-6-phosphate, FBP=fructose-1,6-bisphosphate, DHAP=dihydroxyacetone phosphate, G3P=glyceraldehyde-3-phosphate, 2PG=2-phosphoglycerate, 3PG=3-phosphoglycerate, PEP=phosphoenol pyruvate, Cit=citrate, αKG=α-ketoglutarate, Suc=succinate, Fum=fumarate, Mal=malate, Gln=glutamine, Asp=aspartate, S7P=seduoheptulose-7-phosphate, R5P=ribose-5-phosphate. For all panels, data represent mean ± SD. *p<0.05, **p<0.01, ***p<0.001, ****p<0.0001.

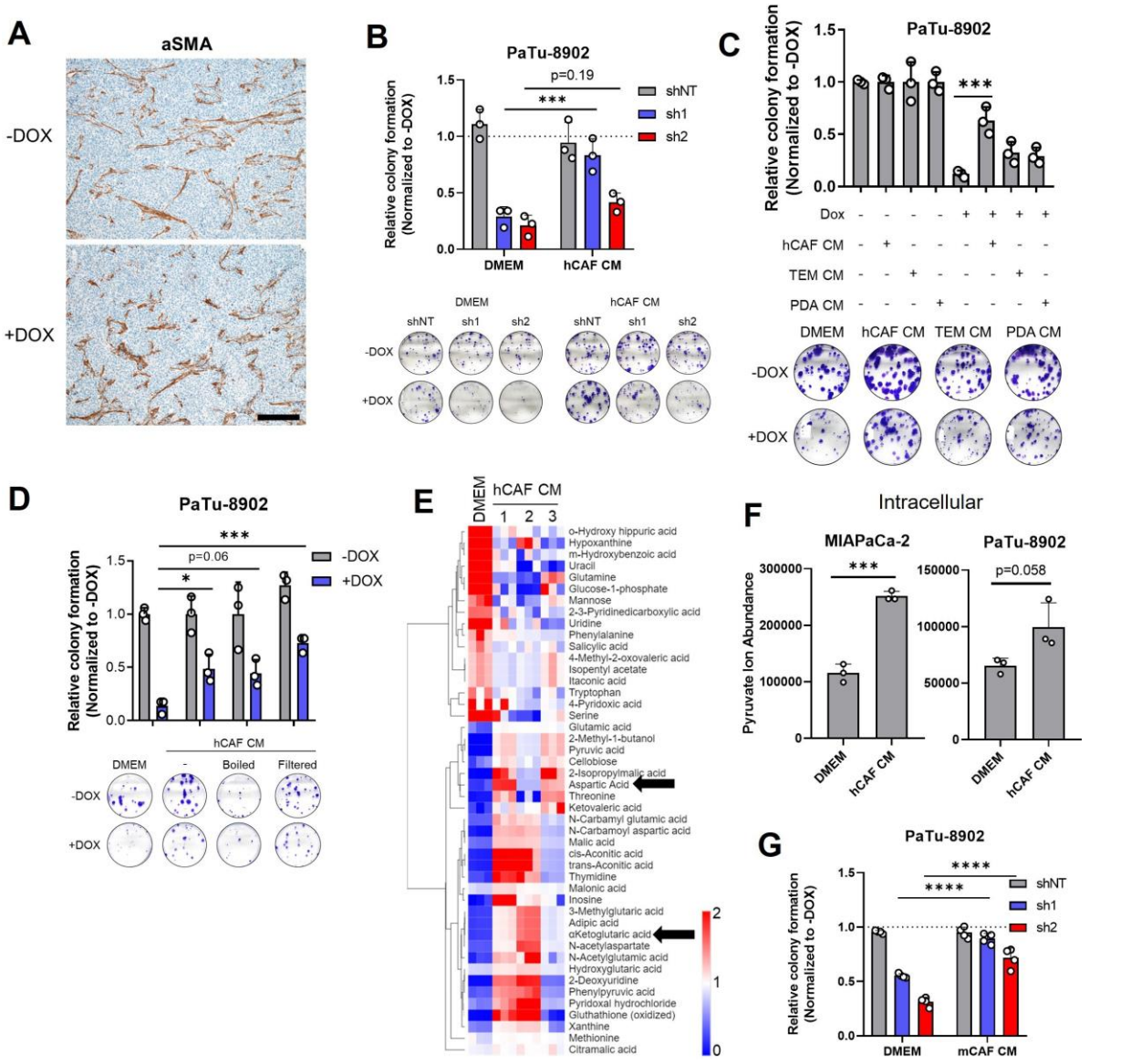

Figure 4-13 Further characterization of CAF CM rescue of GOT2 KD in vitro.

A) Immunohistochemistry (IHC) for α-smooth muscle actin (αSMA) in PaTu-8902 ishGOT2.1 -Dox or +Dox flank xenografts. B) Relative colony formation of PaTu-8902 ishGOT2.1 -Dox (n=3) or +Dox (n=3) cultured in normal media (DMEM) or human CAF (hCAF) CM, normalized to -Dox for each condition. C) Relative colony formation of PaTu-8902 ishGOT2.1 -Dox (n=3) or +Dox (n=3) cultured in DMEM, hCAF CM, PDA CM, or tumor-educated macrophage (TEM) CM, normalized to -Dox for each condition. D) Relative colony formation of PaTu-8902 ishGOT2.1 -Dox (n=3) or +Dox (n=3) cultured in DMEM, hCAF CM, or hCAF CM boiled, 3 kDa filtered, or subjected to freeze/thaw cycles, normalized to -Dox for each condition. E) Heatmap of the relative abundances of metabolites significantly ($p<0.05$) different between normal pyruvate-free DMEM and three independently generated batches of hCAF CM. Black arrows highlight Asp and αKG. F) Ion abundances of intracellular pyruvate in MIAPaCa-2 (left) or PaTu-8902 (right) cultured in normal DMEM media or hCAF CM. G) Relative colony formation of PaTu-8902 ishGOT2.1 -Dox (n=3) or +Dox (n=3) cultured in normal media (DMEM) or mCAF CM, normalized to -Dox for each condition. For all panels, data represent mean ± SD. *$p<0.05$, **$p<0.01$, ***$p<0.001$, ****$p<0.0001$.

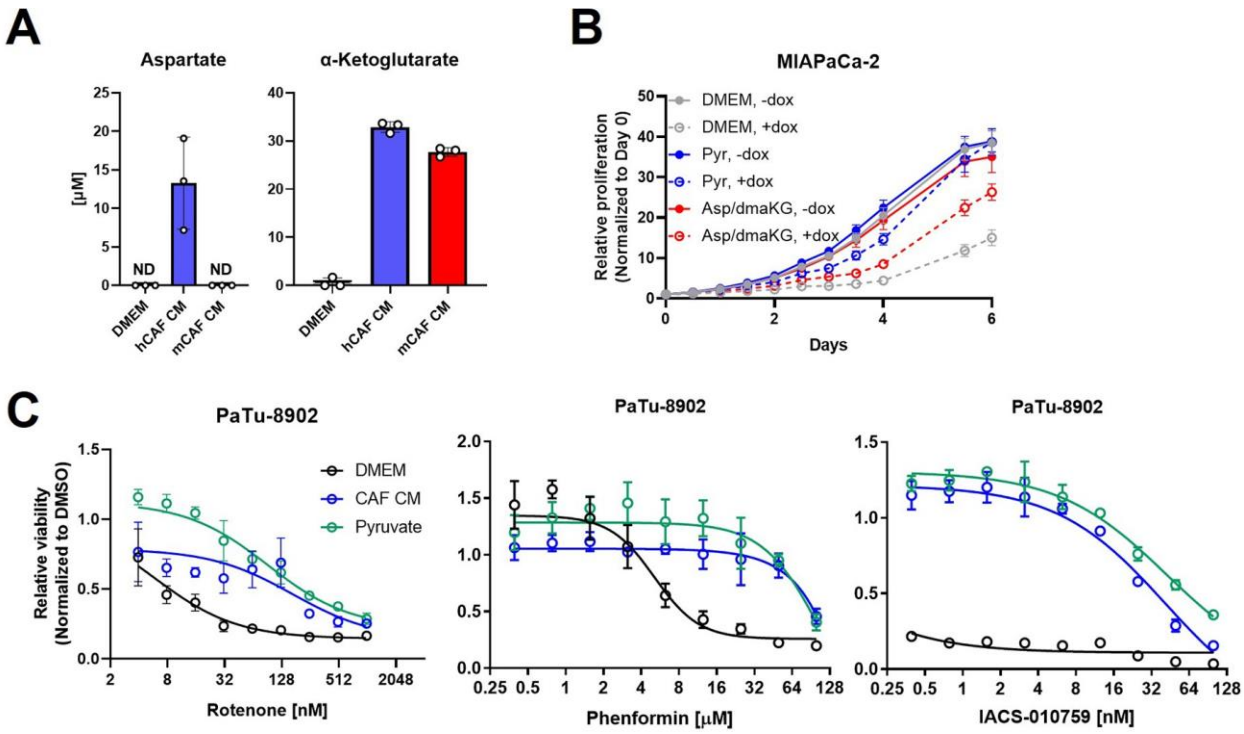

Figure 4-14 Metabolites in in CAF CM and complex I inhibitor rescue activity.

A) Absolute quantitation of aspartate (left) and α-ketoglutarate concentrations (μM) in hCAF or mCAF CM, relative to DMEM control. **B)** Relative proliferation of MIAPaCa-2 ishGOT2.1 -Dox (n=3) or +Dox (n=3) cultured in normal DMEM, 250 μM pyruvate, or a combination of 50 μM aspartate (Asp) and 500 μM dimethyl-α-ketoglutarate (dmαKG). **C)** Relative cell number of PaTu-8902 treated with the indicated concentrations of rotenone (left), phenformin (middle), or IACS-010759 (right), and cultured in normal DMEM, hCAF CM, or 1 mM pyruvate. For all panels, data represent mean ± SD. *p<0.05, **p<0.01, ***p<0.001, ****p<0.0001.

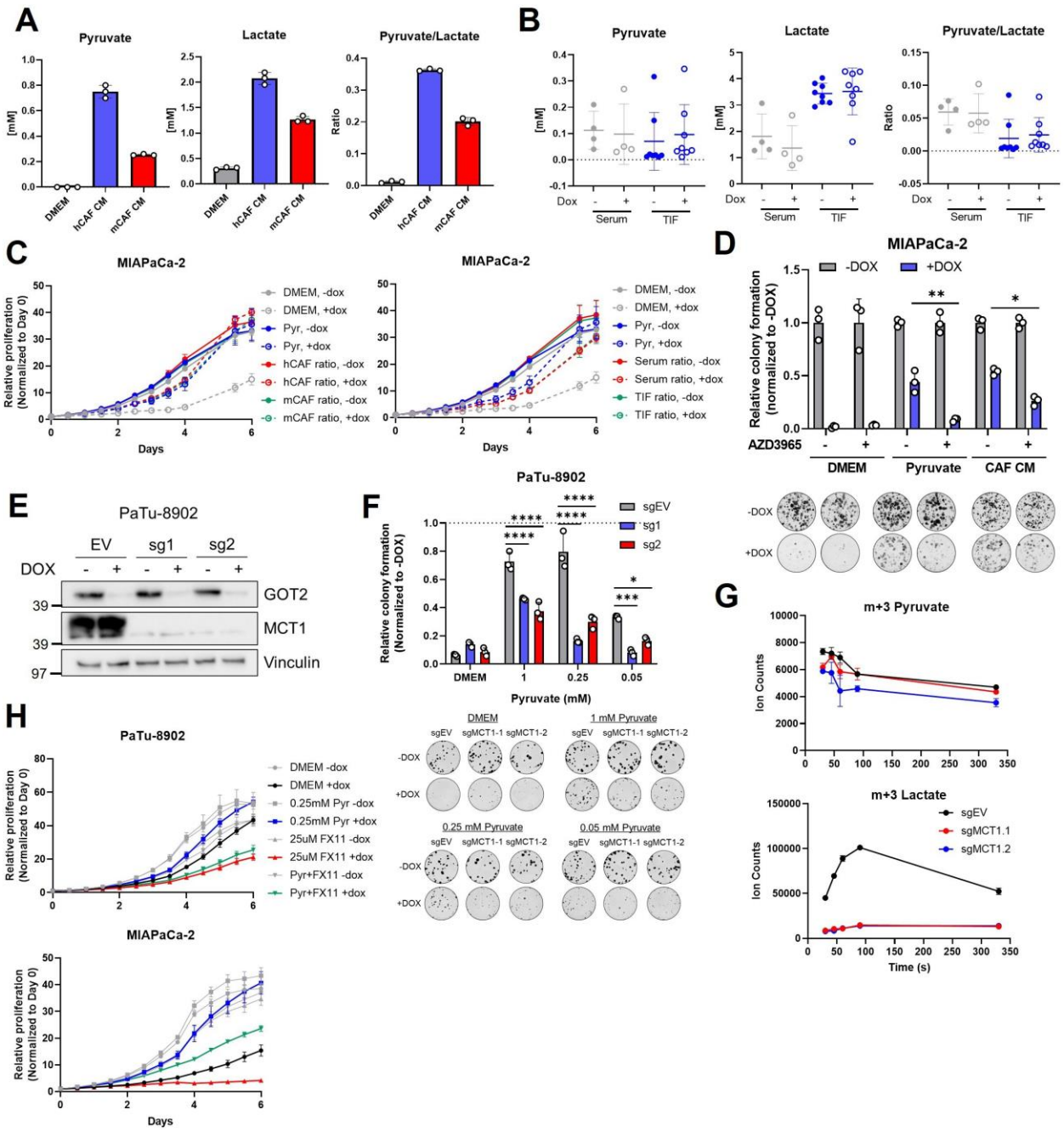

Figure 4-15 MCT1 inhibition prevents pyruvate-mediated restoration of redox balance in vitro after loss of GOT2.

A) Absolute quantitation of pyruvate (left) and lactate (middle), and the relative pyruvate/lactate ratio (right) in normal DMEM, hCAF CM, and mCAF CM. **B)** Absolute quantitation of pyruvate (left) and lactate (middle), and the relative pyruvate/lactate ratio (right) in serum or the tumor interstitial fluid (TIF) from NSG mice harboring PaTu-8902 ishGOT2.1 -Dox (n=8 tumors, 4 mice) or +Dox (n=8 tumors, 4 mice) flank xenografts. **C)** Relative proliferation of MIAPaCa-2 ishGOT2.1 -Dox (n=3) or +Dox (n=3) cultured with the absolute levels and relative ratios of pyruvate/lactate in hCAF and mCAF CM (left) or serum/TIF (right) from A,B), normalized to Day 0 for each condition. **D)** Relative colony formation of MIAPaCa-2 ishGOT2.1 -Dox (n=3) or +Dox (n=3) cultured in normal media (DMEM), 1 mM pyruvate, or human CAF (hCAF) CM, and treated with DMSO control or 100 nM AZD3965, normalized to -Dox for each condition.

E) Immunoblots of GOT2, MCT1, and VINCULIN loading control in PaTu-8902 ishGOT2.1 expressing empty vector (EV), or two sgRNAs targeting MCT1 (sg1, sg2). **F)** Relative colony formation of PaTu-8902 ishGOT2.1 -Dox (n=3) or +Dox (n=3) expressing empty vector (EV), or two sgRNAs targeting MCT1 (sg1, sg2) and cultured in the indicated doses of pyruvate, normalized to -Dox for each condition. **G)** Ion counts of intracellular m+3 pyruvate (top) and lactate (bottom) in PaTu-8902 expressing empty vector (EV), or two sgRNAs targeting MCT1 (sg1, sg2) and cultured in 1 mM 13C3-Pyruvate for the indicated time points. **H)** Relative proliferation of PaTu-8902 (top) and MIAPaCa-2 (bottom) ishGOT2.1 -Dox (n=3) or +Dox (n=3) cultured in normal DMEM or 0.25 mM pyruvate and treated with DMSO vehicle control or 25 μM FX11, normalized to Day 0 for each condition. For all panels, data represent mean ± SD. *p<0.05, **p<0.01, ***p<0.001, ****p<0.0001.

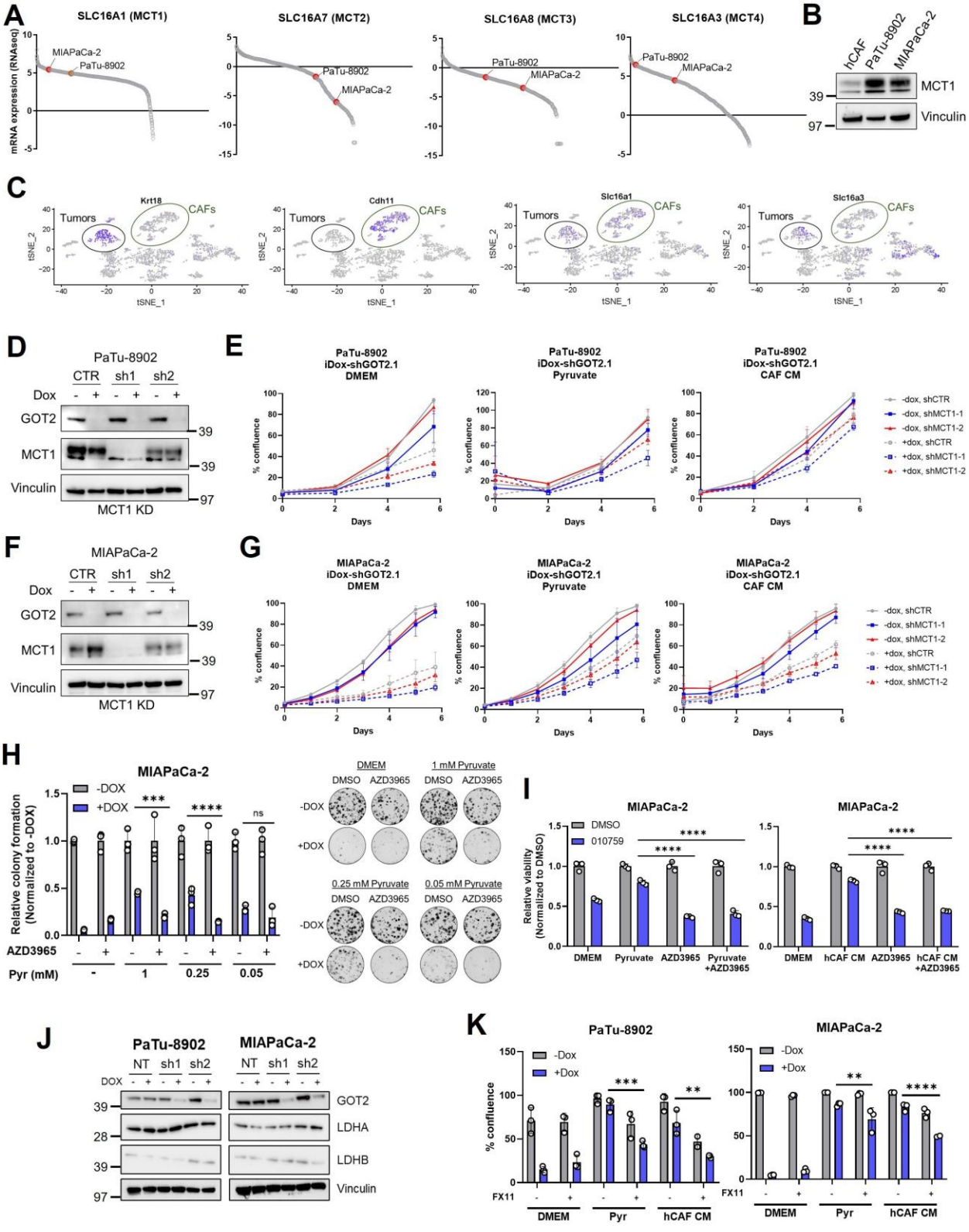

Figure 4-16 Inhibition of pyruvate uptake and catabolism in GOT2 KD cells in vitro.

A) Relative CCLE mRNA expression of the indicated SLC16 family members in PaTu-8902 and MIAPaCa-2. **B)** Immunoblot for MCT1 and VINCULIN loading control the indicated cell lines. **C)** Single-cell RNA sequencing data from murine KPC cell line syngeneic orthotopic tumors showing expression of Slc16a1 (MCT1) and Slc16a3 (MCT4) in CAF (marked by CDH11 expression) and epithelial (marked by Krt18 expression) populations. **D,F)** Immunoblots for GOT2, MCT1, and VINCULIN in PaTu-8902 D) and MIAPaCa-2 F) ishGOT2.1 -Dox or +Dox expressing the indicated control (CTR) or constitutive MCT1-targeting shRNAs (sh1, sh2). **E,G)** Relative proliferation of PaTu-8902 E) and MIAPaCa-2 G) ishGOT2.1 -Dox (n=3) or +Dox (n=3) expressing the indicated shRNAs and cultured in normal DMEM (left), 0.25 mM pyruvate (middle), or hCAF CM (right), normalized to Day 0 for each condition. **H)** Relative colony formation of MIAPaCa-2 ishGOT2.1 -Dox (n=3) or +Dox (n=3) cultured in normal media (DMEM) or the indicated doses of pyruvate, and treated with DMSO control or 100 nM AZD3965, normalized to -Dox for each condition. **I)** Relative viability of MIAPaCa-2 cultured in normal media (DMEM), 0.25 mM pyruvate (left), or hCAF CM (right) and treated with DMSO vehicle control or 100 nM IACS-010759, alone or in combination with 100 nM AZD3965, normalized to -Dox for each condition. **J)** Immunoblots for GOT2, LDHA, LDHB, and VINCULIN in PaTu-8902 and MIAPaCa-2 ishRNA. **K)** Relative number of PaTu-8902 (left) and MIAPaCa-2 (right) ishGOT2.1 -Dox (n=3) or +Dox (n=3) cultured in normal DMEM, 0.25 mM pyruvate, or hCAF CM, and treated with DMSO vehicle control or 25 µM FX11, normalized to -Dox for each condition. For all panels, data represent mean ± SD. *p<0.05, **p<0.01, ***p<0.001, ****p<0.0001.

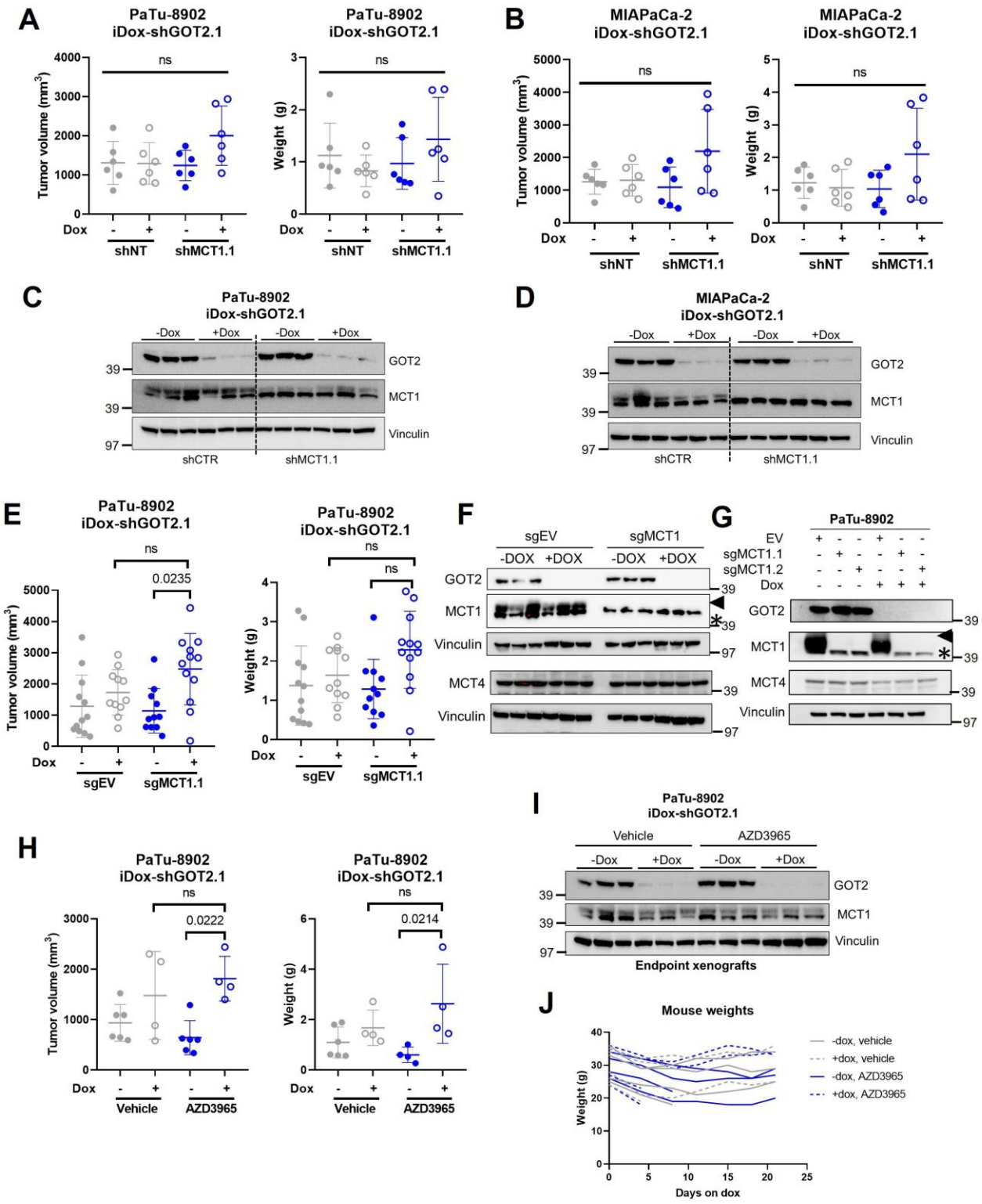

Figure 4-17 MCT1/GOT2 dual inhibition in PDA xenografts.

A,B) Tumor volume (left) and weight (right) of PaTu-8902 A) and tumor volume of MIAPaCa-2 B) ishGOT2.1 flank xenografts in NSG mice fed normal chow (-Dox, n=6) or doxycycline chow (+Dox, n=6) expressing control (shNT) or shMCT1.1. **C,D)** Immunoblots for GOT2, MCT1, and VINCULIN in

representative tumors from PaTu-8902 C) or MIAPaCa-2 D) ishGOT2.1 -Dox (n=3) or +Dox (n=3) flank xenografts with shNT or shMCT1.1. Each lane represents an individual tumor. **E)** Tumor volume (left) and weight (right) of PaTu-8902 flank xenografts in NSG mice fed normal chow (-Dox, n=6) or doxycycline chow (+Dox, n=6) expressing control (sgEV) or sgMCT1.1. **F)** Immunoblot for GOT2, MCT1, MCT4 and VINCULIN in representative, independent tumors from PaTu-8902 ishGOT2.1 -Dox (n=3) or +Dox (n=3) flank xenografts with sgEV or sgMCT1.1. **G)** Immunoblot for GOT2, MCT1, MCT4 and VINCULIN in PaTu-8902 ishGOT2.1 -Dox or +Dox cell lines with sgEV or sgMCT1.1. For F,G) blots, arrow=MCT1 band, asterisk=non-specific band. **H)** Tumor volume (left) and weight (right) of PaTu-8902 flank xenografts in NSG mice fed normal chow (-Dox, n=6) or doxycycline chow (+Dox, n=6) treated with PBS control or 100 mg/kg AZD3965. **I)** Immunoblot for GOT2, MCT1, and VINCULIN in in representative, independent tumors of PaTu-8902 ishGOT2.1 -Dox (n=3) or +Dox (n=3) flank xenografts. **J)** Weights of mice treated in H). For all panels, data represent mean ± SD. *p<0.05, **p<0.01, ***p<0.001, ****p<0.0001.

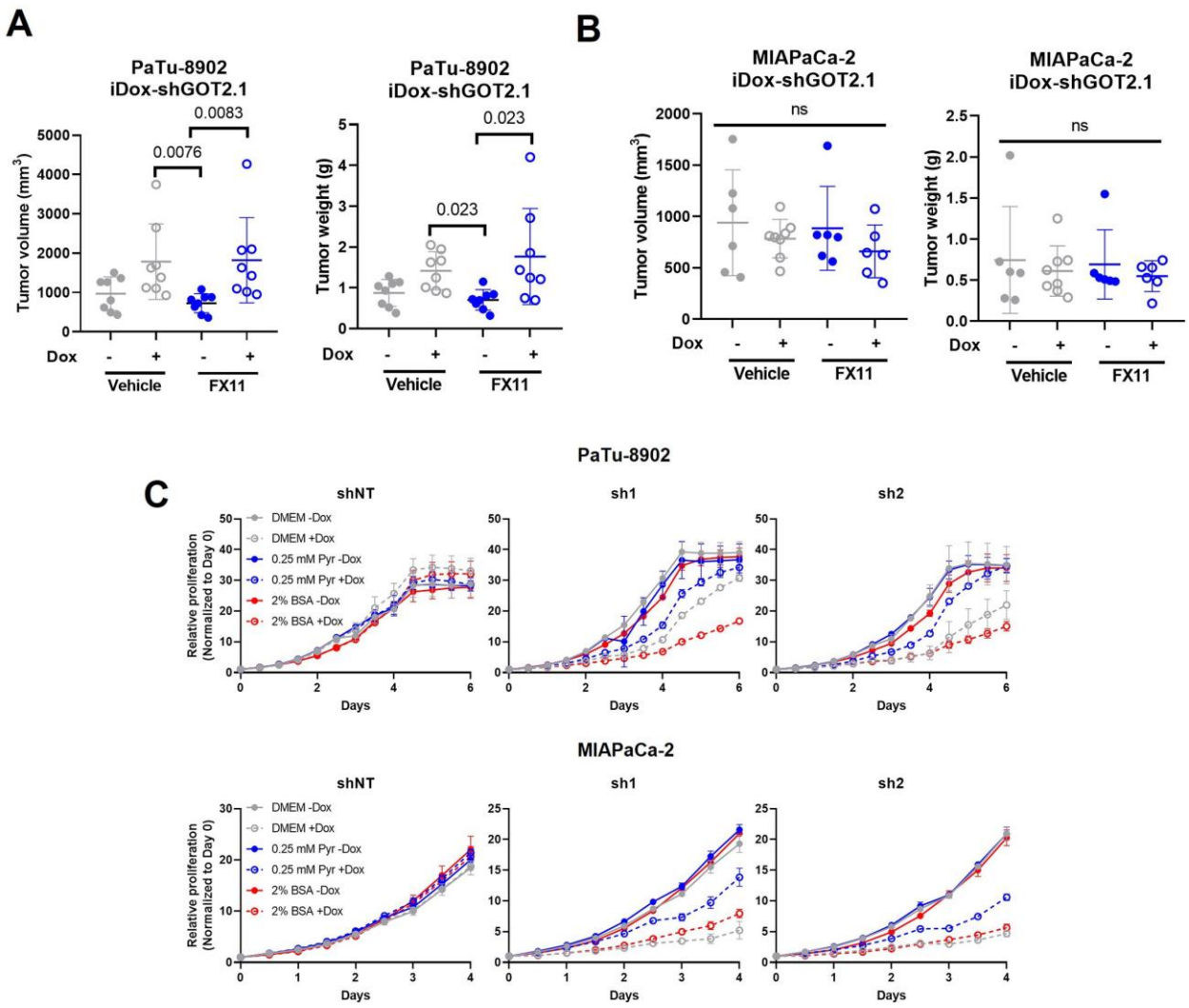

Figure 4-18 LDHA/GOT2 dual inhibition in PDA xenografts.

A,B) Tumor volume (left) and weight (right) of PaTu-8902 A) and MIAPaCa-2 B) ishGOT2.1 flank xenografts in NSG mice fed normal chow (-Dox, n=6) or doxycycline chow (+Dox, n=6) and treated with PBS control or 2 mg/kg FX11. **C)** Relative proliferation of PaTu-8902 (top) and MIAPaCa-2 (bottom) ishRNA -Dox (n=3) or +Dox (n=3) cultured in normal DMEM, 0.25 mM pyruvate, or 2% BSA, normalized to Day 0 for each condition.

Chapter 5 – Genetic Mouse Models of Pancreatic Cancer Metabolism

5.1 Background

Genetically engineered mouse models (GEMMs) of pancreatic cancer accurately recapitulate the genomic profile, progression, and tumor microenvironment (TME) of human disease (1, 2). As such, these models are powerful tools for studying pancreatic metabolism in a more physiologically relevant context. The following chapter builds on the initial finding described in Chapter 4 that Got2 deletion has no impact on mouse pancreatic tumorigenesis. Additionally, as described in Chapter 3, two other studies have drawn into question the role of Got2 in pancreatic cancer (3, 4). Therefore, GEMMs were utilized to address this question more definitively.

5.2 Got2 deletion and pancreatic tumorigenesis

As discussed in Chapter 4, expression of oncogenic Kras^{G12D} driven by exocrine pancreas-specific Ptf1a-Cre (KC) leads to transformation and progression through acinar-ductal metaplasia (ADM) to advanced pancreatic intraepithelial neoplasia (PanIN)(2, 5). Got2 deletion in this KC model of pancreatic tumorigenesis (KC-Got2$^{\Delta/\Delta}$) had no impact on the number or severity of ADM or PanIN lesions at 3, 6, or 12 months of age. However, this initial experiment compared newly generated KC-Got2$^{\Delta/\Delta}$ mice with KC historic controls. A new breeding scheme was designed to generate proper KC-Got2$^{+/+}$, KC-Got2$^{\Delta/+}$, KC-Got2$^{\Delta/\Delta}$ littermate controls (**Fig. 5-1A,B**). Additionally, mice with Got2 deletion driven by Ptf1a-Cre, but lacking Kras^{G12D}, were generated in parallel to

evaluate loss of Got2 in the normal pancreas. These mice were aged to 6 months, as before, at which time pancreata were harvested and weighed. No differences were observed in the pancreas to body weight ratios (P/BW) when Got2 was deleted in the normal pancreas controls (**Fig. 5-1C**). KC pancreas tissue had significantly increased P/BW near 2%, as reported previously (6), yet no differences were observed with loss of one or both copies of Got2 (**Fig. 5-1C**). These results confirm our initial finding that loss of Got2 does not impact pancreatic tumorigenesis in the KC model.

5.3 Got2 deletion in mouse PDA

Progression from PanINs to carcinoma requires the loss of a tumor suppressor gene in addition to transformation by oncogenic Kras (1, 5). In the KC model, this process can take up to a year following sporadic tumor suppressor loss (5). To accelerate this progression, the KPC model combines expression of the inactive p53^{R172H} allele with expression of Kras^{G12D}(1). To evaluate the metabolic dependency for Got2 in carcinoma, I generated KPC-Got2$^{+/+}$, KPC-Got2$^{\Delta/+}$, KPC-Got2$^{\Delta/\Delta}$ mice (**Fig. 5-2A**). The survival experiment with these mice is ongoing, though the time to endpoint of ~4 months is in line with previously reported studies (**Fig. 5-2B**)(5). Endpoint is determined as loss of 10% body weight over two consecutive weeks (20% overall loss).

5.4 Discussion

Thus far, deletion of Got2 in the KC tumorigenesis or the KPC carcinoma models has not induced a phenotype. Since in Chapter 4 GOT2 was shown to be dispensable for human tumors growing in immunocompromised mouse hosts, these models were generated to evaluate the role of GOT2 in an immunocompetent model that accurately

recapitulates the genomic profile, tissue architecture, and progression of human disease(1, 2). Considering several recent studies have raised the profile of GOT2 in cancer(3, 4, 7), and drawn into question its role in compensatory metabolism and tumor-stroma crosstalk, the proposed future work in Chapter 8 will add valuable data to the conversation around GOT2 in pancreatic cancer metabolism.

5.5 Methods

Mouse studies

Mice were maintained in a pure C57BL/6J background and experimental mice were maintained in SPF housing with access to standard diet and water ad libitum at constant ambient temperature and a 12-hour light cycle. All experiments were conducted in accordance with the Office of Laboratory Animal Welfare and approved by the Institutional Animal Care and Use Committees of the University of Michigan.

KC-Got2$^{\Delta/\Delta}$ and KPC-Got2$^{\Delta/\Delta}$ models

Mice containing loxP sites flanking exon 2 of the Got2 gene were generated by Ozgene. These mice were crossed to the KC or the KPC models. Tails from 3-week-old mice were collected at weaning and submitted to Transnetyx for genotyping. The following primers were used: Kras^{G12D} (Fw-GGCCTGCTGAAAATGACTGAGTATA, Rev-CTGTATCGTCAAGGCGCTCTT); Tp53R172H (Fw-CATCTACAAGAAGTCACAGCACATG, Rev- GGAGCAGCGCTCATGGT); Got2 WT (Fw- GCAGATTAAAACCACAAGGCCTGTA, Rev-ATGTTAAAATTGTCATCCCCTTGTGC); Got2 floxed (Fw-GCAGATTAAAACCACAAGGCCTGTA,Rev-

AGAGAATAGGAACTTCGGAATAGGAACT); Cre (Fw-TTAATCCATATTGGCAGAACGAAAACG, Rev-CAGGCTAAGTGCCTTCTCTACA).

Mouse pancreas isolation

At endpoint, mice were euthanized according to the approved IACUC protocol and mouse weights were recorded. Tails were collected to re-confirm genotypes. The mouse body cavity was opened using scissors and the pancreas was visualized. The pancreas was carefully dissected using the spleen and a portion of the intestine as anchor points, avoiding contact with the pancreas itself. Following excision of the pancreas, the spleen and intestine fragment were removed, and the pancreas weight was recorded. The whole pancreas was fixed head-to-tail in formalin for 24 hours and then stored in 70% ethanol before paraffin embedding for later histological analysis.

Statistics

Statistics were performed using Graph Pad Prism 9. Groups of 2 were analyzed with two-tailed students t test, groups greater than 2 were compared using one-way ANOVA analysis with Tukey post hoc test or two-way ANOVA with Dunnett's correction for multiple independent variables. All error bars represent mean with standard deviation, all group numbers and explanation of significant values are presented within the figure legends. Experiments were repeated at least twice to verify results.

5.6 References

1. Hingorani SR, Wang L, Multani AS, Combs C, Deramaudt TB, Hruban RH, Rustgi AK, Chang S, Tuveson DA. Trp53R172H and KrasG12D cooperate to promote chromosomal instability and widely metastatic pancreatic ductal adenocarcinoma in mice. Cancer Cell. 2005;7(5):469-83. Epub 2005/05/17. doi: 10.1016/j.ccr.2005.04.023. PubMed PMID: 15894267.

2. Hingorani SR, Petricoin EF, Maitra A, Rajapakse V, King C, Jacobetz MA, Ross S, Conrads TP, Veenstra TD, Hitt BA, Kawaguchi Y, Johann D, Liotta LA, Crawford HC, Putt ME, Jacks T, Wright CV, Hruban RH, Lowy AM, Tuveson DA. Preinvasive and invasive ductal pancreatic cancer and its early detection in the mouse. Cancer Cell. 2003;4(6):437-50. Epub 2004/01/07. doi: 10.1016/s1535-6108(03)00309-x. PubMed PMID: 14706336.

3. Abrego J, Sanford-Crane H, Oon C, Xiao X, Betts CB, Sun D, Nagarajan S, Diaz L, Sandborg H, Bhattacharyya S, Xia Z, Coussens LM, Tontonoz P, Sherman MH. A cancer cell-intrinsic GOT2-PPARd axis suppresses antitumor immunity. Cancer Discov. 2022. Epub 2022/07/28. doi: 10.1158/2159-8290.Cd-22-0661. PubMed PMID: 35894778.

4. Garcia-Bermudez J, Badgley MA, Prasad S, Baudrier L, Liu Y, La K, Soula M, Williams RT, Yamaguchi N, Hwang RF, Taylor LJ, de Stanchina E, Rostandy B, Alwaseem H, Molina H, Bar-Sagi D, Birsoy K. Adaptive stimulation of macropinocytosis overcomes aspartate limitation in cancer cells under hypoxia. Nature Metabolism. 2022. doi: 10.1038/s42255-022-00583-z.

5. Collins MA, Bednar F, Zhang Y, Brisset JC, Galbán S, Galbán CJ, Rakshit S, Flannagan KS, Adsay NV, Pasca di Magliano M. Oncogenic Kras is required for both the initiation and maintenance of pancreatic cancer in mice. J Clin Invest. 2012;122(2):639-53. Epub 2012/01/11. doi: 10.1172/jci59227. PubMed PMID: 22232209; PMCID: PMC3266788.

6. Ruggeri JM, Franco-Barraza J, Sohail A, Zhang Y, Long D, Pasca di Magliano M, Cukierman E, Fridman R, Crawford HC. Discoidin Domain Receptor 1 (DDR1) Is Necessary for Tissue Homeostasis in Pancreatic Injury and Pathogenesis of Pancreatic Ductal Adenocarcinoma. Am J Pathol. 2020;190(8):1735-51. Epub 2020/04/28. doi: 10.1016/j.ajpath.2020.03.020. PubMed PMID: 32339496; PMCID: PMC7416078.

7. Li Y, Li B, Xu Y, Qian L, Xu T, Meng G, Li H, Wang Y, Zhang L, Jiang X, Liu Q, Xie Y, Cheng C, Sun B, Yu D. GOT2 Silencing Promotes Reprogramming of Glutamine Metabolism and Sensitizes Hepatocellular Carcinoma to Glutaminase Inhibitors. Cancer Res. 2022. Epub 2022/07/28. doi: 10.1158/0008-5472.Can-22-0042. PubMed PMID: 35895805.

5.7 Figures

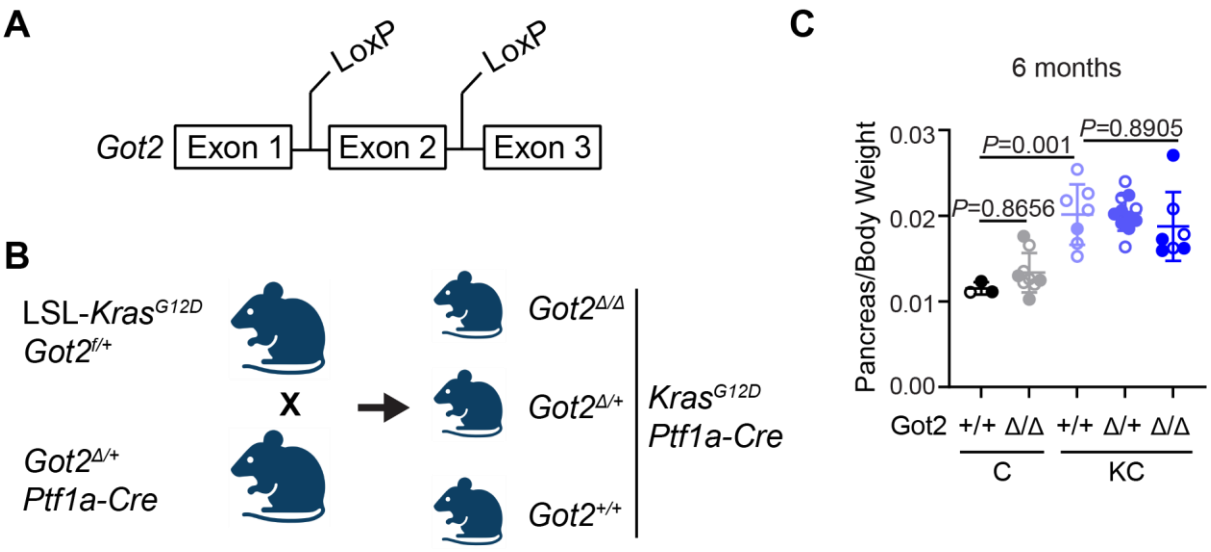

Figure 5-1 Genetic model of Got2 deletion in pancreatic tumorigenesis

A) Schematic for the Got2 floxed mouse depicting the location of loxP sites flanking exon 2 of Got2. **B)** Schematic showing the breeding scheme for generating KC-Got2$^{+/+}$, KC-Got2$^{\Delta/+}$, and KC-Got2$^{\Delta/\Delta}$ littermates. **C)** Pancreas to body weight ratios for Ptf1a-Cre (C) Got2$^{+/+}$ or Got2$^{\Delta/\Delta}$ normal pancreas tissue, or KC-Got2$^{+/+}$, KC-Got2$^{\Delta/+}$, and KC-Got2$^{\Delta/\Delta}$ transformed tissue from 6-month-old mice. Closed circles represent male mice and open circles represent female mice.

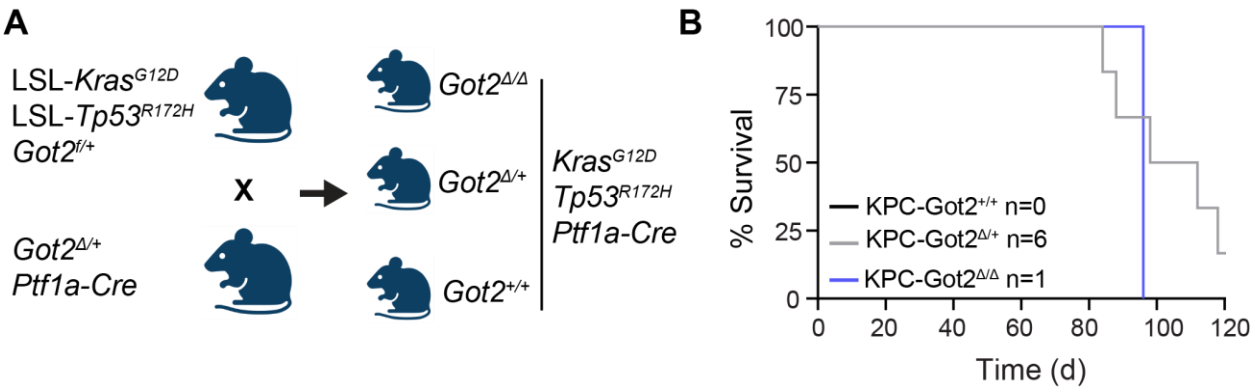

Figure 5-2 Genetic model of Got2 deletion in mouse PDA

A) Schematic showing the breeding scheme for generating KPC-Got2$^{+/+}$, KPC-Got2$^{\Delta/+}$, and KPC-Got2$^{\Delta/\Delta}$ littermates. **B)** Ongoing survival analysis of KPC-Got2$^{+/+}$, KPC-Got2$^{\Delta/+}$, and KPC-Got2$^{\Delta/\Delta}$ littermates.

Chapter 6 – Reprogramming Tumor-Associated Macrophage Metabolism

6.1 Background

Thus far, my dissertation has focused on the role of GOT2 in pancreatic cancer cells. In this chapter, I will instead begin to investigate how GOT2, and the cytosolic isoform GOT1, support pro-tumorigenic immune function in pancreatic tumors. Tumor-associated macrophages (TAM) are the major immune component in pancreatic tumors(1, 2). Mutant KRAS-driven signaling from cancer cells polarizes myeloid-derived innate immune cells towards an anti-inflammatory state that promotes tumorigenesis and suppresses anti-tumor immune activity(3-5). Depleting TAMs from pancreatic tumors improves treatment responses and overall survival(6-10). Our lab has recently uncovered a mechanism by which TAMs confer resistance to PDA cells against the chemotherapy gemcitabine(11). TAMs release high levels of the pyrimidine nucleoside deoxycytidine (dC), which is structurally similar to gemcitabine and dampens its efficacy(11). Ablating TAMs *in vivo* significantly improved the response of mouse PDA tumors to gemcitabine(11). However, depleting TAMs is a harsh approach and undoubtedly affects many processes within a tumor. A more refined approach, and the basis of the work described here, specifically targets dC production and release in TAMs. The amino acid aspartate is required for pyrimidine synthesis and aspartate is produced by glutamate-oxaloacetate transaminases (GOTs).

In addition to protecting PDA cells from chemotherapy, TAMs also suppress the anti-tumor adaptive immune system by promoting regulatory T cell (Treg) activity and

preventing cytotoxic responses by tumor infiltrating effector T (Teff) cells(6, 9, 10, 12). Aside from aspartate synthesis, GOT1 and GOT2 fuel the TCA cycle and maintain redox homeostasis. Recent work has demonstrated that TAMs utilize oxidative metabolism to carry out pro-tumor functions(13-16). Thus, Got1 and Got2 deletion may have broader metabolic implications in TAMs and disrupt key pro-tumorigenic functions through mechanisms unrelated to dC release.

6.2 Mouse models of Got1 and Got2 deletion in myeloid cells

Analysis of both human and mouse PDA single-cell RNA sequencing data (2) revealed that both Got1 and Got2 are expressed across multiple cellular compartments in human and mouse PDA (**Fig. 6-1A,B; Fig. 6-2A,B**). TAMs are part of the myeloid lineage, which in the human PDA dataset expressed GOT1 and GOT2 to similar levels as epithelial cells and fibroblasts (**Fig. 6-1A,B**). Similarly, in both autochthonous and orthotopic allograft models of mouse PDA, macrophages expressed Got1 and Got2 demonstrating these murine models mirror the myeloid Got1/Got2 expression in human disease (**Fig. 6-2A,B**).

Therefore, two mouse models of Got1 or Got2 knockout in macrophages were generated by crossing either $Got1^{f/f}$ or $Got2^{f/f}$ mice into the myeloid-specific LysM-Cre model (LysM-$Got1^{\Delta/\Delta}$ or LysM-$Got2^{\Delta/\Delta}$) (17). Bone marrow-derived macrophages (BMDMs) were generated from these mice and the purity of the macrophage population was confirmed via flow analysis (**Fig. 6-3A**). Next, BMDMs were cultured with either macrophage-colony stimulating factor (M-CSF), lipopolysaccharide (LPS), or interleukin-4 (IL-4) to either maintain a non-polarized state or induce polarization toward the pro-inflammatory or anti-inflammatory states, respectively. Additionally, BMDMs were

cultured in tumor conditioned media (TCM) to induce a tumor-conditioned macrophage phenotype. Following 48 hours of polarization, RNA was collected from these macrophages for RT-qPCR. As expected, Got1 and Got2 were significantly decreased in each of the polarization states (**Fig. 6-3B**).

Next, whether Got1 or Got2 loss affected macrophage polarization was evaluated. LPS induced elevated expression of the inflammatory marker nitric oxide synthase 2 (Nos2), while IL-4 increased anti-inflammatory arginase-1 (Arg1) expression (**Fig. 6-3C,D**). Macrophages cultured in TCM similarly displayed elevated Arg1, as has been reported previously (**Fig. 6-3C,D**) (18, 19). Furthermore, neither Got1 nor Got2 deletion prevented macrophage polarization (**Fig. 6-3C,D**).

6.3 Metabolic effects of Got2 loss in polarized macrophages

Having validated Got2 loss in the LysM-Got2$^{\Delta/\Delta}$ system and confirmed Got2-null BMDMs are viable and functional, next, the metabolic effects on macrophages in different polarization states were characterized. BMDMs were generated from LysM-Got2$^{\Delta/\Delta}$ mice or Got2$^{f/f}$ controls and polarized with M-CSF, LPS, IL-4, or TCM. Metabolites were then isolated from both intra- and extracellular fractions and analyzed via liquid chromatography/mass spectrometry (LC/MS). Broad changes were observed both across polarization states and with Got2 loss in each of these states (**Fig. 6-4A**). More specifically, aspartate and α-ketoglutarate (αKG) were significantly decreased (**Fig. 6-4B**). M(LPS) macrophages had reduced αKG levels even at baseline, in accordance with previous findings (**Fig. 6-4B**) (20, 21). Additionally, looking at the TCA cycle more broadly, several metabolites followed previously reported patterns across polarization states. For instance, M(LPS) macrophages had increased expression of

itaconate and succinate which was unaffected by loss of Got2 (**Fig. 6-4C**) (22, 23). These changes in αKG also impacted the αKG/succinate ratio in M(MCSF), M(IL4), and M(TCM) macrophages, but not M(LPS) macrophages (**Fig. 6-4D**). This ratio is intricately linked to epigenetic-modifying enzymes suggesting that Got2 loss could also have implications for cell state and gene expression programs in these macrophages. Finally, the reductive stress signature caused by NADH build-up due to an impaired malate-aspartate shuttle (MAS) with Got2 loss, which was identified in PDA cells in my previous work, was similarly observed in macrophages (**Fig. 6-4E**). Furthermore, an increase in the extracellular pyruvate/lactate ratio, which is an indicator of the intracellular macrophage NAD/NADH ratio, confirmed the accumulation of NADH and reductive stress in Got2-null macrophages regardless of polarization state (**Fig. 6-4F**). In sum, this ex vivo metabolomics analysis demonstrates several critical metabolic pathways are impacted following Got2 loss in pro-inflammatory, anti-inflammatory, and tumor-conditioned macrophages.

6.4 Pyrimidine metabolism and Got2 deletion in TAMs

An unbiased analysis identified glycolysis and pathways branching from glycolysis as the top intracellular metabolic pathways significantly different between LysM-Got2$^{\Delta/\Delta}$ or Got2$^{f/f}$ TAMs, further supporting that Got2 loss in this cell type induces reductive stress similar to PDA cells (**Fig. 6-5A**). In control MCSF-stimulated BMDMs, loss of Got2 led to a significant reduction in aspartate levels and a concurrent decrease in pyrimidine synthesis intermediates (**Fig. 6-5C**) carbamoyl aspartate, orotate, or uridine monophosphate (UMP) (**Fig. 6-5D**). However, despite a significant reduction in aspartate levels (**Fig. 6-5E**), no differences were detected in the intracellular levels of

these pyrimidine synthesis intermediates in BMDMs cultured in tumor-conditioned medium (TCM) (**Fig. 6-5E**). Additionally, while pyrimidine biosynthesis was the top extracellular metabolic pathway between LysM-Got2$^{\Delta/\Delta}$ or Got2$^{f/f}$ TAMs (**Fig. 6-5B**), secreted dC levels were unchanged (**Fig. 6-5F**). However, Got2 loss did result in a significant decrease in extracellular uridine (**Fig. 6-5F**), which has recently been identified by our lab as an alternative fuel source for PDA cells. Interestingly, orotate is abundant in TCM compared to regular growth media, and orotate is decreased in the media following incubation with TAMs (**Fig. 6-5F**). Perhaps, these findings suggest a potential crosstalk mechanism whereby TAMs take up pancreatic cancer cell-derived orotate for downstream pyrimidine synthesis/release, though this would require extensive further elucidation (**Fig. 6-5G**).

6.5 Gemcitabine efficacy with loss of Got1 or Got2 in TAMs in vivo

At baseline, both subcutaneous and orthotopic allografts of KPC-7940B mouse PDA cells implanted into either LysM-Got1 or LysM-Got2 mice grew uninhibited (**Fig. 6-6A-D**). Loss of Got2 in TAMs from orthotopic LysM-Got2 tumors was confirmed by confocal imaging of immunofluorescence staining for co-localized Got2 and F4/80 (**Fig. 6-6E**). Finally, in both the subcutaneous and orthotopic LysM-Got2 models, while gemcitabine slowed overall tumor growth, no difference was observed between the tumors in LysM-Got2$^{\Delta/\Delta}$ or Got2$^{f/f}$ mice (**Fig. 6-6F,G**).

6.6 Viral utilization of GOT2 in myeloid cells

Viruses hijack host metabolism to support sustained replication of viral machinery(24-27). Recently, GOT2 activity was shown to be implicated in supporting

viral life cycles. Infection of peritoneal macrophages with several types of viruses led to expression of a long non-coding RNA (lncRNA) which bound directly to GOT2 and increased its activity, leading to elevated aspartate and α-ketoglutarate production. Presumably, increased levels of these metabolites were utilized to generate the requisite viral nucleotides and capsid proteins, as exogenous supplementation of either metabolite correlated with decreased survival in mice infected with vesicular stomatitis virus (VSV) also lacking expression of the lncRNA promoting GOT2 activity. Furthermore, in vitro knockdown of GOT2 in peritoneal macrophages decreased viral load and increased host survival(27). A second, more recent investigation into the proteome of epithelial cells infected with SARS-CoV2 revealed GOT2 as part of a differentially upregulated central carbon metabolism network driven by viral infection(25).

In light of these studies, we asked two questions surrounding whether GOT2 plays a role in H1N1 influenza lung infections. First, given that macrophages are a target for H1N1 influenza(28), is GOT2 required in lung macrophages for productive viral infection? Second, lung infections by foreign pathogens can lead to initial acute inflammation followed by subsequent pulmonary fibrosis during resolution of inflammation(29, 30). Both of these processes are driven by lung macrophages; M1-like macrophages drive inflammation and host defense, while M2-like macrophages direct wound healing and fibrosis(31, 32). Since loss of Got2 induced a stronger metabolic phenotype in M2-like than M1-like BMDMs (**Fig. 6-4A,B**), we asked if GOT2-deleted lung macrophages display a blunted wound healing response, thereby preventing the

development of pulmonary fibrosis and indirectly improving host survival following infection.

To begin to answer these questions, LysM-Got2$^{\Delta/\Delta}$ or Got2$^{f/f}$ littermate control mice were infected with the H1N1 influenza strain through inhalation of viral droplets, and lung tissue was collected for analysis after three days (**Fig. 6-7A**). No difference was observed in total viral load between the two groups, as determined by the relative abundance of the virus-specific polymerase A gene (**Fig. 6-7B**). Additionally, the pro-inflammatory cytokine genes *Il6* and *Tnfα* were similarly unchanged (**Fig. 6-7C,D**). These data suggest that loss of Got2 specifically in lung myeloid cells has no impact on overall viral load or host inflammation with H1N1 influenza infection.

6.7 Discussion

Macrophages are dynamic innate immune cells with myriad roles in health and disease. Critical metabolic networks underly these diverse functions. Given this principle, reprogramming macrophage metabolism could be an avenue to redirect activity during pathological states, including cancer and viral infection. Having generated novel models of Got1, Got2, or Got1/Got2 knockout in myeloid cells, the future work described in Chapter 8 will continue to evaluate how loss of these enzymes ultimately impacts macrophage phenotypes.

6.8 Methods

Mouse studies

Mice were maintained in a pure C57BL/6J background and experimental mice were maintained in SPF housing with access to standard diet and water ad libitum at constant

ambient temperature and a 12-hour light cycle. All experiments were conducted in accordance with the Office of Laboratory Animal Welfare and approved by the Institutional Animal Care and Use Committees of the University of Michigan.

LysM-Got1 or Got2 mice

LysM-Cre mice on a pure C57BL/6J background were a generous gift from Dr. Howard Crawford (Henry Ford Pancreatic Cancer Center). These mice were crossed with either $Got1^{f/f}$ or $Got2^{f/f}$ mice also on a pure C57BL/6J background generated for the Lyssiotis lab by Ozgene. LysM-Cre;$Got^{f/f}$ (either male or female) mice were crossed with $Got^{f/f}$ mice to generate an F1 generation of all $Got^{f/f}$ pups with or without LysM-Cre expression. Tails from 3-week-old mice were collected at weaning and submitted to Transnetyx for genotyping. The following primers were used: Got1 WT (Fw: ACTGGTGACTGAGCAGGGACTTC, Rv: CTTAAGTGTATGAGTTCCTCAAACCATTGC); Got1 floxed (Fw: ACTGGTGACTGAGCAGGGACTTC, Rv: CCTTAAGTGTATGAGTTCCTCAAACCATTG); Got2 WT (Fw: GCAGATTAAAACCACAAGGCCTGTA, Rev: ATGTTAAAATTGTCATCCCCTTGTGC); Got2 floxed (Fw: GCAGATTAAAACCACAAGGCCTGTA, Rev: AGAGAATAGGAACTTCGGAATAGGAACT); Cre (Fw: TTAATCCATATTGGCAGAACGAAAACG, Rev: CAGGCTAAGTGCCTTCTCTACA).

Bone marrow isolation and BMDM differentiation

Mice were euthanized according to the approved IACUC protocol and tails were collected to re-confirm genotypes. The tibia/femur were isolated from the mouse and the ends of the bones were removed. Bones were placed in a 0.2 mL PCR tube with a small

hole cut in the bottom, inside a 1.5 mL tube. The bone marrow was collected by spinning the tubes on a table-top centrifuge until pelleted in the bottom of the tube. The pellet was resuspended in PBS and passed through a 0.4 µm filter to remove debris, clots, and bone fragments. The filtered bone marrow was pelleted for 5 minutes at 400xg, 4°C and then re-suspended in bone marrow medium (BMM, 30% L929 CM + 70% DMEM with 10% FBS). Bone marrow cells were plated in 10 cm petri dishes. After 2 days, 2-3 mL of BMM was added to the plates. On days 4 and 6, the old BMM was removed and 8-10 mL of fresh BMM was added. BMDM differentiation was complete by Day 7.

Flow cytometry

For BMDMs in culture, on day 7 of differentiation, old BMM was removed, cells were washed once with PBS, and incubated with Accutase (Innovative Cell Technologies, #AT-104) until detached. The Accutase was neutralized with an equal volume of growth medium (DMEM + 10% FBS). BMDMs were then collected and centrifuged for 5 minutes at 400xg, 4°C, re-suspended in flow buffer (PBS + 1% FBS), passed through a 40 µm cell strainer, and counted. 1 million cells were added to each flow tube and incubated on ice for 30 minutes with the following antibodies (all 1:100 dilutions): CD45-BV510 (Fisher #BDB563891), F4/80-PE-Cy5 (Fisher #50-112-8964), Cd11b-APC-Cy7 (Fisher #BDB557657), Ly6C-PE (Fisher #BDB560592), Ly6G-FITC (Fisher #BDB551460), Live/Dead stain (Fisher #L34965). Following the incubation, BMDMs were washed twice with flow buffer before being re-suspended in 300 µL of flow buffer for analysis on the Bigfoot Spectral Cell Sorter (ThermoFisher).

BMDM polarization

On day 6 of differentiation, BMDMs were collected as described above. Cells were counted and seeded at 2 million cells in 2 mL of BMM per well in 6 well plates and incubated overnight to complete the 7-day differentiation. On day 7, the old BMM was removed, and cells were washed once with PBS. BMDMs were then polarized in 2 mL per well of 10 ng/mL M-CSF (Peprotech #315-02), 10 ng/mL LPS (Enzo #ALX-581-011-L001), 10 ng/mL IL4 (Peprotech #214-14), or tumor conditioned medium (TCM, 75% PDA CM + 25% DMEM with 10% FBS) and incubated for 48 hours.

RT-qPCR

RNA was isolated from BMDMs using the RNeasy Plus Mini Kit (Qiagen #74134) and 1 µg of cDNA synthesized using the iScript kit (Biorad #1708891). The 20 µL cDNA samples were diluted in 80 µL water for a final volume of 100 µL. RT-qPCR was conducted using the Fast SYBR Green Master Mix (Thermo #4385612) according to the manufacturer's instructions. Primers for the indicated targets are as follows: 18S (Fw: GCAATTATTCCCCATGAACG, Rv: GGCCTCACTAAACCATCCAA); Got1 (Fw: TGTGCTTCTCGCCTAGTTC, Rv: AAGTCAGCTCCAATCCGAAG); Got2 (Fw: AGAGAGATACCAACAGCAAGAAG, Rv: CAATGGGCAGGTATTCTTTGTC); Nos2 (Fw: GTTCTCAGCCCAACAATACAAGA, Rv: GTGGACGGGTCGATGTCAC); Arg1 (Fw: CTCCAAGCCAAAGTCCTTAGAG, Rv: GGAGCTGTCATTAGGGACATCA).

Polar metabolite isolation

BMDMs were polarized as described above. For the extracellular fraction 200 uL of each media was collected in a 1.5 mL tube, centrifuged at 200xg for 3 minutes to pellet floating cells or debris, and the supernatant was transferred to a fresh 1.5 mL tube. 800

µL of ice-cold 100% methanol was added to the 200 µL media, mixed well, and incubated on dry ice for 10 minutes. For the intracellular fraction, the remaining media was removed from the cells. 1 mL of ice-cold 80% methanol was immediately added to the cells and incubated on dry ice for 10 minutes, after which cells were scraped and the supernatant collected in 1.5 mL tubes. For both fractions, the supernatant was then centrifuged at 10,000xg for 10 min at 4°C to clarify, and the supernatant was transferred to fresh tubes. The final metabolite volume dried on the SpeedVac was normalized to total protein concentration.

Targeted metabolomics

Samples were run on an Agilent 1290 Infinity II LC -6470 Triple Quadrupole (QqQ) tandem mass spectrometer (MS/MS) system. The MassHunter Metabolomics Dynamic MRM Database and Method was used for target identification. The QqQ data were pre-processed with Agilent MassHunter Workstation QqQ Quantitative Analysis Software (B0700). Each metabolite abundance level in each sample was divided by the median of all abundance levels across all samples for proper comparisons, statistical analyses, and visualizations among metabolites. Metabolites with values >1 are higher in the experimental conditions and metabolites with values <1 are lower in the experimental condition. The statistical significance test was done by a two-tailed t-test with a significance threshold level of 0.05.

Heatmaps were generated and data clustered using Morpheus Matrix Visualization and analysis tool (https://software.broadinstitute.org/morpheus).

Pathway analyses were conducted using MetaboAnalyst (https://www.metaboanalyst.ca).

Immunofluorescence

Tissue slides from one Got2$^{f/f}$ and one LysM-Cre;Got2$^{\Delta/\Delta}$ orthotopic KPC-7940B tumor were rehydrated, quenched in hydrogen peroxide, followed by antigen retrieval in sodium citrate buffer. Tissue was blocked in BSA followed by incubation with anti-rabbit Got2 primary antibody (Sigma, #HPA018139) at 1:250 overnight at 4'C. The next day, the tissue was incubated with anti-rabbit poly-HRP-conjugated secondary antibody before stripping in tyramide solution. Antigen retrieval and blocking was then repeated as before, followed by incubation with anti-rabbit F4/80 at 1:250 overnight at 4'C. The next day, the tissue was incubated in goat anti-rabbit Alexa 594 secondary antibody at 1:1,000. Finally, slides with mounted with Prolong Gold with DAPI and imaged on the Stellaris Confocal Microscope.

In vivo allograft studies

KPC-7940B mouse PDA cells were collected with 25% trypsin followed by neutralization in an equal volume of growth medium. The cells were then washed twice in serum-free DMEM and counted. For subcutaneous tumors, 500,000 cells were injected in a 1:1 mixture of 100 uL Matrigel:serum-free medium, and for orthotopic tumor 50,000 cells were injected in a 1:1 mixture of 50 uL Matrigel:serum-free medium. Tumors were established for 7 days before randomization and treated with PBS vehicle control or 100 mg/kg Gemcitabine once per week for 3 weeks.

H1N1 influenze lung infection model

Male and female Got2$^{f/f}$ and LysM-Cre;Got2$^{\Delta/\Delta}$ mice were infected oropharyngeally with 100 plaque-forming units (PFU) of influenza H1N1 A/PR/8/34 and harvested three days later. All lung lobes were homogenized together in 1 mL of PBS containing protease

inhibitors, plated on nutrient agar for determination of bacterial burden, and the rest of the lung homogenate frozen for later analysis. A portion of each lung homogenate was placed directly into Trizol pre-freezing for RNA extraction followed by real-time PCR analysis of influenza burden (real-time PCR of influenza polymerase normalized to the housekeeping gene RPL38), as well as real-time PCR analysis of inflammation (TNFa and IL-6 normalized to the housekeeping gene RPL38). For histology, lungs were inflated with 1 mL of 10% formalin and placed in 50 mL conical tubes containing 5 mL of 10% formalin for later paraffin embedding and sectioning.

6.9 References

1. Zhang Y, Crawford HC, Pasca di Magliano M. Epithelial-Stromal Interactions in Pancreatic Cancer. Annu Rev Physiol. 2019;81:211-33. Epub 2018/11/13. doi: 10.1146/annurev-physiol-020518-114515. PubMed PMID: 30418798.

2. Steele NG, Carpenter ES, Kemp SB, Sirihorachai VR, The S, Delrosario L, Lazarus J, Amir E-aD, Gunchick V, Espinoza C, Bell S, Harris L, Lima F, Irizarry-Negron V, Paglia D, Macchia J, Chu AKY, Schofield H, Wamsteker E-J, Kwon R, Schulman A, Prabhu A, Law R, Sondhi A, Yu J, Patel A, Donahue K, Nathan H, Cho C, Anderson MA, Sahai V, Lyssiotis CA, Zou W, Allen BL, Rao A, Crawford HC, Bednar F, Frankel TL, Pasca di Magliano M. Multimodal mapping of the tumor and peripheral blood immune landscape in human pancreatic cancer. Nature Cancer. 2020;1(11):1097-112. doi: 10.1038/s43018-020-00121-4.

3. Crawford HC, Pasca di Magliano M, Banerjee S. Signaling Networks That Control Cellular Plasticity in Pancreatic Tumorigenesis, Progression, and Metastasis. Gastroenterology. 2019;156(7):2073-84. doi: 10.1053/j.gastro.2018.12.042.

4. Halbrook CJ, Pasca di Magliano M, Lyssiotis CA. Tumor cross-talk networks promote growth and support immune evasion in pancreatic cancer. Am J Physiol Gastrointest Liver Physiol. 2018;315(1):G27-g35. Epub 2018/03/16. doi: 10.1152/ajpgi.00416.2017. PubMed PMID: 29543507; PMCID: PMC6109710.

5. Zhu Y, Herndon JM, Sojka DK, Kim KW, Knolhoff BL, Zuo C, Cullinan DR, Luo J, Bearden AR, Lavine KJ, Yokoyama WM, Hawkins WG, Fields RC, Randolph GJ, DeNardo DG. Tissue-Resident Macrophages in Pancreatic Ductal Adenocarcinoma Originate from Embryonic Hematopoiesis and Promote Tumor Progression. Immunity. 2017;47(2):323-38.e6. Epub 2017/08/17. doi: 10.1016/j.immuni.2017.07.014. PubMed PMID: 28813661; PMCID: PMC5578409.

6. Candido JB, Morton JP, Bailey P, Campbell AD, Karim SA, Jamieson T, Lapienyte L, Gopinathan A, Clark W, McGhee EJ, Wang J, Escorcio-Correia M, Zollinger R, Roshani R, Drew L, Rishi L, Arkell R, Evans TRJ, Nixon C, Jodrell DI, Wilkinson RW, Biankin AV, Barry ST, Balkwill FR, Sansom OJ. CSF1R(+) Macrophages Sustain Pancreatic Tumor Growth through T Cell Suppression and Maintenance of Key Gene Programs that Define the Squamous Subtype. Cell Rep. 2018;23(5):1448-60. Epub 2018/05/03. doi: 10.1016/j.celrep.2018.03.131. PubMed PMID: 29719257; PMCID: PMC5946718.

7. Di Caro G, Cortese N, Castino GF, Grizzi F, Gavazzi F, Ridolfi C, Capretti G, Mineri R, Todoric J, Zerbi A, Allavena P, Mantovani A, Marchesi F. Dual prognostic significance of tumour-associated macrophages in human pancreatic adenocarcinoma treated or untreated with chemotherapy. Gut. 2016;65(10):1710-20. doi: 10.1136/gutjnl-2015-309193. PubMed PMID: 26156960.

8. Weizman N, Krelin Y, Shabtay-Orbach A, Amit M, Binenbaum Y, Wong RJ, Gil Z. Macrophages mediate gemcitabine resistance of pancreatic adenocarcinoma by upregulating cytidine deaminase. Oncogene. 2014;33(29):3812-9. Epub 2013/09/03. doi: 10.1038/onc.2013.357. PubMed PMID: 23995783.

9. Mitchem JB, Brennan DJ, Knolhoff BL, Belt BA, Zhu Y, Sanford DE, Belaygorod L, Carpenter D, Collins L, Piwnica-Worms D, Hewitt S, Udupi GM, Gallagher WM, Wegner C, West BL, Wang-Gillam A, Goedegebuure P, Linehan DC, DeNardo DG. Targeting tumor-infiltrating macrophages decreases tumor-initiating cells, relieves immunosuppression, and improves chemotherapeutic responses. Cancer Res. 2013;73(3):1128-41. Epub 2012/12/12. doi: 10.1158/0008-5472.Can-12-2731. PubMed PMID: 23221383; PMCID: PMC3563931.

10. Helm O, Held-Feindt J, Grage-Griebenow E, Reiling N, Ungefroren H, Vogel I, Krüger U, Becker T, Ebsen M, Röcken C, Kabelitz D, Schäfer H, Sebens S. Tumor-associated macrophages exhibit pro- and anti-inflammatory properties by which they impact on pancreatic tumorigenesis. Int J Cancer. 2014;135(4):843-61. Epub 2014/01/25. doi: 10.1002/ijc.28736. PubMed PMID: 24458546.

11. Halbrook CJ, Pontious C, Kovalenko I, Lapienyte L, Dreyer S, Lee HJ, Thurston G, Zhang Y, Lazarus J, Sajjakulnukit P, Hong HS, Kremer DM, Nelson BS, Kemp S, Zhang L, Chang D, Biankin A, Shi J, Frankel TL, Crawford HC, Morton JP, Pasca di Magliano M, Lyssiotis CA. Macrophage-Released Pyrimidines Inhibit Gemcitabine Therapy in Pancreatic Cancer. Cell Metab. 2019;29(6):1390-9.e6. Epub 2019/03/05. doi: 10.1016/j.cmet.2019.02.001. PubMed PMID: 30827862; PMCID: PMC6602533.

12. Zhang Y, Velez-Delgado A, Mathew E, Li D, Mendez FM, Flannagan K, Rhim AD, Simeone DM, Beatty GL, Pasca di Magliano M. Myeloid cells are required for PD-1/PD-L1 checkpoint activation and the establishment of an immunosuppressive environment in pancreatic cancer. Gut. 2017;66(1):124-36. Epub 2016/07/13. doi: 10.1136/gutjnl-2016-312078. PubMed PMID: 27402485; PMCID: PMC5256390.

13. Leone RD, Powell JD. Metabolism of immune cells in cancer. Nature reviews Cancer. 2020;20(9):516-31. Epub 2020/07/08. doi: 10.1038/s41568-020-0273-y. PubMed PMID: 32632251.

14. Hossain F, Al-Khami AA, Wyczechowska D, Hernandez C, Zheng L, Reiss K, Valle LD, Trillo-Tinoco J, Maj T, Zou W, Rodriguez PC, Ochoa AC. Inhibition of Fatty Acid Oxidation Modulates Immunosuppressive Functions of Myeloid-Derived Suppressor Cells and Enhances Cancer Therapies. Cancer immunology research. 2015;3(11):1236-47. Epub 2015/05/31. doi: 10.1158/2326-6066.Cir-15-0036. PubMed PMID: 26025381; PMCID: PMC4636942.

15. Jha AK, Huang SC, Sergushichev A, Lampropoulou V, Ivanova Y, Loginicheva E, Chmielewski K, Stewart KM, Ashall J, Everts B, Pearce EJ, Driggers EM, Artyomov MN. Network integration of parallel metabolic and transcriptional data reveals metabolic modules that regulate macrophage polarization. Immunity. 2015;42(3):419-30. Epub 2015/03/19. doi: 10.1016/j.immuni.2015.02.005. PubMed PMID: 25786174.

16. Olenchock BA, Rathmell JC, Vander Heiden MG. Biochemical Underpinnings of Immune Cell Metabolic Phenotypes. Immunity. 2017;46(5):703-13. doi: https://doi.org/10.1016/j.immuni.2017.04.013.

17. Wen HJ, Gao S, Wang Y, Ray M, Magnuson MA, Wright CVE, Di Magliano MP, Frankel TL, Crawford HC. Myeloid Cell-Derived HB-EGF Drives Tissue Recovery After Pancreatitis. Cell Mol Gastroenterol Hepatol. 2019;8(2):173-92. Epub 2019/05/28. doi: 10.1016/j.jcmgh.2019.05.006. PubMed PMID: 31125624; PMCID: PMC6661420.

18. Boyer S, Lee HJ, Steele N, Zhang L, Sajjakulnukit P, Andren A, Ward MH, Singh R, Basrur V, Zhang Y, Nesvizhskii AI, Pasca di Magliano M, Halbrook CJ, Lyssiotis CA. Multiomic characterization of pancreatic cancer-associated macrophage polarization reveals deregulated metabolic programs driven by the GM-CSF-PI3K pathway. Elife. 2022;11. Epub 2022/02/15. doi: 10.7554/eLife.73796. PubMed PMID: 35156921; PMCID: PMC8843093.

19. Menjivar RE, Nwosu ZC, Du W, Donahue KL, Hong HS, Espinoza C, Brown K, Velez-Delgado A, Yan W, Lima F, Bischoff A, Kadiyala P, Salas-Escabillas D, Crawford HC, Bednar F, Carpenter E, Zhang Y, Halbrook CJ, Lyssiotis CA, Pasca di Magliano M. Arginase 1 is a key driver of immune suppression in pancreatic cancer. Elife. 2023;12. Epub 2023/02/03. doi: 10.7554/eLife.80721. PubMed PMID: 36727849.

20. Jha Abhishek K, Huang Stanley C-C, Sergushichev A, Lampropoulou V, Ivanova Y, Loginicheva E, Chmielewski K, Stewart Kelly M, Ashall J, Everts B, Pearce Edward J, Driggers Edward M, Artyomov Maxim N. Network Integration of Parallel Metabolic and Transcriptional Data Reveals Metabolic Modules that Regulate Macrophage Polarization. Immunity. 2015;42(3):419-30. doi: https://doi.org/10.1016/j.immuni.2015.02.005.

21. Liu P-S, Wang H, Li X, Chao T, Teav T, Christen S, Di Conza G, Cheng W-C, Chou C-H, Vavakova M, Muret C, Debackere K, Mazzone M, Huang H-D, Fendt S-M,

Ivanisevic J, Ho P-C. α-ketoglutarate orchestrates macrophage activation through metabolic and epigenetic reprogramming. Nature Immunology. 2017;18(9):985-94. doi: 10.1038/ni.3796.

22. Tannahill GM, Curtis AM, Adamik J, Palsson-McDermott EM, McGettrick AF, Goel G, Frezza C, Bernard NJ, Kelly B, Foley NH, Zheng L, Gardet A, Tong Z, Jany SS, Corr SC, Haneklaus M, Caffrey BE, Pierce K, Walmsley S, Beasley FC, Cummins E, Nizet V, Whyte M, Taylor CT, Lin H, Masters SL, Gottlieb E, Kelly VP, Clish C, Auron PE, Xavier RJ, O'Neill LA. Succinate is an inflammatory signal that induces IL-1β through HIF-1α. Nature. 2013;496(7444):238-42. Epub 2013/03/29. doi: 10.1038/nature11986. PubMed PMID: 23535595; PMCID: PMC4031686.

23. Lampropoulou V, Sergushichev A, Bambouskova M, Nair S, Vincent EE, Loginicheva E, Cervantes-Barragan L, Ma X, Huang SC, Griss T, Weinheimer CJ, Khader S, Randolph GJ, Pearce EJ, Jones RG, Diwan A, Diamond MS, Artyomov MN. Itaconate Links Inhibition of Succinate Dehydrogenase with Macrophage Metabolic Remodeling and Regulation of Inflammation. Cell Metab. 2016;24(1):158-66. Epub 2016/07/05. doi: 10.1016/j.cmet.2016.06.004. PubMed PMID: 27374498; PMCID: PMC5108454.

24. Bharadwaj S, Singh M, Kirtipal N, Kang SG. SARS-CoV-2 and Glutamine: SARS-CoV-2 Triggered Pathogenesis via Metabolic Reprograming of Glutamine in Host Cells. Front Mol Biosci. 2020;7:627842. Epub 2021/02/16. doi: 10.3389/fmolb.2020.627842. PubMed PMID: 33585567; PMCID: PMC7873863.

25. Bojkova D, Klann K, Koch B, Widera M, Krause D, Ciesek S, Cinatl J, Münch C. Proteomics of SARS-CoV-2-infected host cells reveals therapy targets. Nature. 2020;583(7816):469-72. Epub 2020/05/15. doi: 10.1038/s41586-020-2332-7. PubMed PMID: 32408336.

26. Codo AC, Davanzo GG, Monteiro LB, de Souza GF, Muraro SP, Virgilio-da-Silva JV, Prodonoff JS, Carregari VC, de Biagi Junior CAO, Crunfli F, Jimenez Restrepo JL, Vendramini PH, Reis-de-Oliveira G, Bispo Dos Santos K, Toledo-Teixeira DA, Parise PL, Martini MC, Marques RE, Carmo HR, Borin A, Coimbra LD, Boldrini VO, Brunetti NS, Vieira AS, Mansour E, Ulaf RG, Bernardes AF, Nunes TA, Ribeiro LC, Palma AC, Agrela MV, Moretti ML, Sposito AC, Pereira FB, Velloso LA, Vinolo MAR, Damasio A, Proença-Módena JL, Carvalho RF, Mori MA, Martins-de-Souza D, Nakaya HI, Farias AS, Moraes-Vieira PM. Elevated Glucose Levels Favor SARS-CoV-2 Infection and Monocyte Response through a HIF-1α/Glycolysis-Dependent Axis. Cell Metab. 2020;32(3):437-46.e5. Epub 2020/07/23. doi: 10.1016/j.cmet.2020.07.007. PubMed PMID: 32697943; PMCID: PMC7367032.

27. Wang P, Xu J, Wang Y, Cao X. An interferon-independent lncRNA promotes viral replication by modulating cellular metabolism. Science. 2017;358(6366):1051-5. Epub 2017/10/28. doi: 10.1126/science.aao0409. PubMed PMID: 29074580.

28. Yu WC, Chan RW, Wang J, Travanty EA, Nicholls JM, Peiris JS, Mason RJ, Chan MC. Viral replication and innate host responses in primary human alveolar epithelial cells and alveolar macrophages infected with influenza H5N1 and H1N1 viruses. J Virol. 2011;85(14):6844-55. Epub 2011/05/06. doi: 10.1128/jvi.02200-10. PubMed PMID: 21543489; PMCID: PMC3126566.

29. Warheit-Niemi HI, Hult EM, Moore BB. A pathologic two-way street: how innate immunity impacts lung fibrosis and fibrosis impacts lung immunity. Clin Transl Immunology. 2019;8(6):e1065. Epub 2019/07/12. doi: 10.1002/cti2.1065. PubMed PMID: 31293783; PMCID: PMC6593479.

30. Warheit-Niemi HI, Edwards SJ, SenGupta S, Parent CA, Zhou X, O'Dwyer DN, Moore BB. Fibrotic lung disease inhibits immune responses to staphylococcal pneumonia via impaired neutrophil and macrophage function. JCI Insight. 2022;7(4). Epub 2022/01/07. doi: 10.1172/jci.insight.152690. PubMed PMID: 34990413; PMCID: PMC8876506.

31. Schneider DJ, Smith KA, Latuszek CE, Wilke CA, Lyons DM, Penke LR, Speth JM, Marthi M, Swanson JA, Moore BB, Lauring AS, Peters-Golden M. Alveolar macrophage-derived extracellular vesicles inhibit endosomal fusion of influenza virus. Embo j. 2020;39(16):e105057. Epub 2020/07/10. doi: 10.15252/embj.2020105057. PubMed PMID: 32643835; PMCID: PMC7429743.

32. Hult EM, Gurczynski SJ, O'Dwyer DN, Zemans RL, Rasky A, Wang Y, Murray S, Crawford HC, Moore BB. Myeloid- and Epithelial-derived Heparin-Binding Epidermal Growth Factor-like Growth Factor Promotes Pulmonary Fibrosis. Am J Respir Cell Mol Biol. 2022;67(6):641-53. Epub 2022/08/30. doi: 10.1165/rcmb.2022-0174OC. PubMed PMID: 36036796; PMCID: PMC9743186.

6.10 Figures

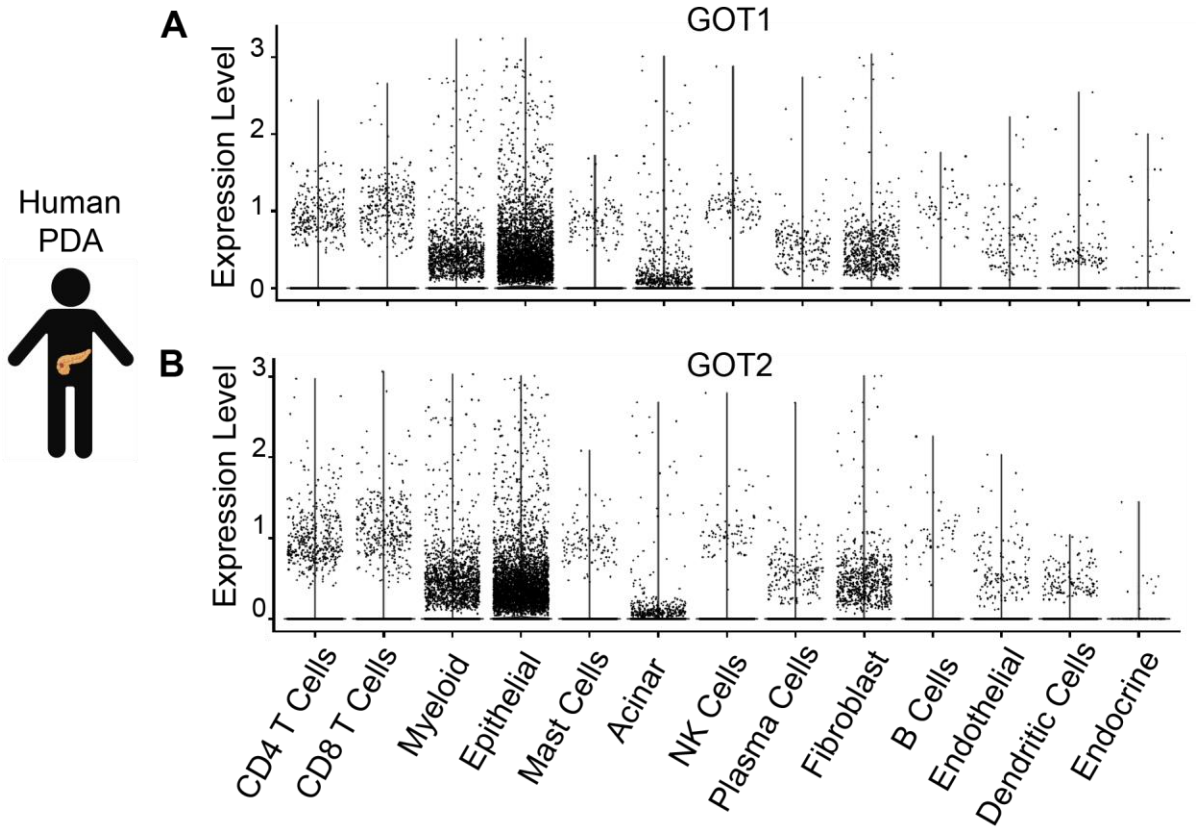

Figure 6-1 Single-cell RNA sequencing analysis of GOT1 and GOT2 in human PDA

A) GOT1 and **B)** GOT2 expression in the indicated cellular populations.

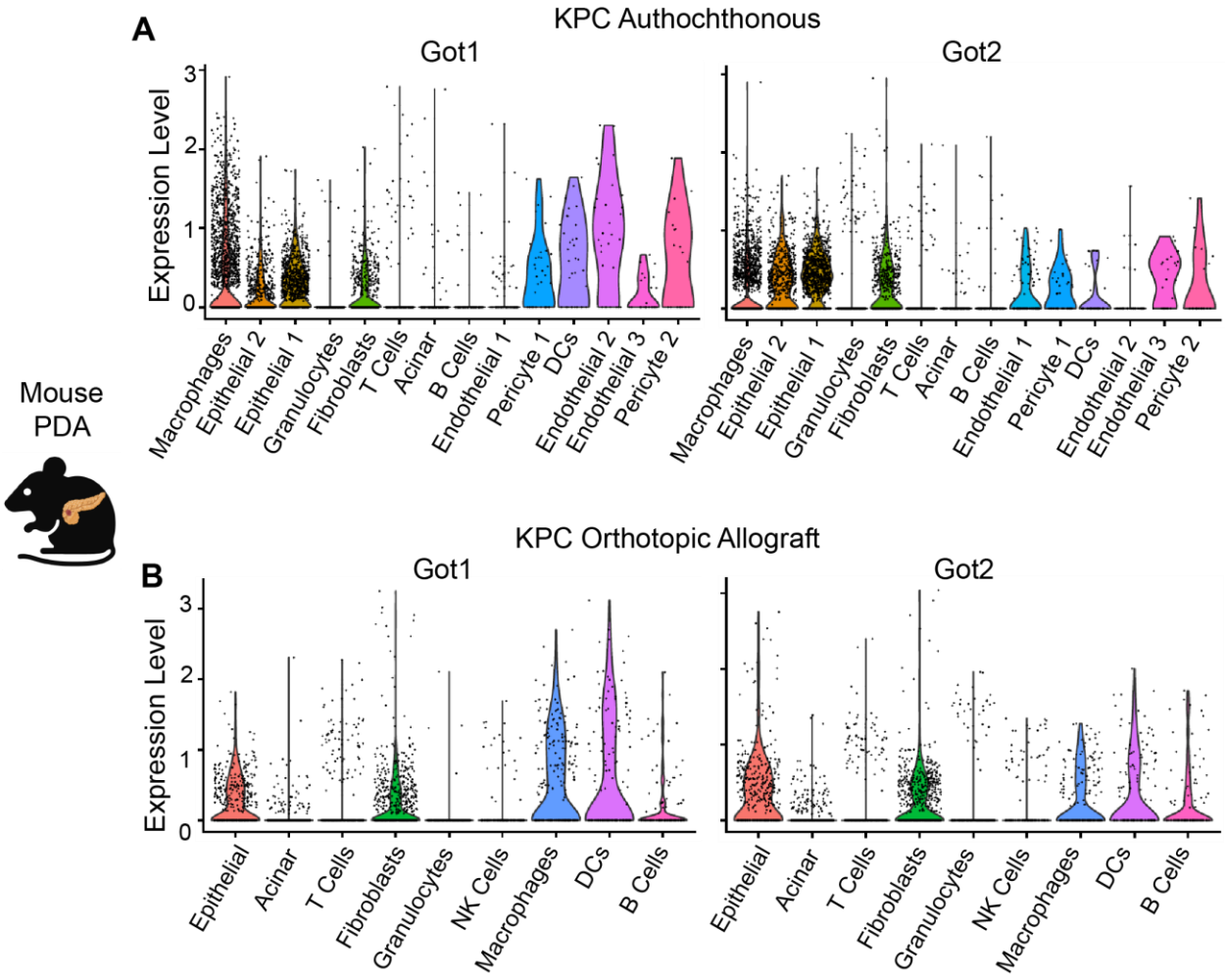

Figure 6-2 Single-cell RNA sequencing analysis of Got1 and Got2 in mouse PDA

Expression of Got1 and Got2 in the indicated cellular populations in tissue from the **A)** KPC autochthonous model and an **B)** orthotopic allograft from a KPC cell line.

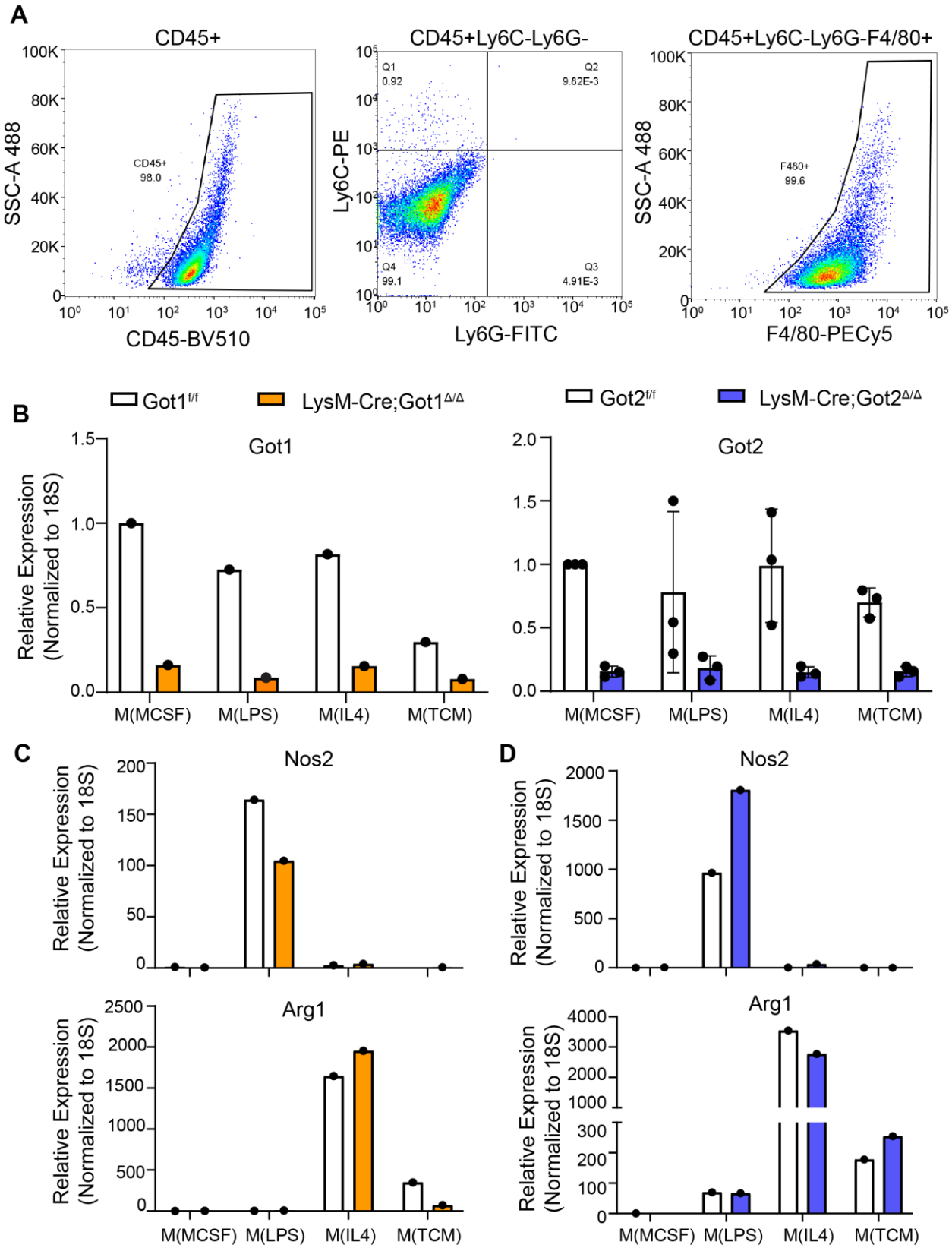

Figure 6-3 Validation of LysM-Got1 and LysM-Got2 models

A) Gating strategy for evaluating the purity of BMDMs generated ex vivo from bone marrow. **B)** RT-qPCR for Got1 and Got2 in BMDMs from either LysM-Got1 or LysM-Got2 mice polarized with MCSF, LPS, IL4, or TCM. **C)** RT-qPCR for Nos2 and Arg1 in BMDMs from either LysM-Got1 or LysM-Got2 mice polarized with MCSF, LPS, IL4, or TCM.

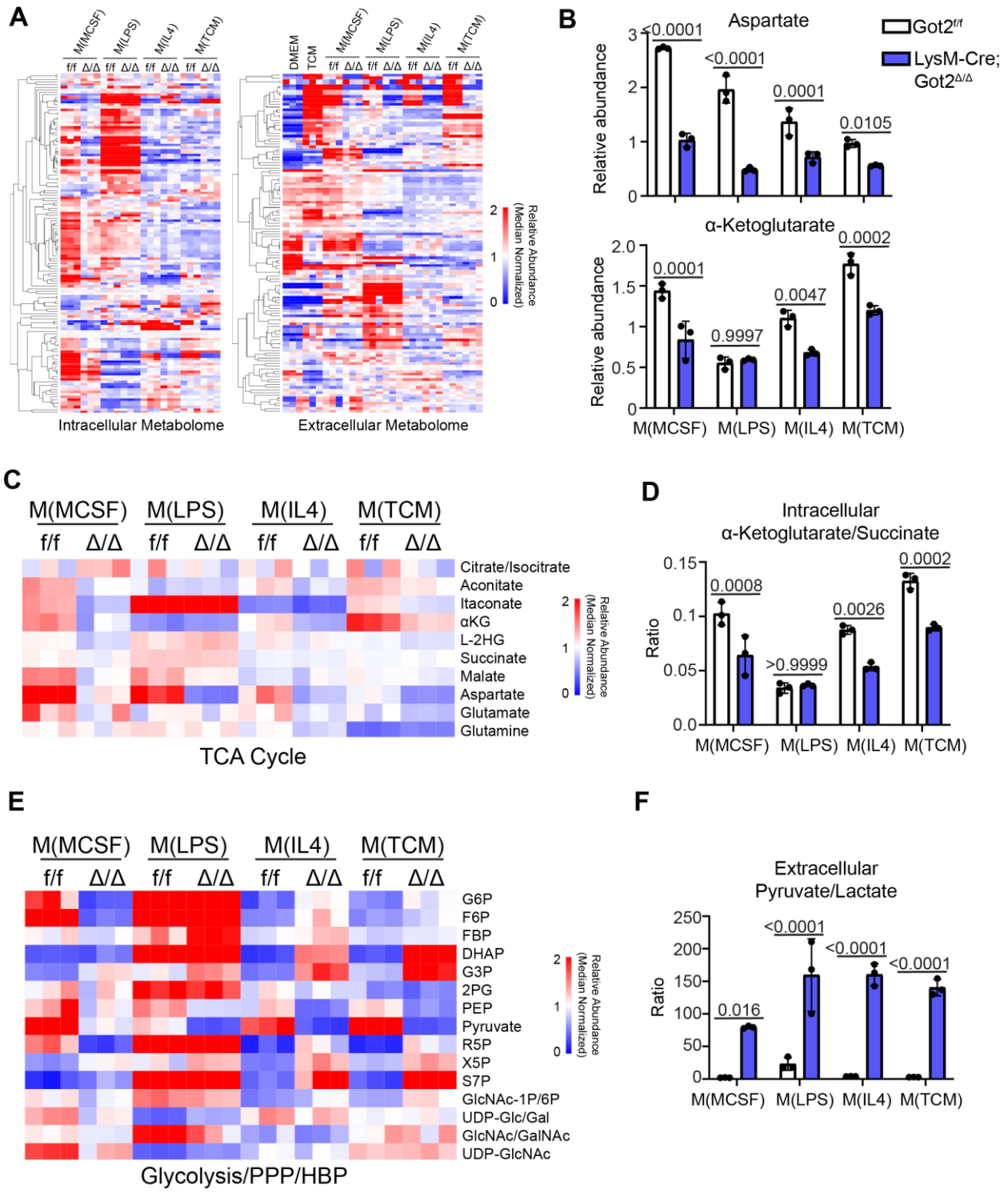

Figure 6-4 Metabolic characterization of LysM-Got2 BMDMs

A) Heatmaps depicting the intra- and extracellular metabolomes, **B)** relative abundances of aspartate and αKG, **C)** heatmap depicting TCA cycle intermediates, **D)** ratio of intracellular succinate/αKG **E)** heatmap depicting glycolytic, PPP, and HBP intermediates, and **F)** ratio of extracellular pyruvate/lactate in LysM-Got2 BMDMs polarized with MCSF, LPS, IL4, or TCM.

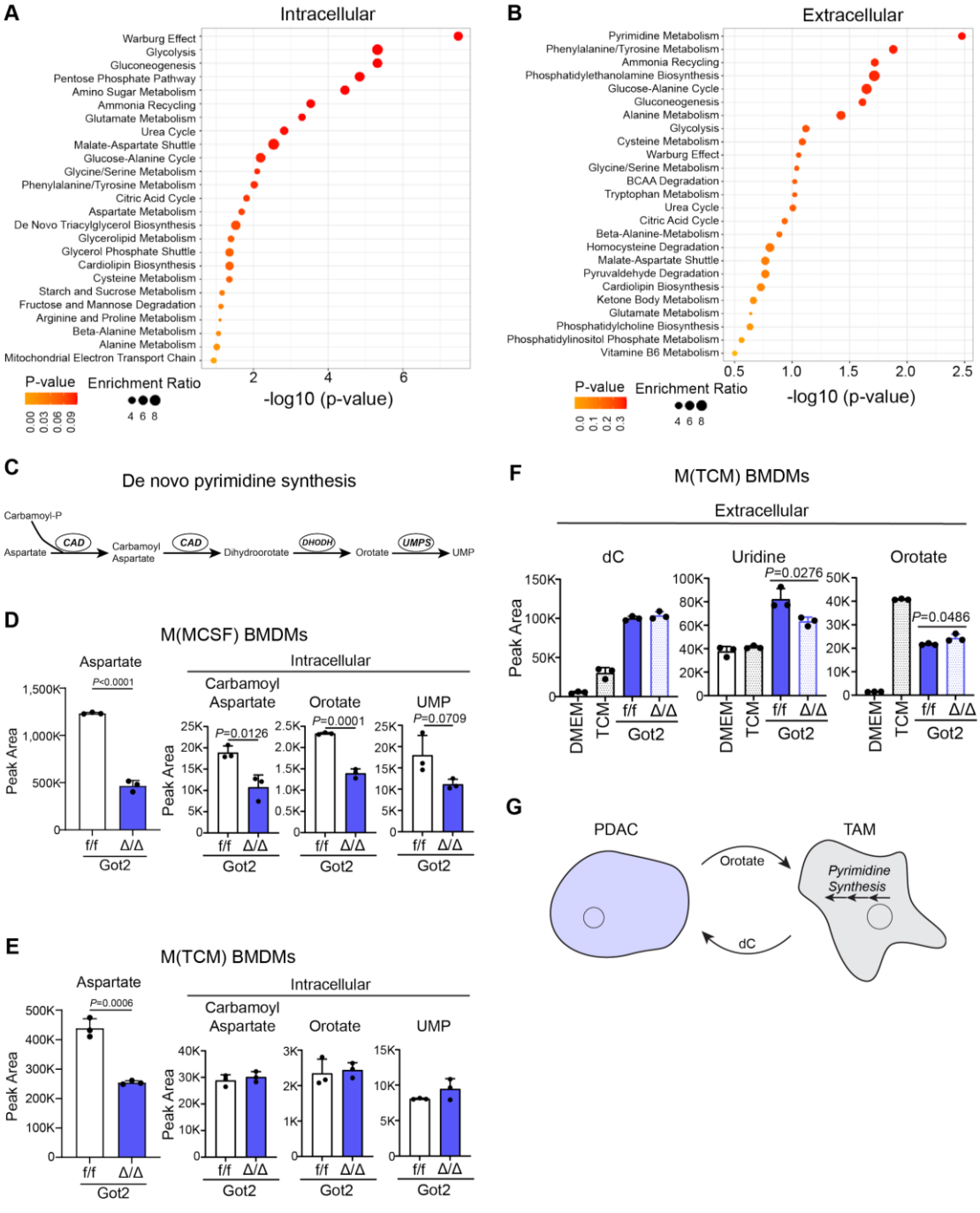

Figure 6-5 Pyrimidine metabolism in LysM-Got2 TAMs

A) Intracellular and **B)** extracellular pathway analyses of differentially expressed metabolites between LysM-Got2$^{\Delta/\Delta}$ and Got2$^{f/f}$ TAMs ex vivo. **C)** Schematic of *de novo* pyrimidine synthesis. **D)** Intracellular abundances of pyrimidine synthesis metabolites in BMDMs maintained in MCSF. **E)** Intracellular abundances of pyrimidine synthesis metabolites in BMDMs cultured in tumor-conditioned media (TCM). **F)** Extracellular abundances of deoxycytidine (dC), uridine, and orotate in the media from BMDMs cultured in tumor-conditioned media.

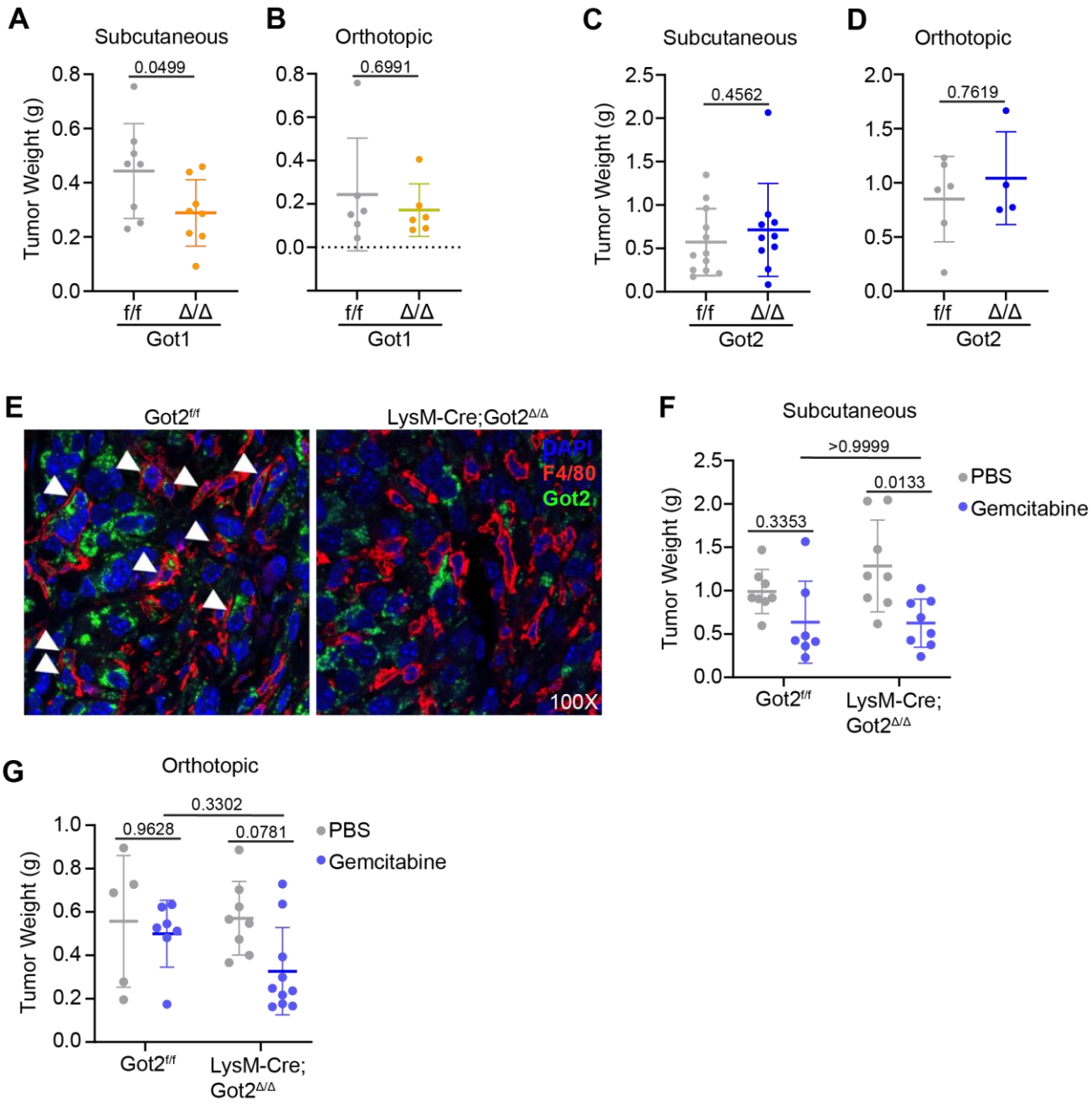

Figure 6-6 Efficacy of gemcitabine against PDA allografts in LysM-Got1 or LysM-Got2 hosts

A) Subcutaneous and **B)** orthotopic allograft tumor weights in LysM-Got1 hosts. **C)** Subcutaneous and **D)** orthotopic allograft tumor weights in LysM-Got2 hosts. **E)** Confocal images of immunofluorescent staining for DAPI, F4/80, and Got2 in orthotopic allografts from LysM-Got2 hosts. **C)** Subcutaneous and **D)** orthotopic allograft tumor weights after treatment with PBS or gemcitabine in LysM-Got2 hosts.

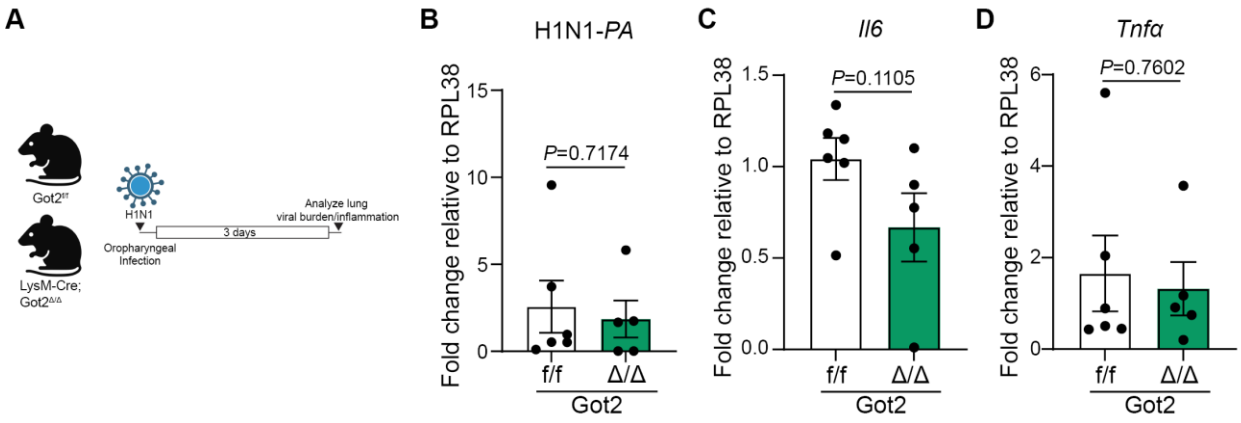

Figure 6-7 Infection of Got2-deficient macrophages in the lung with H1N1 influenza virus.

(A) Schematic depicting oropharyngeal infection of LysM-Cre;Got2$^{\Delta/\Delta}$ or Got2$^{f/f}$ littermate control mice with H1N1 virus for 3 days. **(B-D)** qPCR analysis of **(B)** H1N1 polymerase A (*PA*), **(C)** interleukin-6 (*Il6*), or **(D)** tumor necrosis factor α (*Tnfα*) expression levels in lung tissue after 3 days of H1N1 infection.

Chapter 7 – Inborn Errors of Mitochondrial Metabolism

7.1 Background

This final chapter focuses on GOT2 in developmental and normal metabolism. While not directly related to cancer metabolism, the phenotype induced by GOT2 insufficiency is similar to the mechanisms elucidated in Chapters 4-6. Also, developmental programs are often improperly activated in cancer cells. Furthermore, cancer cells hijack the intrinsic biology of the cells of origin. As such, investigations into developmental and normal metabolism can illuminate the metabolic underpinnings of cancer cells.

Relevance to cancer biology aside, loss of function mutations to malate-aspartate shuttle (MAS) components such as GOT2, while rare, induce neurological defects, learning impairment, feeding difficulties, lactic acidemia, insufficient ammonia recycling, and an overall failure to thrive in human patients (1, 2). An improved understanding of the mechanisms underlying inborn errors of metabolism can inform therapeutic interventions to alleviate metabolic dysregulation and improve outcomes for these patients. To accomplish this, global Got2 knockout and inducible, whole-body Got2 knockout mouse models were utilized to study Got2 in developmental and adult mouse metabolism.

7.2 Got2$^{-/-}$ embryonic lethality

Got2 deletion is embryonic lethal, as has been reported previously(2). According to publicly available data through the International Mouse Phenotyping Consortium (IMPC), this occurs at embryonic day (ED) 9.5 presumably due to improper neurological and cardiac development. To test this, Got2$^{+/-}$ breeders were used to generate Got2$^{+/+}$, Got2$^{+/-}$, and Got2$^{-/-}$ pups (**Fig. 7-1A**). No Got2$^{-/-}$ pups were identified, while Got2$^{+/+}$ and Got2$^{+/-}$ pups were born at the expected Mendelian ratios (**Fig. 7-1B**). This confirms Got2 loss is embryonic lethal. Next, embryos were isolated from pregnant Got2$^{+/-}$ dams on ED9.5. At this timepoint, Got2$^{-/-}$ embryos were identified (**Fig. 7-1C**), though more litters will need to be genotyped to determine if this is at the expected Mendelian ratios (**Fig. 7-1D**). Got2$^{-/-}$ embryos displayed a stark phenotype compared to Got2$^{+/+}$ and Got2$^{+/-}$ controls, despite being of similar developmental stage as determined by somite count. This included a turning defect, incomplete neural tube closure and forebrain development, stunted cardiac looping, and swelling around the heart (**Fig. 7-1C**), again in accordance with the IMPC publicly available data, and phenocopying certain aspects of human GOT2 insufficiency(2).

7.3 Keto diet and Got2$^{-/-}$ embryos

The MAS transfers reducing equivalents generated during glucose oxidation from the cytosol to the mitochondria for deposition into the electron transport chain to drive ATP production via oxidative phosphorylation (**Fig. 7-2A**). Disruption of the MAS caused by loss of GOT2 therefore disturbs redox balance and induces cytosolic NADH accumulation as electrons are unable to be transferred into the mitochondrial (**Fig. 7-2A**). Unlike glucose, ketones are oxidized in the mitochondria, generating mitochondrial

NADH and obviating the need for transport of NADH from the cytosol to the mitochondria (**Fig. 7-2A**). Therefore, I hypothesized that administering a high fat, ketogenic (keto) diet to pregnant $Got2^{+/-}$ females could rescue $Got2^{-/-}$ embryonic lethality(1). $Got2^{+/-}$ females were fed the keto diet for 1 week to induce ketosis before breeding with $Got2^{+/-}$ males. After checking plugs, pregnant females were monitored through gestation until birth, at which point neonates were genotyped (**Fig. 7-2B**). Elevated ketone levels were confirmed after one week in the serum of $Got2^{+/-}$ females on the keto diet compared to $Got2^{+/-}$ females on normal chow (**Fig. 7-2C**), while no difference was observed in blood glucose levels (**Fig. 7-2D**). Thus far, after two litters of 9 pups total, no $Got2^{-/-}$ pups have been born, though more litters and pups need to be generated to confirm lack of rescue with the keto diet (**Fig. 7-2E**).

7.4 Inducible Got2 deletion in adult mice

Since Got2 deletion is embryonic lethal, I also generated an inducible, whole-body Got2 knockout model to study loss of Got2 in the adult mouse (Ub-Cre^{ERT2};$Got2^{\Delta/\Delta}$) (**Fig. 7-3A**). Ub-Cre^{ERT2};$Got2^{+/+}$ and Ub-Cre^{ERT2};$Got2^{\Delta/+}$ littermate controls were generated in parallel (**Fig. 7-3A**). Tamoxifen was administered to these mice via oral gavage for 5 days followed by ad libitum tamoxifen chow for two weeks until experimental endpoint (**Fig. 7-3A**). Ub-Cre^{ERT2};$Got2^{\Delta/\Delta}$ mice exhibited modest but significant weight loss (**Fig. 7-3B**), and Got2 knockdown was confirmed in liver, brain, and small intestine (**Fig. 7-3C**). A complete blood cell (CBC) analysis of these mice also detected modest anemia (**Fig. 7-3D**) and perturbed leukocyte populations (**Fig. 7-3E**).

7.5 Discussion

Inborn errors of metabolism are inherited genetic defects that compromise enzymatic activity, proper metabolic flux, and induce a failure to thrive or lethality. While rare, mutations in the catalytic site of GOT2 result in devastating effects for patients. Therefore, a better understanding of the metabolic underpinnings for GOT2 deficiency could lead to better therapeutic options. This requires experimental models that adequately recapitulate human disease. For this reason, we generated two such models: a global constitutive Got2-null mouse and a tamoxifen-inducible, ubiquitously expressed Cre-driven Got2 floxed mouse. Got2 KO proved to be embryonic lethal at ED9.5 due to a turning defect and severe neurological and cardiac defects. Similarly, induction of Got2 loss in the adult mouse led to weight loss, anemia, and a disrupted immune profile. Collectively, these phenotypes mirror those reported in human disease and will serve as a launch pad for future mechanistic work described in Chapter 8.

7.6 Methods

Mouse studies

$Got2^{-/-}$ mice were generated for the Lyssiotis laboratory by Ozgene and were maintained in a pure C57BL/6J background. Ub-Cre^{ERT2} on a mixed background was a generous gift from Dr. Alec Kimmelman (NYU) and crossed into the $Got2^{f/f}$ model to generate the Ub-Cre^{ERT2};$Got2^{\Delta/\Delta}$ with appropriate littermate controls. Tails from 3-week-old mice were collected at weaning and submitted to Transnetyx for genotyping. The following primers were used: Got2 WT (Fw: GCAGATTAAAACCACAAGGCCTGTA, Rev: ATGTTAAAATTGTCATCCCCTTGTGC); Got2 floxed (Fw: GCAGATTAAAACCACAAGGCCTGTA, Rev:

AGAGAATAGGAACTTCGGAATAGGAACT); Cre (Fw: TTAATCCATATTGGCAGAACGAAAACG, Rev: CAGGCTAAGTGCCTTCTCTACA).

Experimental mice were maintained in SPF housing with access to standard diet and water ad libitum at constant ambient temperature and a 12-hour light cycle. High-fat, ketogenic diet (Envigo, Teklad TD.210721) was administered ad libitum. All experiments were conducted in accordance with the Office of Laboratory Animal Welfare and approved by the Institutional Animal Care and Use Committees of the University of Michigan.

Timed breeding and embryo isolation

$Got2^{+/-}$ male studs were placed with $Got2^{+/-}$ females in the evening. The next morning, females were checked for plugs with a sterile, metal probe. If found, this was considered ED0.5 and the plugged female was transferred to single housing. On ED9.5, the pregnant female was euthanized according to the IACUC protocol, the uterus was dissected, and embryos were imaged and flash frozen in liquid nitrogen. Embryonic yolk sacs were collected for genotyping.

Blood ketone and glucose measurement

After being fed normal chow or ketogenic diet for 7 days, blood was drawn from the tail veins of $Got2^{+/-}$ females. Blood ketone and glucose levels were determined using the Precision Xtra Blood Glucose and Ketone Measure kit.

RT-qPCR

RNA was isolated from mouse tissue using the RNeasy Plus Mini Kit (Qiagen #74134) and 1 µg of cDNA synthesized using the iScript kit (Biorad #1708891). The 20

µL cDNA samples were diluted in 80 µL water for a final volume of 100 µL. RT-qPCR was conducted using the Fast SYBR Green Master Mix (Thermo #4385612) according to the manufacturer's instructions. Primers for the indicated targets are as follows: 18S (Fw: GCAATTATTCCCCATGAACG, Rv: GGCCTCACTAAACCATCCAA); Got2 (Fw: AGAGAGATACCAACAGCAAGAAG, Rv: CAATGGGCAGGTATTCTTTGTC).

7.7 References

1. Broeks MH, van Karnebeek CDM, Wanders RJA, Jans JJM, Verhoeven-Duif NM. Inborn disorders of the malate aspartate shuttle. Journal of inherited metabolic disease. 2021;44(4):792-808. Epub 2021/05/16. doi: 10.1002/jimd.12402. PubMed PMID: 33990986; PMCID: PMC8362162.

2. van Karnebeek CDM, Ramos RJ, Wen XY, Tarailo-Graovac M, Gleeson JG, Skrypnyk C, Brand-Arzamendi K, Karbassi F, Issa MY, van der Lee R, Drögemöller BI, Koster J, Rousseau J, Campeau PM, Wang Y, Cao F, Li M, Ruiter J, Ciapaite J, Kluijtmans LAJ, Willemsen M, Jans JJ, Ross CJ, Wintjes LT, Rodenburg RJ, Huigen M, Jia Z, Waterham HR, Wasserman WW, Wanders RJA, Verhoeven-Duif NM, Zaki MS, Wevers RA. Bi-allelic GOT2 Mutations Cause a Treatable Malate-Aspartate Shuttle-Related Encephalopathy. American journal of human genetics. 2019;105(3):534-48. Epub 2019/08/20. doi: 10.1016/j.ajhg.2019.07.015. PubMed PMID: 31422819; PMCID: PMC6732527.

3. Diaz-Cuadros M, Miettinen TP, Skinner OS, Sheedy D, Díaz-García CM, Gapon S, Hubaud A, Yellen G, Manalis SR, Oldham WM, Pourquié O. Metabolic regulation of species-specific developmental rates. Nature. 2023;613(7944):550-7. doi: 10.1038/s41586-022-05574-4.

4. Solmonson A, Faubert B, Gu W, Rao A, Cowdin MA, Menendez-Montes I, Kelekar S, Rogers TJ, Pan C, Guevara G, Tarangelo A, Zacharias LG, Martin-Sandoval MS, Do D, Pachnis P, Dumesnil D, Mathews TP, Tasdogan A, Pham A, Cai L, Zhao Z, Ni M, Cleaver O, Sadek HA, Morrison SJ, DeBerardinis RJ. Compartmentalized metabolism supports midgestation mammalian development. Nature. 2022;604(7905):349-53. Epub 2022/04/08. doi: 10.1038/s41586-022-04557-9. PubMed PMID: 35388219; PMCID: PMC9007737 of Atavistik Bio. The other authors declare no competing interests.

5. Titov DV, Cracan V, Goodman RP, Peng J, Grabarek Z, Mootha VK. Complementation of mitochondrial electron transport chain by manipulation of the NAD+/NADH ratio. Science. 2016;352(6282):231-5. Epub 2016/04/29. doi: 10.1126/science.aad4017. PubMed PMID: 27124460; PMCID: PMC4850741.

6. Goodman RP, Markhard AL, Shah H, Sharma R, Skinner OS, Clish CB, Deik A, Patgiri A, Hsu YH, Masia R, Noh HL, Suk S, Goldberger O, Hirschhorn JN, Yellen G, Kim JK, Mootha VK. Hepatic NADH reductive stress underlies common variation in metabolic traits. Nature. 2020;583(7814):122-6. Epub 2020/05/29. doi: 10.1038/s41586-020-2337-2. PubMed PMID: 32461692; PMCID: PMC7536642.

7. Alcantara IC, Tapia APM, Aponte Y, Krashes MJ. Acts of appetite: neural circuits governing the appetitive, consummatory, and terminating phases of feeding. Nat Metab. 2022;4(7):836-47. Epub 2022/07/26. doi: 10.1038/s42255-022-00611-y. PubMed PMID: 35879462.

7.8 Figures

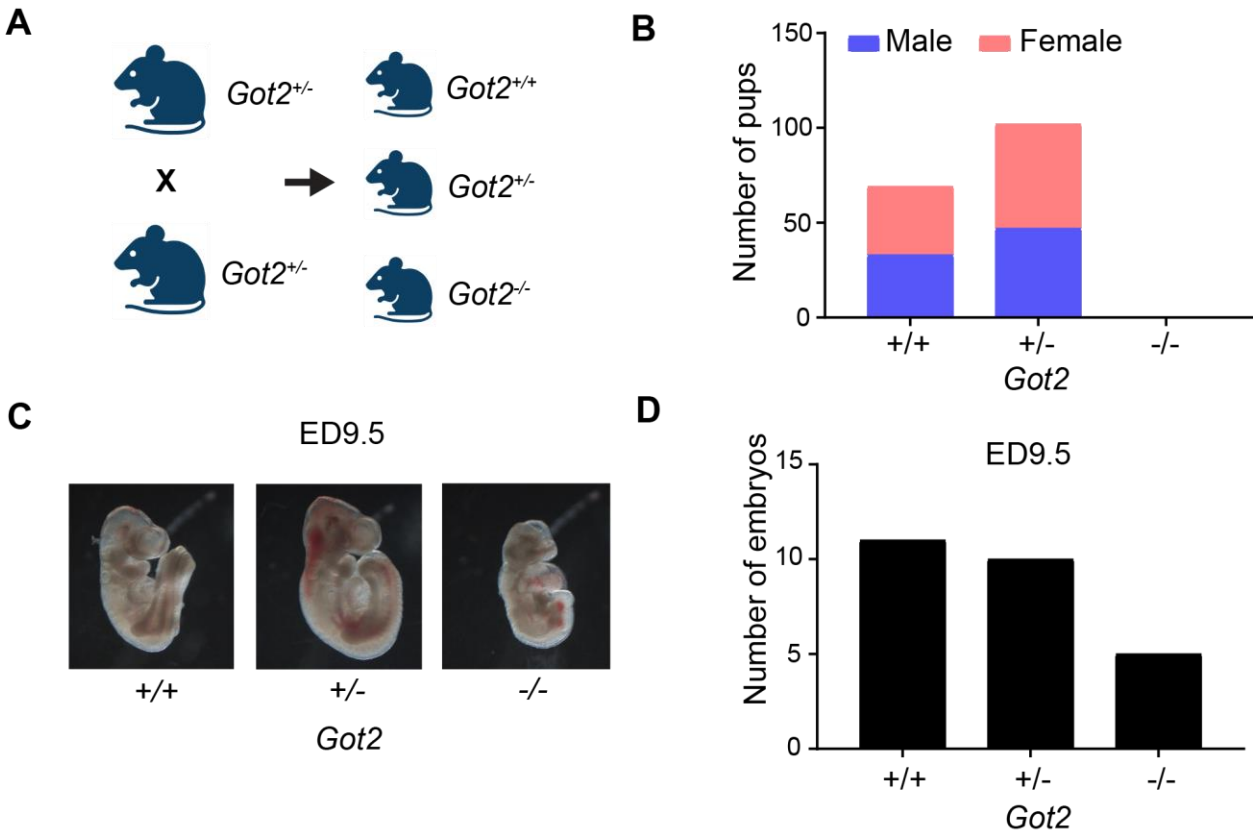

Figure 7-1 Got2 deletion is embryonic lethal

A) Schematic of the breeding scheme to generate Got2 wild-type, heterozygous, and homozygous deleted pups. **B)** Number of male and female pups of each indicated genotype generated from Got2 heterozygous crosses. **C)** Representative images of ED9.5 embryos of the indicated genotypes. **D)** Number of embryos of each indicated genotype generated from Got2 heterozygous crosses.

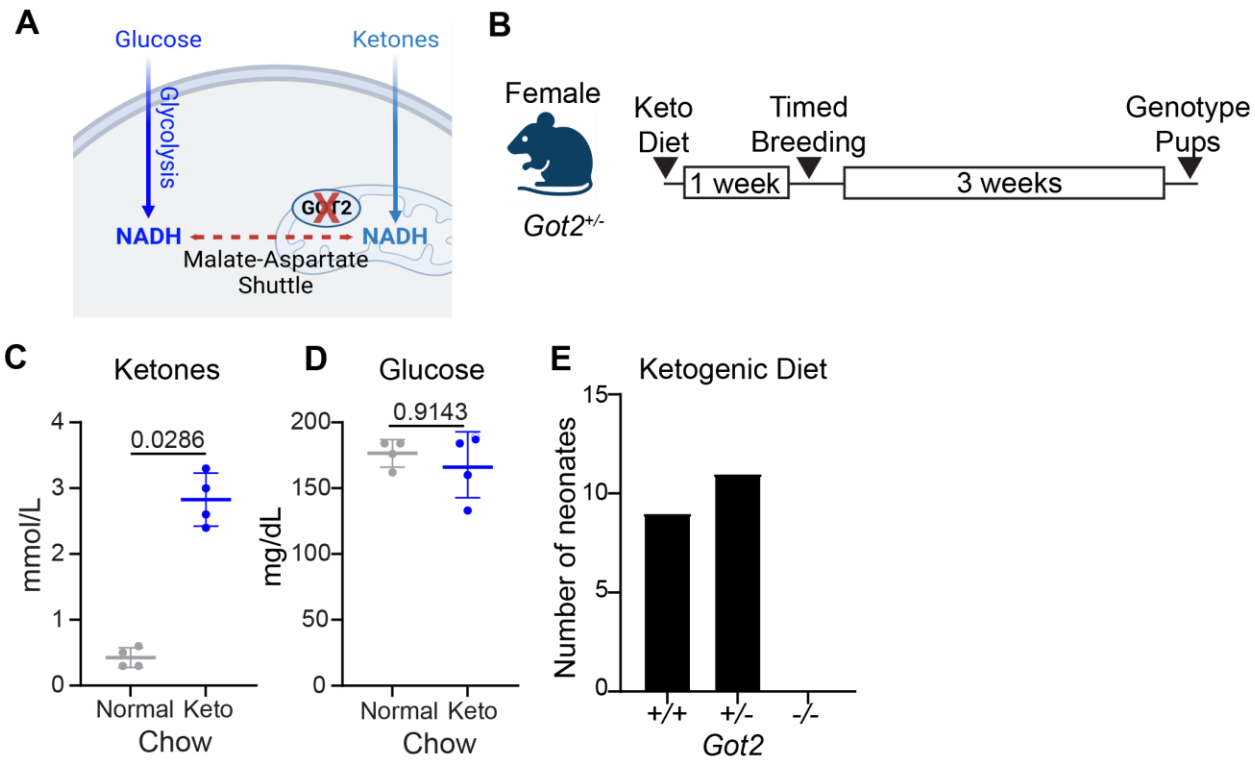

Figure 7-2 Ketogenic diet and Got2 embryonic lethality

A) Schematic depicting an impaired malate-aspartate shuttle with Got2 deletion and differential NADH generation from glucose or ketone oxidation. **B)** Experimental design for ketogenic diet rescue of Got2 embryonic lethality. **C)** Ketone and **D)** Glucose levels in the blood of Got2 heterozygous females after one week of ketogenic diet or normal chow. **E)** Number of neonates of each indicated genotype generated from Got2 heterozygous crosses with female breeders in ketosis.

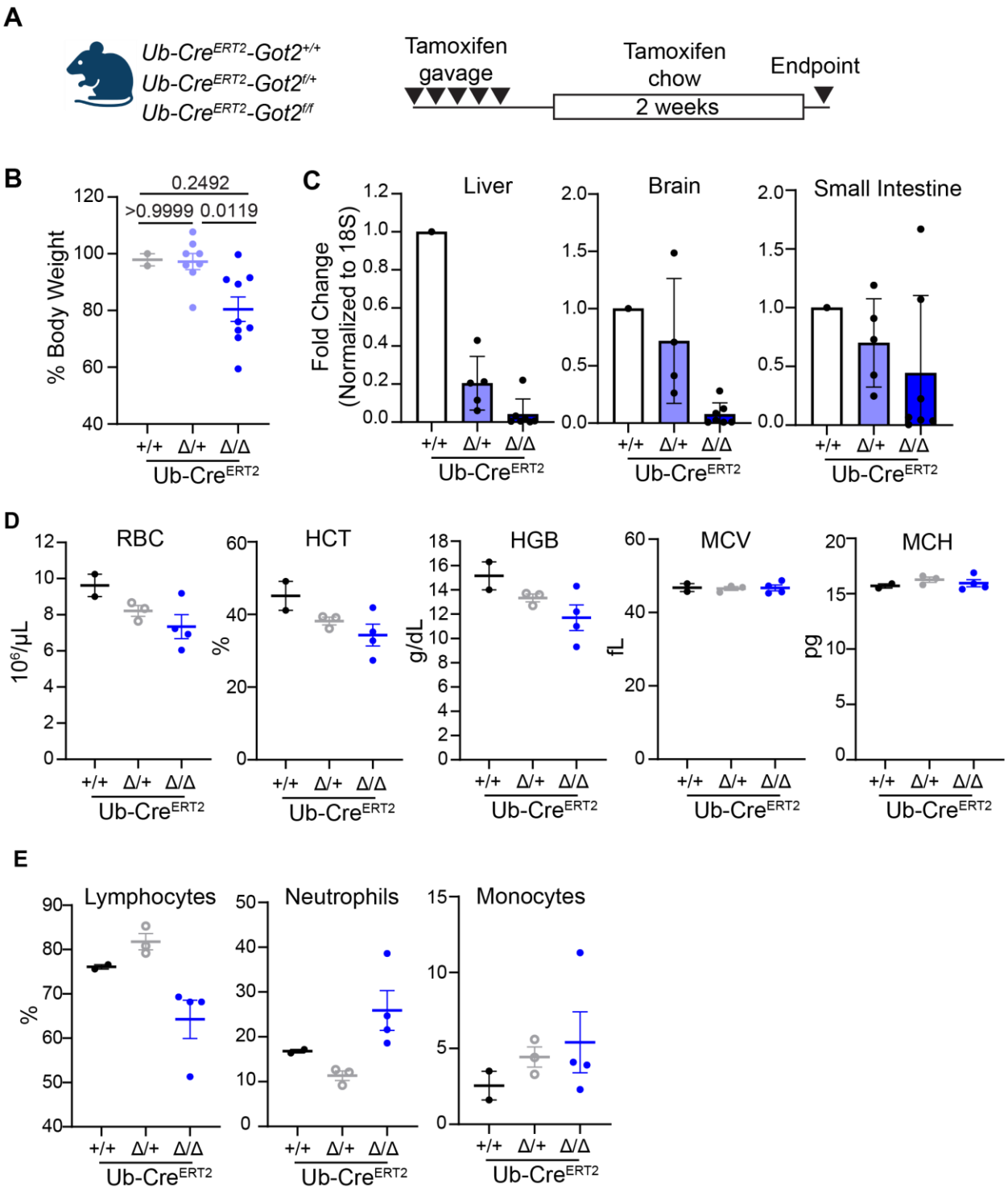

Figure 7-3 Inducible Got2 deletion in adult mice

A) Experimental design for tamoxifen-inducible deletion of Got2 in the whole body of adult mice, with appropriate littermate controls. **B)** Body weights of Got2 deleted mice and littermate controls at endpoint. **C)** RT-qPCR for relative levels of Got2 in brain, liver, and small intestine. Complete blood cell (CBC) analysis of **D)** red blood cells and **E)** leukocytes.

Chapter 8 – Future Directions & Conclusions

The work presented in Chapters 5-7 represents preliminary data for each project. As such, in this chapter, I will briefly discuss the next experiments that could be conducted to build on these initial findings. Finally, to conclude, I will discuss key concepts in cancer metabolism illustrated by these projects to distill the knowledge I have gained throughout my dissertation and will apply toward my future research endeavors.

8.1 Future Directions: Genetic Mouse Models of Got2 Loss in Pancreatic Cancer

For the KC-Got2$^{\Delta/\Delta}$ model, more mice are continuing to age to 6 months to increase the sample size in each group, with P/BW being recorded at endpoint. Got2 loss in pancreatic lesions will be confirmed via immunohistochemistry (IHC), as before. Hematoxylin and eosin (H&E) staining of this tissue will be analyzed by a blinded pathologist to quantify healthy acinar area, ADM, and PanINs. As an orthogonal approach, tissue will be analyzed for cytokeratin 19 (CK19, ductal) and amylase (acinar) expression via IHC. The ratio of CK19/amylase area is another indicator of transformation and lesion progression(1). Given previous findings with KC-Got2$^{\Delta/\Delta}$ compared to historic KC controls, Got2 loss is not expected to impact lesion number and/or severity. Finally, a more reductionist approach to understanding the role of Got2 in pancreatic tumorigenesis is to perform acinar preps to model ADM ex vivo(2, 3). Acinar cells from KC-Got2$^{\Delta/\Delta}$ and KC-Got2$^{+/+}$ mice will be cultured and transformation

and transition to ductal cell structures will be evaluated. This ex vivo approach is also amenable to -omics analyses. For instance, RNA sequencing could identify compensatory mechanisms for Got2 loss and metabolomics could be compared to our previous findings described in Chapter 4 with GOT2 knockdown in human PDA.

For the KPC-Got2$^{\Delta/\Delta}$ model, the survival experiment is ongoing to determine whether Got2 loss accelerates, impairs, or has no effect on pancreatic tumor growth. At endpoint, tumor tissue will be harvested, P/BW will be recorded, Got2 loss will be confirmed via IHC, and carcinoma severity will be evaluated by a blinded pathologist. As with the tumorigenesis model, Got2 loss is not expected to impact KPC tumor progression. Despite pursuing an expected negative phenotype, these studies will provide valuable information for the field given the recent debate regarding the role of Got2 in pancreatic cancer metabolism.

8.2 Future Directions: Metabolic Reprogramming of Macrophages via Got1/Got2 Deletion

Thus far, ex vivo metabolomics analysis and in vivo tumor studies suggest Got2 deletion in TAMs is insufficient to block dC production and improve gemcitabine efficacy. Tumor interstitial fluid (TIF) was isolated from the tumors described in **Fig. 6-6A,C**. An immediate future experiment is to quantify dC in TIF from LysM-Got2$^{\Delta/\Delta}$ or Got2$^{f/f}$. Furthermore, in vitro gemcitabine dose-response curves with PDA cell lines in conditioned media from LysM-Got2$^{\Delta/\Delta}$ TAMs will provide further indication if loss of Got2 impacts dC release. Given the lack of a decrease in extracellular dC observed in **Fig. 6-5D**, no difference in gemcitabine sensitivity is expected in vitro, similar to the in vivo results from **Fig. 6-6F,G**.

Cytosolic GOT1 and mitochondrial GOT2 catalyze reciprocal reactions at steady state, though given the proper conditions these reactions are bidirectional. Therefore, Got1 could compensate for loss of Got2 in TAMs, especially considering that while Got2 loss decreases aspartate levels in macrophages, aspartate is not completely ablated (**Fig. 6-4B**). To address this, further work will characterize the metabolic effects of Got1 loss in TAMs, similar to **Fig. 6-4 and 6-5**. Additionally, LysM-Got1/Got2 double knockout (DKO) mice are currently being generated.

Even if loss of both Got1 and Got2 completely block intracellular aspartate synthesis in macrophages, several cell-intrinsic mechanisms could support sustained dC levels in the tumor microenvironment (TME) and resistance to gemcitabine. First, macrophages are professional scavengers. The pancreatic TME is rich in extracellular matrix (ECM) protein, and engulfment of the ECM has been shown to be a source of protein for PDA cells. This mechanism could be similarly operant in TAMs to non-specifically supply aspartate and support pyrimidine biosynthesis even with Got1 and Got2 loss. Second, TAMs are not the only cell type to release dC. Pancreatic cancer-associated fibroblasts (CAFs) have also been shown to release dC, so blocking dC production in TAMs may be insufficient to lower overall tumor dC levels. Again, this possibility would be addressed by quantifying the dC levels in TIF from the tumor tissue from **Fig. 6-6A,C**. Finally, metabolite exchange between cancer cells and TAMs could also explain the lack of dC decrease with loss of Got2 in TAMs. Orotate is a metabolite downstream of aspartate in pyrimidine biosynthesis. Interestingly, orotate seems to be released by PDA cell lines and taken up by TAMs in vitro (**Fig. 6-5D**), however this potential crosstalk needs to be elucidated in greater mechanistic detail and in vivo.

Got1 and Got2 could also be involved in other pro-tumorigenic TAM functions. For instance, in **Fig. 6-3C,D** Got1 loss dampened pro-inflammatory Nos2 expression and promoted anti-inflammatory Arg1 expression, while Got2 promoted pro-inflammatory Nos2 and dampened anti-inflammatory Arg1. A more extensive characterization of the polarization state in Got1 or Got2 depleted macrophages could reveal a potential reciprocal phenotype. Additionally, in agreement with previous reports, the data shown in **Fig. 6-4B-D** demonstrate LPS-stimulated macrophages downregulate αKG. As proposed previously, a decreased αKG/succinate ratio alters the activity of epigenetic enzymes to support pro-inflammatory programs. Therefore, increasing or decreasing αKG via Got1 or Got2 deletion, respectively, could reprogram the polarization state of macrophages. In TAMs, this could also be measured by evaluating if loss of Got2 or Got2 affects T cell infiltration, or if conditioned media from these TAMs cultured ex vivo impacts T cell proliferation or killing.

The current data presented herein have primarily relied on BMDM polarization ex vivo. An alternative approach is to rapidly isolate TAMs directly from mouse pancreatic tumors. This can be accomplished using commercially available macrophage-specific bead isolation kits. Conducting unbiased transcriptomics and metabolomics analyses on both ex vivo polarized BMDMs and in vivo bead-isolated pancreatic TAMs from LysM-Got1, Got2, or Got1/Got2 DKO mice will provide a more complete picture of how Got1 and Got2 are involved in macrophage biology.

Lastly, further investigations into the role of Got2 in viral infection are warranted. While Got2 loss in myeloid cells had no effect on viral load or inflammation in the lungs following H1N1 influenza infection, which addresses our first proposed question, the

collected lung tissue could be analyzed for fibrosis markers to answer our second question. Also, this experiment was ended at an acute, 3-day timepoint; a longer timepoint might reveal subtle differences in overall host survival, viral burden, inflammation, and fibrosis. Additionally, influenza viruses also target epithelial cells(4). Therefore, this infection experiment could be repeated in a lung epithelial cell-specific or whole-body Got2 knockout model, such as the $Ub^{CreERT2}$;$Got2^{f/f}$ model discussed in Chapter 7. Finally, the H1N1 influenza virus is different from the viruses used to analyze the role of GOT2 in host metabolism in the aforementioned studies(5, 6). Exploratory experiments in both ex vivo and in vivo models of these viral infections could prove useful to identify strain-specific metabolic dependencies of other viral species.

8.3 Future Directions: Role of Got2 in Development and Normal Physiology

The phenotypes observed with Got2 loss in both the embryonic and adult mouse mirror those reported in humans with inborn errors in Got2 function(7). This includes impaired neurological and cardiac development along with difficulty feeding and weight loss. Future work will further characterize the mechanisms underlying these phenotypes and evaluating whether metabolic interventions can rescue loss of GOT2 function.

One next step is to characterize $Got2^{-/-}$ ED9.5 embryonic metabolism via metabolomics analysis of whole embryo lysates collected in Fig. 7-1D. ED9.5 is a critical metabolic timepoint in gestation whereby increased vascularization supplies more nutrients to the embryo, and increased organ size and development, specifically the nervous and cardiovascular systems, relies more heavily on elevated oxidative metabolism(8, 9). Indeed, the $Got2^{-/-}$ embryonic lethality phenotype is similar to the reported deficits in other mitochondrial enzymes(9). Therefore, I would expect to find the

reductive stress signature indicative of NADH accumulation along with TCA cycle perturbation, similar to the phenotypes observed with GOT2 loss in pancreatic cancer cells and tumor-associated macrophages and described in Chapters 4 and 6. Additionally, mouse embryonic fibroblasts (MEFs) could be generated from ED9.5 embryos and used to conducted in vitro growth assay metabolite rescue experiments, including supplementation with pyruvate, α-ketobutyrate, aspartate/α-ketoglutarate, and serine(7). MEFs could also be analyzed via metabolomics as an orthogonal approach to the metabolomics analysis on whole ED9.5 embryos.

While the ketogenic diet has not led to the birth of $Got2^{-/-}$ neonates, this experiment is ongoing, and more pups/litters are needed to definitively rule out this dietary intervention. Nevertheless, it is possible that embryos are not supplied with sufficient ketones even with elevated blood ketone levels in the pregnant female. To address this, both ED9.5 embryos and maternal placenta could be isolated from pregnant females on normal chow or ketogenic diet and analyzed via metabolomics. Finally, while the ketogenic diet should replenish the mitochondrial NADH pool during impaired MAS activity, it does not alleviate cytosolic NADH accumulation. A more direct intervention would involve the systemic expression of *Lactobacillus brevis* NADH oxidase (LbNOX) to more precisely oxidize cytosolic NADH (10), as was done in pancreatic cancer lines with GOT2 knockdown in Chapter 4. LbNOX has been expressed in mouse liver via adenovirus-mediated delivery (11). Given the metabolite exchange between mother and embryos, adeno-LbNOX injected into pregnant females could relieve the redox imbalance of $Got2^{-/-}$ embryos, though this would also need to be verified through metabolomics analyses of both placenta and embryo.

In the adult mouse, further work is required to determine the cause of the phenotype. Several tissue specific Got2 knockout models have been developed by our laboratory including in myeloid cells, pancreas, and intestinal epithelium, with no observable phenotypes (data not shown). The weight loss observed in Ub-Cre^{ERT2};Got2$^{\Delta/\Delta}$ mice has also been reported in human patients and could be explained in these mice by 1) a neurological defect impacting feeding circuitry (12), or 2) impaired nutrient absorption. Metabolic phenotyping on Ub-Cre^{ERT2};Got2$^{\Delta/\Delta}$ could measure food/water intake, oxygen consumption, and carbon dioxide release to more accurately determine which of these two options is responsible for the phenotype. Additionally, analysis of H&E from the tissue from Fig. 7-3B could inform which tissue type(s) is most impacted by Got2 deletion. Furthermore, additional metabolomics analyses on tissue and serum collected from Ub-Cre^{ERT2};Got2$^{\Delta/\Delta}$ mice and littermate controls could determine if this mouse model recapitulates the lactic acidemia and hyperammonemia described in human patients(13), as well as broad metabolic differences across tissue types. Lastly, similar interventions proposed for embryonic lethality rescue could also be tested in rescuing whole-body, inducible Got2 deletion in the adult mouse.

8.4 Conclusion

The work described herein has focused primarily on pancreatic cancer metabolism in an effort to better understand the fundamental biology of this dreadful disease, with the ultimate intent to develop more effective therapeutics. During my graduate tenure, these projects have taught me three critical lessons in cancer metabolism.

First, environmental context influences metabolic dependencies (**Fig. 8-1A**). The nutrients and metabolic byproducts surrounding pancreatic cancer cells dictate pathway flux. As such, rapidly growing cells in culture with media containing supraphysiological levels of certain metabolites, like glucose and glutamine, will employ different metabolism compared to slow growing tumors in human or mouse hosts. This is illustrated in Chapters 4 and 5 as GOT2 is required for in vitro, but not in vivo, pancreatic cancer cell growth. At the time I began this project, this differential usage of GOT2 presented an interesting phenomenon. Now, distinct in vitro and in vivo metabolism is practically canon in the field of cancer metabolism. Indeed, the context in which pancreatic cancer cells are studied is critical to accurately identify relevant metabolic pathways that could be targeted in human patients. Coupling intricate model systems involving both mice and humans with simpler, yet still powerful, in vitro systems could present a fuller picture of the metabolism employed by pancreatic cancer.

Second, crosstalk within pancreatic tumors compensates for metabolic interventions (**Fig. 8-1B**). For instance, previous work has demonstrated how the release of deoxycytidine from stromal and immune cells blunts the efficacy of the frontline chemotherapy gemcitabine in pancreatic cancer. In an attempt to block this mechanism, we targeted de novo pyrimidine synthesis in tumor-associated macrophages (TAMs), one of the primary culprits of elevated deoxycytidine in the tumor microenvironment. While we were able to successfully decrease aspartate, a building block for pyrimidines, in TAMs, we were unable to induce a subsequent decrease in dC production and release. Preliminary data indicate that orotate, a metabolite downstream of aspartate in de novo pyrimidine synthesis, is released by pancreatic cancer cells and

taken up by TAMs. This presents an intriguing, yet complicated, potential metabolic crosstalk whereby cancer cells release orotate to sustain pyrimidine production and dC release from TAMs as a survival mechanism against gemcitabine treatment. If correct, even dual treatment with gemcitabine and a de novo pyrimidine synthesis inhibitor could still prove ineffective against a pancreatic tumor. Therefore, metabolic crosstalk must be considered when investigating the metabolism of pancreatic cancer and designing novel therapies.

Thirdly, developmental metabolic pathways are inappropriately activated or hijacked in tumors (**Fig. 8-1C**). Furthermore, the intersection of developmental and cancer biology can inform treatments for either developmental defects or cancer. For example, GOT2 loss in pancreatic cancer cells is detrimental to growth in vitro. In Chapter 4, we described how we were able to rescue proliferation using chemical and genetic interventions to alleviate reductive stress. Additionally, pancreatic cancer cells are able engage similar mechanisms to grow without GOT2 in vivo. In contrast, loss of GOT2 activity is embryonic lethal in mice and induces a failure to thrive in adult mice and human patients. As such, the same rescue mechanisms utilized to study how GOT2 is involved in cancer metabolism could instead be used to benefit human patients with inborn errors of GOT2 metabolism. On the other hand, investigations into why GOT2 is embryonic lethal could shed light on pathways inactive in developing embryos that are inappropriately active in pancreatic cancer cells.

In conclusion, pancreatic cancer metabolism is complex and highly dynamic. As such, studying metabolism in the relevant context, considering metabolic networks between cancer cells and the broader tumor milieu, and utilizing seemingly diverse yet

potentially convergent systems are crucial emerging concepts in the field. This dissertation has aimed to highlight these principles to provide some benefit to ongoing and future work in pancreatic cancer metabolism.

8.5 References

1. Collins MA, Bednar F, Zhang Y, Brisset JC, Galbán S, Galbán CJ, Rakshit S, Flannagan KS, Adsay NV, Pasca di Magliano M. Oncogenic Kras is required for both the initiation and maintenance of pancreatic cancer in mice. J Clin Invest. 2012;122(2):639-53. Epub 2012/01/11. doi: 10.1172/jci59227. PubMed PMID: 22232209; PMCID: PMC3266788.

2. Wang L, Yang H, Zamperone A, Diolaiti D, Palmbos PL, Abel EV, Purohit V, Dolgalev I, Rhim AD, Ljungman M, Hadju CH, Halbrook CJ, Bar-Sagi D, di Magliano MP, Crawford HC, Simeone DM. ATDC is required for the initiation of KRAS-induced pancreatic tumorigenesis. Genes Dev. 2019;33(11-12):641-55. Epub 2019/05/03. doi: 10.1101/gad.323303.118. PubMed PMID: 31048544; PMCID: PMC6546061.

3. Liou GY, Döppler H, DelGiorno KE, Zhang L, Leitges M, Crawford HC, Murphy MP, Storz P. Mutant KRas-Induced Mitochondrial Oxidative Stress in Acinar Cells Upregulates EGFR Signaling to Drive Formation of Pancreatic Precancerous Lesions. Cell Rep. 2016;14(10):2325-36. Epub 2016/03/08. doi: 10.1016/j.celrep.2016.02.029. PubMed PMID: 26947075; PMCID: PMC4794374.

4. Yu WC, Chan RW, Wang J, Travanty EA, Nicholls JM, Peiris JS, Mason RJ, Chan MC. Viral replication and innate host responses in primary human alveolar epithelial cells and alveolar macrophages infected with influenza H5N1 and H1N1 viruses. J Virol. 2011;85(14):6844-55. Epub 2011/05/06. doi: 10.1128/jvi.02200-10. PubMed PMID: 21543489; PMCID: PMC3126566.

5. Bojkova D, Klann K, Koch B, Widera M, Krause D, Ciesek S, Cinatl J, Münch C. Proteomics of SARS-CoV-2-infected host cells reveals therapy targets. Nature. 2020;583(7816):469-72. Epub 2020/05/15. doi: 10.1038/s41586-020-2332-7. PubMed PMID: 32408336.

6. Wang P, Xu J, Wang Y, Cao X. An interferon-independent lncRNA promotes viral replication by modulating cellular metabolism. Science. 2017;358(6366):1051-5. Epub 2017/10/28. doi: 10.1126/science.aao0409. PubMed PMID: 29074580.

7. van Karnebeek CDM, Ramos RJ, Wen XY, Tarailo-Graovac M, Gleeson JG, Skrypnyk C, Brand-Arzamendi K, Karbassi F, Issa MY, van der Lee R, Drögemöller BI, Koster J, Rousseau J, Campeau PM, Wang Y, Cao F, Li M, Ruiter J, Ciapaite J, Kluijtmans LAJ, Willemsen M, Jans JJ, Ross CJ, Wintjes LT, Rodenburg RJ, Huigen M, Jia Z, Waterham HR, Wasserman WW, Wanders RJA, Verhoeven-Duif NM, Zaki MS,

Wevers RA. Bi-allelic GOT2 Mutations Cause a Treatable Malate-Aspartate Shuttle-Related Encephalopathy. American journal of human genetics. 2019;105(3):534-48. Epub 2019/08/20. doi: 10.1016/j.ajhg.2019.07.015. PubMed PMID: 31422819; PMCID: PMC6732527.

8. Diaz-Cuadros M, Miettinen TP, Skinner OS, Sheedy D, Díaz-García CM, Gapon S, Hubaud A, Yellen G, Manalis SR, Oldham WM, Pourquié O. Metabolic regulation of species-specific developmental rates. Nature. 2023;613(7944):550-7. doi: 10.1038/s41586-022-05574-4.

9. Solmonson A, Faubert B, Gu W, Rao A, Cowdin MA, Menendez-Montes I, Kelekar S, Rogers TJ, Pan C, Guevara G, Tarangelo A, Zacharias LG, Martin-Sandoval MS, Do D, Pachnis P, Dumesnil D, Mathews TP, Tasdogan A, Pham A, Cai L, Zhao Z, Ni M, Cleaver O, Sadek HA, Morrison SJ, DeBerardinis RJ. Compartmentalized metabolism supports midgestation mammalian development. Nature. 2022;604(7905):349-53. Epub 2022/04/08. doi: 10.1038/s41586-022-04557-9. PubMed PMID: 35388219; PMCID: PMC9007737 of Atavistik Bio. The other authors declare no competing interests.

10. Titov DV, Cracan V, Goodman RP, Peng J, Grabarek Z, Mootha VK. Complementation of mitochondrial electron transport chain by manipulation of the NAD+/NADH ratio. Science. 2016;352(6282):231-5. Epub 2016/04/29. doi: 10.1126/science.aad4017. PubMed PMID: 27124460; PMCID: PMC4850741.

11. Goodman RP, Markhard AL, Shah H, Sharma R, Skinner OS, Clish CB, Deik A, Patgiri A, Hsu YH, Masia R, Noh HL, Suk S, Goldberger O, Hirschhorn JN, Yellen G, Kim JK, Mootha VK. Hepatic NADH reductive stress underlies common variation in metabolic traits. Nature. 2020;583(7814):122-6. Epub 2020/05/29. doi: 10.1038/s41586-020-2337-2. PubMed PMID: 32461692; PMCID: PMC7536642.

12. Alcantara IC, Tapia APM, Aponte Y, Krashes MJ. Acts of appetite: neural circuits governing the appetitive, consummatory, and terminating phases of feeding. Nat Metab. 2022;4(7):836-47. Epub 2022/07/26. doi: 10.1038/s42255-022-00611-y. PubMed PMID: 35879462.

13. Broeks MH, van Karnebeek CDM, Wanders RJA, Jans JJM, Verhoeven-Duif NM. Inborn disorders of the malate aspartate shuttle. Journal of inherited metabolic disease. 2021;44(4):792-808. Epub 2021/05/16. doi: 10.1002/jimd.12402. PubMed PMID: 33990986; PMCID: PMC8362162.

8.6 Figures

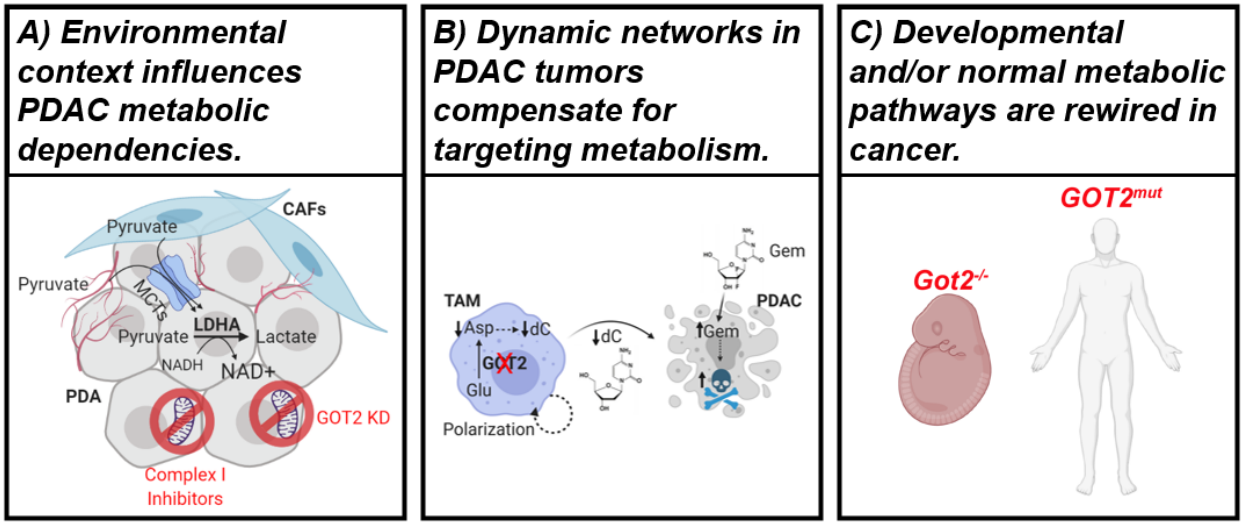

Figure 8-1 Key concepts in cancer metabolism